



UNIVERSITY OF
LIVERPOOL

Photocatalytic Materials for the Reduction of CO₂ to Fuels

Verity L. Piercy

Prof. M. J. Rosseinsky and Prof. A. J. Cowan

Thesis submitted to the University of Liverpool in partial fulfilment of the
degree of Doctor in Philosophy.

February 2021

Department of Chemistry and Stephenson Institute for Renewable Energy

Abstract

Photocatalytic Materials for the Reduction of CO₂ to Fuels

Verity Piercy

The production of solar fuels has become a topic of great interest in recent years. The focus of this work has been to study a range of photocatalytic materials and assessment of their activity towards solar fuel generation, specifically water splitting coupled with CO₂ reduction for CO and H₂ production in aqueous solution in the presence of charge scavengers. The materials chosen for study in this project can be split in to two distinct classes: carbon nitrides and metal oxides.

Carbon nitride is a well-known photocatalytic material that has been applied to a variety of applications, including fuel generation. A range of carbon nitride materials were synthesised using different conditions and precursors and characterised to understand and tune the band structure of the materials towards improved photocatalytic CO₂ reduction. Materials were characterised by elemental analysis (CHN), powder X-ray diffraction (PXRD), diffuse reflectance infrared Fourier transform spectroscopy (DRIFTS), UV-Vis spectroscopy, X-ray photoelectron spectroscopy (XPS), Mott-Schottky, steady state photoluminescence, Raman spectroscopy, transient absorption spectroscopy (TAS) and time resolved resonant Raman spectroscopy (TR³), among others. It was found that incorporation of barbituric acid into the carbon nitride structure led to carbon doping, decreased band gap, enhanced charge lifetimes and variations in band structure and gave improved photocatalytic H₂ production for the bulk materials. On their own, the bulk carbon nitrides were not capable of performing CO₂ reduction, so modification of the materials was investigated. A number of different methods for modification were explored including exfoliation and attachment of co-catalysts (NiCyc, NiCycC, NiCycP and FeTCPP). The highest activity for photocatalytic CO₂ reduction to CO and H₂ was obtained for the high surface area 5% barbituric acid doped carbon nitride combined with the FeTCPP molecular catalyst in 10% TEOA solution under UV-Vis illumination.

In comparison to the carbon nitride materials, the metal oxides synthesised within this work (CuFeO_2 , CuCrO_2 , CuAlO_2 , CuRhO_2 , CuNbO_3 and CuNb_3O_8) have been studied as photocatalysts only a handful of times. These materials were synthesised and characterised via PXRD, UV-Vis spectroscopy, BET surface area, scanning electron microscopy and energy-dispersive X-ray spectroscopy. Photocatalysts were then tested for photocatalytic CO_2 reduction in the presence of NiCycP molecular co-catalyst and EDTA hole scavenger. Unfortunately, it was found that none of the metal oxides presented in this work were capable of CO_2 reduction, which is likely due to low surface areas leading to poor catalyst absorption and in turn low/no activity.

Acknowledgements

Throughout my PhD studies there have been so many people who have helped and supported me. Without them none of this would have been possible. Here I would like to express my gratitude to just some of the many people in my life that have supported me and contributed to my work.

First of all, I would like to express my utmost gratitude to both of my supervisors, Prof. Matt Rosseinsky and Prof. Alex Cowan, for giving me the opportunity to do this PhD and work alongside some fantastic scientists. You have both provided me with invaluable guidance, help and support over the course of my studies and have always pushed me to do the best science that I can and not accepting silly mistakes, I am a better scientist for having worked with you both.

Thank you to members of the Rosseinsky group who have provided me with vital input and advice over the years, specifically the wider supervisory team including Dr John Claridge, Dr Mike Pitcher, Dr Luke Daniels and Dr Alex Katsoulidis. Thank you to Dr Marco Zanella, Dr Hongjun Nui, Richard Feetham, Dr Wesley Surta and Dr Alex Grigoropoulos for your support and help in the lab. I would especially like to thank my research co-ordinator Dr Troy Manning for being there when I've needed help. Thank you for putting up with my constant questions and emails and the occasional breakdown in your office.

To my collaborators, colleagues and those who provided me with help on experimental work and data analysis, I would like to say thank you. Thank you to Prof. Vinod Dhanak and Prof. Robert Palgrave for your help with XPS measurements and thank you to members of Vin's group, Dr Jose Coca-Clemente, Holly Edwards, Huw Shiel, Leanne Jones and Hatem Amlı, who helped me so much with using the equipment and running measurements. Thank you to Dr Marco Zanella and Liam Banerji for running SEM measurements for me. Thank you to Dr Igor Sazanovich for all your help during our visit at the CLF. Thank you to Dr Mark Forster and Khezar Saeed for all your spectroscopy help, especially with TAS. Thank you to Dr Frederic Blanc and Andrea Pugliese for your help with the solid-state NMR measurements and analysis. I would also like to thank my colleagues in the SIRE who have helped me, including

Dr Alex Neale, Dr Tom Galloway, and Dr Mike Graham. I would especially like to thank Vince Vasey for all his help whenever I asked him, including helping with fume hoods, gas cylinders, GC maintenance and the building of the high throughput set up.

As a whole, I would like to thank both past and present members of the Cowan and Rosseinsky research groups. During my time at Liverpool, it has been a pleasure to work with you all. I couldn't possibly thank each of you individually, but I will highlight just a few of you who have been there for me: Dr Charlotte Smith, Will Thomas, Jess Smith, Tolly Robinson, Bernhard Leube, Rachel Kearsey, Daniel Cheung, Dr Stefano Mensa, Alicia Garcia Osorio, Francesca Greenwell, Dr Jin Jiarui, Dr Pamela Carrillo Sanchez, Oliver Rogan, Ben Greeves, Dr Jason Jackson, Dr Luis Alvarado Rupflin and Dr Laura Mears. This is by no means an exhaustive list and I am sorry to those of you I have not mentioned.

Thank you, Gaia, for all your help and support, you have always been there for me, helping me both in and out of the lab and long after you left. I'm not sure how you have put up with my constant questions, but I am so grateful that you have.

Thank you to my family and friends, you have all been so supportive and helpful during these tough times. A special thanks must go to my parents, without you I would literally not exist and would not be where I am today without your love and support. You have taught me so much and have always been there when I have needed you.

To my fiancé James, words alone cannot thank you for all that you have done and do for me each day. You are my best friend and my partner in everything that I do. Together we have achieved so much, from undergraduate degrees and throughout our PhDs, who knows what we might accomplish together in the future.

For these and many more reasons, I dedicate this thesis to my parents and my fiancé, I cannot thank the three of you enough and I hope this small token shows how much I appreciate you all.

List of Abbreviations

Commonly abbreviated terms used throughout this thesis are listed below and will be explained the first time they are used within the main text.

BA	Barbituric Acid
BET	Brunner-Emmett-Teller
CB	Conduction Band
CH ₃ OH	Methanol
CH ₄	Methane
CHN	Elemental Analysis
CLF	Central Laser Facility
CN	Carbon Nitride
CO	Carbon Monoxide
CO ₂	Carbon Dioxide
CP	Cross Polarisation
Cyc	1,4,8,11-tetraazacyclotetradecane
CycC	1,4,8,11-tetraazacyclotetradecane-6-carboxylic acid
CycP	1,4,8,11-tetraazacyclotetradecan-1-yl(methylene)phosphonic acid
DCDA	Dicyandiamide
DRIFTS	Diffuse Reflectance Infrared Fourier Transform Spectroscopy
DRS	Diffuse Reflectance Spectroscopy
e ⁻	Electron
EC	Electrochemical Cell
EDTA	Ethylenediaminetetraacetic acid disodium salt
EDX	Energy-Dispersive X-ray Spectroscopy
FeTCPP	Fe(III) meso-Tetra(4-carboxyphenyl)porphine chloride
FT	Fourier Transform
FTIR	Fourier Transform Infrared Spectroscopy
FTO	fluorine-doped tin oxide
GC	Gas Chromatography
GC/MS	Gas Chromatography-Mass Spectrometry
H ⁺	Proton
h ⁺	Hole
H ₂	Hydrogen
H ₂ O	Water
H ₂ SO ₄	Sulphuric Acid
HCHO	Formaldehyde
HCl	Hydrochloric Acid
HCOOH	Formic Acid
HOMO	Highest Occupied Molecular Orbital
HSA	High surface area
HT	High Throughput
IC	Ion Chromatography
ICP OES	Inductively Coupled Plasma Optical Emission Spectroscopy

IPA	Isopropyl Alcohol
IPCE	Incident Photon-to-Current Efficiency
IRF	Instrument Response Function
IUPAC	International Union of Pure and Applied Chemistry
KG	Kerr-Gated
LED	Light Emitting Diode
LUMO	Lowest Unoccupied Molecular Orbital
MAS	Magic Angle Spinning
MeCN	Acetonitrile
MOF	Metal Organic Framework
MS	Mott-Schottky
N ₂	Nitrogen
NHE	Normal Hydrogen Electrode
NMP	n-methyl-2-pyrrolidine
NMR	Nuclear Magnetic Resonance Spectroscopy
O ₂	Oxygen
OTEC	Ocean Thermal Energy Conversion
PEC	Photoelectrochemical Cell
PL	Photoluminescence
PTFE	Polytetrafluoroethylene
PV	Photovoltaic
PXRD	Powder X-ray Diffraction
SEC	Secondary Electron Cut-off
SEM	Scanning Electron Microscopy
SS NMR	Steady State Nuclear Magnetic Resonance
TA	Transient Absorption
TAS	Transient Absorption Spectroscopy
TEOA	Triethanolamine
TR3	Time Resolved Resonant Raman Spectroscopy
UV	Ultraviolet
UV-Vis	Ultraviolet-Visible Spectroscopy
UV-Vis-NIR	Ultraviolet-Visible-Near Infrared Spectroscopy
VB	Valence Band
VBM	Valence Band Maximum
WF	Work Function
XPS	X-ray Photoelectron Spectroscopy

Contents

Abstract	i
Acknowledgements	iii
List of Abbreviations	v
Contents	vii
1. Introduction	1
1.1 Renewable Energy	2
1.2 Utilisation of Solar Energy	3
1.2.1 Water Splitting	5
1.2.2 CO ₂ Reduction	5
1.3 Principles of Semiconductor Photocatalysis	8
1.4 Photocatalytic Materials	11
1.4.1 Inorganic Materials	11
1.4.2 Carbon-Based Materials	12
1.5 Improving Semiconductor Photocatalytic Activity	13
1.5.1 Photocatalyst modification	13
1.5.2 Co-catalysts	14
1.5.3 Sensitisation	15
1.5.4 Formation of heterojunctions	16
1.6 General Issues with Semiconductor Photocatalytic CO ₂ Reduction	18
1.7 Thesis Overview	21
1.8 References	22
2. Experimental and Analytical Methods and Set-up Development	26
2.1 Materials and Synthesis	27
2.1.1 Metal Oxides	27
2.1.1.1 Delafossites	27
2.1.1.2 Niobates	28
2.1.2 Carbon Nitrides	28
2.1.2.1 Barbituric Acid Series (CN-BA)	28
2.1.2.2 Varying Calcination Conditions Series (CN-Temp and CN-Time)	29
2.1.2.3 Varying Precursors (CN-Precursor)	29
2.1.2.4 Varying Precursor Ratios (CN-UT)	29
2.2 Modification of Materials	30
2.3 Characterisation	31
2.3.1 General Methods	31
2.3.2 Powder X-ray Diffraction (PXRD)	31

2.3.3	Diffuse Reflectance Infrared Fourier Transform Spectroscopy (DRIFTS)	31
2.3.4	Cross Polarisation (CP) Magic Angle Spinning (MAS) Solid State Nuclear Magnetic Resonance (SS NMR).....	32
2.3.5	Scanning Electron Microscopy (SEM) and Energy-Dispersive X-ray Spectroscopy (EDX).....	32
2.3.6	Ultraviolet- Visible-Near Infrared (UV-Vis-NIR) Spectroscopy	33
2.3.7	X-ray Photoelectron Spectroscopy (XPS).....	34
2.3.8	Mott-Schottky (MS) Measurement	37
2.3.9	Steady-State Photoluminescence (PL) and Time-Resolved Emission Lifetime Spectroscopy	39
2.3.10	Transient Absorption (TA) Spectroscopy	41
2.3.11	Fourier Transform (FT) and Kerr-Gated (KG) Raman and Time Resolved Resonant Raman (TR ³).....	43
2.4	Photocatalytic Testing	48
2.4.1	Xe Lamp Photocatalysis.....	49
2.4.2	High Throughput (HT) Photocatalysis	50
2.5	References	54
3.	Carbon Nitrides	56
3.1	Introduction.....	57
3.1.1	History	57
3.1.2	Structure and Formation	60
3.1.3	Properties	62
3.1.4	Photocatalysis	63
3.1.5	Electronic Structure Modification.....	65
3.1.5.1	Element Doping.....	66
3.1.5.2	Co-polymerisation or Molecular doping.....	67
3.2	Aim of Work.....	68
3.3	Results and Discussion	72
3.3.1	Synthesis and Initial Characterisation	72
3.3.1.1	Elemental Analysis (CHN).....	73
3.3.1.2	Surface Area Measurement	75
3.3.1.3	Powder X-ray Diffraction (PXRD).....	77
3.3.1.4	Scanning Electron Microscopy (SEM)	81
3.3.1.5	Diffuse Reflectance Infrared Fourier Transform Spectroscopy (DRIFTS)	82
3.3.1.6	X-ray Photoelectron Spectroscopy (XPS) Surface States	85
3.3.1.7	Cross Polarisation (CP) Magic Angle Spinning (MAS) Solid State Nuclear Magnetic Resonance (SS NMR)	90
3.3.1.8	Ultraviolet-Visible-Near Infrared (UV-Vis-NIR) Spectroscopy	92
3.3.2	Photocatalytic Testing	94
3.3.2.1	Baseline Photocatalytic Activity.....	94
3.3.3	Time Resolved and Transient Studies	98

3.3.3.1	Steady-State Photoluminescence (PL) and Time-Resolved Emission Lifetime spectroscopy	98
3.3.3.2	Transient Absorption (TA) Spectroscopy	100
3.3.3.3	Raman Spectroscopy	104
3.3.4	Band Structure Determination	115
3.3.4.1	Mott-Schottky (MS) Method	115
3.3.4.2	XPS Band Structure	117
3.4	Conclusions and Future Work	121
3.5	References	124

4. Carbon Nitride Hybrid Materials 132

4.1	Introduction.....	133
4.1.1	Nanostructure Control	133
4.1.1.1	Exfoliation (top-down)	133
4.1.1.2	Templating (bottom-up)	135
4.1.2	Heterostructure formation	137
4.1.2.1	Metal Particles	137
4.1.2.2	Dye-Sensitised	137
4.1.2.3	Molecular co-catalysts	138
4.1.2.4	Semiconductor Heterojunctions	139
4.1.2.5	Metal-Organic Framework (MOF) Composites	139
4.1.2.6	Carbon Based Systems	140
4.2	Aim of Work.....	141
4.3	Results and Discussion	144
4.3.1	Initial Attachment and Screening of Co-catalysts	144
4.3.2	Exfoliation of Carbon nitrides	149
4.3.2.1	Characterisation	149
4.3.2.2	Photocatalytic Activity	157
4.3.3	Attachment of Co-catalysts to High Surface Area Materials.....	158
4.3.3.1	Characterisation	159
4.3.3.2	Photocatalytic Activity	164
4.4	Conclusions and Future work.....	177
4.5	References	179

5. Metal Oxides and Hybrid Materials 186

5.1	Introduction.....	187
5.2	Aim of Work.....	188
5.2.1	Materials and Previous Activity	189
5.2.1.1	Delafossite Materials	189
5.2.1.2	Copper Niobate Materials	196

5.2.2	This Work	198
5.3	Results and Discussion	200
5.3.1	Synthesis and Characterisation	200
5.3.1.1	Powder X-ray Diffraction (PXRD).....	200
5.3.1.2	Ultraviolet-Visible-Near Infrared (UV-Vis-NIR) Spectroscopy	202
5.3.1.3	Surface Area Measurement	204
5.3.1.4	Scanning Electron Microscopy (SEM) and Energy-Dispersive X-ray Spectroscopy (EDX).....	205
5.3.2	Photocatalytic Testing	209
5.3.2.1	H ₂ Evolution Studies.....	209
5.3.2.2	CO ₂ Reduction	211
5.4	Conclusions and Future Work.....	222
5.5	References	224
6. Conclusions and Future Work.....		229
i. Appendix		234
i.i	Carbon Nitride XPS Surface States Spectra	235

1

Introduction

1.1 Renewable Energy

The development of renewable energy technologies has gained much attention in recent years due to the ever-increasing global energy demand and decreasing fossil fuel stocks.¹² The burning of these fossil fuels has led to increased amounts of atmospheric CO₂, leading to increased global temperatures; therefore, the development of clean energy resources is crucial to slow the effects of global warming. There are several renewable energy sources (i.e. wind, waves, geothermal heat) that provide clean energy and many methods have been employed to utilise these resources.³ Solar energy is a promising route to sustainable energy as it is a supposedly infinite energy source.^{4,5}

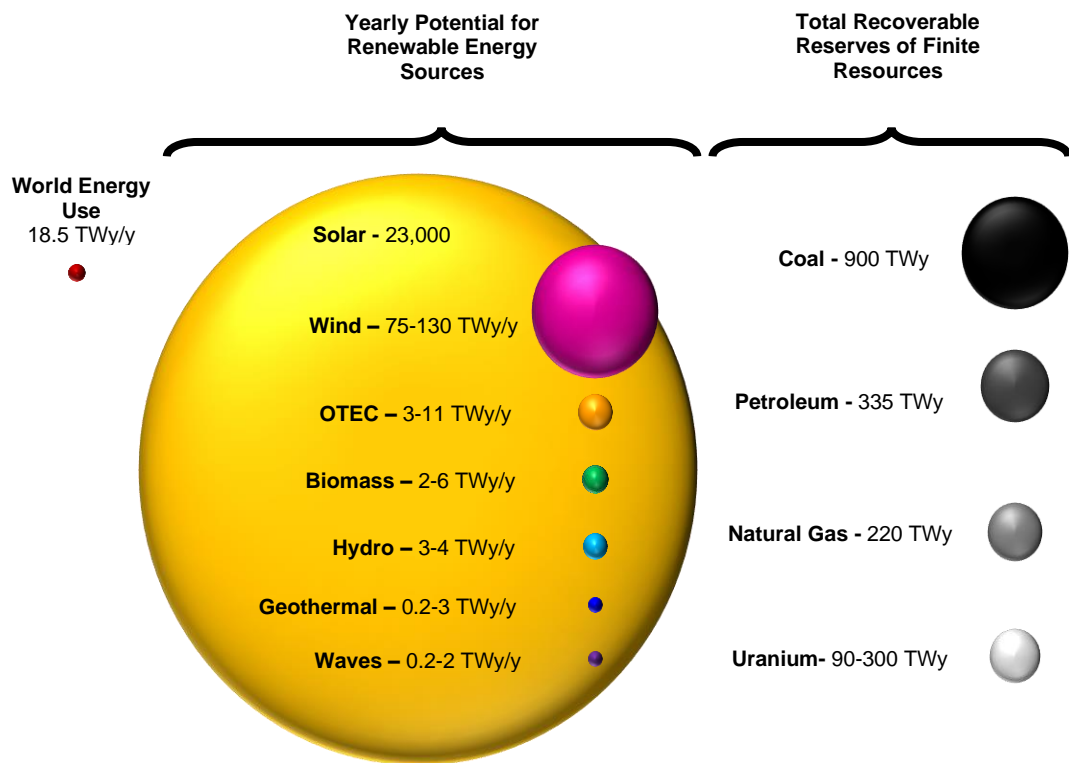


Figure 1 - Depiction of the yearly potential of renewable energy resources compared with the world energy use in Terawatt-years per year and the total recoverable reserves of finite resources in Terawatt-years as of 2015. Source: IEA SHC solar update 2015.⁶

1.2 Utilisation of Solar Energy

Despite solar energy being the most abundant, it can be difficult to utilise efficiently due to it being intermittent and unreliable.^{2,7-9} The viable ways to use this energy include capture and conversion to electrical or chemical energy. There are a number of ways that solar energy can be utilised and stored. One of the more common methods is the use of photovoltaic cells which can convert solar energy into electrical energy. This energy must then be used immediately or it can be stored in a second device, such as batteries for later use, these batteries can then be re-charged and used again and again.^{10,11} However, this is not the best way to store energy for use in the transportation sector e.g. boats and aeroplanes. Theoretically, based on current battery technologies, the battery needed for these larger transport vehicles is much larger than the actual vehicle. Another way to store this energy is within chemical bonds, as solar fuels, via a process analogous with natural photosynthesis.

Harnessing this solar energy to drive the production of fuels from available feedstocks, such as CO₂ and H₂O, is a route towards renewable energy which has gained a lot of attention in recent years. This area of research began with 'water splitting' to generate hydrogen.^{12,13} The first report of photoelectrochemical hydrogen production using a semiconductor electrode was published in 1972.¹⁴ Fujishima and Honda reported the use of a TiO₂ photoelectrode capable of splitting water under ultraviolet (UV) illumination. Over the past 50 years or so, there have been great developments in the field of solar fuel production. There are three main ways that are typically used to generate solar fuels:

- Photovoltaic (PV) combined with an electrochemical cell (EC) (Figure 2(a)).
- Photoelectrochemical cell (PEC) in which one or both electrodes are photoactive (Figure 2(b)).
- Particulate photocatalyst systems which can use either solid-liquid (Figure 2(c)) or solid-gas (Figure 2(d)) interfaces.

A two component device consisting of a PV used in conjunction with an EC (Figure 2(a)), can be used to drive solar fuel production, via absorption of light by the PV which it directly converts to electricity, powering an EC containing electrodes that can perform various electrochemical

redox reactions to produce fuels.^{2,7,15} A PEC is a single component device which incorporates both photoabsorption and electrochemical reactions (Figure 2(b)). In this device one or both electrodes can be semiconductors which are able to absorb UV or visible light, generating charge carriers which can then transfer to adsorbed species and perform redox reactions, often with the help of an external power source.^{2,7,16–18} Of each of these set-ups depicted in Figure 2, a photocatalyst particulate based system is by far the most simple arrangement, in terms of reactor design, it typically has the lowest engineering costs and does not require an external power source, beyond the light source. A dispersion of photocatalyst powders either as a suspension in solution (Figure 2(c)) or immobilised on an inert support (Figure 2(d)) can be utilised for solar fuel production.^{2,8,18,19}

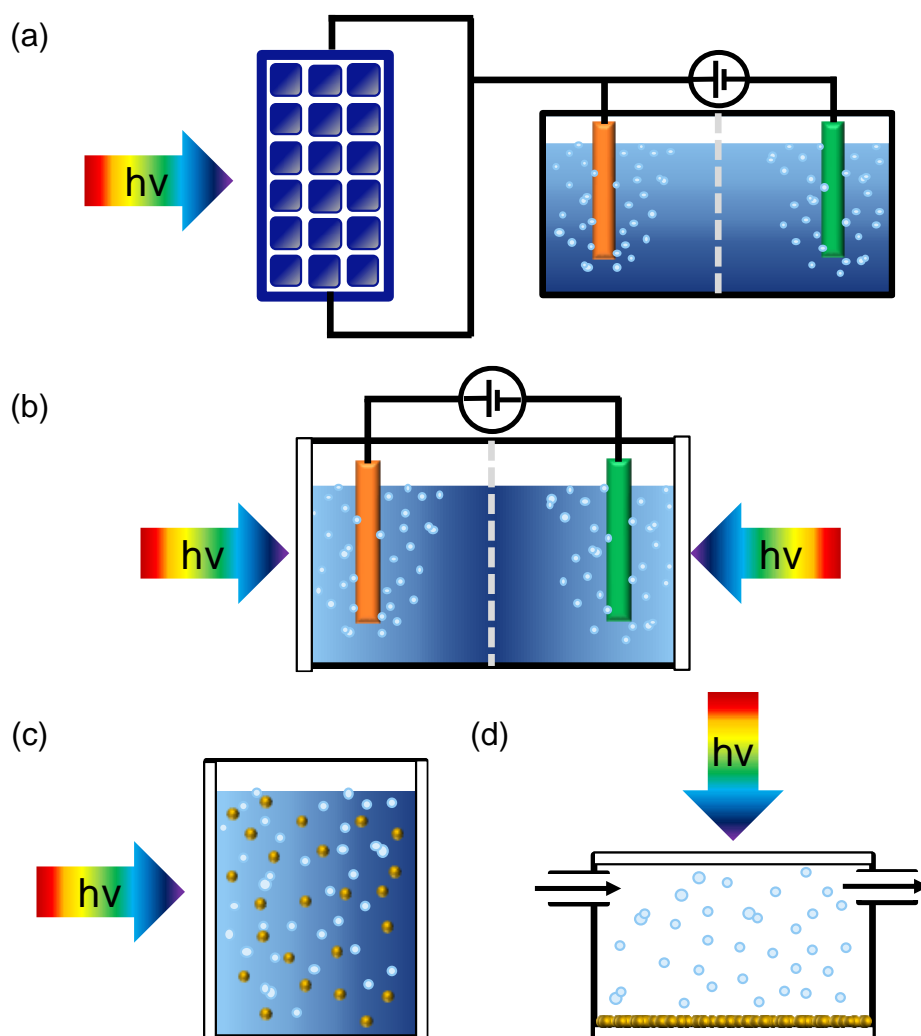


Figure 2 – Simplified depictions of (a) a photovoltaic combined with an electrochemical cell, (b) a photoelectrochemical cell and particulate photocatalyst systems; (c) a solid-liquid-gas photocatalyst system and (d) a solid-gas photocatalyst system.

Typically, when using the term solar fuel production, it refers to either water splitting, to produce H₂ and O₂, or CO₂ reduction, to produce various carbon-based fuels as feedstocks. Ideally the systems depicted above would be able to perform both oxidative and reductive reactions, however systems which are capable of doing so are extremely challenging to produce. Instead, research tends to focus on either the oxidation or reduction reaction, with fewer studies aiming for systems capable of performing both simultaneously. The work presented here will be focussing solely on reduction reactions for H₂ evolution and CO₂ reduction, mainly looking at photocatalyst particulate suspensions in aqueous solution.

1.2.1 Water Splitting

Water splitting refers to the production of H₂ and O₂ from water and can be performed via a number of different methods including electrochemically, photoelectrochemically and photocatalytically (Table 1). H₂ is considered to be an environmentally friendly fuel as its combustion produces only water.^{20–22} Unfortunately, at this time, H₂ is mainly produced from natural gas through steam reforming, which uses fossil fuels, but also releases CO₂ into the atmosphere causing further environmental issues.^{15,22,23} One of the main issues in using H₂ as a fuel source is that it has cost penalties associated with storage when used as a transportation fuel.^{12,15,24} In comparison to most other industrial methods for H₂ production, photo- or electro-chemical production is much too expensive.²⁵

Table 1 – Thermodynamic potentials (E^0) for water splitting in aqueous solution vs a normal hydrogen electrode (NHE), at pH 7, 25 °C and 1 atmosphere.^{2,26}

Reaction	E^0 (V)
$2H^+ + 2e^- \rightarrow H_2$	-0.41 (1)
$2H_2O \rightarrow O_2 + 4H^+ + 4e^-$	+0.82 (2)

1.2.2 CO₂ Reduction

Photocatalytic CO₂ reduction aims to mimic photosynthesis by converting CO₂ using solar energy to produce carbon based fuels.²⁴ The reduction of CO₂ to solar fuels, can utilise waste CO₂ converting it into useful compounds which can then be combusted in fuel cells, effectively closing the carbon cycle.^{2,22} Additionally, the fuels that are produced in this manner are

compatible with existing technologies and can be applied without the need for massive investments to change well established systems.^{2,7} CO₂ reduction may seem like a simple enough idea, however photocatalytic reduction of CO₂ is a thermodynamically unfavourable reaction.^{1,26,27} Due to the stability of CO₂ in its linear geometry, the reduction leads to increased repulsion owing to the addition of an electron and loss of symmetry, forming a bent radical, CO₂^{•-}, causing the reduction potential for this reaction to be highly negative.^{2,28} A more favourable pathway is multi-electron proton assisted CO₂ reduction, this is achieved by coupling the CO₂ reduction and water splitting reactions. As shown in Table 2, the redox potentials for these reactions are less negative and are therefore more feasible.^{2,27} However, the reduction of H⁺ to H₂ often competes with reduction of CO₂ as it has a comparable redox potential (Table 2).^{12,15,19,29}

Table 2 - Thermodynamic potentials (E^0) for water splitting, CO₂ reduction and proton assisted multi-electron CO₂ reduction reactions in aqueous solution vs a normal hydrogen electrode (NHE), at pH 7, 25 °C and 1 atmosphere. ^{2,10,12,16,19,22,26,28–33}

Reaction	E^0 (V)
$CO_2 + e^- \rightarrow CO_2^{\bullet-}$	-1.90 (1)
$CO_2 + 2H^+ + 2e^- \rightarrow CO + H_2O$	-0.53 (2)
$CO_2 + 2H^+ + 2e^- \rightarrow HCOOH$	-0.61 (3)
$CO_2 + 4H^+ + 4e^- \rightarrow HCHO + H_2O$	-0.48 (4)
$CO_2 + 6H^+ + 6e^- \rightarrow CH_3OH + H_2O$	-0.38 (5)
$CO_2 + 8H^+ + 8e^- \rightarrow CH_4 + 2H_2O$	-0.24 (6)
$2H^+ + 2e^- \rightarrow H_2$	-0.41 (7)
$2H_2O \rightarrow O_2 + 4H^+ + 4e^-$	+0.82 (8)

CO₂ can be converted into highly useful products such as CO, CH₃OH or CH₄, which in comparison to H₂ are easier to store and use under ambient conditions.³⁴ Furthermore, CO and H₂ are important feedstocks which can be used in a wide range of industrial processes for the synthesis of other carbon products such as alcohols, aldehydes and olefins, which can be used with existing technologies ⁷

The first case of photocatalytic CO₂ reduction was reported by Inoue *et al* in 1979.³⁵ They reported a number of semiconductor photocatalyst suspensions in water capable of producing

formic acid, formaldehyde and methanol under visible illumination (>500 nm). The semiconductors explored were TiO_2 , ZnO , CdS , GaP , SiC and, WO_3 , all of which were able to reduce CO_2 , with the exception WO_3 . Following this initial report many different materials and combinations of materials have been employed as photocatalysts for solar fuel production.

1.3 Principles of Semiconductor Photocatalysis

Semiconductors are an attractive material for photocatalytic reduction of CO₂ due to their band gap (E_g), giving them the ability to absorb light and directly convert it to electrical power or be used to produce chemical fuels through the reduction of CO₂.⁴ The band gap refers to the energy difference between the valence band (VB) and the conduction band (CB) of a material, this terminology is commonly applied to inorganic semiconductors.^{2,36} Organic semiconductors also have an associated energy gap but this refers to the energy difference between the highest occupied molecular orbital (HOMO) and lowest unoccupied molecular orbital (LUMO).³⁷ Materials with a wide band gap, can only utilise UV light, this accounts for a small fraction of solar energy. For example, a band gap of 3.3 eV corresponds to absorption of light with wavelengths of <375 nm. On the other hand, materials with narrower band gaps, around 2.0 eV, can work under visible light, absorbing light with wavelengths of <619 nm.^{21,38}

When an inorganic or organic semiconductor absorbs a photon of light with energy greater than or equal to their band/optical gap, the material moves from a ground state to an excited state, generating an electron-hole pair, a neutral quasi-particle known as an exciton. Inorganic materials have relatively high dielectric constants ($\epsilon > 10$), this means that the Coulombic interaction is relatively weak, so charges can easily dissociate to form free charge carriers with high mobility and charge separation. Also, the exciton has an extremely short life-time (fs) and is often not considered within mechanisms of inorganic photocatalysis.^{39,40} However, within organic semiconductors, the generated electron-hole pair is tightly bound, due to organic materials having relatively low dielectric constants ($\epsilon \sim 3$), leading to strong coulombic interaction, severely impairing dissociation.^{37,39,40} This tightly bound charge pair is known as a Frenkel exciton, which has relatively low mobility. These Frenkel excitons can then either dissociate to form free charge carriers, or become localised charges, known as polarons, both of which can go on to perform various redox reactions, or they can recombine.^{40,41} Exciton dissociation can occur at semiconductor interfaces and can be due to interaction with trapped carriers or autoionization due to charge transfer between donor and acceptor moieties of a molecule.⁴⁰

Transitions from the VB/HOMO and the CB/LUMO can be described as direct or indirect in nature. This refers to the relative wavevector positions of the maximum energy of the VB and the minimum energy of the CB. For a direct band gap, the maximum of the VB is aligned with the minimum of the CB, whereas for an indirect band gap they are not aligned, requiring excitation to also result in a change in momentum.^{42,43}

Due to the presence of charge carriers within a semiconductor, materials can be described to have n- or p-type semiconductivity, if the majority charge carriers are electrons or holes, respectively. The charge carriers form because of the presence of dopants within the semiconductor structure which can create either acceptor levels just above the VB (p-type) or donor levels just below the CB (n-type).^{42–45} This also leads to a shift in the position of the Fermi level, which is the position that there is a 50% probability that an energy level will contain an electron. For n-type semiconductors, the Fermi level lies close to the CB, but for p-type the Fermi level lies close to the VB.

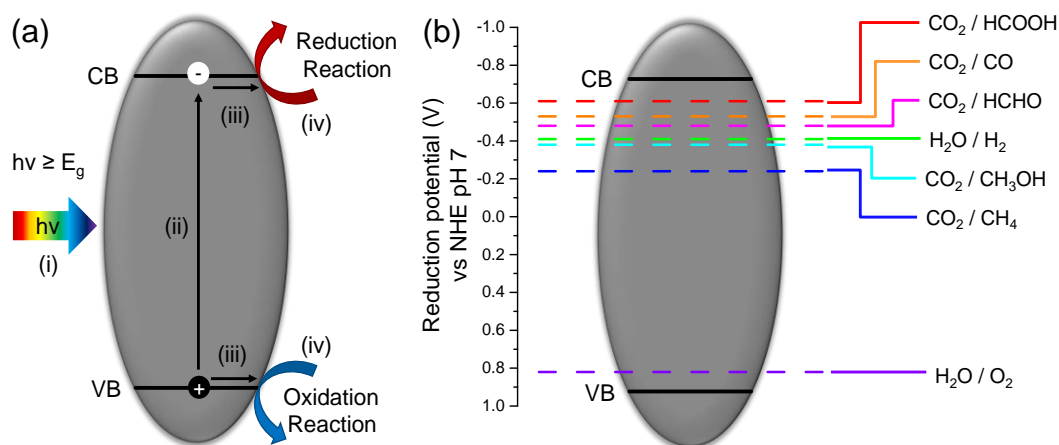


Figure 3 – Diagrams of (a) Photocatalytic redox reactions over a semiconductor particle and (b) semiconductor with ideal band positions for CO₂ reduction and total water splitting.

For photocatalytic reduction of CO₂ using semiconductors to occur, three crucial steps must take place: (i) absorption of an incident photon with $E \geq E_g$ generating an electron-hole (e⁻ h⁺) pair, (ii) separation of these photogenerated charges, (iii) followed by migration to the surface of the material and (iv) transfer of charges to species adsorbed on to the surface of the photocatalysts, which can then participate in various redox reactions (Figure 3(a)).^{2,5,8,11,19,21,46,47} However, this is not the only route the photogenerated charges can take;

if unable to reach the surface, charges can recombine inside the semiconductor, or if unable to transfer to adsorbed species at the surface as they do not meet the energy requirement, they can also recombine, these are known as volume and surface recombination, respectively.⁴⁶ When charges recombine, they can do so via non-radiative and radiative pathways leading to the release of energy in the form of heat or light.^{7,8,13,22,46}

The ability of a semiconductor to reduce or oxidise materials is governed by the positions of the CB and VB, and its surface states. To reduce CO₂ in water, the CB should be more negative than the reduction potential of relevant reduction potential of CO₂. For example to reduce CO₂ to methanol, the CB would have to lie above -0.38 V vs NHE at pH 7 (Figure 3(b)).^{2,28} Furthermore, the VB should be more positive than the HOMO of the oxidation product (Figure 3(b)).^{2,13,21} For an effective semiconductor photocatalyst, the energy difference or overpotential between the CB or VB and the corresponding redox potential should be relatively large to increase charge carrier transfer rates, to enhance photoactivities.^{35,48} Typically materials studied as photocatalysts should consist of widely available and low-cost elements, be inexpensive to fabricate into their final form and have a band gap of appropriate magnitude to work in the visible region. They should also be able to withstand continuous and long-term use over a wide pH range.^{17,26}

1.4 Photocatalytic Materials

Since Inoue's paper in 1979 a wide range of systems have been explored for photocatalytic CO₂ reduction.^{22,23,31,35,49–59} Generally, photocatalytic CO₂ reduction can be performed by heterogeneous or homogeneous photocatalysis. Heterogeneous photocatalysis can be performed using suspensions or dispersions of semiconductors, inorganic, and carbon-based materials. Discussed below are just some of the dominant materials which have been developed for photocatalytic fuel production.

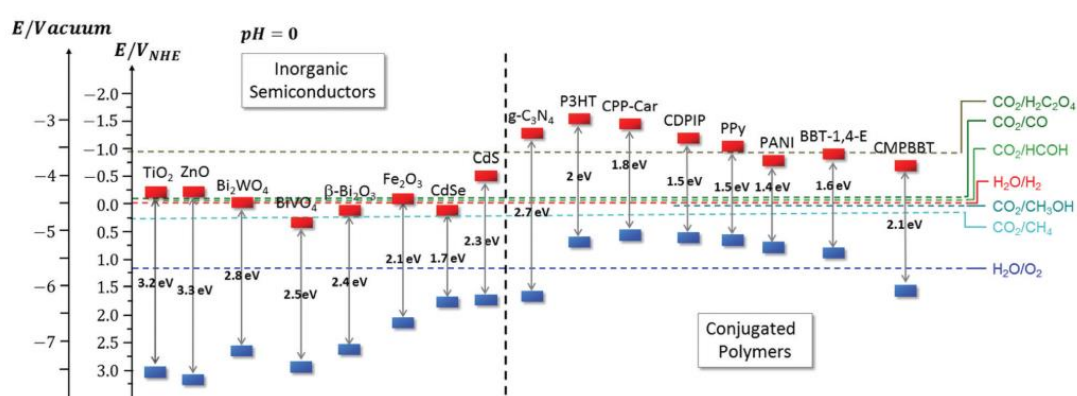


Figure 4 – Energy level diagram for a range inorganic semiconductors and conjugated polymers taken from reference⁶⁰. VB and CB edge positions are represented by the red and blue squares, respectively and are compared with the redox potentials for water splitting and CO₂ reduction reactions versus vacuum and NHE pH=0.

1.4.1 Inorganic Materials

One of the most widely used metal oxide photocatalysts for CO₂ reduction is TiO₂, as it is inert, inexpensive, stable over a wide pH range and does not easily undergo photocorrosion.² It occurs in nature as three polymorphs, anatase, rutile and brookite, the last of which is not a particularly active photocatalyst.² Depending on the polymorph used, the band gap of the material varies. Rutile, the most stable polymorph, has a band gap of 3.0 eV, whilst anatase, which is stable under ambient conditions, has a band gap of 3.2 eV. Both polymorphs have been widely studied as photocatalyst because they are highly active and efficient under UV irradiation. However, due to the size of the band gap, activity is mainly limited to UV irradiation, which only makes up about 4% of the solar energy incident on the earth's surface.⁶¹ It has also been found that TiO₂ generally has low efficiencies for CO₂ reduction in water, unless

modified.^{2,15,19,36,38,62,63} Therefore, the development of photocatalysts that have suitable band positions and a relatively small band gap, to enable greater light absorption, are of paramount importance.

A great number of other inorganic materials have been reported for CO₂ reduction and water splitting, including metal sulphides (CdS, Bi₂S₃),^{34,35,64–68} metal phosphides (GaP, InP)^{35,69–74}, various metal oxides (ZnO, Cu₂O, SrTiO₃)^{2,12,34,35,75–78}, layered double hydroxides^{22,79–84} and metal organic frameworks (MOFs)^{56,85,86}, among numerous others.

1.4.2 Carbon-Based Materials

Mostly studied for water splitting reactions, conjugated organic materials can be prepared under mild conditions and have highly tuneable optical and electronic properties due to fine-tuning of the molecular structures of the repeating units.^{9,87} Conjugation along the polymer back-bone provides the materials with excellent charge transport and separation properties. The properties of these materials are highly dependent on the repeating unit, shape, and size of the polymer chains. In recent years, there have been a number of studies using a range of structures including conjugated polymers^{88,89}, covalent triazine frameworks^{90,91}, conjugated microporous polymers^{92,93} and covalent organic frameworks^{94,95} towards CO₂ reduction.

Sometimes considered a conjugated polymer, carbon nitride, which in principal is a 2D material containing sheets of tri-s-triazine repeating units that are connected via planar tertiary amino groups, is a material which has garnered a lot of attention in recent years.^{29,53,57,96–117} This class of materials has been widely studied for a number of photocatalytic applications, including photocatalytic CO₂ reduction, and is discussed in detail in Chapters 3 and 4.

1.5 Improving Semiconductor Photocatalytic Activity

Many photocatalysts have been developed for CO₂ reduction but generally most have low energy conversion efficiencies, selectivity's or stabilities, which severely hinder their use.⁵ To combat this, there are various routes that can be taken to alter the photocatalyst to improve activity and stability, some of which are discussed here.

1.5.1 Photocatalyst modification

Modification of the photocatalyst either through electronic structure alteration or control of the nano-/micro-structure and morphology can be efficient methods for improving photocatalytic activity. Doping, which is the incorporation of a co-metal, noble metal, transition metal or non-metal into the semiconductor structure, can be used to adjust a materials electronic structure extending light absorption of semiconductors into the visible region, increasing the photocatalysts activity. It does this by introducing states near the electronic bands, altering the band positions of the material, or can be used to change the distribution of electrons, acting as charge traps, reducing recombination rates and influence product selectivity.^{3,19,26,38,46,118}

Surface functionalisation and vacancy formation at the semiconductors surface has been found to improve photocatalytic activities.^{19,54,58,119} Introduction of different types of vacancies and functional groups can be used to donate/accept electrons and can provide sites for CO₂ adsorption, giving an enhancement in activity.^{54,55,59} Though it often can lead to improved activity, doping and functionalisation can also lead to the formation of defects which act as charge trapping and recombination sites. It can also lead to the movement of band positions, lowering the oxidation and reduction ability of the photogenerated charges, decreasing photoactivity.⁴⁶ Increasing the crystallinity of the material can lead to a reduction in the concentration of these defects which can act as charge recombination centres.⁴⁶ Control of crystal phase and the exposed facets on the photocatalysts can also be used to increase stability and improve selectivity using facet dependent molecular adsorption.^{19,46,58}

Morphology and nano-/micro-structure control can be an effective method for improving photocatalytic activity. Introducing nanostructure, unique morphologies or porosity and

reducing particle size can be used to shorten charge carrier pathways allowing charges to reach the surface more easily and transfer to adsorbed species, increasing activities.¹²⁰ Higher surface area can also lead to improved light absorption due to increased area in which light is incident.^{54,86} High surface to volume ratios of nanoparticles provide shorter distances to the surface and a higher probability of charges reaching the interface before recombination. Furthermore nanostructuring provides a larger reactive surface for catalysis.^{2,46,50,54,87,120,121}

1.5.2 Co-catalysts

Materials can often suffer from high charge recombination rates and one of the most commonly used methods for enhancing charge lifetimes and in turn photoactivity is via the incorporation of a co-catalyst (Figure 5).⁵⁸ Co-catalysts not only assist in charge separation, suppressing recombination and preventing photocorrosion leading to increased stability, but they can also be used to lower the activation energy or overpotential for certain reactions.^{11,29,99,122} Initial additions of a co-catalyst often improve activity, but past a certain point high loadings can cause issues such as agglomeration leading to covering of active sites, shielding the semiconductor from incident light and in some cases act as recombination centres.^{11,57}

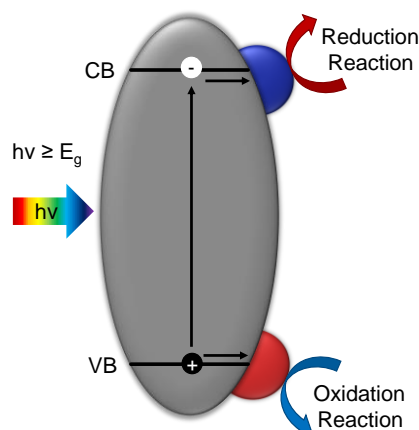


Figure 5 - Diagrams of photocatalytic redox reactions over a semiconductor particle (grey) combined with oxidation (red) and reduction (blue) co-catalysts.

Typically, the main class of co-catalysts that are utilised within photocatalysis are noble metal nanoparticles, such as Pt, Pd, Rh, Au and Ag.^{46,53} The formation of the semiconductor-metal junction between the photocatalyst and co-catalyst creates a space-charge region known as a Schottky barrier or contact at the interface.^{2,21,29,46,53,101,107,122} This Schottky barrier forms

because the Fermi level of the metal is usually below that of the semiconductor CB which induces band bending in the semiconductor facilitating electron transfer from the semiconductor to the co-catalyst. Essentially this means that the metal nanoparticles act as electron traps, increasing photogenerated charge separation, preventing recombination.^{46,53,122} Additionally, metal particles of a suitable size, such as Au and Ag, have been shown to improve photocatalytic activity by surface plasmon resonance excitation creating localised electric fields which aid in charge separation and have been found to enable materials to utilise extended range of visible light.^{29,53,105,122,123} The scarcity of noble metals limits their long term and large-scale development, so noble metal free co-catalysts and more abundant elements along with bimetallic systems have also been explored.^{21,46,101,105,124,125}

Semiconductor photocatalysts with metallic co-catalysts lack the selectivity that is often required for efficient CO₂ reduction.³⁰ Molecular catalysts and metal complexes work in a similar way to metal co-catalysts, in that they can act as electron traps, enhancing charge separation, reducing recombination rates. Additionally, the synthetic tunability of molecular catalysts provides control of the binding geometry of semiconductor surface and of the catalytic site. Semiconductor-molecular catalysts systems can only be effective if the CB (or VB) lies at a more negative (or positive) potential than the onset potential for catalysis. The use of molecular catalysts in combination with semiconductor photocatalysts is explored in greater detail in Chapters 4 and 5.

1.5.3 Sensitisation

Wide band gap semiconductors, such as TiO₂, are unable to utilise a significant portion of visible light. An effective method for combating insufficient light harvesting is to sensitise the semiconductor with a second component which has a better response under visible illumination, extending light absorption of the system further into the visible region.^{2,3,31,126–128} Appropriate dyes can be attached to the surface of a semiconductor and act as photosensitisers, absorbing photons of light and injecting electrons into the CB of the semiconductor. This can aid in charge separation improving overall photoactivity. For this system to work the CB of the semiconductor should lie at a more positive potential than the LUMO of the dye (Figure 6). Smaller band gap semiconductors and quantum dots can also

act as sensitising agents to harvest light when coupled to wide band gap semiconductors, enhancing absorption in the visible range and improving charge separation.^{2,3,21,62}

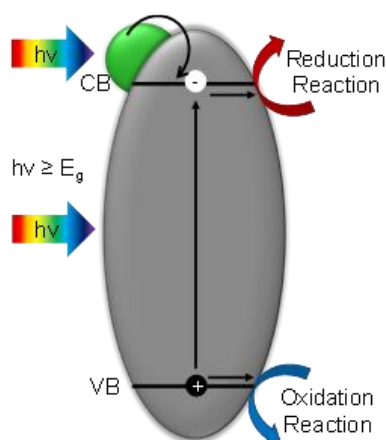


Figure 6 - Diagrams of photocatalytic redox reactions over a semiconductor particle (grey) combined with a sensitizer (green).

1.5.4 Formation of heterojunctions

Forming composite and heterostructured photocatalysts has been proven to improve charge separation, selectivities and generally improve photocatalytic activities. A heterojunction involves the combination of at least 2 semiconductors and can be classified based on the alignment of band structures and how charge transfer proceeds.^{21,46,60,63,100}

- Type I, straddling alignment (Figure 7 (a)) – The VB and CB of semiconductor 2 lie within the VB and CB of semiconductor 1.
 - Due to the movement of charges (electrons down and holes up), charges accumulate on one semiconductor, yielding no improvement in charge separation and does not lead to enhanced photoactivity.^{46,100}
- Type II, staggered alignment (Figure 7 (b)) – The VB and CB of semiconductor 1 lie at a more negative potential than the VB and CB of semiconductor 2.
 - Electrons transfer from the CB of semiconductor 1 to the CB of semiconductor 2, whilst holes move from VB to VB in the opposite direction, providing improved charge separation. However these systems can suffer from steric hindrance of charge transfer due to repulsion of the transferring and existing electrons.¹⁰⁰

- Z-scheme systems – These types of systems were developed to mitigate this charge transfer steric hindrance.
 - Liquid phase Z-schemes (Figure 7 (c)) consist of 2 semiconductors with a liquid phase redox mediator which facilitates charge transfer between the 2 semiconductors.
 - All solid-state Z-scheme (Figure 7 (d)) can utilise materials, such as metal nanoparticles, as charge mediators, enabling charge transfer.
 - Direct Z-scheme (Figure 7 (e)) consist of 2 semiconductors in direct contact with one another. This system differs from a type II heterojunction in that the electron transfer occurs from the CB of semiconductor 1 to the VB of semiconductor 2. The CB and VB of the semiconductors must be aligned for charge transfer to occur.

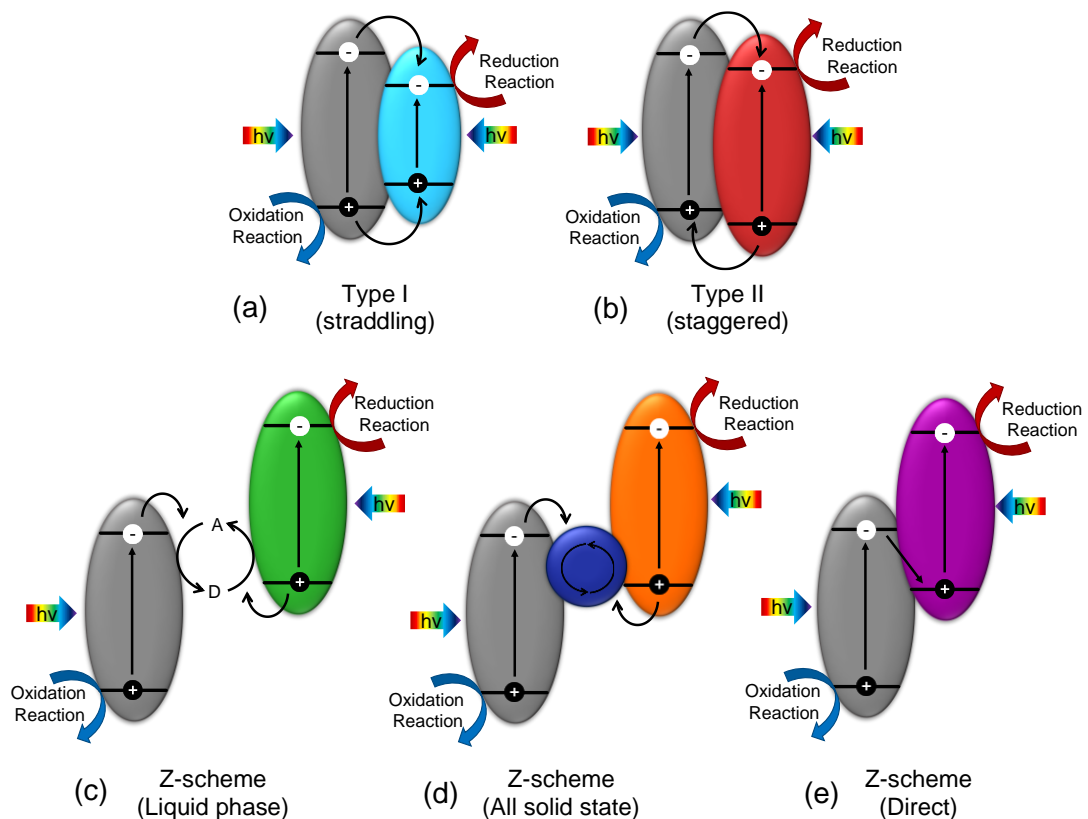


Figure 7 – Schematic diagram of the charge transfer mechanisms for various heterojunctions; (a) type I, (b) type II, (c) liquid phase Z-scheme, (d) all solid-state Z-scheme and (e) direct Z-scheme. Semiconductor 1 is shown in grey on the left-hand side of each diagram and semiconductor 2 is shown in various colours on the right-hand side of each diagram. The VB of each semiconductor is as the bottom of each particle, whilst the CB is at the top.^{21,46,60,63,100}

1.6 General Issues with Semiconductor Photocatalytic CO₂ Reduction

Photocatalysts often suffer from low rates of activity unless modified and this can be caused by a range of reasons including, low surface areas, unsuitable band structures, high rates of charge recombination and instability, but as discussed in the previous section modification of the photocatalysts and combinations with other materials can lead to improved activities.

Back reactions occur when products and intermediates undergo redox reactions or when charge recombination proceeds via reaction intermediates. This often arises if both reduction and oxidation reactions occur on the same catalyst surface, the redox products can undergo opposite reactions, when they are in close proximity to reactive sites.⁷ These back reactions can lead to poor activities and are often caused by the type of photocatalyst used and the reactor set-up. Additionally, in some photocatalytic reactors, like a simple batch reactor, mixing of products occurs which can lead to re-oxidation or re-reduction of products, lowering yields, but can also mean that products are difficult to separate.^{2,18} Removal of products via the use of flow cell set-ups can help to prevent back reactions.

Generally, the field of photocatalysis as a whole, has many issues associated with testing and comparison. Comparison of photocatalytic activity between papers published by different groups is often difficult. This is due to a lack of consistency in how photocatalysts are tested and how procedures and results are reported.^{2,129} For example, often activities are reported in terms of μmol of products per photocatalyst weight, but this does not take into consideration the amount of the catalyst that is exposed to illumination, which is based on catalyst surface area and the reactor set-up.¹²⁹ Often, full testing conditions are not reported including; light intensity, temperature, pressure and pH, which can have a great effect on photocatalytic activities. The class of set-up that is used can have a significant impact on activities and also product selection. Within the literature there are a wide range of reactor set-ups that have been reported. Generally there are two types of reactor systems that are used; gaseous systems which utilises a dispersion of the photocatalyst immobilised onto a surface in a wet CO₂ atmosphere and liquid systems which use a suspension of the photocatalyst in some kind of

CO₂ purged solution.^{8,53,129,130} Within these systems there are a number of different types of reactors, such as monolith, fibre optic, annular and suspension, which can also be run as batch or flow processes. Variations in these systems can have a profound effect on the types and quantities of products.

For photocatalyst suspensions, the solution media can have a great effect on product yields. When experiments are performed in aqueous solution, H₂ evolution can be a competing reaction and can lead to low efficiencies due to preferential H₂ evolution over CO₂ reduction.^{53,131} Selectivity for the CO₂ reduction reaction in aqueous systems can be achieved through the use of selective co-catalysts, such as metal complexes. The solubility of CO₂ in aqueous solution can also be a challenge, the concentration of free CO₂ in a saturated CO₂ aqueous solution reaches around 33 mM under standard conditions at pH 7.^{132,133} In comparison to organic solvents the solubility of CO₂ in water is low, for example the concentration of CO₂ in saturated acetonitrile solutions is around 0.28 M under standard conditions.^{23,26,53,133–138} The solubility of carbon materials (CO₂, HCO₃⁻, CO₃²⁻, etc.) in water can be increased by performing experiments in basic solution, however this leads to the formation of other carbonate species in solution, which are more stable and are said to be more difficult to reduce, but these species can also act as hole scavengers.

There are relatively few reports of systems that are capable of performing overall redox reactions, consequently only one side of a redox reaction is typically explored. To prevent accumulation of charges, which lead to increased recombination rates, a sacrificial charge donor (hole or electron scavenger) is used.^{2,130} In the case of H₂ evolution and CO₂ reduction, hole scavengers, such as methanol (MeOH), sodium hydroxide (NaOH), ethylenediaminetetraacetic acid (EDTA), triethanolamine (TEOA) and sodium sulphite (Na₂SO₃), are employed to donate electrons to the semiconductor, decreasing hole concentrations in the semiconductor, preventing recombination, back reactions and in some cases increasing catalyst stability.^{2,5,16,18,19,24,139,140}

Determining the origin of carbonaceous products is crucial for CO₂ reduction studies. There are number of different carbon sources that can lead to false positive results, such as organic solvents/solution or organic impurities from the air which can be adsorbed onto photocatalyst

surfaces and can be reduced during the photocatalytic experiments.^{57,129} Furthermore, it has been determined that organic species found on the surface of TiO₂, either through adsorption of contaminants from the air, or from the use of organic precursors lead to the formation of CO₂ reduction products, which do not originate from the purged CO₂.^{141,142} The best method for confirmation of the carbon source is performing an isotopic labelling experiment, in which the photocatalytic system is purged with ¹³CO₂ and testing products via gas chromatography-mass spectrometry (GC/MS), nuclear magnetic resonance spectroscopy (NMR) or Fourier-transform infrared spectroscopy (FTIR), in which ¹²C and ¹³C can be differentiated.^{2,29,57,129} However, these experiments are not always performed, instead a series of blank experiments can be performed, in the absence of CO₂, photocatalysts, scavengers, light, etc., but these experiments alone are not always an adequate substitute for isotopic labelling experiments.

1.7 Thesis Overview

Within this work, a selection of inorganic and organic semiconductors have been studied as photocatalysts for CO₂ reduction in water. Materials were chosen based upon previously reported activity and band positions relative to CO₂ reduction potentials. They were synthesised via solid state methods and characterised to understand chemical and electronic properties. Photocatalytic activity was then evaluated, in the presence of a hole scavenger, first for water splitting, then CO₂ reduction. When activity was found to be poor, materials were modified and/or combined with co-catalysts, all in the hopes of improving photoactivity.

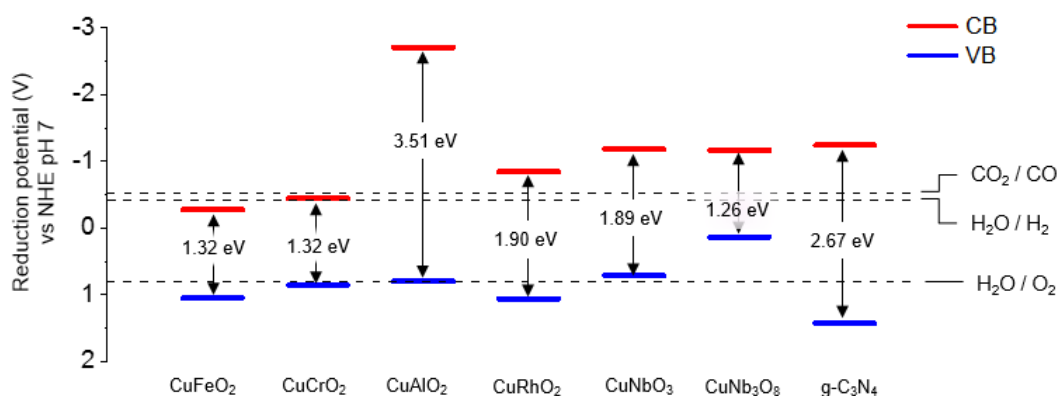


Figure 8 - Conduction and valence band positions and band gaps of chosen materials compared with CO₂ and water splitting redox potentials vs NHE at pH 7.^{18,143–150}

Chapter 3 discusses exclusively carbon nitride, its history, properties, characterisation, and initial photocatalytic activities towards H₂ evolution. Within Chapter 4 the various methods which have previously been used for modification of carbon nitride are briefly reviewed and applied to the materials presented in Chapter 3. The modified and hybrid systems are then assessed for photocatalytic CO₂ reduction. Chapter 5 focuses on the Cu(I) oxides shown in Figure 8, looking at previous photocatalytic activities. The materials were synthesised, characterised, and then employed as photocatalysts for CO₂ reduction, with and without the aid of a molecular catalyst.

1.8 References

- 1 G. Sahara and O. Ishitani, *Inorg. Chem.*, 2015, **54**, 5096–5104.
- 2 S. N. Habisreutinger, L. Schmidt-Mende and J. K. Stolarczyk, *Angew. Chemie Int. Ed.*, 2013, **52**, 7372–7408.
- 3 S. Das and W. M. a. Wan Daud, *RSC Adv.*, 2014, **4**, 20856–20893.
- 4 I. Sullivan, B. Zoellner and P. A. Maggard, *Chem. Mater.*, 2016, **28**, 5999–6016.
- 5 X. Chang, T. Wang and J. Gong, *Energy Environ. Sci.*, 2016, **9**, 2177–2196.
- 6 R. Perez, *A Fundamental Look At Supply Side Energy Reserves For The Planet*, IEA SHC Solar Update General Programme Report, 2015.
- 7 G. Neri, M. Forster and A. J. Cowan, in *Issues in Environmental Science and Technology*, 2019, pp. 184–209.
- 8 M. Tahir and N. S. Amin, *Renew. Sustain. Energy Rev.*, 2013, **25**, 560–579.
- 9 C. Dai and B. Liu, *Energy Environ. Sci.*, 2020, **13**, 24–52.
- 10 P. D. Tran, L. H. Wong, J. Barber and J. S. C. Loo, *Energy Environ. Sci.*, 2012, **5**, 5902–5918.
- 11 J. Ran, J. Zhang, J. Yu, M. Jaroniec and S. Z. Qiao, *Chem. Soc. Rev.*, 2014, **43**, 7787–7812.
- 12 J. L. White, M. F. Baruch, J. E. Pander, Y. Hu, I. C. Fortmeyer, J. E. Park, T. Zhang, K. Liao, J. Gu, Y. Yan, T. W. Shaw, E. Abelev and A. B. Bocarsly, *Chem. Rev.*, 2015, **115**, 12888–12935.
- 13 K. Maeda, *ACS Catal.*, 2013, **3**, 1486–1503.
- 14 A. Fujishima and K. Honda, *Nature*, 1972, **238**, 37–38.
- 15 A. Corma and H. Garcia, *J. Catal.*, 2013, **308**, 168–175.
- 16 A. J. Cowan and J. R. Durrant, *Chem. Soc. Rev.*, 2013, **42**, 2281–2293.
- 17 K. Sivula and R. van de Krol, *Nat. Rev. Mater.*, 2016, **1**, 15010.
- 18 S. Bassaid, M. Chaib, S. Omeiri, A. Bouguelia and M. Trari, *J. Photochem. Photobiol. A Chem.*, 2009, **201**, 62–68.
- 19 J. Mao, K. Li and T. Peng, *Catal. Sci. Technol.*, 2013, **3**, 2481–2498.
- 20 X. Li, J. Yu, J. Low, Y. Fang, J. Xiao and X. Chen, *J. Mater. Chem. A*, 2015, **3**, 2485–2534.
- 21 W. Fan, Q. Zhang and Y. Wang, *Phys. Chem. Chem. Phys.*, 2013, **15**, 2632–49.
- 22 A. Nikokavoura and C. Trapalis, *Appl. Surf. Sci.*, 2017, **391**, 149–174.
- 23 K. C. Christoforidis and P. Fornasiero, *ChemCatChem*, 2019, **11**, 368–382.
- 24 X. Liu, S. Inagaki and J. Gong, *Angew. Chemie Int. Ed.*, 2016, **55**, 2–29.
- 25 B. A. Pinaud, J. D. Benck, L. C. Seitz, A. J. Forman, Z. Chen, T. G. Deutsch, B. D. James, K. N. Baum, G. N. Baum, S. Ardo, H. Wang, E. Miller and T. F. Jaramillo, *Energy Environ. Sci.*, 2013, **6**, 1983–2002.
- 26 S. R. Lingampalli, M. M. Ayyub and C. N. R. Rao, *ACS Omega*, 2017, **2**, 2740–2748.
- 27 A. J. Morris, G. J. Meyer and E. Fujita, *Acc. Chem. Res.*, 2009, **42**, 1983–1994.
- 28 E. Fujita, *Coord. Chem. Rev.*, 1999, **185–186**, 373–384.
- 29 Y. Fang and X. Wang, *Chem. Commun.*, 2018, **54**, 5674–5687.
- 30 S. Hennessey and P. Farràs, *Chem. Commun.*, 2018, **54**, 6662–6680.
- 31 K. Maeda, *Adv. Mater.*, 2019, **31**, 1808205.
- 32 H. Tian, *ChemSusChem*, 2015, **8**, 3746–3759.
- 33 B. Kumar, M. Llorente, J. Froehlich, T. Dang, A. Sathrum and C. P. Kubiak, *Annu. Rev. Phys. Chem.*, 2012, **63**, 541–569.
- 34 S. Navalón, A. Dhakshinamoorthy, M. Álvaro and H. Garcia, *ChemSusChem*, 2013, **6**, 562–577.
- 35 T. Inoue, A. Fujishima, S. Konishi and K. Honda, *Nature*, 1979, **277**, 637–638.
- 36 Y. Ma, X. L. Wang, Y. S. Jia, X. B. Chen, H. X. Han and C. Li, *Chem. Rev.*, 2014, **114**, 9987–10043.
- 37 A. Boudrioua, M. Chakaroun and A. Fischer, in *Organic Lasers*, Elsevier, 2017, vol. 1, pp. 1–47.
- 38 J. Low, B. Cheng and J. Yu, *Appl. Surf. Sci.*, 2016, **392**, 658–686.
- 39 H. Bässler and A. Köhler, *Top. Curr. Chem.*, 2012, **312**, 1–65.
- 40 P.-A. Blanche, *Photorefractive Organic Materials and Applications*, Springer, 2016.
- 41 H. F. Haneef, A. M. Zeidell and O. D. Jurchescu, *J. Mater. Chem. C*, 2020, **8**, 759–787.

- 42 M. I. Pech-Canul and R. Nugehalli, *Semiconductors: Synthesis, Properties and Applications*, Springer International Publishing, Cham, 2019.
- 43 H. Kisch, *Semiconductor Photocatalysis: Principles and Applications*, John Wiley & Sons Incorporated, 2015.
- 44 C. Housecroft and A. G. Sharpe, *Inorganic Chemistry*, Pearson Education Limited, 4th Editio., 2012.
- 45 P. Atkins and J. de Paula, *Physical Chemistry*, Oxford University Press, Ninth Edit., 2010.
- 46 R. Marschall, *Adv. Funct. Mater.*, 2014, **24**, 2421–2440.
- 47 X. Xiang, F. Pan and Y. Li, *Adv. Compos. Hybrid Mater.*, 2018, **1**, 6–31.
- 48 P. Niu, Y. Yang, J. C. Yu, G. Liu and H. M. Cheng, *Chem. Commun.*, 2014, **50**, 10837–10840.
- 49 J. Z. Y. Tan and M. M. Maroto-Valer, *J. Mater. Chem. A*, 2019, **7**, 9368–9385.
- 50 J. Y. Li, L. Yuan, S. H. Li, Z. R. Tang and Y. J. Xu, *J. Mater. Chem. A*, 2019, **7**, 8676–8689.
- 51 H. Wu, X. Li, C. Tung and L. Wu, *Adv. Mater.*, 2019, **31**, 1900709.
- 52 Y. Zhao and Z. Liu, *Chinese J. Chem.*, 2018, **36**, 455–460.
- 53 Z. Sun, H. Wang, Z. Wu and L. Wang, *Catal. Today*, 2018, **300**, 160–172.
- 54 J. Y. Choi, W. Choi, J. W. Park, C. K. Lim and H. Song, *Chem. – An Asian J.*, 2020, **15**, 253–265.
- 55 J. Fu, K. Jiang, X. Qiu, J. Yu and M. Liu, *Mater. Today*, 2020, **32**, 222–243.
- 56 C. W. Huang, V. H. Nguyen, S. R. Zhou, S. Y. Hsu, J. X. Tan and K. C. W. Wu, *Sustain. Energy Fuels*, 2020, **4**, 504–521.
- 57 M. M. Kandy, *Sustain. Energy Fuels*, 2020, **4**, 469–484.
- 58 T. P. Nguyen, D. L. T. Nguyen, V. H. Nguyen, T. H. Le, D. V. N. Vo, Q. T. Trinh, S. R. Bae, S. Y. Chae, S. Y. Kim and Q. Van Le, *Nanomaterials*, 2020, **10**, 337.
- 59 Y. Zhang, B. Xia, J. Ran, K. Davey and S. Z. Qiao, *Adv. Energy Mater.*, 2020, **10**, 1903879.
- 60 M. Liras, M. Barawi and V. A. De La Peña O’Shea, *Chem. Soc. Rev.*, 2019, **48**, 5454–5487.
- 61 T. Hisatomi, J. Kubota and K. Domen, *Chem. Soc. Rev.*, 2014, **43**, 7520–7535.
- 62 A. Dhakshinamoorthy, S. Navalon, A. Corma and H. Garcia, *Energy Environ. Sci.*, 2012, **5**, 9217.
- 63 S. J. A. Moniz, S. A. Shevlin, D. J. Martin, Z. X. Guo and J. Tang, *Energy Environ. Sci.*, 2015, **8**, 731–759.
- 64 X. Li, J. Chen, H. Li, J. Li, Y. Xu, Y. Liu and J. Zhou, *J. Nat. Gas Chem.*, 2011, **20**, 413–417.
- 65 B. R. Eggins, J. T. S. Irvine, E. P. Murphy and J. Grimshaw, *J. Chem. Soc. Chem. Commun.*, 1988, 1123–1124.
- 66 J. T. S. Irvine, B. R. Eggins and J. Grimshaw, *Sol. Energy*, 1990, **45**, 27–33.
- 67 P. Johne and H. Kisch, *J. Photochem. Photobiol. A Chem.*, 1997, **111**, 223–228.
- 68 J. Chen, S. Qin, G. Song, T. Xiang, F. Xin and X. Yin, *Dalton Trans.*, 2013, **42**, 15133–8.
- 69 B. Aurian-Blajeni, M. Halmann and J. Manassen, *Sol. Energy Mater.*, 1983, **8**, 425–440.
- 70 M. Halmann, *Nature*, 1978, **275**, 115–116.
- 71 Y. Bi, S. Ouyang, J. Cao and J. Ye, *Phys. Chem. Chem. Phys.*, 2011, **13**, 10071–10075.
- 72 E. E. Barton, D. M. Rampulla and A. B. Bocarsly, *J. Am. Chem. Soc.*, 2008, **130**, 6342–6344.
- 73 T. Arai, S. Sato, K. Uemura, T. Morikawa, T. Kajino and T. Motohiro, *Chem. Commun.*, 2010, **46**, 6944–6946.
- 74 S. Kaneco, H. Katsumata, T. Suzuki and K. Ohta, *Chem. Eng. J.*, 2006, **116**, 227–231.
- 75 L. Wan, X. Wang, S. Yan, H. Yu, Z. Li and Z. Zou, *CrystEngComm*, 2012, **14**, 154–159.
- 76 A. D. Handoko and J. Tang, *Int. J. Hydrogen Energy*, 2013, **38**, 13017–13022.
- 77 P. Acharyya, K. Kundu and K. Biswas, *Nanoscale*, 2020, **12**, 21094–21117.
- 78 Y. W. Teh, M. K. T. Chee, X. Y. Kong, S. T. Yong and S. P. Chai, *Sustain. Energy Fuels*, 2020, **4**, 973–984.
- 79 R. Chong, C. Su, Y. Du, Y. Fan, Z. Ling, Z. Chang and D. Li, *J. Catal.*, 2018, **363**, 92–

- 101.
- 80 H. Jiang, K. ichi Katsumata, J. Hong, A. Yamaguchi, K. Nakata, C. Terashima, N. Matsushita, M. Miyauchi and A. Fujishima, *Appl. Catal. B Environ.*, 2018, **224**, 783–790.
- 81 S. Kumar, M. A. Isaacs, R. Trofimovaite, L. Durndell, C. M. A. Parlett, R. E. Douthwaite, B. Coulson, M. C. R. Cockett, K. Wilson and A. F. Lee, *Appl. Catal. B Environ.*, 2017, **209**, 394–404.
- 82 Q. Guo, Q. Zhang, H. Wang, Z. Liu and Z. Zhao, *Catal. Commun.*, 2016, **77**, 118–122.
- 83 K. Teramura, S. Iguchi, Y. Mizuno, T. Shishido and T. Tanaka, *Angew. Chemie Int. Ed.*, 2012, **51**, 8008–8011.
- 84 N. Ahmed, Y. Shibata, T. Taniguchi and Y. Izumi, , DOI:10.1016/j.jcat.2011.01.004.
- 85 D. Li, M. Kassymova, X. Cai, S. Q. Zang and H. L. Jiang, *Coord. Chem. Rev.*, 2020, 412.
- 86 W. Zhan, L. Sun and X. Han, *Nano-Micro Lett.*, 2019, **11**, 1–28.
- 87 S. Luo, Z. Zeng, G. Zeng, Z. Liu, R. Xiao, P. Xu, H. Wang, D. Huang, Y. Liu, B. Shao, Q. Liang, D. Wang, Q. He, L. Qin and Y. Fu, *J. Mater. Chem. A*, 2020, **8**, 6434–6470.
- 88 Y. Chen, G. Ji, S. Guo, B. Yu, Y. Zhao, Y. Wu, H. Zhang, Z. Liu, B. Han and Z. Liu, *Green Chem.*, 2017, **19**, 5777–5781.
- 89 X. Yu, Z. Yang, B. Qiu, S. Guo, P. Yang, B. Yu, H. Zhang, Y. Zhao, X. Yang, B. Han and Z. Liu, *Angew. Chemie - Int. Ed.*, 2019, **58**, 632–636.
- 90 C. Yang, W. Huang, L. C. da Silva, K. A. I. Zhang and X. Wang, *Chem. - A Eur. J.*, 2018, **24**, 17454–17458.
- 91 S. Zhang, S. Wang, L. Guo, H. Chen, B. Tan and S. Jin, *J. Mater. Chem. C*, 2019, **8**, 192–200.
- 92 F. M. Wisser, M. Duguet, Q. Perrinet, A. C. Ghosh, M. Alves-Favaro, Y. Mohr, C. Lorentz, E. A. Quadrelli, R. Palkovits, D. Farrusseng, C. Mellot-Draznieks, V. Waele and J. Canivet, *Angew. Chemie Int. Ed.*, 2020, **59**, 5116–5122.
- 93 C. Dai, L. Zhong, X. Gong, L. Zeng, C. Xue, S. Li and B. Liu, *Green Chem.*, 2019, **21**, 6606–6610.
- 94 S. Yang, W. Hu, X. Zhang, P. He, B. Pattengale, C. Liu, M. Cendejas, I. Hermans, X. Zhang, J. Zhang and J. Huang, *J. Am. Chem. Soc.*, 2018, **140**, 14614–14618.
- 95 Y. Fu, X. Zhu, L. Huang, X. Zhang, F. Zhang and W. Zhu, *Appl. Catal. B Environ.*, 2018, **239**, 46–51.
- 96 W.-J. Ong, L.-L. Tan, Y. H. Ng, S.-T. Yong and S.-P. Chai, *Chem. Rev.*, 2016, **116**, 7159–7329.
- 97 S. Yang, Y. Gong, J. Zhang, L. Zhan, L. Ma, Z. Fang, R. Vajtai, X. Wang and P. M. Ajayan, *Adv. Mater.*, 2013, **25**, 2452–2456.
- 98 X. Wang, K. Maeda, A. Thomas, K. Takanebe, G. Xin, J. M. Carlsson, K. Domen and M. Antonietti, *Nat. Mater.*, 2009, **8**, 76–80.
- 99 J. Zhu, P. Xiao, H. Li and S. A. C. Carabineiro, *ACS Appl. Mater. Interfaces*, 2014, **6**, 16449–16465.
- 100 W. K. Darkwah and K. A. Oswald, *Nanoscale Res. Lett.*, 2019, **14**, 234.
- 101 Y. Li, T. Kong and S. Shen, *Small*, 2019, **15**, 1900772.
- 102 M. Shen, L. Zhang and J. Shi, *Nanotechnology*, 2018, **29**, 412001.
- 103 Y. Chen, G. Jia, Y. Hu, G. Fan, Y. H. Tsang, Z. Li and Z. Zou, *Sustain. Energy Fuels*, 2017, **1**, 1875–1898.
- 104 R. Kuriki and K. Maeda, *Phys. Chem. Chem. Phys.*, 2017, **19**, 4938–4950.
- 105 S. Cao, J. Low, J. Yu and M. Jaroniec, *Adv. Mater.*, 2015, **27**, 2150–2176.
- 106 Y. Zheng, L. Lin, B. Wang and X. Wang, *Angew. Chemie Int. Ed.*, 2015, **54**, 12868–12884.
- 107 S. Cao and J. Yu, *J. Phys. Chem. Lett.*, 2014, **5**, 2101–2107.
- 108 S. Ye, R. Wang, M. Z. Wu and Y. P. Yuan, *Appl. Surf. Sci.*, 2015, **358**, 15–27.
- 109 G. Dong, Y. Zhang, Q. Pan and J. Qiu, *J. Photochem. Photobiol. C Photochem. Rev.*, 2014, **20**, 33–50.
- 110 X. Wang, S. Blechert and M. Antonietti, *ACS Catal.*, 2012, **2**, 1596–1606.
- 111 J. Liebig, *Ann. der Pharm.*, 1834, **10**, 1–47.
- 112 Y. Wang, X. Wang and M. Antonietti, *Angew. Chemie Int. Ed.*, 2012, **51**, 68–89.
- 113 T. Komatsu and T. Nakamura, *J. Mater. Chem.*, 2001, **11**, 474–478.
- 114 Y. Luo, Y. Yan, S. Zheng, H. Xue and H. Pang, *J. Mater. Chem. A*, 2019, **7**, 901–924.
- 115 C. Prasad, H. Tang and I. Bahadur, *J. Mol. Liq.*, 2019, **281**, 634–654.

- 116 A. Thomas, A. Fischer, F. Goettmann, M. Antonietti, J.-O. Müller, R. Schlögl and J. M. Carlsson, *J. Mater. Chem.*, 2008, **18**, 4893.
- 117 B. V. Lotsch, M. Döblinger, J. Sehnert, L. Seyfarth, J. Senker, O. Oeckler and W. Schnick, *Chem. - A Eur. J.*, 2007, **13**, 4969–4980.
- 118 A. Nishimura, G. Mitsui, M. Hirota and E. Hu, *Int. J. Chem. Eng.*, 2010, **2010**, 1–9.
- 119 D. Adekoya, M. Tahir and N. A. S. Amin, *Renew. Sustain. Energy Rev.*, 2019, 116.
- 120 F. E. Osterloh, *Chem. Soc. Rev.*, 2013, **42**, 2294–2320.
- 121 S. Wang, Y. Wang, S. Zang and X. W. Lou, *Small Methods*, 2020, **4**, 1900586.
- 122 Z. Zhao, Y. Sun and F. Dong, *Nanoscale*, 2015, **7**, 15–37.
- 123 K. R. Reddy, C. V. Reddy, M. N. Nadagouda, N. P. Shetti, S. Jaesool and T. M. Aminabhavi, *J. Environ. Manage.*, 2019, **238**, 25–40.
- 124 S. Wang, J. Lin and X. Wang, *Phys. Chem. Chem. Phys.*, 2014, **16**, 14656.
- 125 X. Dai and Y. Sun, *Nanoscale*, 2019, **11**, 16723–16732.
- 126 G. Reginato, L. Zani, M. Calamante, A. Mordini and A. Dessì, *Eur. J. Inorg. Chem.*, 2020, **2020**, 899–917.
- 127 N. Zhang, L. Wen, J. Yan and Y. Liu, *Chem. Pap.*, 2020, **74**, 389–406.
- 128 X. Lang, X. Chen and J. Zhao, *Chem. Soc. Rev.*, 2014, **43**, 473–486.
- 129 S. Ali, M. C. Flores, A. Razzaq, S. Sorcar, C. B. Hiragond, H. R. Kim, Y. H. Park, Y. Hwang, H. S. Kim, H. Kim, E. H. Gong, J. Lee, D. Kim and S. Il In, *Catalysts*, 2019, **9**, 727.
- 130 R. K. De_Richter, T. Ming and S. Caillol, *Renew. Sustain. Energy Rev.*, 2013, **19**, 82–106.
- 131 S. Sato, T. Arai and T. Morikawa, *Inorg. Chem.*, 2015, **54**, 5105–5113.
- 132 J. Schneider, H. Jia, K. Kobiro, D. E. Cabelli, J. T. Muckerman and E. Fujita, *Energy Environ. Sci.*, 2012, **5**, 9502–9510.
- 133 B. P. Sullivan, K. Kristi and H. E. Guard, *Electrochemical and Electrocatalytic Reactions of Carbon Dioxide*, Elsevier, 1993.
- 134 J. Mao, T. Peng, X. Zhang, K. Li, L. Ye and L. Zan, *Catal. Sci. Technol.*, 2013, **3**, 1253.
- 135 H. Rao, J. Bonin and M. Robert, *J. Phys. Chem. C*, 2018, **122**, 13834–13839.
- 136 U. Kang, S. K. Choi, D. J. Ham, S. M. Ji, W. Choi, D. S. Han, A. Abdel-Wahab and H. Park, *Energy Environ. Sci.*, 2015, **8**, 2638–2643.
- 137 J. Qiao, Y. Liu, F. Hong and J. Zhang, *Chem. Soc. Rev.*, 2014, **43**, 631–675.
- 138 G. Neri, M. Forster, J. J. Walsh, C. M. Robertson, T. J. Whittles, P. Farràs and A. J. Cowan, *Chem. Commun.*, 2016, **52**, 14200–14203.
- 139 C. Liu, Y. Zhang, F. Dong, A. H. Reshak, L. Ye, N. Pinna, C. Zeng, T. Zhang and H. Huang, *Appl. Catal. B Environ.*, 2017, **203**, 465–474.
- 140 L. Shi, P. Li, W. Zhou, T. Wang, K. Chang, H. Zhang, T. Kako, G. Liu and J. Ye, *Nano Energy*, 2016, **28**, 158–163.
- 141 R. Shi and Y. Chen, *ChemCatChem*, 2019, **11**, 2270–2276.
- 142 T. Yui, A. Kan, C. Saitoh, K. Koike, T. Ibusuki and O. Ishitani, *ACS Appl. Mater. Interfaces*, 2011, **3**, 2594–2600.
- 143 S. Saadi, A. Bouguelia and M. Trari, *Sol. Energy*, 2006, **80**, 272–280.
- 144 M. S. Prévot, Y. Li, N. Guijarro and K. Sivula, *J. Mater. Chem. A*, 2016, **4**, 3018–3026.
- 145 J. Gu, Y. Yan, J. W. Krizan, Q. D. Gibson, Z. M. Detweiler, R. J. Cava and A. B. Bocarsly, *J. Am. Chem. Soc.*, 2014, **136**, 830–833.
- 146 B. Zoellner, S. Stuart, C.-C. Chung, D. B. Dougherty, J. L. Jones and P. A. Maggard, *J. Mater. Chem. A*, 2016, **4**, 3115–3126.
- 147 U. A. Joshi and P. A. Maggard, *J. Phys. Chem. Lett.*, 2012, **3**, 1577–1581.
- 148 J. Zhang, X. Chen, K. Takanabe, K. Maeda, K. Domen, J. D. Epping, X. Fu, M. Antonietti and X. Wang, *Angew. Chemie - Int. Ed.*, 2010, **49**, 441–444.
- 149 V. V. Pavlishchuk and A. W. Addison, *Inorganica Chim. Acta*, 2000, **298**, 97–102.
- 150 A. Kay, I. Cesar and M. Grätzel, *J. Am. Chem. Soc.*, 2006, 15714–15721.

2

**Experimental and Analytical
Methods and Set-up
Development**

2.1 Materials and Synthesis

Starting materials and solvents were purchased from Sigma-Aldrich (Merck), Fisher Scientific and VWR and were used as received without further purification, with the exceptions of Fe(III) meso-Tetra(4-carboxyphenyl)porphine chloride (FeTCPP) which was purchased from Santa Cruz Biotechnology and Ni^{II}(1,4,8,11-tetraazacyclotetradecane), (NiCyc), Ni^{II}(1,4,8,11-tetraazacyclotetradecane-6-carboxylic acid) (NiCycC) and Ni^{II}([(1,4,8,11-tetraazacyclotetradecan-1-yl)methylene]phosphonic acid) (NiCycP), which were synthesised by Dr Gaia Neri using literature procedures.^{1,2} Unless otherwise stated aqueous solutions were prepared with Milli-Q water (Millipore Corp, 18.2 MΩ cm at 25 °C). Ar, N₂ and CO₂ were purchased from BOC at CP or higher grade.

2.1.1 Metal Oxides

2.1.1.1 Delafossites

Synthetic procedures for the delafossite materials; CuFeO₂, CuAlO₂ and CuRhO₂ were repeated from the literature, but a general procedure was used, as follows.³⁻⁵ Stoichiometric amounts of Cu₂O and M₂O₃ (M= Fe, Al or Rh) were ground for 15 minutes using a pestle and mortar. Powders were transferred to alumina crucibles (3 mL), covered, and placed in a box or tube furnace (see Table 3 for conditions).

Table 3 - Reaction conditions for delafossite materials.

Compound	Starting Materials	Temperature (°C)	Atmosphere	Time (Hours)
CuFeO ₂	Cu ₂ O, Fe ₂ O ₃	1050	N ₂	36
CuAlO ₂	Cu ₂ O, Al ₂ O ₃	1150	N ₂	10
CuRhO ₂	Cu ₂ O, Rh ₂ O ₃	1050	Air	48

As previously described in the literature, the synthesis of CuCrO₂ was carried out by ball-milling stoichiometric amounts of Cu₂O and Cr₂O₃ in ethanol for 6 hours and then calcining at 1100 °C for 8 hours in air.⁶ The loose powder was then pressed into a pellet and heated at 1200 °C for 12 hours in air and furnace cooled.

2.1.1.2 Niobates

The copper niobates were synthesised using literature methods.^{7,8} CuNbO_3 was synthesized by grinding stoichiometric amounts of Nb_2O_5 and Cu_2O (with a 20% molar excess) for 15 minutes with a pestle and mortar. The mixture was dried at 80 °C overnight and then placed in a quartz tube and sealed under vacuum. The quartz tube was then heated to 900 °C over a 12-hour period, held at 900 °C for 24 hours, then cooled down to room temperature over the course of 12 hours. The product was then stirred in 0.5 M hydrochloric acid (HCl) for 30 minutes followed by centrifugation with Milli-Q water until the pH of the supernatant was neutral. The powder was collected by suction filtration and dried under vacuum overnight. CuNb_3O_8 was prepared by grinding stoichiometric amounts of Cu_2O and Nb_2O_5 for 15 minutes, the powder was then placed in a quartz tube, sealed under vacuum, and then heated at 750 °C for 24 hours (heating and cooling rate of 5 °C/min).

2.1.2 Carbon Nitrides

Each of the carbon nitrides were synthesised by calcination of precursors, which were placed in an alumina crucible (10 mL) with a lid and then calcined in a muffle furnace.

2.1.2.1 Barbituric Acid Series (CN-BA)

3 g of dicyandiamide (DCDA) and X g of barbituric acid (BA) (see Table 4) were placed in a glass beaker with 15 mL Milli-Q water and stirred for 30 minutes. Mixtures were then heated to 100 °C to remove water. The solid was then transferred to an alumina crucible with a lid and covered in aluminium foil, then placed in muffle furnace. Materials were calcined at 550 °C for 4 hours with a heating and cooling rate of 5 °C/min in static air.

Table 4 - Quantity of barbituric acid used.

Compound	X (g)
CN-DCDA	0.00
CN-BA(5)	0.15
CN-BA(10)	0.30
CN-BA(20)	0.60

2.1.2.2 Varying Calcination Conditions Series (CN-Temp and CN-Time)

3 g of dicyandiamide was transferred to an alumina crucible with a lid and covered in aluminium foil, then placed in muffle furnace. Materials were calcined at X °C for Y hours (see Table 5) with a heating and cooling rate of 5 °C/min in static air.

Table 5 - Calcination temperatures and times.

Compound	X (°C)	Y (Hours)
CN-500°C	500	4
CN-600°C	600	4
CN-2hr	550	2
CN-6hr	550	6
CN-8hr	550	8
CN-10hr	550	10

2.1.2.3 Varying Precursors (CN-Precursor)

3 g of melamine (CN-M), urea (CN-U) or thiourea (CN-T) was transferred to an alumina crucible with a lid and covered in aluminium foil, then placed in muffle furnace. Materials were calcined at 550 °C for 4 hours with a heating and cooling rate of 5 °C/min in static air.

2.1.2.4 Varying Precursor Ratios (CN-UT)

X g of urea and Y g of thiourea (see Table 6) was placed in a glass beaker with 15 mL deionised water and stirred for 30 minutes. Mixtures were then heated to 100 °C to remove water. The solid was then transferred to an alumina crucible with a lid and covered in aluminium foil, then placed in muffle furnace. Materials were calcined at 550 °C for 4 hours with a heating and cooling rate of 5 °C/min.

Table 6 - Quantity of urea and thiourea used.

Compound	X (g)	Y (g)
CN-UT(3:1)	2.25	0.75
CN-UT(1:1)	1.50	1.50
CN-UT(1:3)	0.75	2.25

2.2 Modification of Materials

Loading of Pt co-catalyst (1 wt%) onto the surface of materials was performed via photodeposition of H_2PtCl_6 *in-situ*. For *in-situ* experiments, the equivalent amount of H_2PtCl_6 (8 wt% solution) which would provide a maximum of 1 wt% loading (1 mL:0.5 μL , water: H_2PtCl_6 (8 wt% solution), v:v) was added to the photocatalyst suspension, purged with N_2 for 30 minutes and placed under illumination, with gas evolution monitored by gas chromatography (GC).

Molecular catalyst attachment was performed via mechanical mixing of the photocatalyst powders in solutions of the molecular catalysts. For the Ni cyclam catalysts, materials were soaked in photocatalytic solutions containing the Ni cyclam catalyst and left to soak for 24 hours before purging and placing under illumination. In detail 2 mg photocatalyst was placed in 10 mM ethylenediaminetetraacetic acid disodium salt (EDTA) and 1mM Ni catalyst in aqueous solution, left stirring in the dark for 24 hours before being purged with N_2 or CO_2 for 30 minutes and being placed in front of a light source.

FeTCPP modified carbon nitrides were prepared by mechanical mixing of 50 mg carbon nitride in 50 mL 90 μM FeTCPP (4 mg) ethanolic solution, left stirring for 24 hours in the dark. The suspension was then centrifuged, using a Heraeus Megafuge 16R, to remove the FeTCPP solution and then washed twice with 50 mL ethanol. Powders were then dried overnight at 60 $^\circ\text{C}$. Solutions pre- and post-soaking were measured via UV-Vis spectroscopy.

Higher surface area carbon nitrides were prepared by thermal oxidation etching of the bulk materials. In detail, 400 mg of carbon nitride was placed into an open alumina boat crucible and heated to 500 $^\circ\text{C}$ for 2 hours with a ramp rate of 5 $^\circ\text{C}/\text{min}$ in a muffle furnace, in air.

2.3 Characterisation

2.3.1 General Methods

Elemental Analysis (CHN) and Inductively Coupled Plasma Optical Emission Spectroscopy (ICP OES) were performed by the University of Liverpool analytical services. Samples were prepared by placing 5 mg of the material in 1 mL ~17 M H₂SO₄ and heating at ~100 °C for 1 hour or until particulates had completely dissolved. N₂ adsorption-desorption isotherms at 77 K were collected on a Micromeritics Tristar instrument. Samples were degassed under vacuum at 130 °C for 20 h before measurement. The specific surface area was calculated by applying the BET model for the adsorption data over the range of $p/p^0 = 0.05 - 0.3$.

2.3.2 Powder X-ray Diffraction (PXRD)

Powder X-ray diffraction (PXRD) was carried out using a Philips Panalytical X'Pert diffractometer with Co K α 1 of $\lambda = 0.178901$ nm for metal oxide samples and a Bruker D8-Advance X-ray diffractometer operating with Cu K α 1 of $\lambda = 0.15418$ nm for carbon nitride samples. The samples were analysed using 'Xpert Highscore Plus software for phase identification.

2.3.3 Diffuse Reflectance Infrared Fourier Transform Spectroscopy (DRIFTS)

Carbon nitride samples were studied by Diffuse Reflectance Infrared Fourier Transform Spectroscopy (DRIFTS) on a Bruker Vertex 70 spectrometer, fitted with a detachable DRIFTS attachment. Sample discs were prepared by dilution in KBr, specifically, 2 mg of sample in 100 mg KBr, mixed by grinding with a pestle and mortar till reaching homogeneity and then loaded into sample well. Spectra were collected at a resolution of 2 cm⁻¹ over 64 accumulations and were baselined with a KBr powder in air.

2.3.4 Cross Polarisation (CP) Magic Angle Spinning (MAS) Solid State Nuclear Magnetic Resonance (SS NMR)

Measurements and analysis were performed by Andrea Pugliese in Dr Frederic Blanc's group. Details of the measurement provided by Andrea are as follows. All NMR spectra were recorded on a Bruker DSX 400 MHz NMR spectrometer equipped with a 4 mm HXY probe tuned to X = ^{13}C at 101 MHz and Y = ^{15}N at 40 MHz NMR spectra were obtained with cross-polarization (CP). ^1H pulses and SPINAL 64 decoupling⁹ were performed at a radio frequency (rf) field amplitude of 83 kHz. For the ^{13}C CP step, a 70 – 100 % ramped rf field of 1 ms centred at 35 kHz was applied on ^{13}C , while the ^1H rf field was matched to obtain optimum signal at around 66 kHz. For the ^{15}N CP step, a 70 – 100 % ramped rf field of 6 ms centred at 40 kHz was applied on ^{15}N , while the ^1H rf field was matched to obtain optimum signal at around 60 kHz. The Magic angle Spinning (MAS) rates were 10 and 5 kHz for ^{13}C and ^{15}N , respectively. ^{13}C and ^{15}N chemical shift were referenced to CH signal of adamantane at 29.45 ppm¹⁰ and the NH_3^+ signal of glycine at 33.40 ppm¹¹.

2.3.5 Scanning Electron Microscopy (SEM) and Energy-Dispersive X-ray Spectroscopy (EDX)

SEM measurements of carbon nitrides were performed by Dr Marco Zanella on a Hitachi S4800 SEM. Powder samples were dispersed on a carbon tape attached to an alumina stub. SEM EDX measurements of the metal oxides were carried out and partially analysed by Liam Banerji. Measurements were made using a Hitachi S4800 SEM. Imaging uses an in-chamber Everart-Thornley detector and a cold field emission gun microscope, giving a resolution of ~2 nm. Energy dispersive x-ray spectroscopy (EDX) performed using the Oxford instruments AztecOne equipment, comprising of a 10 mm² silicon drift detector. Resolution of EDX was about 130 eV using Mn K α , spatial resolution ~1 μm and detection limit was typically ~0.1%. Samples were prepared by loading onto an aluminium stub with carbon tape and coated with chromium for imaging and carbon for EDX. For imaging, a working distance of 8 mm and a voltage of 5 kV were used and for the EDX a working distance of 15 mm and a voltage of 20 kV were used.

2.3.6 Ultraviolet- Visible-Near Infrared (UV-Vis-NIR) Spectroscopy

UV-Vis-NIR diffuse reflectance spectroscopy (DRS) data was obtained with a Shimadzu UV-2550 UV/Vis spectrometer, equipped with an integrating sphere, over the spectral range of 200-1400 nm and BaSO₄ was used as a reflectance standard.¹² The diffuse reflectance spectra were then converted from reflectance to absorption according to the Kubelka-Munk function:

$$F(R) = \frac{k}{s} = \frac{(1 - R_{\infty})^2}{(2R_{\infty})}$$

where k and s are absorption and scattering coefficients, respectively and R is the diffuse reflectance based on the Kubelka–Munk theory of diffuse reflectance. The data can then be plotted using the equation:

$$(\alpha h\nu)^{\frac{1}{n}} = A(h\nu - E_{BG})$$

Where α is the absorption coefficient, h is Planck's constant, ν is the frequency of light, A is the proportionality constant and E_{BG} is the band gap. The value of n denotes the nature of the transition, $n = \frac{1}{2}$ for direct transitions or $n = 2$ for indirect transitions. A Tauc plot of $(\alpha h\nu)^{\frac{1}{n}}$ versus $h\nu$ can be used to estimate the band gap of the material by linear extrapolation to find the x-intercept.¹²

UV-Vis spectra of solutions were collected on the same piece of equipment with a standard sample compartment, using a 4 mL (path length, 10 mm) or 0.4 mL (path length, 1 mm) quartz cuvette. Determination of concentrations of soaking samples were determined using the Beer-Lambert equation:

$$A = \varepsilon l c = \log_{10} \frac{I_0}{I}$$

Where, A is the absorbance, ε is molar absorptivity, l is the path length, c is the concentration, I_0 is the incident light intensity and I is the transmitted light intensity.

2.3.7 X-ray Photoelectron Spectroscopy (XPS)

Photoemission spectroscopy is based on the principle that when a solid is illuminated with particular forms of irradiation it will emit energy in a certain form, which can be detected, and this energy can provide different types of information about the material from which it originated. X-ray photoelectron spectroscopy uses an X-ray source (e.g. Mg K_{α} (1253.6 eV) or Al K_{α} (1486.6 eV)) which produces X-rays of a certain energy. When a sample is irradiated with this X-ray source, the X-rays can interact with electrons in core-orbitals and can lead to the ejection of photoelectrons with specific kinetic energy (E_K).¹³⁻¹⁶ The kinetic energy of the electron is related to the binding energy (E_B), the energy of the photon ($h\nu$), and the work function of the material (Φ) in the following equation:

$$E_K = h\nu - E_B - \phi$$

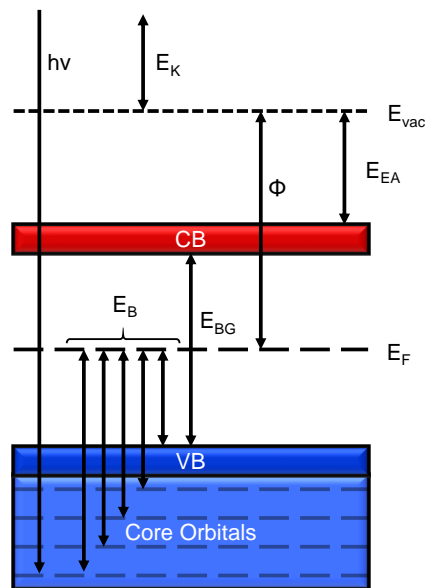


Figure 9 – Schematic energy level diagram of a semiconductor, depicting the core orbitals, valence band (VB), conduction band (CB), Fermi level (E_F), vacuum level (E_{vac}), photon energy ($h\nu$), binding energy (E_B), kinetic energy (E_K), band gap energy (E_{BG}), work function (Φ) and electron affinity (E_{EA}).^{13,14,17-20}

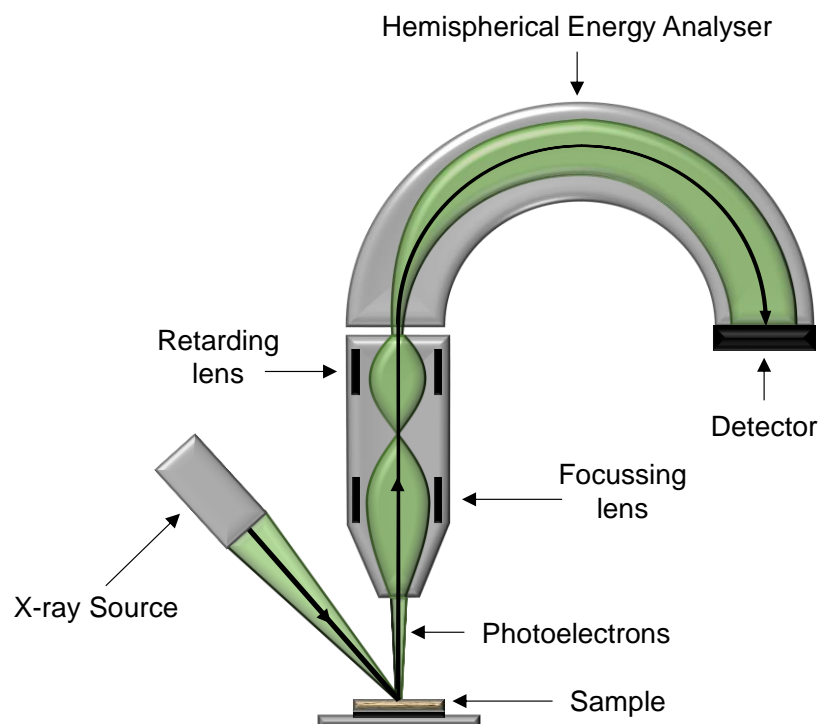


Figure 10 – Schematic representation of the XPS experiment with a hemispherical electron energy analyser.^{14,15,18–20}

The binding energy of an electron is specific to the element and core orbital that the electron originated from before photoemission and is reported relative to the Fermi level of the material. XPS probes surface and near surface states giving information on element type and environment. XPS can also be used to determine the position of the valence band maximum (VBM), by first measuring the VBM spectra relative to the Fermi level and then determining the work function of the material, the value of the valence band vs the vacuum level can be calculated. The work function can be determined using the equation:

$$\phi = h\nu - E_{SEC}$$

where E_{SEC} is the energy of the secondary electron cut-off (SEC). If the photoelectrons undergo multiple inelastic collisions before reaching the surface, the kinetic energy of the electron is affected, and the information associated with the electron's origin is lost. These inelastically scattered electrons, known as secondary electrons, contribute to the background signal and are almost featureless. The secondary electron cut-off is where the secondary electrons have hardly enough energy to escape the surface, where kinetic energy is basically 0 eV. Measuring the secondary electron cut-off is achieved by applying a bias to the sample,

this provides the secondary electrons with an increase in kinetic energy, which means that they can reach the detector, also the applied potential shifts the SEC of the sample from that of the analyser.^{21–26} The SEC measurement must be calibrated to the applied potential, then the work function can be determined. Calculation of the VB position relative to the vacuum level is accomplished by addition of work function and VBM.

XPS surface states for a number of carbon nitrides (CN-UT, CN-Precursor, CN-Time, and CN-Temp) were measured by Prof. Rob Palgrave at University College London and was carried out with a two chamber Thermo Theta Probe spectrometer using a monochromated Al K α X-ray source (1486.6 eV) in constant analyser energy mode. X-rays were focused to a 400 micron spot at the sample surface, which defined the analysis area. Sample charging was prevented by use of a dual beam flood gun. High resolution core line spectra were recorded at 50 eV pass energy, and survey spectra were recorded at 150 eV pass energy. Further XPS surface states and band structure determination for the CN-BA series of materials were performed at Stephenson Institute for Renewable Energy at the University of Liverpool, with help from members of Prof. Vinod Dhanak's group; Holly Edwards, Dr Jose Coca-Clemente, Huw Shiel, Leanne Jones, and Hatem Amlı. XPS core level spectra were measured using a Mg K α (1253.6 eV) X-ray source operating at 144 W and a hemispherical PSP Vacuum Technology electron energy analyser, operating with a typical constant pass energy of 20 eV. A sputtered polycrystalline Ag sample was used for calibration, to determine the precision of the analyser. The secondary electron cut-off (SEC) at low kinetic energies was measured with the X-ray source operating at 9 W with an applied bias of 10 V between the sample and analyser, to separate the spectrometer response.

All XPS spectra were fitted using CasaXPS software which fits spectra using a Gaussian/Lorentzian product function to approximate a Voigt function after Shirley background removal with a binding energy determination precision of ± 0.1 eV and all spectra were calibrated to an adventitious carbon peak of 284.6 eV.

2.3.8 Mott-Schottky (MS) Measurement

The Mott-Schottky method is a type of impedance measurement which is often used for the determination of flat band potentials in semiconductors and involves measuring the differential capacity at a semiconductor-electrolyte interface.²⁷⁻²⁹ The Mott-Schottky equation is:

$$\frac{1}{C^2} = \frac{2}{\epsilon \epsilon_0 A^2 e N_D} \left(V - V_{fb} - \frac{k_B T}{e} \right)$$

Where C is the capacitance, ϵ is the dielectric constant, ϵ_0 is the permittivity of free space, A is the area, N_D is the number of donors, V is the applied potential, V_{fb} is the flat band potential, k_B is Boltzmann's constant, T is the absolute temperature and e is the electronic charge. A plot of $1/C^2$ against V is known as a Mott-Schottky plot and usually provides a straight line. The direction of the slope of the data can be used to determine the nature of the semiconductor and the x-intercept gives the value of the V_{fb} . A positive slope infers that the semiconductor is n-type and from the flat band potential, the conduction band position can be estimated, whereas a negative slope indicates the semiconductor is p-type and the valence band position can be approximated. Usually, these types of measurements are performed at a number of frequencies as the x-intercept should be frequency independent. However, the use of this equation is based on several assumptions, including; that the electrode behaves ideally, in that it is perfectly planar and contains no defects, there are no interfacial layers present, any impedance of different phases is negligible, among others.²⁸⁻³⁰ This method is widely used within the carbon nitride literature; however, this is not necessarily the most appropriate method for certain classes of materials, this is discussed in greater depth in Chapter 3 Section 3.3.4.2.

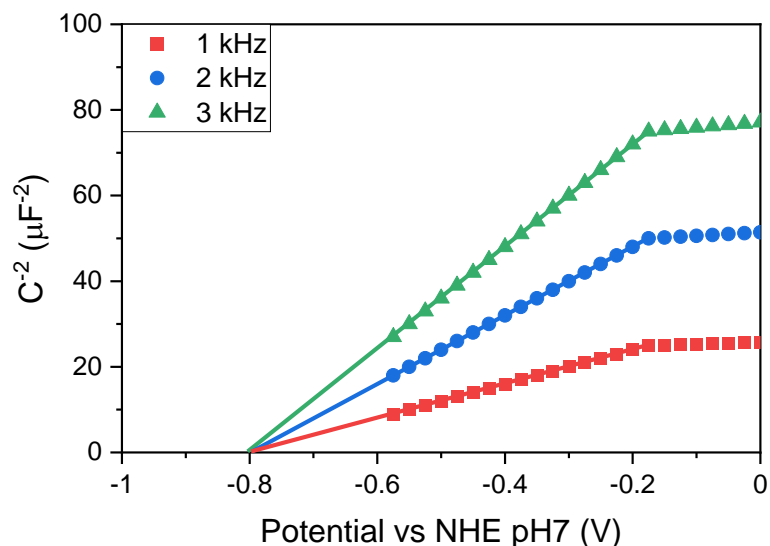


Figure 11 – Representative ideal Mott-Schottky plot for an n-type semiconductor with a flat band potential of -0.8V vs NHE pH7 at 1, 2 and 3 kHz.

Mott-Schottky measurements were carried out on a 3-electrode cell with a carbon nitride film as a working electrode, Ag/AgCl reference electrode and Pt mesh counter electrode. The working electrodes were prepared by drop-casting carbon nitride slurries onto fluorine-doped tin oxide (FTO). The FTO was first cut down to pieces approximately 2 cm x 1.2 cm and cleaned via sonication for 20 minutes, in acetone first, then ethanol and finally water. After drying with compressed air, the FTO pieces were placed, with the conductive side facing upwards, into a muffle furnace and dried at 400 °C (20 °C/min ramp rate) for 20 minutes. To keep the area of the working electrode the same, a 1 cm x 1 cm square was marked out on the FTO using epoxy to create a well for the slurries. Carbon nitride slurries were prepared by sonicating 20 mg carbon nitride in 1 mL acetone and 50 μL Nafion (5 wt% solution) for 20 minutes, 200 μL of this slurry was deposited into the FTO wells. The electrodes were then left to dry overnight beneath a cover to prevent changes in air flow affecting the homogeneity of the films. Measurements were performed in aqueous solutions of 0.1 M KCl electrolyte and electrodes were soaked for 1 hour prior to purging with Ar for 30 min and setting up to measure. Mott-Schottky data was collected on a BioLogic SP300 workstation at room temperature, in the dark and inside a Faraday cage. Data was collected between -0.4 and 0.4 V vs Ag/AgCl pH 7 and 17 frequencies between 1 MHz and 10 mHz. The Bio-Logic software performs all calculations and gives the data in the form of the Mott-Schottky plot.

2.3.9 Steady-State Photoluminescence (PL) and Time-Resolved Emission Lifetime Spectroscopy

Photoluminescence or fluorescence occurs when an excited state relaxes back down to ground state via the recombination of photogenerated electron-hole pairs triggering emission of a photon of light.^{31–35} In a typical steady-state PL experiment, the equipment consists of a Xe lamp, which is used as an excitation source, a monochromator is used to filter the light to give an excitation source of a chosen wavelength and bandwidth, a sample chamber, for solid or liquid samples and a detector.³¹ To measure the PL emission, a wavelength and bandwidth is chosen with sufficient energy to excite the sample from the ground state to the higher energy excited state generating an electron-hole pair. When a material is excited to a higher energy excited state, emission occurs as an electron transitions to an empty lower energy state recombining with a hole, this emission can be radiative or non-radiative in nature. Radiative emission occurs when a photon or other form of electromagnetic radiation is emitted, non-radiative emission usually leads to the emission of heat. Depending on the mechanism by which recombination occur, these photons have different energies, so PL emission yields a broad spectrum. Time-resolved emission lifetime spectroscopy can be used to determine the lifetimes of charges that decay via emissive pathways. Measurements involve excitation of the sample by a pulsed light source and then monitoring a single emission wavelength over a certain time-period after excitation has occurred.

ISC = Inter-System Crossing
 IC = Internal Conversion

P = Phosphorescence
 F = Fluorescence

ESA = Excited State Absorption
 A = Absorption

v = vibrational states
 S_2 = 2nd Singlet excited state
 S_1 = 1st Singlet excited state
 T_1 = Triplet excited state
 S_0 = Singlet ground state

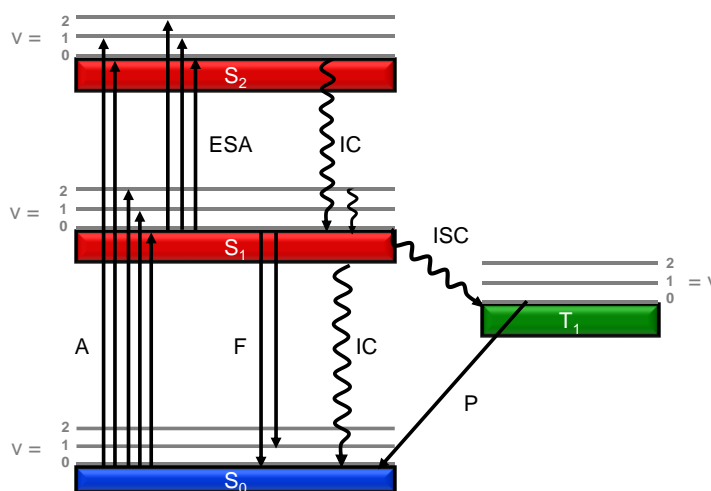


Figure 12 – A Jablonski diagram showing the ground, excited electronic and vibration states of a system. ^{17,34,36–38}

Steady-State Photoluminescence (PL) and Time-Resolved Emission Lifetime Spectroscopy measurements were recorded on an Edinburgh Instruments FLS980-D2S2-STM spectrophotometer, equipped with a 450 W Ozone free Xe arc lamp, excitation and emission monochromators and a photomultiplier tube detector. Samples were prepared by sandwiching powders in a demountable quartz cuvette (130 μ L). Steady-state photoluminescence spectra were collected in air by a single measurement with an excitation wavelength of 390 nm, monitoring between 410 and 700 nm (2 nm step and 0.1 s dwell time).

Time-resolved emission lifetime spectra were obtained from time-correlated single photon counting measurements, in which a single wavelength is monitored over a certain time period. Spectra were acquired with a 371 nm pulsed laser diode (pulse period of 2 μ s in air) between 0 and 2000 ns and a stop condition of 10,000 counts. The monitored emission wavelength is specified for each sample in the figure heading.

As the instrument has a certain electronic response time, the instrument response function (IRF) of the equipment must be determined by measuring the response of the instrument to a purely scattering solution. The IRF of the instrument was determined using a Ludox sample (aqueous dispersion of silica particles) under the same conditions as those used for the actual samples.

The emission lifetime data was analysed using DecayFit software³⁹ as this can be used to fit the emission decay to a number of exponential functions, taking the IRF into consideration. The lifetimes were determined by fitting the exponential decay to a multi-component exponential function:

$$y = y_0 + A_1 e^{-x/\tau_1} + A_2 e^{-x/\tau_2} + A_3 e^{-x/\tau_3} + \dots$$

Where y_0 is the y offset, τ is a lifetime and A is the amplitude of that lifetime and the number of exponentials used is dependent on the number of lifetimes present.

2.3.10 Transient Absorption (TA) Spectroscopy

Transient absorption spectroscopy, also known as flash photolysis, is a pump-probe technique that can be employed to understand photogenerated charge carrier dynamics.^{40–43} The experiment involves probing a sample with a light source (probe) and measuring absorbance of the ground state sample, which is then photoexcited with a second light source (pump) and transient absorption, the difference between the absorbance of the ground and excited state samples, is measured as a function of both wavelength and time. The change in absorbance is measured by subtracting the absorption spectrum of the ground state from the excited state. TA spectroscopy allows both emissive and non-emissive states to be investigated and by altering the time delay between the pump and probe, the evolution of these photogenerated states can be studied.⁴² Generally a weak probe is used as its low intensity does not affect the population of the excited state and will avoid multiphoton/multistep processes during probing.⁴⁰

Depending on the probe source used, different sorts of information can be obtained.^{41,42} X-ray or extreme UV sources can be used to examine transitions between core and valence states. UV-visible-NIR probes can look at a number of transitions including band gap, sub-band gap and intraband transitions and can be used to study deeper trap states whereas mid-IR is sensitive to shallow states, whilst free charge states can be studied using Terahertz and microwave irradiation. Within this thesis, the focus is solely on diffuse reflectance TA kinetics of carbon nitride powders in the visible region 450-900 nm on the μ s to s timescale.

Typically, a TA spectrum is the sum of these 3 types of contributions:

- Ground-state bleach – The sample has been excited, so the population of the ground state in the excited sample is lower than in the non-excited state, resulting in a negative signal.^{40,43}
- Stimulated emission – Upon excitation by the pump, stimulated emission occurs as the sample relaxes to the ground state. This emission occurs in the same direction as the probe photon, causing both to be detected, so results in a negative signal. This will only occur for optically allowed transitions and can occur at similar positions to those found in the fluorescence spectrum.^{40,43}

- Excited-state and product absorption – Once excited by the pump, the sample can be excited to a higher excited state, which may lead to the generation of longer-lived excited states, e.g. triplet or charge separated states. This can lead to a positive signal.^{40,43}

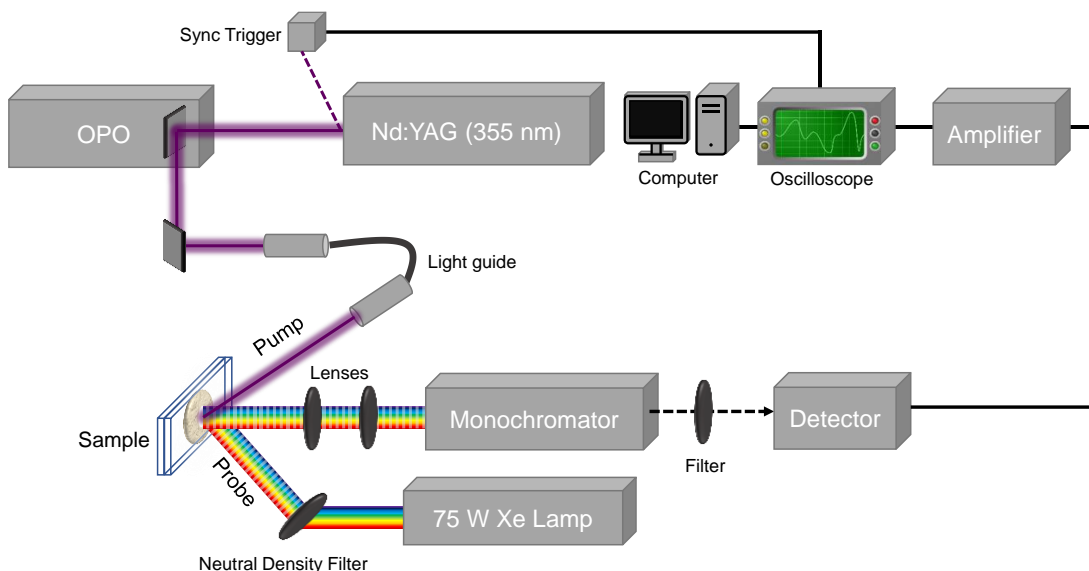


Figure 13 – Schematic representation of microsecond TA system in diffuse reflectance mode.

Diffuse reflectance microsecond TA spectra were measured using the set-up depicted in Figure 13 with the help of Dr Mark Forster. The set-up was used in diffuse reflectance mode as all measurements were performed on powder samples in air. First the sample is illuminated with a probe light, produced by a 75 W Xe lamp (OBB Corp.) focussed through a neutral density (50%) filter on to the sample. The reflected light is then focussed by a series of lenses to the entrance of the monochromator, which is used to select a specific wavelength to monitor. Once the light has passed through the monochromator, it reaches a filter before passing to the detector, this filter is used to prevent stray laser light from entering the detector. The optical density is measured by a Si Photodiode (Hamamatsu) and a homemade amplification system coupled to an oscilloscope (Textronix TDS 220) and data acquisition card (National Instruments NI-6221). TA experiments are based on measuring the change in optical density over time after a sample has been excited by a pump source. The 355 nm pump laser produced by a Nd: YAG laser (Continuum, Surelite I-10, 4-6 ns pulse width, 0.33 Hz, 200 μ J incident on slide) was transmitted via a light guide (0.5 cm diameter) and used to excite the

carbon nitride samples. Full spectra were collected by measuring the decays over microsecond-second timescales, every 50 nm between 450-900 nm and were averaged over 100 laser pulses. Samples were prepared by sandwiching carbon nitride powder between two microscope slides.

The TA spectra were analysed in Origin and the lifetimes of states were determined by fitting the exponential decay to a multi-component exponential function:

$$y = y_0 + A_1 e^{-x/\tau_1} + A_2 e^{-x/\tau_2} + A_3 e^{-x/\tau_3} + \dots$$

Where y_0 is the y offset, τ is a lifetime and A is the amplitude of that lifetime and the number of exponentials used is dependent on the number of lifetimes present.

2.3.11 Fourier Transform (FT) and Kerr-Gated (KG) Raman and Time Resolved Resonant Raman (TR³)

For some materials it can be difficult to obtain good Raman spectra, this is due to the Raman signal being very weak and can be obscured by strong emission.⁴⁴⁻⁵⁶ This is because of the lasers that are used for Raman experiments lie within the visible region causing excitation, leading to strong fluorescence when the material relaxes. Probing in the NIR region where electronic absorption and emission transitions do not occur can be an effective approach for avoiding emission. FT-Raman utilises near-IR lasers (1064 nm) and an interferometer which greatly reduces the effects of emission. However, the use of NIR lasers means that it cannot utilise the resonance effect, so suffer from low sensitivities.^{50,54,57,58}

Another method which can be used to block the emission is to employ a gating system. Kerr-gated Raman can employ visible wavelength lasers, taking advantage of the resonance enhancement effect, increasing Raman scattering.^{56,58} Furthermore, a Kerr-gate can be used to effectively block emission due to the different lifetimes of emission and Raman scattering signal upon excitation, typically Raman scattering occurs instantaneously, whilst emission occurs over longer timescales.⁵¹⁻⁵⁵ Figure 14 and Figure 15 show a schematic representation of the Kerr-gated Raman and TR³ set-up, the Kerr-gate consist of a Kerr-medium (CS₂), a

polariser and a cross-polariser. A high energy laser pulse, or gate pulse can be used to induce a transient anisotropy in the Kerr-medium for a brief time (~ 4 ps), during which any light propagating through this medium can be polarised. ^{46,47,51,53–55,58,59}

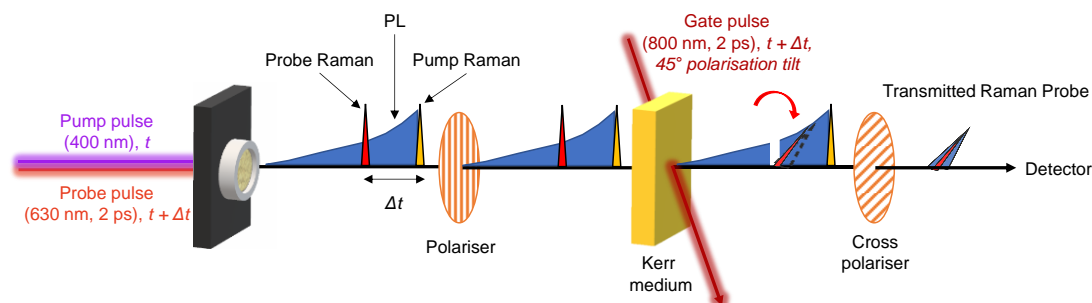


Figure 14 - Schematic representation of Kerr-gated Raman Spectroscopy experimental set-up, adapted from the Central Laser Facility website <https://www.clf.stfc.ac.uk/Pages/Kerr-Gated-Raman-Spectroscopy.aspx> and applicable publications. ^{47,51,59}

The sample is illuminated with a monochromatic probe pulse (630 nm) to induce Raman scattering, which is then polarised by the first polariser. When correctly timed with the gate pulse, the Raman signal can propagate through the Kerr-medium and is polarised, rotated 90° with respect to its original polarisation and can pass through the cross-polariser to the detector. The slower emission, however, passes through the Kerr-medium without being rotated, so when it reaches the cross-polariser it is blocked from reaching the detector. ^{46,51}

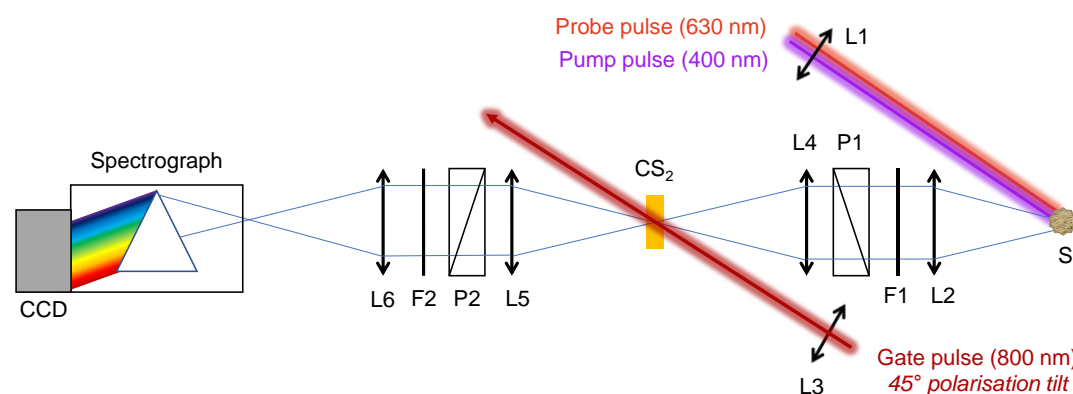


Figure 15 - Schematic diagram of the Kerr-gate, where: S – sample, L1 – L6 – lenses, F1, F2 – cut-off filters, P1, P2 – polarisers, CS₂ – the Kerr cell filled with carbon disulphide. ⁵⁹

Time-resolved resonance Raman (TR³) belongs to the pump-probe family of techniques and can yield both structural and kinetic information about the excited material. ^{46,51,53,56,60} It uses a pump pulse to excite the material and an appropriately timed probe pulse to produce Raman

scattering of the excited sample, so it can be used to gain structural information of the excited material at different time delays. However, due to the use of a pump and a probe pulse, it can lead to excitation to emissive states, causing greater emission, therefore a Kerr-gate can be employed to reject this emission and obtain high quality temporally resolved resonance Raman data.^{46,53,60} The Kerr-gate effectively blocks the emission signal from the pump and probe pulses and any Raman signal generated by the pump pulse as these signals are not rotated by the Kerr-medium and are blocked by the polariser.

To the best of our knowledge Kerr-gated Raman or TR³ have not previously been reported for carbon nitride samples. FT-Raman, KG Raman and TR³ experiments were performed at ULTRA laser facilities at the Central Laser Facility (CLF), STFC, Rutherford Appleton Laboratories, with the help of Dr Igor Sazanovich and Dr Gaia Neri.

FT-Raman was performed on a BRUKER MultiRAM, IRFS27 at the CLF equipped with a 1064 nm laser. Powder samples were loaded into well sample holders for measurements. KG Raman and TR³ were performed on purpose-built equipment, depicted in Figure 15, driven by the picosecond arm of the ULTRA laser system.⁵⁹

Raman scattering of the sample, S, was induced by a 630 nm laser pulse (4 mW, 10 kHz, 1 ps) with a spot size of 75 x 75 μm and excitation of the sample was achieved using a 400 nm pump pulse (5 mW, 1 kHz, 2 ps) with a spot size of 100 x 100 μm , which were focussed on to the sample with L1. Raman and fluorescence signal are collimated with L2 and then passed through the long pass filter F1, which acts to block Rayleigh scattering, before reaching the Kerr-gate. The Kerr-gate consists of a Kerr-medium (2 mm path length quartz cell filled with CS₂) and a vertical entrance polariser P1 and a horizontal vertical polariser P2 (25 mm aperture, Halbo Optics PS25). Activation of the Kerr-gate was achieved using a gating pulse (800 nm, 250 μJ , 2 ps, 2.4 W, 10 kHz), which was produced by a ps arm of the ULTRA Laser System⁶¹ and was polarised at 45 ° with respect to the polarisers and was focused onto the Kerr-medium using L3. Collimated light passes through P1 and is then focused by L4 onto the Kerr-medium, which then rotates the collimated light. The rotated Raman (and non-rotated fluorescence) is then collected by L5 and collimated to pass through polariser P2, which blocks the fluorescence and allows the Raman to pass through, where it can be filtered by the short

pass-filter F2 before being focussed into the entrance slit of the spectrograph (Shamrock 303i, Andor) equipped with a CCD camera (iDus DU-420A-BU2, Andor). To make sure that the Kerr-gate allows only the Raman scattering to reach the detector, the gating and probe pulses must be precisely timed, this was done using an optical delay line comprising a hollow retroreflector and a motorized linear stage (IMS-600LM from Newport, 600 mm travel range).

Spectra were collected and averaged over 3 repeats, each with an acquisition time of 20s and were collected at different probe (2 delays, -100 and 0 ps) and pump delays (47 delays between -100 and 2800 ps) relative to the gating pulse. The Raman shift was calibrated by comparing spectra obtained for toluene and acetonitrile. Due to the set-up of the system, measurements were only performed over a certain range, so Raman spectra were collected over two regions, 100-1500 cm^{-1} and 1260-2400 cm^{-1} .

Samples were prepared by sandwiching powders between two CaF_2 windows with a 300 μm spacer and loaded into a Harrick cell which was purged with N_2 for about an hour before measurements were taken. Sample powders were measured in reflectance and Raman spectra was collected under rastering conditions.

The KG was successful in removing the majority of the emission from the Raman signal, but there was still some emission presence in the data, however this could be easily removed by baseline correction using the data collected from measurements when the probe laser was set to a negative delay. However, there was an issue which arose for some of the materials in the barbituric acid series of materials, as the probe laser slightly overlapped with the UV-Vis absorption spectra. This could not be removed by emission subtraction. Instead, this data was baseline corrected by a subtraction of a single point in the Raman spectra baseline.

The lifetimes of excited states were determined by fitting the emission and Raman bleach kinetics to a multi-component exponential function:

$$y = y_0 + A_1 e^{-x/\tau_1} + A_2 e^{-x/\tau_2} + A_3 e^{-x/\tau_3} + \dots$$

Where y_0 is the y offset, τ is a lifetime and A is the amplitude of that lifetime and the number of exponentials used is dependent on the number of lifetimes present. Further processing and analysis of the data is discussed in the Chapter 3.

2.4 Photocatalytic Testing

Photocatalytic testing, for both H₂ production and CO₂ reduction, was performed on one of two set-ups:

- A Xe lamp set up, allowing for testing of up to 2 experiments at a time.
- A high throughput set-up, allowing up to 10 experiments at once.

Typically, a suspension of the photocatalyst, 1 mg of photocatalyst per 1 mL of solution, was placed under illumination for several hours before analysis of gaseous and liquid products via gas and ion chromatography. The solutions used in most cases contained a sacrificial reagent (a hole scavenger) as this allows for investigation of just the reduction reactions.

Gases evolved (H₂ and CO) were detected by an Agilent technologies 6890N instrument equipped with a pulsed discharge detector (D-3-I-HP, Valco Vici) and a 5 Å molecular sieve column (ValcoPLOT, 30 m length, 0.53 mm ID) with N6 Helium as the carrier gas (5 mL/min). Quantities of gas were calculated using calibrant gas (~500 ppm H₂, 200 ppm CH₄ and 200 ppm CO, with CO₂ balance gas). In this work quantity of CH₄ has not been reported as we do not have an accurate method for methane detection.

Detection of formate and other liquid products was attempted using Ion Chromatography (IC). Measurements were performed on an Eco IC set up for the detection of anions. The column used was a metrosep A sup 5-150/4 with a metrosep A sup 5 guard/4.0. The eluent used was 3.8 mM potassium carbonate and 1.2 mM potassium bicarbonate. Regeneration was performed using a solution of 350 mM sulphuric acid and 100 mM oxalic acid with 5% acetone. Solutions were pumped at a rate of 0.7 mL/min, pressure of 7.3 MPa and conductivity of ca. 16.17 μS.cm⁻¹.

Isotopic labelling experiments were performed using a similar procedure to the typical Xe lamp experiments in which the photocatalyst was placed in a hole scavenger containing solution in a concentration of 1 mg/mL and then illuminated with visible light for 4-24 hours. The only variation from the typical photocatalysis procedure was the way in which the suspensions were purged; samples were first purged with N₂ for 30 minutes and then purged with ¹³CO₂ for

several minutes before being placed under illumination. The headspace of the experiment was sampled using a gas syringe, the sample was then injected into a special made pre-purged cell and the FTIR spectra was measured at a resolution of 0.5 cm^{-1} and averaged over 200 accumulations. The cell used for FTIR measurements consisted of a tube with CaF_2 windows attached to either end and a septa port for purging and sample injection.

2.4.1 Xe Lamp Photocatalysis

In a typical experiment, 2 mg of photocatalyst was dispersed in 2 mL solution in either a 4 mL glass vial sealed with a PTFE/Silicone septa cap or a 4 mL quartz cuvette with added headspace sealed with a rubber septum, unless stated otherwise. Systems were purged with $\text{Ar}/\text{N}_2/\text{CO}_2$ for 30 minutes prior to photocatalytic testing. The tests were carried out using a 300 W Xe lamp (Newport) with a 375 nm long pass filter or a KG1 filter, unless stated otherwise, and solutions were kept under constant stirring to maintain a suspension (Figure 16 and Figure 17). The light intensity incident on the vial/cuvette was measured with an optical power meter and a thermal sensor (Thorlabs). Typically, experiments were carried out at $\sim 100\text{ mW cm}^{-2}$ unless stated otherwise and the average temperature under illumination was about $34\text{ }^\circ\text{C}$.

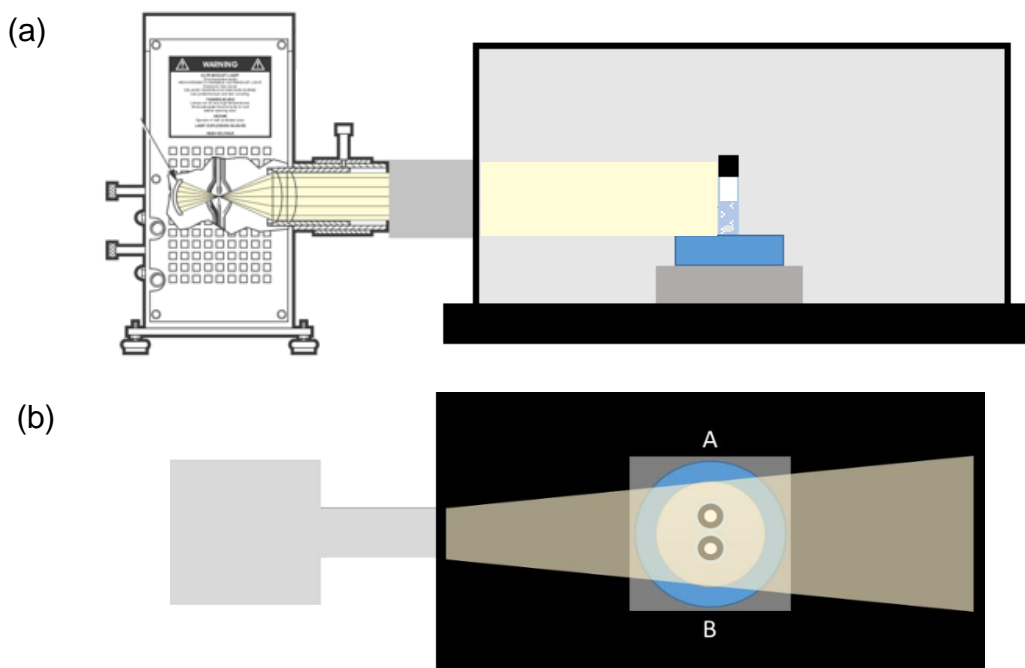


Figure 16 - Schematic of Xe lamp set-up - (a) side view and (b) top view.

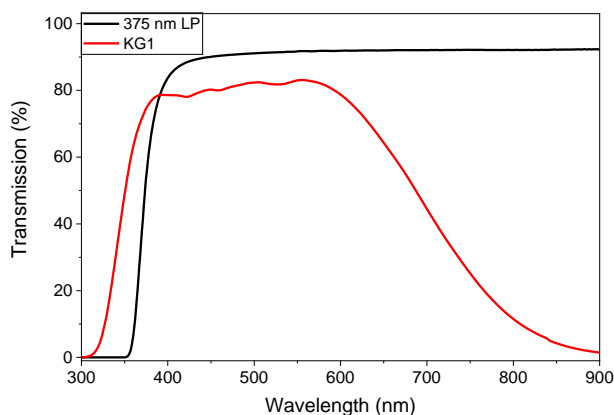


Figure 17 – UV-Vis transmission spectra of the 375 nm long pass and KG1 filters.

2.4.2 High Throughput (HT) Photocatalysis

Within this project, a large number of materials were synthesised, all of which required photocatalytic testing. The original Xe lamp set-up allowed for only 2 tests to be performed at any one time, so due to the time constraints of the project, a quicker screening method was necessary. This led to the development of a high throughput (HT) screening system (Figure 19). The HT set-up consists of an array of 20 gallery white visible light (~450-720 nm, Figure 18) LEDs (LED Engin. LZ9-M0GW00-0030) mounted onto a large heat sink, providing 10 testing positions. A roller bed was used to keep the system constantly stirring, to maintain a suspension and a system height was chosen to provide a light intensity of $\sim 100 \text{ mW cm}^{-2}$ incident on the glass vial. Due to heating of the LEDs the temperature beneath the LEDs was controlled using air-conditioning and fan-assisted cooling.

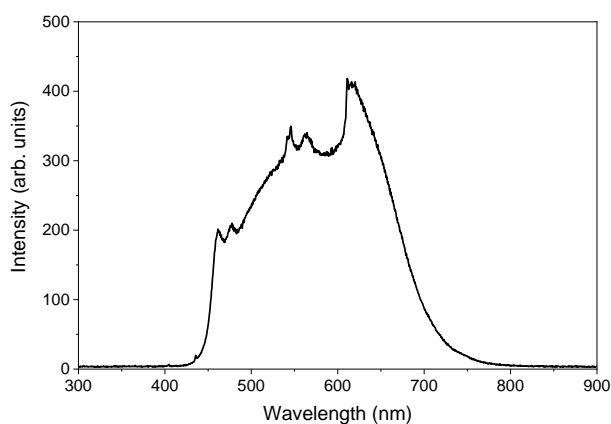


Figure 18 – HT set-up LED spectral output.

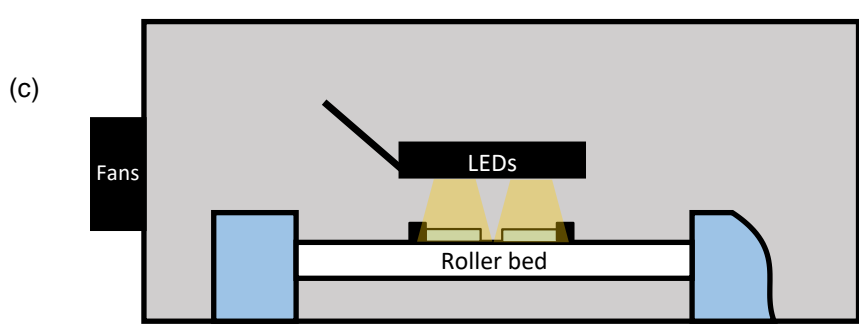
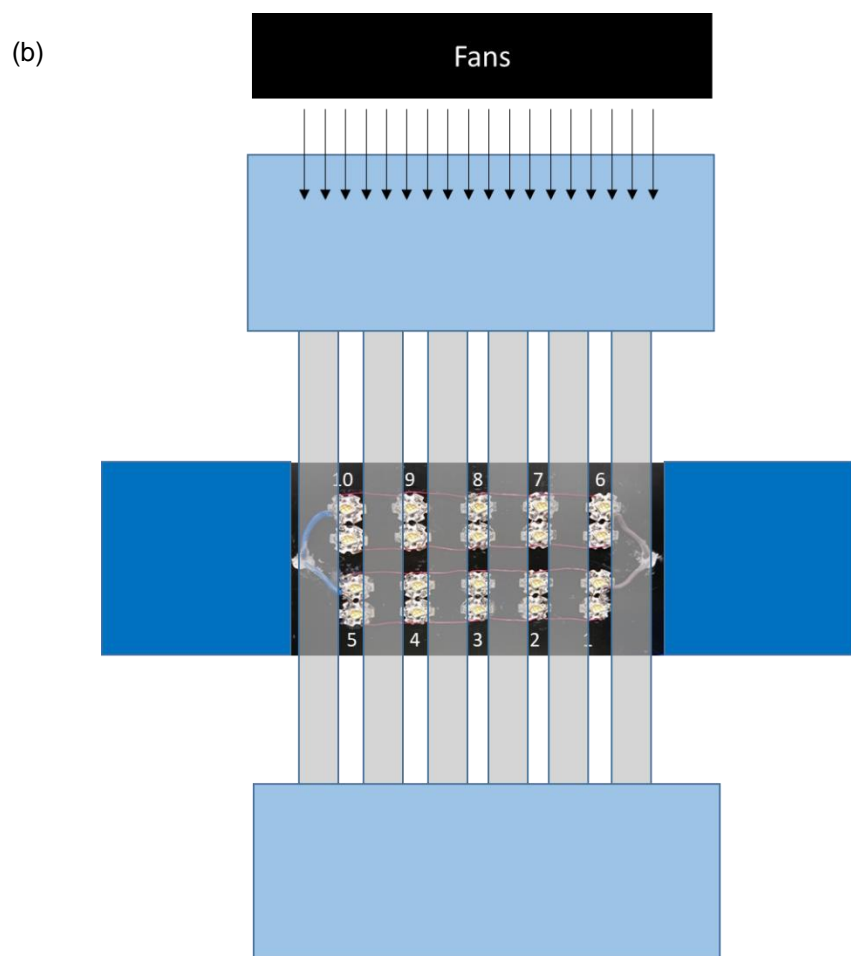
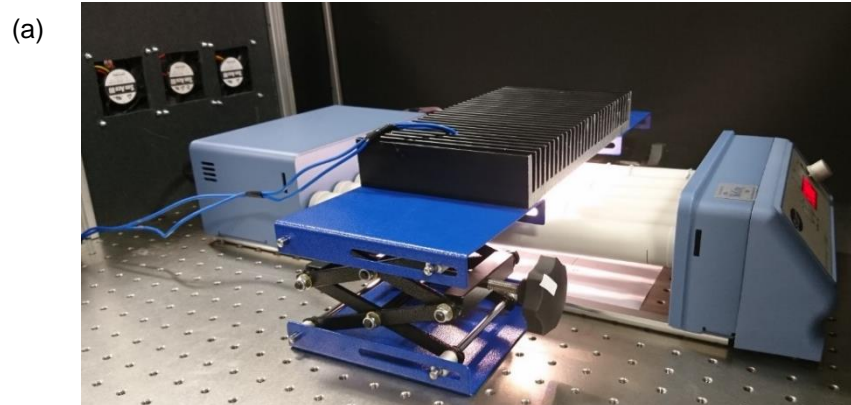


Figure 19 - (a) photograph of HT system and schematic of HT set-up (b) top view and (c) side view.

In a typical experiment, 2 mg of photocatalyst was dispersed in 2 mL solution in a 4mL glass vial sealed with a PTFE/Silicone septa cap. The system was purged with Ar/N₂/CO₂ for 30 minutes prior to photocatalytic testing. The light intensity incident on the glass vial was measured with an optical power meter and a thermal sensor (Thorlabs). Experiments were carried out at ~100 mW cm⁻².

During development of the high throughput system, the set-up took several forms before settling on the format shown in Figure 19. Once built, the conditions under each LED position were measured and compared. Measurements of temperature and light intensity were measured every 1-2 hours over the course of 8 hours of illumination over several days. Furthermore, a carbon nitride photocatalyst was chosen to test at each LED position for H₂ evolution in the presence of 10 mM ethylenediaminetetraacetic acid disodium salt (EDTA) and H₂PtCl₆ (8 wt% solution), for *in-situ* 1 wt% Pt loading. Experiments were performed on four consecutive days, to obtain error bars for each position. This was done to understand how variations in conditions effected the photocatalytic activity of a material.

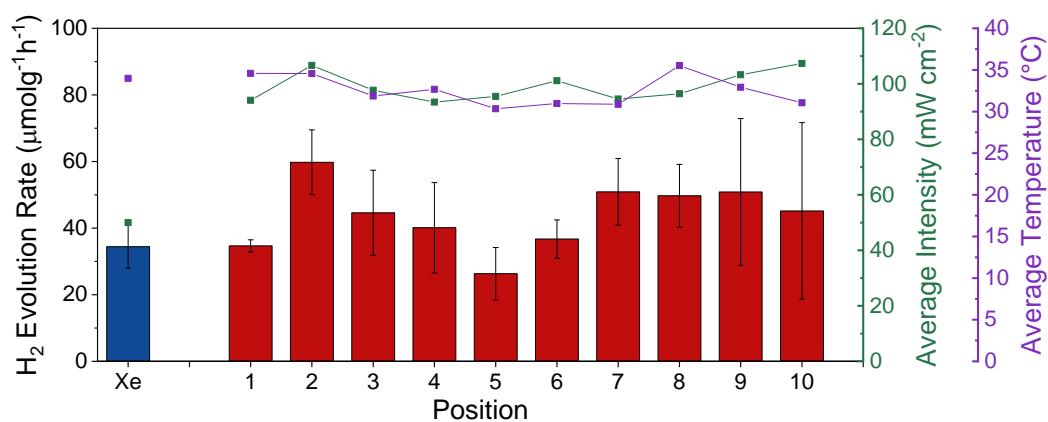


Figure 20 - Rate of H₂ evolved in µmol per gram of photocatalyst per hour for 2 mg of photocatalyst in 2 ml 10 mM EDTA with 1 µl H₂PtCl₆ (8 wt%) over 4 hours visible light irradiation at ~100 mWcm⁻² in a glass vial, at each LED position, tested on the screening set-up. With average light intensity and temperature measured at each LED position 1-10 (red), compared with experiments performed on the Xe lamp (blue) around the same time.

Figure 20 shows the rate of H₂ evolution for a carbon nitride (CN-BA(5)) tested at each LED position on the high throughput screening system, compared with the Xe lamp set-up and the average light intensity and temperature determined for each position. The numbered positions refer to the LED position on the high throughput system shown in Figure 19 (b). The measured

photoactivities, light intensity and temperature seems to differ significantly between LED positions and experiment runs. Normalisation to temperature or light intensity did not help minimise variations across the array, this is likely due to the effect on photocatalytic activity not following linearly with changes in temperature and light intensity. To ensure that the variation across the array was not due to errors in weighing small quantities of samples a larger amount of photocatalyst was used in the same volume of solution (Figure 21). It was found that increasing the amount of photocatalyst did not improve variations between LED positions and only yielded a decrease in the photoactivity, due to an increase in photocatalyst concentration leading to reduced light transmission through the sample. Attempts were not made to increase the similarity between LED positions as the set-up performed to a level that was acceptable for screening experiments. To reduce the effect of LED position, experiments were done in duplicate, placing an experiment randomly on positions 1-5 with the other placed randomly on positions 6-10. Once fully set up and evaluated, the HT photocatalytic testing system allowed for testing of around 250 photocatalyst experiments, which were carried out in duplicate, in 1 year of the PhD.

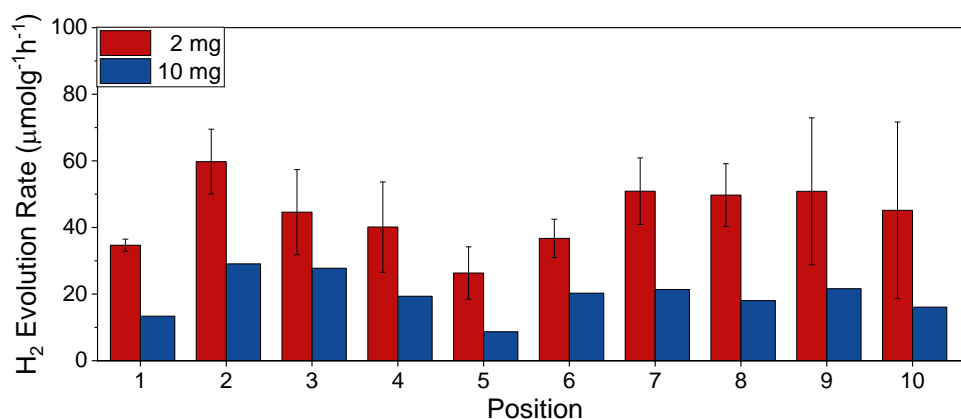


Figure 21 - Rate of H₂ evolved in µmol per gram of photocatalyst per hour for 2 and 10 mg of photocatalyst in 2 ml 10 mM EDTA with H₂PtCl₆ (8 wt%) over 4 hours visible light irradiation at ~100 mWcm⁻² in a glass vial, at each LED position, tested on the screening set-up.

2.5 References

- 1 G. Neri, M. Forster, J. J. Walsh, C. M. Robertson, T. J. Whittles, P. Farràs and A. J. Cowan, *Chem. Commun.*, 2016, **52**, 14200–14203.
- 2 G. Neri, J. J. Walsh, C. Wilson, A. Reynal, J. Y. C. Lim, X. Li, A. J. P. White, N. J. Long, J. R. Durrant and A. J. Cowan, *Phys. Chem. Chem. Phys.*, 2015, **17**, 1562–1566.
- 3 R. Hinogami, K. Toyoda, M. Aizawa, S. Yoshii, T. Kawasaki and H. Gyoten, *Electrochem. commun.*, 2013, **35**, 142–145.
- 4 J. Gu, A. Wuttig, J. W. Krizan, Y. Hu, Z. M. Detweiler, R. J. Cava and A. B. Bocarsly, *J. Phys. Chem. C*, 2013, **117**, 12415–12422.
- 5 Q. Meng, S. S. Lu and Y. Xiang, *J. Sol-gel Sci. Technol.*, 2012, **63**, 1–7.
- 6 K. Toyoda, R. Hinogami, N. Miyata and M. Aizawa, *J. Phys. Chem. C*, 2015, **119**, 6495–6501.
- 7 U. A. Joshi and P. A. Maggard, *J. Phys. Chem. Lett.*, 2012, **3**, 1577–1581.
- 8 B. Zoellner, S. Stuart, C.-C. Chung, D. B. Dougherty, J. L. Jones and P. A. Maggard, *J. Mater. Chem. A*, 2016, **4**, 3115–3126.
- 9 B. M. Fung, A. K. Khitrin and K. Ermolaev, *J. Magn. Reson.*, 2000, **142**, 97–101.
- 10 C. R. Morcombe and K. W. Zilm, *J. Magn. Reson.*, 2003, **162**, 479–486.
- 11 P. Bertani, J. Raya and B. Bechinger, *Solid State Nucl. Magn. Reson.*, 2014, **61–62**, 15–18.
- 12 T. Wada and S. Yamazoe, *Shimadzu Appl. News - Spectrophotometric Anal.*, A428.
- 13 S. Hofmann, *Auger- and X-Ray Photoelectron Spectroscopy in Materials Science: A User-Oriented Guide*, Springer Science and Business Media, Heidelberg, 2013, vol. 49.
- 14 J. F. Moulder, J. Chastain, W. F. Stickle, P. E. Sobol and K. D. Bomben, *Handbook of x-ray photoelectron spectroscopy: a reference book of standard spectra for identification and interpretation of XPS data*, Physical Electronics Division, Perkin-Elmer Corporation, 1992.
- 15 S. K. Sharma, D. S. Verma, L. U. Khan, S. Kumar and S. B. Khan, *Handbook of Materials Characterization*, 2018.
- 16 D. R. Vij, *Handbook of Applied Solid State Spectroscopy*, Springer, 2006.
- 17 A. Boudrioua, M. Chakaroun and A. Fischer, in *Organic Lasers*, Elsevier, 2017, vol. 1, pp. 1–47.
- 18 A. T. Mane and V. B. Patil, in *Spectroscopy of Polymer Nanocomposites*, 2016, pp. 452–467.
- 19 M. Sardela, *Practical materials characterization*, 2014.
- 20 G. Greczynski and L. Hultman, *Prog. Mater. Sci.*, 2020, **107**, 100591.
- 21 O. I. Klyushnikov, *J. Struct. Chem.*, 1998, **39**, 944–947.
- 22 M. G. Helander, M. T. Greiner, Z. B. Wang and Z. H. Lu, *Appl. Surf. Sci.*, 2010, **256**, 2602–2605.
- 23 M. T. Greiner, M. G. Helander, W.-M. Tang, Z.-B. Wang, J. Qiu and Z.-H. Lu, *Nat. Mater.*, 2012, **11**, 76–81.
- 24 S. Evans, *Chem. Phys. Lett.*, 1973, **23**, 134–138.
- 25 Y. Baer, *Solid State Commun.*, 1976, **19**, 669–671.
- 26 C. Heine, M. Hävecker, A. Trunschke, R. Schlögl and M. Eichelbaum, *Phys. Chem. Chem. Phys.*, 2015, **17**, 8983–8993.
- 27 K. Gelderman, L. Lee and S. W. Donne, *J. Chem. Educ.*, 2007, **84**, 685–688.
- 28 A. Hankin, F. E. Bedoya-Lora, J. C. Alexander, A. Regoutz and G. H. Kelsall, *J. Mater. Chem. A*, 2019, **7**, 26162–26176.
- 29 G. V Govindaraju, G. P. Wheeler, D. Lee and K. S. Choi, *Chem. Mater.*, 2017, **29**, 355–370.
- 30 F. Cardon and W. P. Gomest, *J. Phys. D Appl. Phys.*, 1978, **11**, L63–L67.
- 31 Z. Zhang and J. T. Yates, *Chem. Rev.*, 2012, **112**, 5520–5551.
- 32 A. Singha, P. Dhar and A. Roy, *Am. J. Phys.*, 2005, **73**, 224–233.
- 33 G. D. Gilliland, *Mater. Sci. Eng. R Reports*, 1997, **18**, 99–399.
- 34 J. R. Lakowicz and B. R. Masters, *Principles of Fluorescence Spectroscopy, Third Edition*, Springer Science+Business Media, New York, Third., 2008.
- 35 M. Matsuoka, T. Kamegawa and M. Anpo, in *Handbook of Heterogeneous Catalysis*,

- Wiley-VCH Verlag GmbH & Co. KGaA, Weinheim, Germany, 2008, pp. 1065–1073.
- 36 U. Noomnarm and R. M. Clegg, *Photosynth. Res.*, 2009, **101**, 181–194.
- 37 M. Geoghegan, G. Hadziioannou, M. Geoghegan and G. Hadziioannou, in *Polymer Electronics*, 2013, pp. 56–76.
- 38 J. Zimmermann, A. Zeug and B. Röder, *Phys. Chem. Chem. Phys.*, 2003, **5**, 2964–2969.
- 39 DecayFit - Fluorescence Decay Analysis Software 1.3, FluorTools, <http://www.fluortools.com/software/decayfit>.
- 40 R. Berera, R. van Grondelle and J. T. M. Kennis, *Photosynth. Res.*, 2009, **101**, 105–118.
- 41 T. J. Miao and J. Tang, *J. Chem. Phys.*, 2020, **152**, 194201.
- 42 K. E. Knowles, M. D. Koch and J. L. Shelton, *J. Mater. Chem. C*, 2018, **6**, 11853.
- 43 C. Ruckebusch, M. Sliwa, P. Pernot, A. De Juan and R. Tauler, *J. Photochem. Photobiol. C Photochem. Rev.*, 2012, **13**, 1–27.
- 44 J. Coates, *Interpretation of Infrared Spectra, A Practical Approach, Encyclopedia of Analytical Chemistry*, John Wiley & Sons, Ltd, Chichester, UK, 2006.
- 45 A. C. Ferrari, S. E. Rodil, J. Robertson, S. E. Rodil and J. Robertson, *Phys. Rev. B - Condens. Matter Mater. Phys.*, 2003, **67**, 155306.
- 46 A. C. Benniston, P. Matousek, I. E. McCulloch, A. W. Parker and M. Towrie, *J. Phys. Chem. A*, 2003, **107**, 4347–4353.
- 47 M. C. H. Prieto, P. Matousek, M. Towrie, A. W. Parker, M. Wright, A. W. Ritchie and N. Stone, *J. Biomed. Opt.*, 2005, **10**, 044006.
- 48 S. K. Sahoo, S. Umapathy and A. W. Parker, *Appl. Spectrosc.*, 2011, **65**, 1087–1115.
- 49 G. Socrates, *Infrared and Raman characteristic group frequencies. Tables and charts*, John Wiley & Sons Ltd, Chichester, Third., 2001.
- 50 P. Larkin, *Infrared and Raman spectroscopy*, Elsevier, Amsterdam, Second., 2018.
- 51 L. Cabo-Fernandez, A. R. Neale, F. Braga, I. V. Sazanovich, R. Kostecky and L. J. Hardwick, *Phys. Chem. Chem. Phys.*, 2019, **21**, 23833–23842.
- 52 K. Vikman, H. Iitti, P. Matousek, M. Towrie, A. W. Parker and T. Vuorinen, *Vib. Spectrosc.*, 2005, **37**, 123–131.
- 53 P. Matousek, M. Towrie, A. Stanley and A. W. Parker, *Appl. Spectrosc.*, 1999, **53**, 1485–1489.
- 54 N. Everall, T. A. Hahn, P. M. Atousek, A. W. Parker and M. I. Towrie, *Appl. Spectrosc.*, 2001, **55**, 1701–1708.
- 55 P. Matousek, M. Towrie, C. Ma, W. M. Kwok, D. Phillips, W. T. Toner and A. W. Parker, *J. Raman Spectrosc.*, 2001, **32**, 983–988.
- 56 A. Vlček Jr., I. R. Farrell, D. J. Liard, P. Matousek, M. Towrie, A. W. Parker, D. C. Grills and M. W. George, *J. Chem. Soc. Dalt. Trans.*, 2002, 701–712.
- 57 P. F. McMillan, V. Lees, E. Quirico, G. Montagnac, A. Sella, B. Reynard, P. Simon, E. Bailey, M. Deifallah and F. Corà, *J. Solid State Chem.*, 2009, **182**, 2670–2677.
- 58 P. Matousek, M. Towrie and A. W. Parker, *J. Raman Spectrosc.*, 2002, **33**, 238–242.
- 59 I. V Sazanovich, G. M. Greetham, B. C. Coles, I. P. Clark, P. Matousek, A. W. Parker and M. Towrie, *Facility development update : The Kerr-gated Raman / ultrafast time-resolved fluorescence instrument*, Centra Laser Facilities Annual Report, 2014.
- 60 A. C. Benniston, P. Matousek and A. W. Parker, *J. Raman Spectrosc.*, 2000, **31**, 503–507.
- 61 G. M. Greetham, P. Burgos, C. Qian, I. P. Clark, P. S. Codd, R. C. Farrow, M. W. George, M. Kogimtzis, P. Matousek, A. W. Parker, M. R. Pollard, D. A. Robinson, X. Zhi-Jun and M. Towrie, *Appl. Spectrosc.*, 2010, **64**, 1311–1319.

3

Carbon Nitrides

3.1 Introduction

As of 15th January 2021, when using the search term “carbon nitride” on SciFinder, over 24,000 papers are available. Figure 22 shows a plot of the number of publications on carbon nitride per year and it can be seen that the number of publications has been rising exponentially since around 2010. This introduction does not aim to be an exhaustive literature review of all the papers published in carbon nitride, instead it aims to give an overview of key properties of carbon nitride materials and their applications in photocatalysis.

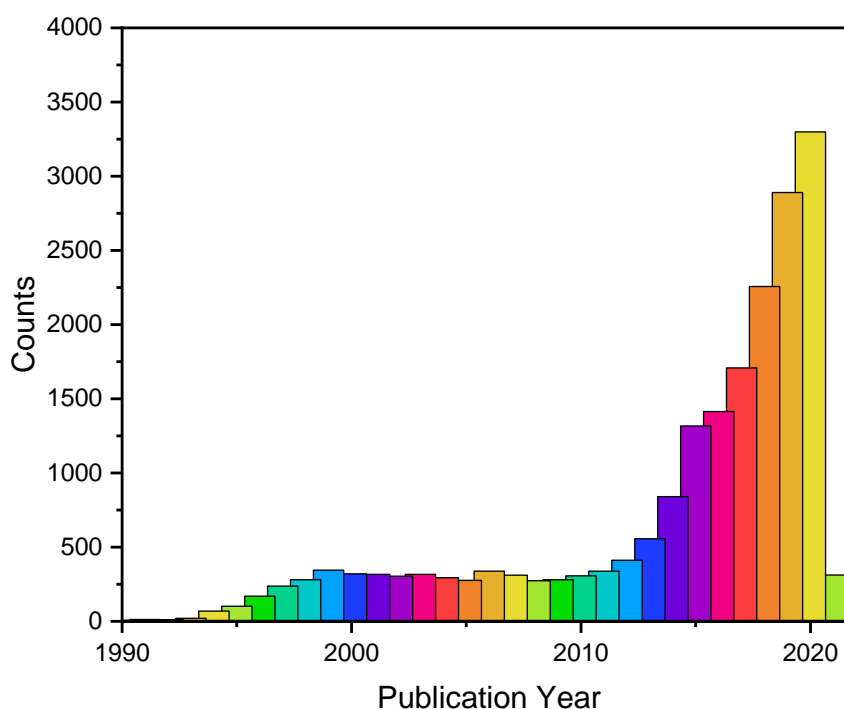


Figure 22 - Plot of number of publications per year when searching the term “carbon nitride” on SciFinder. Data collected on 15th January 2021.

3.1.1 History

In principle, carbon nitride refers to any material composed of only carbon and nitrogen and is thought to be one of the oldest known synthetic polymers. The first synthesis of a polymeric carbon nitride, was reported in 1834 by Berzelius and termed melon by Liebig (Figure 24 (a)).¹⁻⁸ However, at that time, it was not possible to characterise the material due to its very low solubility in water and organic solvents.⁹⁻¹¹ In 1922 Franklin first introduced carbonic nitride (C_3N_4) which was proposed to be the final de-ammonation product of melon.¹² A heptazine

based structure for similar carbon and nitrogen containing materials was first proposed by Pauling and Sturdivant in 1937.¹³ Then 3 years later in 1940, Redemann and Lucas assigned this heptazine based structure to melon.¹⁴ Research on carbon nitride then slowed until, in 1989, Cohen *et al* calculated that a tetrahedral carbon and nitrogen material (beta-CN) would have a bulk modulus comparable to diamond ($\beta\text{-C}_3\text{N}_4$ - 4.27 Mbar and diamond - 4.43 Mbar).¹⁵ He also suggested that it could be synthesised from amorphous carbon nitride at high temperature and pressure, much like diamonds synthesis from graphite. After these studies, many groups attempted to synthesise this ultrahard material. In the years that followed there were many attempts to synthesise ultrahard carbon nitride, ultimately leading to the formation of amorphous materials with low nitrogen contents.^{16–20} In 1996, Teter and Hemely investigated 5 allotropes of carbon nitride; $\alpha\text{-C}_3\text{N}_4$, $\beta\text{-C}_3\text{N}_4$, cubic, pseudo-cubic and graphitic (Figure 23 (a-e)).²¹ First principle calculations of these allotropes determined graphitic-carbon nitride, based on triazine units, to be the most stable. (graphitic > $\alpha\text{-C}_3\text{N}_4$ > $\beta\text{-C}_3\text{N}_4$ > cubic > pseudo-cubic).

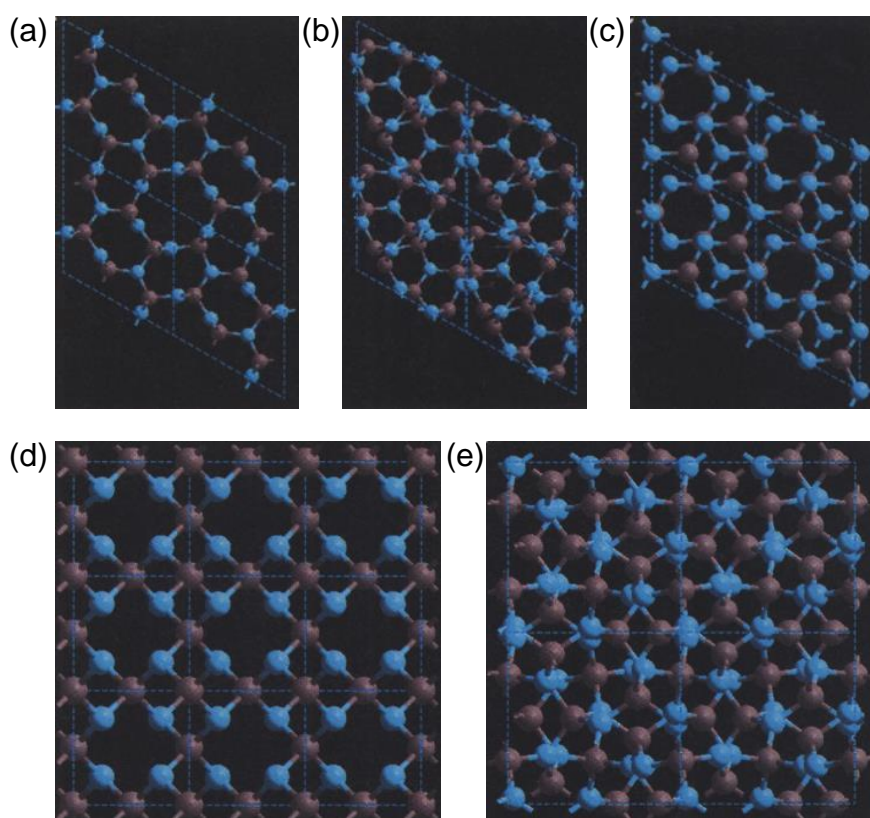


Figure 23 -Representation of (a) $\beta\text{-C}_3\text{N}_4$, (b) $\alpha\text{-C}_3\text{N}_4$, (c) graphitic, (d) pseudo-cubic and (e) cubic structures taken from reference²¹.

In 2002 Kroke *et al* studied trichloro-tri-s-triazine experimentally and calculated total energy values for a number of different triazine and tri-s-triazine based carbon nitride materials (Figure 24).¹⁰ They determined that materials based on tri-s-triazine repeating units are lower in energy and therefore more favourable than triazine based materials at ambient conditions. They proposed that graphitic carbon nitride consist of sheets of highly ordered tri-s-triazine moieties connected through planarized tertiary amino groups and suggested that many carbon nitrides published in the literature at that time were based on this structure.

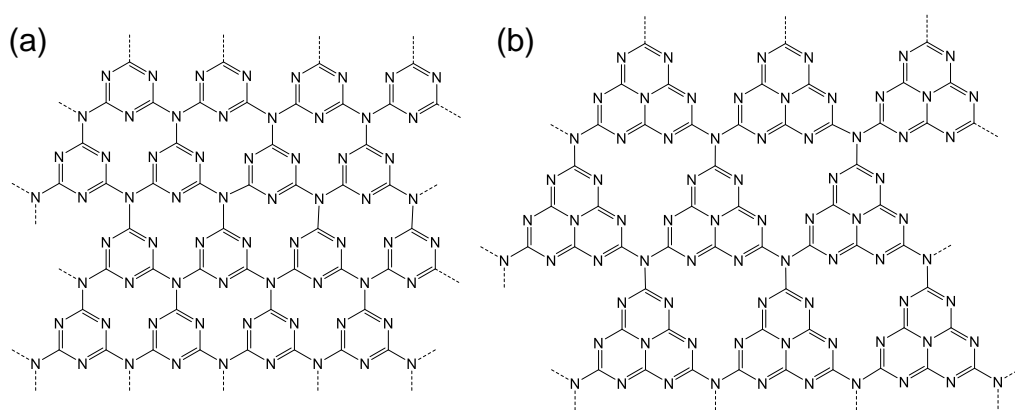


Figure 24 – Fully condensed graphitic carbon nitride structure based on (a) triazine and (b) tri-s-triazine repeating units.¹⁰

Further computational studies have examined different structures for graphitic carbon nitride. In 2008, Deifallah *et al* looked at 3 different structures of graphitic carbon nitride studying stability of the planar structure over the buckled conformation.²² The 3 carbon nitrides differed in the repeating and bridging units, structures of which can be seen in Figure 25. They determined that a single sheet of carbon nitride based on heptazine repeating units is most stable in a buckled conformation and stability in this form stems from a reduction in steric repulsion between the heterocyclic nitrogen lone pairs. A later study published in 2012 examined all 7 carbon nitride phases, based on the 5 materials studied by Teter and Hemely, and the 3 models of graphitic carbon nitride studied by Deifallah *et al*, and gave further proof of the stability of heptazine based carbon nitride over other phases.²³

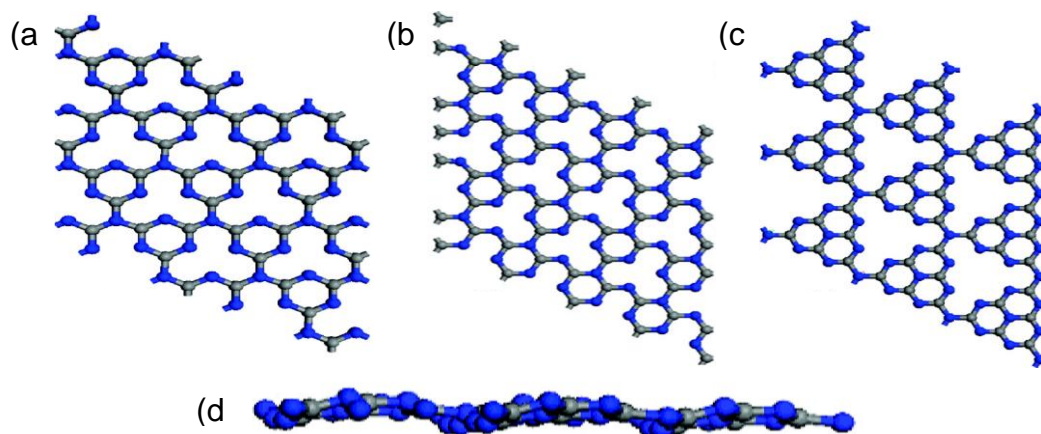


Figure 25 - Structures of (a) orthorhombic triazine, (b) hexagonal triazine, (c) hexagonal tri-s-triazine and buckled conformation of the tri-s-triazine based structure taken from reference ²³ and nomenclature taken from reference ²².

In 2007, Lotsch *et al*, confirmed experimentally the structure of Liebig’s “melon” to be made up of linear heptazine based polymers.⁷ They stated that melon is composed of layers made up from infinite 1D chains of NH bridged melem monomers. The strands adopt zig-zag type geometry and are tightly linked by hydrogen bonds giving 2D array. They also encouraged, the re-evaluation of accepted paradigms about the structure of so-called graphitic carbon nitride, g-C₃N₄, and hypothesised that many materials synthesised at the time were in fact polymers similar to melon.

3.1.2 Structure and Formation

Over 180 years there have been a wide range of reports for the synthesis of graphitic carbon nitride using a broad array of nitrogen rich organic precursors which have led to the formation of very different materials that are all referred to using the umbrella term “graphitic carbon nitride” or “g-C₃N₄”. Ideally this g-C₃N₄, is analogous to graphite, possessing 2D stacked sheets, consisting solely of N and C, however most of the reported materials contain small amounts of hydrogen, indicating incomplete condensation of precursors and the presence of surface defects.²⁴ The structures of the materials are based on tri-s-triazine repeating units, bridged via planar tertiary amino groups, creating large graphitic sheets of carbon nitride terminated by primary/secondary amine groups, held together by weak van der Waals forces.^{2,5,30–39,8,12,24–29} In terms of the work presented here, carbon nitride refers to the bulk

graphitic carbon nitride ($C_xN_yH_z$ or CN), which has a structure that lies somewhere in between melon and fully polymerised tri-s-triazine based sheets.^{7,40,41}

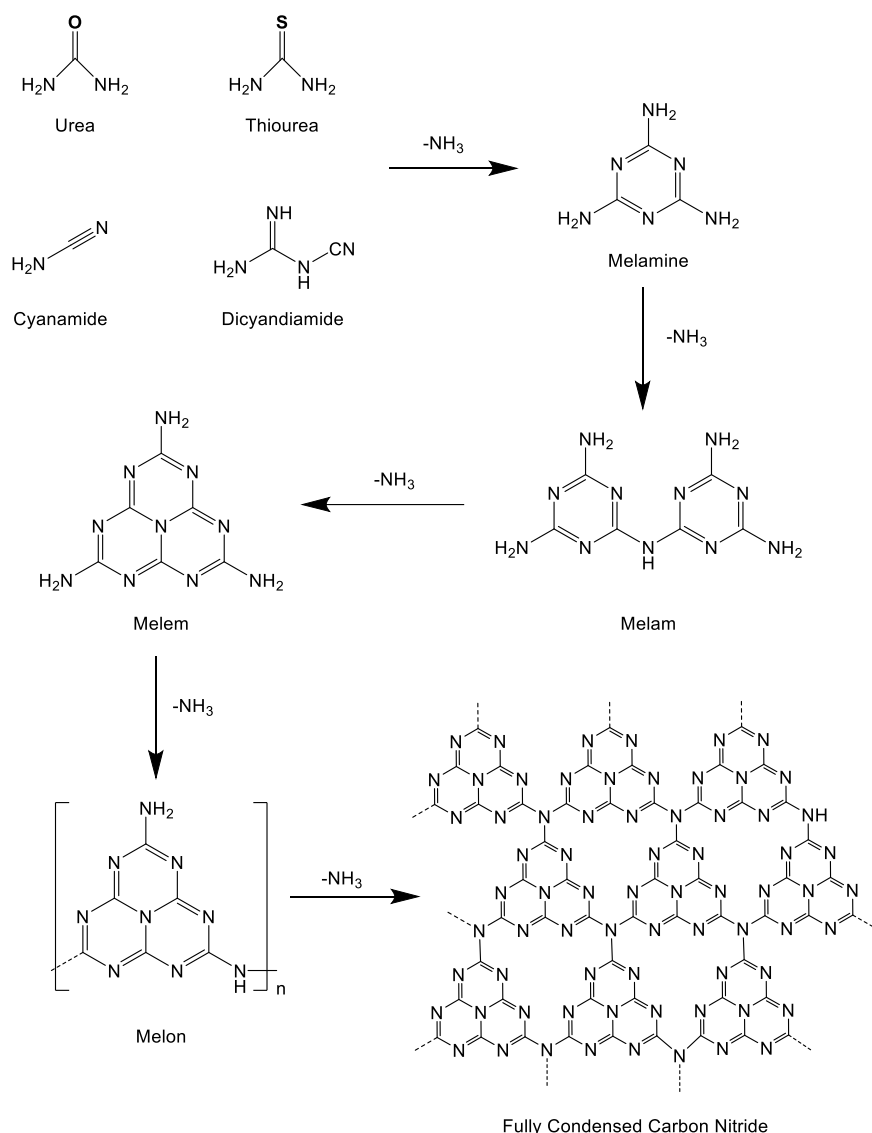


Figure 26 - Scheme of condensation of common precursors to fully condensed graphitic carbon nitride.^{6,7,11,36,42-44}

These materials can be synthesised relatively easily via thermal condensation of nitrogen rich organic precursors, in air or under a nitrogen atmosphere.^{2,12,28,30,31,37,39,40,45,46} Precursors can include cyanamide, dicyandiamide, urea, thiourea and melamine. Formation of graphitic carbon nitride proceeds via polyaddition and polycondensation of nitrogen rich organic precursors at about 240 °C, after which melamine-based products are formed. Condensation of these products via concomitant loss of ammonia leads to production of melam, which undergoes further rearrangements to form melem at around 390 °C. Polymerisation of melem

leads to the formation of melon chains, which can fuse and further condense at temperatures above 520 °C to form sheets of so-called “graphitic carbon nitride”. Above 600 °C it becomes unstable and it fully decomposes at temperatures above 700°C.^{2,6,11,36,44,47}

3.1.3 Properties

One of the main reasons that it has taken such a long time to gain a better understanding of carbon nitride structures is due to the materials being generally chemically inert. Most reported carbon nitrides are stable in both acidic and basic media across the full pH range, are insoluble in practically all solvents and are thermally stable up to 600 °C.^{2,12,26,48} These properties alone mean that it has wide applications in heterogeneous catalysis.²⁴

The choice of precursors and condensation methods can lead to the synthesis of very different materials with a wide range of reported band gaps. Typically, bulk carbon nitride is reported as an n-type semiconductor with an indirect band gap of around 2.7 eV, which lies just within the visible region, allowing for absorption of wavelengths >460 nm.^{2,24,30,31,38,49–51}

The band structure of carbon nitride has been determined by Antonietti and co-workers via density-functional theory (DFT) calculations²⁶ and experimental measurements using both the Mott-Schottky method⁵⁰ and measuring the onset of photocurrent⁵². The exact band structure is again dependent on precursors and calcination conditions, but generally carbon nitrides have been reported to have a conduction band (CB) and valence band (VB) straddling the water redox potentials, meaning it can facilitate overall photocatalytic water splitting and also CO₂ reduction. It has been determined computationally that the VB is made up of N p_z orbitals, whilst the CB is made up of primarily of C and N mixed p_z orbitals^{26,53–56}

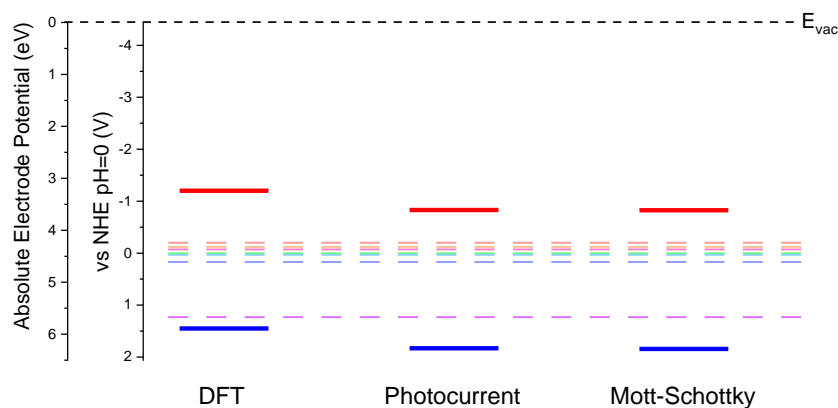


Figure 27 – Reported band structures of carbon nitride obtained via different methods. All potentials were converted to a common reference electrode and pH.^{26,50,52} The carbon nitrides were both synthesised via calcination of dicyandiamide at 550 °C for 4 hours.

3.1.4 Photocatalysis

Carbon nitride is a very promising material in the field of photocatalysis due to it; (1) being synthesised via low cost and facile methods; (2) having relatively good stability; (3) having a suitable electronic structure which should allow for conversion of a wide range of molecules (4) being rich in nitrogen with terminating amine groups which are promising for CO₂ activation; (5) having a 2D structure which can facilitate electron transfer to the surface due to shorter diffusion lengths; (6) having a highly tuneable structure which can be easily achieved by changing synthesis methods and precursors.^{2,5,33–39,8,12,27–32}

The first instance of a carbon nitrides use as a photocatalyst was in November 2008 when Wang *et al* reported its activity towards H₂ evolution.²⁶ They reported a carbon nitride photocatalyst capable of performing H₂ evolution in 10% triethanolamine (TEOA) under visible light illumination (>420 nm) and materials were found to be stable after several cycling experiments. Materials were also tested without Pt but found that activity on the bare material fluctuated and varied between batches, while this did not occur when Pt was used as a co-catalyst. They tested the carbon nitride with several hole scavengers; methanol (MeOH), ethanol (EtOH) and ethylenediaminetetraacetic acid (EDTA) and found H₂ was produced in the presence of all scavengers, but the highest activity was obtained when using TEOA. They determined that H₂ evolution proceeded via light absorption by measuring the volume of H₂ produced under specific wavelengths of light and found the trend in activity at each wavelength

matched well with the UV-Vis spectra. Also, it was found that the material was capable of photocatalytic O₂ evolution with RuO₂ as a cocatalyst in the presence of AgNO₃ under visible light.

A few months later in January 2009, the same group reported a mesoporous carbon nitride synthesised using cyanamide with different ratios of a silica template, leading to materials with larger surface areas.⁵⁷ They found using greater amounts of the template led to increased surface area, but only an initial increase in photoactivity for the lowest quantity of template was observed when tested with a Pt co-catalyst, in the presence of a scavenger and under visible illumination (>420 nm). A decrease in activity with greater quantities of templates used was attributed to an increase in defects.

Carbon nitride was first explored for and found capable of CO₂ activation in 2006, but it wasn't until November 2011, that the first report of photocatalytic CO₂ reduction over carbon nitride was published by Dong and Zhang.^{58,59} They reported melamine based carbon nitrides capable of reducing CO₂ to CO in the presence of water vapour under visible illumination (>420 nm), though they gave no data on control or isotopically labelled experiments, confirming the carbon source.

In January 2013, Mao *et al* used urea and melamine based carbon nitride as photocatalyst suspensions in sodium hydroxide producing liquid carbon products under visible illumination.⁶⁰ They found that depending on the precursor used the relative quantities of products differed. Whilst the urea-based carbon nitride was capable of producing ethanol and methanol as the major product, the melamine-based material selectively produced ethanol with only trace amounts of methanol formed. Control experiments in the absence of photocatalyst, light or CO₂ showed no appreciable activity, but again no isotopic labelled experiments were performed. Three months later, carbon nitride was reported as a co-catalyst on red phosphorus for enhanced photocatalytic CO₂ reduction.⁶¹ The hybrid red phosphorus/carbon nitride catalysts with Pt co-catalyst under illumination in the presence of water vapor showed greater activity for CO₂ reduction to CH₄ than the singular materials. Though again no control experiments were shown to confirm if the activity was real.

The first report of full control and isotopic labelling experiments being performed to confirm the source of the carbon product was by Maeda *et al.*⁶² In August 2013 they reported a mesoporous carbon nitride photocatalyst combined with a ruthenium complex (*cis,trans*-[Ru{4,4'- (CH₂PO₃H₂)₂-2,2'-bipyridine}(CO)₂Cl₂}] for CO₂ reduction to HCOOH and CO. Photocatalyst suspensions were tested in acetonitrile (MeCN) and TEOA (4:1 v/v) solutions under visible illumination (>400 nm) and were found to produce H₂, CO and HCOOH as the major product. Control experiments showed no activity towards CO₂ reduction in the absence of the photocatalyst, co-catalyst or CO₂ and only small quantities were observed without a hole scavenger present. Isotopic labelling experiments with ¹³CO₂ were conducted and confirmed that almost all HCOOH and 87% of the produced CO originated from the labelled CO₂.

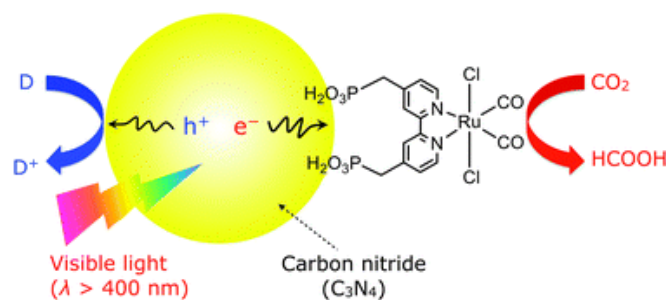


Figure 28 - Image taken from online publication graphical abstract of reference ⁶², depicting a carbon nitride particle combined with a ruthenium complex performing CO₂ reduction under visible illumination in the presence of a sacrificial donor.

One thing that remains an issue for pristine bulk carbon nitride is that its efficiency is limited due to reduced absorption in the visible range and fast recombination of photogenerated charges.^{2,5,32-39,63,8,12,24,27-31} Many strategies have been undertaken to improve photocatalytic activity, which are discussed in greater depth in Chapter 4, while within this chapter the modification of the electronic structure of carbon nitride materials is explored.

3.1.5 Electronic Structure Modification

Doping carbon nitride materials *in-situ* or post-synthesis with various elements or impurities can be an effective method for electronic modification which can lead to enhanced photocatalytic activity.^{2,8,33,35,37,64} Often it can be employed to extend photo-adsorption further into the visible region, adjusting band positions and can be used to introduce certain functionalities to improve photocatalytic activities.

3.1.5.1 Element Doping

Many non-metal atoms have been used as dopants in carbon nitride including, H^{48,65–68}, S^{69–73}, C⁵⁰, O^{74,75}, B^{76–77}, F^{78–76}, Cl⁷⁸, I⁷⁸, Br⁷⁸, P^{77,79,80}. Generally non-metal atoms dope via substitution of C or N atoms within the carbon nitride skeleton and can be achieved by addition of the heteroatom containing material into precursor mixtures and calcining.^{35,71,72,79–85}

In 2014, Zhang et al found that doping carbon nitrides with halogens could be accomplished by calcining mixtures of dicyandiamide with ammonium halogen salts.⁷⁸ This led to increased and slightly extended light absorption via addition of impurity energy levels above the valence band giving enhanced photoactivity.

Many methods designed for increasing surface area, both acid washing, thermal exfoliation and templating can often lead to doping.⁷⁹ Protonation of carbon nitride is most easily achieved by acid washing which also leads to increased surface areas and larger band gaps, but overall give higher levels of photoactivity.^{48,65} Calcination under an atmosphere of air, NH₃, N₂ and H₂S are proven to be effective methods of O, N or S doping.^{69,75} Even washing in acids, such as sulphuric acid or phosphoric acid has led to sulphur and phosphorus doping.^{72,86,87} Also the use of ionic liquids such as BmimBF₄ and BmimPF₆ have been used as soft templates during precursor calcination resulting in B/F and P doping, respectively.^{76,79}

Carbon doping is most commonly achieved by molecular doping which can also introduce additional functionalities and extend light absorption.^{88–92} Nitrogen doping and amine functionalisation has also been used to increase the amount of amino groups in carbon nitride which are essential for CO₂ adsorption and activation, leading to enhanced photocatalytic CO₂ reduction.^{93–96}

Metals such as Zn⁹⁷, Fe^{98,99}, Na^{100,101}, K^{100,102}, Ca¹⁰⁰, Mg¹⁰⁰, Mn^{103,104}, Co^{105–107}, Mo^{107,108} and Ti¹⁰⁹ have also been explored as dopants for carbon nitride and have been found to improve photocatalytic activity. Some have reported that carbon nitrides are able to be doped with metal atoms due to the structures containing large pores with multiple lone pairs that could coordinate with the metal atoms.^{97,110} They have also been found to improve charge mobility within materials.

3.1.5.2 Co-polymerisation or Molecular doping

As mentioned in the previous section co-polymerisation has shown to be an effective way of improving photocatalytic activity. The incorporation of other aromatic and aliphatic molecules pre- or post- synthesis can be used to dope atoms or structures into carbon nitride materials.

There have been many reports that by co-polymerising typical carbon nitride precursors with other organic molecules has led to enhanced photocatalytic activity. Reports include the use of barbituric acid (BA)^{50,91,118–125,92,111–117}, phenylurea⁸⁹, terphthalaldehyde¹²⁶, p-nitrobenzoic acid¹²⁷, cyanuric acid¹²⁴, 3-aminothiophene-2-carbonitrile^{128,129}, diaminomaleonitrile¹²⁹, 2,4,6-triaminopyrimidine¹³⁰, 2,4-diamino-1,3,5-triazine¹³¹, 2,4-diamino-6-methyl-1,3,5-triazine¹³¹, 2,4-diamino-6-phenyl-1,3,5-triazine¹³¹, 2-aminobenzonitrile^{88,129,132} and nucleobases^{90,133} among many other aromatic species.

In some cases the copolymerisation of these organic molecules has led to the production of materials with increased carbon content, decreased band gap, decreased photoluminescence emission, increased photocurrents or Nyquist plots with significantly decreased diameters, which all infer materials with extended visible light absorption and improved charge generation/separation which gave improvements in photoactivity over the bulk carbon nitride.^{50,88,133,89–92,111,112,122,128}

3.2 Aim of Work

Within this project a range of carbon nitrides have been synthesised to investigate how variations in calcination conditions and precursors effect the produced materials, not just how these conditions affect structure but also its knock-on effect on photocatalytic activity. This chapter focuses primarily on characterisation and baseline photocatalytic testing for H₂ evolution. The ultimate aim of this work was to combine these carbon nitrides with molecular catalysts for enhanced photocatalytic CO₂ reduction, which is discussed in detail in Chapter 4. Therefore, detailed characterisation is required to allow for targeting of carbon nitrides with suitable properties to enable modification with a co-catalyst, for example CB position.

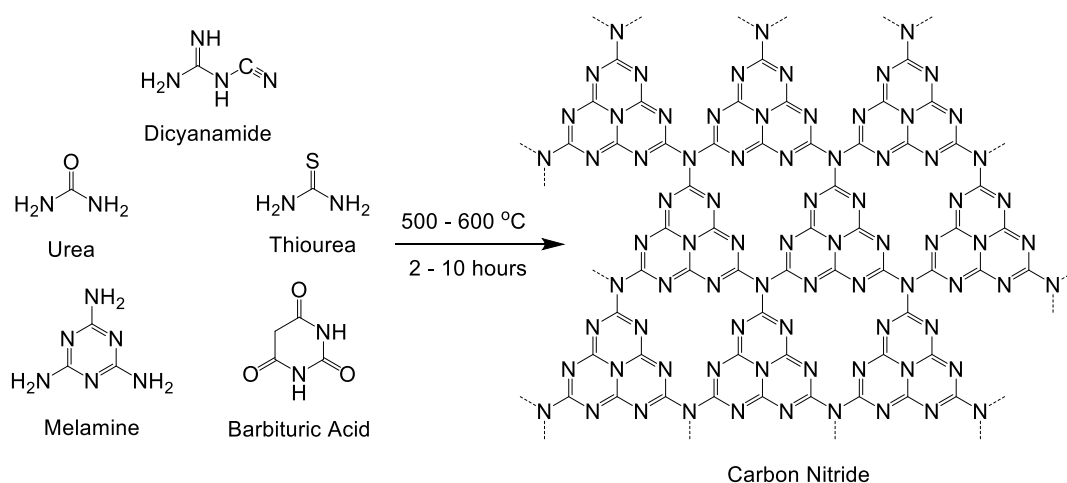


Figure 29 - Scheme of carbon nitride synthesis.

The routes that have been explored are as follows:

- Co-polymerisation with barbituric acid
 - Dicyandiamide and different quantities of barbituric acid (CN-BA)
- Variation of precursor and/or ratios of precursors
 - Dicyandiamide, melamine, urea and thiourea (CN-Precursor)
 - Mixtures of different ratios of urea and thiourea (CN-UT)
- Variation of calcination conditions
 - Calcination temperature; 500, 550 and 600°C (CN-Temp)
 - Calcination time; 2, 4, 6, 8 and 10 hours (CN-Time)

Copolymerisation of typical carbon nitride precursors or bulk carbon nitride with various aromatic molecules has been proven as an effective method for enhancing photocatalytic activity.^{50,88,115–124,89,125–133,90–92,111–114} The first compound used for copolymerisation with any carbon nitride precursor was barbituric acid in 2010.⁵⁰ Wang and co-workers synthesised a series of carbon nitrides by mixing DCDA with different amount of BA. They stated that in principle, the “barbituric acid can be directly incorporated into the classical carbon nitride condensation scheme” (Figure 30 (a)).

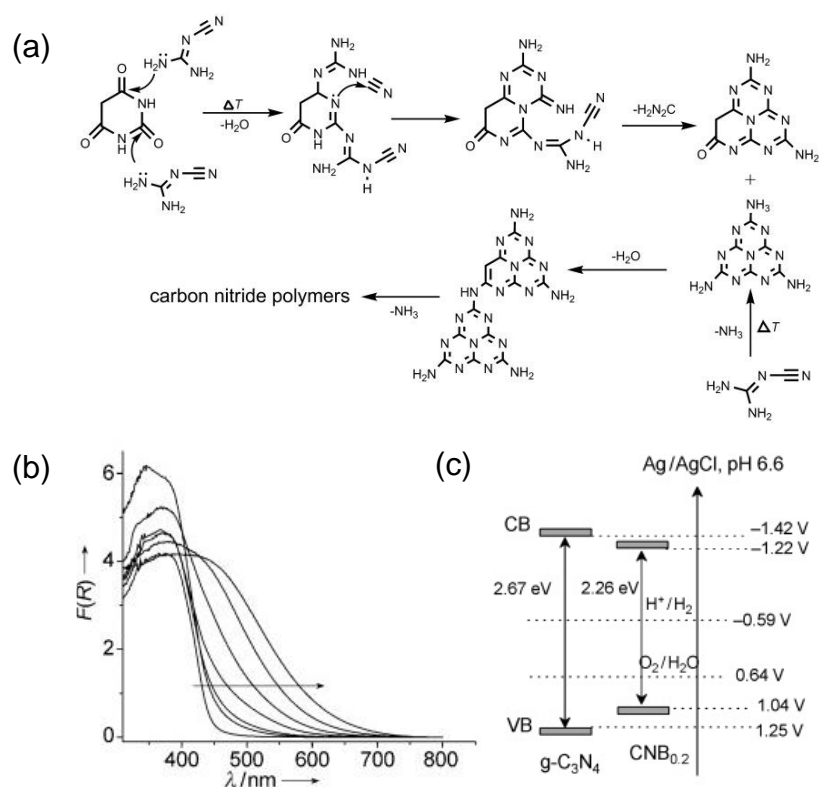


Figure 30 – Images taken from reference ⁵⁰. (a) proposed scheme for copolymerisation of DCDA and barbituric acid at high temperature. (b) UV/Vis diffuse reflectance spectra of carbon nitride and barbituric acid samples, arrow indicates the increasing amount of barbituric acid in the samples. (c) Mott-Schottky derived band structures for the $g-C_3N_4$ and $CNB_{0.2}$ samples.

The resultant materials showed trends with the quantity of barbituric acid used; with increasing amounts of barbituric acid used, the materials carbon content increased. Diffuse reflectance ultraviolet-visible (UV-Vis) spectroscopy showed extended absorption into the visible range, which in turn led to increased photocurrent and electrochemical impedance spectroscopy showed enhanced charge separation. Using the Mott-Schottky method in combination with the UV-vis band gap they were able to elucidate the band structure of two of the materials (Figure

30 (c)). The materials were tested for photocatalytic H₂ evolution under UV and visible illumination, in the presence of TEOA hole scavenger and chloroplatinic acid (H₂PtCl₆) for *in-situ* Pt deposition. It was found that copolymerisation with barbituric acid resulted in enhanced photoactivity for hydrogen evolution, but only up to a certain level of barbituric acid used; past it, activity decreased significantly which was taken to be due to excessive doping introducing recombination centres and hindering activity.

The materials synthesised in this work were synthesised with slightly different ratios of DCDA to barbituric acid and calcination conditions as the paper did not give great detail on the synthetic procedure, this is reflected in the slightly different properties that have been measured within this work. The main aim of this work is to combine these carbon nitrides with molecular co-catalyst for photocatalytic CO₂ reduction and the addition of barbituric acid presents a potentially useful way to tune band energetics, and hence the ability of electron transfer to a co-catalyst.

Since its first use in 2010, barbituric acid has been used for copolymerisation with a number of carbon nitride precursors and various studies have reported similar observations.^{91,92,111,112,115–117,119,122,125} In 2015 Wang and co-workers reported the synthesis of carbon nitride from urea and barbituric acid which showed a 15-fold improvement in activity for CO₂ reduction to CO over the bulk urea-based carbon nitride when in the presence of Co 2,2'-bipyridine complex (Co(bpy)₃²⁺).¹¹² Then in 2019 Li *et al* reported polydopamine and barbituric acid co-modified carbon nitride nanospheres.¹²² Photocatalytic CO₂ reduction tests in the presence of TEOA and Co(bpy)₃²⁺ gave 4.9 times higher CO produced than the undoped carbon nitride nanospheres under visible irradiation.

It has previously been reported that by using thiourea as a carbon nitride precursor or in a mixture with other carbon nitride precursors that the produced materials have enhanced photoactivities in comparison to other precursors and in many cases this improvement was assigned to doping sulphur into the carbon nitride structure causing a decrease in the band gap.^{70,71,84,134–137} Moreover, it has been reported that varying the ratios of thiourea with melamine or urea can lead to the *in-situ* formation of a CN-CN heterojunction and has led to improved charge separation and lifetimes.^{85,138–140} Within this study, urea and thiourea have

been used as precursors for the synthesis of carbon nitride in different ratios, which was thought to potentially lead to sulphur doping and/or the formation of *in-situ* heterojunctions which should improve photoactivity.

Previous reports on variation in calcination temperature and time have shown that the carbon nitride structure can vary greatly, such as degree of polymerisation. These structural variations can cause a significant difference in optical properties and photocatalytic activity. There have been many reports on the synthesis of carbon nitrides at temperatures from 350 °C-700 °C for a number of different photocatalytic uses.^{26,47,146,147,55,136,137,141–145} Generally, these studies have found that at calcination temperatures of 450 °C and below, typical carbon nitride is not formed and above 600 °C the material begins to decompose and in both these cases the photocatalytic activity of the materials is poor.^{55,136,141,143,145–147} Within these studies, results show that in some cases the material with highest activity was synthesised at 550 °C, whilst others find 600 °C to be the optimum calcination temperature.^{26,55,147,148,136,137,141–146} Studies on varying calcination time have been far less reported. Generally it is considered that with increasing calcination times, the produced materials achieve a higher degree of polymerisation, slightly smaller band gaps and in some cases increased surface area and charge lifetimes, which all can lead to higher photocatalytic activities.^{147,149–151} The materials synthesised within this project have been calcined at 500 °C, 550 °C or 600 °C for 2, 4, 6, 8 or 10 hours.

Lastly, carbon nitrides have been synthesised using the well-known precursors, DCDA, melamine, urea and thiourea, as it is widely reported that the produced materials can have greatly differing properties and photoactivities.^{26,55,60,71,95,134,142,152,153}

3.3 Results and Discussion

3.3.1 Synthesis and Initial Characterisation

All materials were synthesised via simple calcination of nitrogen rich precursors in air, conditions of the synthesis of each material are summarised in Table 7 and are described in more detail in Chapter 2. In general, the carbon nitrides synthesised are yellow/cream in colour, but it is worth noting that there are some differences in the physical appearance depending on the starting materials and the calcination temperature used (Figure 31).

Table 7 – Carbon nitride synthesis conditions.

Material	Weight Used in Precursor Mixtures (g)					Calcination Temperature (°C)	Calcination Time (hours)
	DCDA	BA	M	U	T		
CN-DCDA	3	-	-	-	-	550	4
CN-BA (5)	3	0.15	-	-	-	550	4
CN-BA(10)	3	0.3	-	-	-	550	4
CN-BA(20)	3	0.6	-	-	-	550	4
CN-M	-	-	3	-	-	550	4
CN-U	-	-	-	3	-	550	4
CN-UT(3:1)	-	-	-	2.25	2.25	550	4
CN-UT(1:1)	-	-	-	1.5	1.5	550	4
CN-UT(1:3)	-	-	-	0.75	0.75	550	4
CN-T	-	-	-	-	3	550	4
CN-500	3	-	-	-	-	500	4
CN-600	3	-	-	-	-	600	4
CN-2hr	3	-	-	-	-	550	2
CN-6hr	3	-	-	-	-	550	6
CN-8hr	3	-	-	-	-	550	8
CN-10hr	3	-	-	-	-	550	10

Precursors used: dicyandiamide (DCDA), barbituric acid (BA), melamine (M), urea (U) and thiourea (T)

When DCDA and melamine are used as precursors, there is little difference in their appearance, but when urea and thiourea are used the resultant carbon nitrides are a pale-

yellow static powder and a darker yellow coarse powder, respectively. On the addition of the barbituric acid copolymer, the powders become more golden in colour, with the highest copolymer content carbon nitride appearing brown. By increasing the amount of thiourea used in the materials, they become more yellow in colour. Varying calcination temperature also effects the colour of these materials, at lower temperatures the carbon nitride is a much paler yellow and darkens when synthesised at higher temperatures.

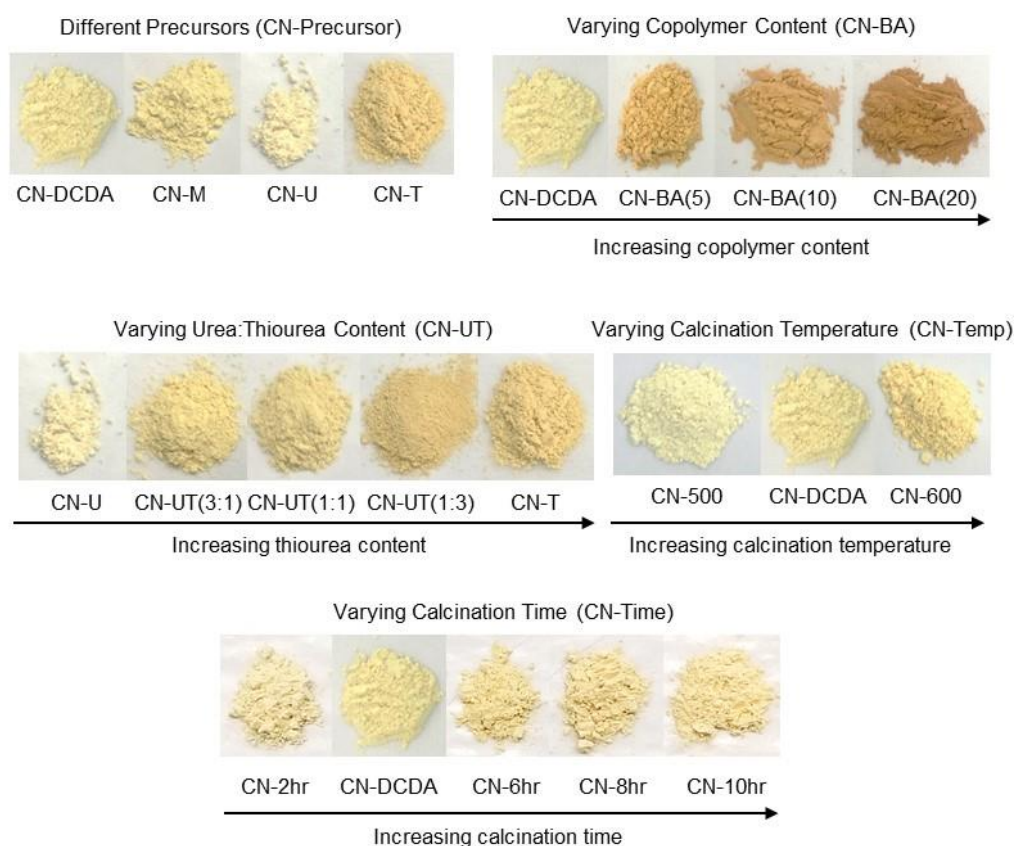


Figure 31 – Photographs of carbon nitride powders.

3.3.1.1 Elemental Analysis (CHN)

Elemental analysis (CHN) results are summarised in Table 8. The CHN results reveal that each of the materials have C:N ratios much lower than theoretical g-C₃N₄ (0.75) and are closer to that of the polymer melon (0.68), inferring that the materials are not fully polymerised and are likely rich in defects.^{6,7,95,98,135,154–158} Furthermore, each of the carbon nitrides contains a small amount of hydrogen, between 1.64-1.92 %. The presence of hydrogen indicates potential moisture in the samples but also incomplete polymerisation of the carbon nitrides,

likely due to the existence of amine groups, which can terminate the carbon nitride sheets or exist as defects within the structure.^{6,44,50,98,135,156,159,160} This is further confirmed by diffuse reflectance infrared Fourier transform spectroscopy (DRIFTS) (see 3.3.1.4).

Table 8 - Elemental compositions, calculated C:N molar ratios and normalised composition of each carbon nitride.

Material	Measured Mass (%)			C:N (molar ratio)	Composition (Normalised)
	C	H	N		
CN-DCDA	34.84	1.83	61.30	0.663	C _{0.31} H _{0.20} N _{0.47} O _{0.01}
CN-BA (5)	35.53	1.74	61.52	0.674	C _{0.32} H _{0.19} N _{0.48} O _{0.01}
CN-BA(10)	36.12	1.75	60.55	0.696	C _{0.33} H _{0.19} N _{0.47} O _{0.01}
CN-BA(20)	37.28	1.79	59.05	0.736	C _{0.34} H _{0.19} N _{0.46} O _{0.01}
CN-M	35.15	1.64	61.99	0.661	C _{0.32} H _{0.18} N _{0.49} O _{0.01}
CN-U	34.98	1.59	61.25	0.666	C _{0.32} H _{0.17} N _{0.48} O _{0.02}
CN-UT(3:1)	33.68	1.77	59.31	0.662	C _{0.30} H _{0.19} N _{0.46} O _{0.05}
CN-UT(1:1)	34.02	1.80	60.1	0.660	C _{0.30} H _{0.19} N _{0.46} O _{0.04}
CN-UT(1:3)	33.95	1.85	59.97	0.660	C _{0.30} H _{0.20} N _{0.46} O _{0.04}
CN-T	34.07	1.84	59.91	0.663	C _{0.30} H _{0.20} N _{0.46} O _{0.04}
CN-500	34.48	1.92	61.09	0.658	C _{0.31} H _{0.20} N _{0.47} O _{0.03}
CN-600	35.1	1.68	61.04	0.671	C _{0.32} H _{0.18} N _{0.48} O _{0.02}
CN-2hr	34.72	1.88	61.21	0.661	C _{0.31} H _{0.20} N _{0.47} O _{0.01}
CN-6hr	34.84	1.80	61.07	0.665	C _{0.31} H _{0.19} N _{0.47} O _{0.02}
CN-8hr	34.85	1.83	61.41	0.662	C _{0.31} H _{0.20} N _{0.47} O _{0.02}
CN-10hr	34.88	1.81	61.44	0.662	C _{0.31} H _{0.19} N _{0.47} O _{0.02}

*Oxygen content was estimated from balance.

Oxygen content in the carbon nitride was calculated from the balance of the measured mass percentage. All materials appear to show a small amount of oxygen, which could originate from several different sources, including adsorbed CO₂, O₂ or moisture. Also, calcination of precursors being performed in air could have led to the formation oxygen impurities and some of the precursors contain oxygen, which when pyrolysed could form oxygen containing intermediates, which may lead to further impurities or defects.^{40,55,98,118,121,143,161} The presence of oxygen was also confirmed by X-ray photoelectron spectroscopy (XPS) (see 3.3.1.6).

The greatest variation in composition and C:N ratios lies with the series of carbon nitrides synthesised via co-polymerisation of DCDA with barbituric acid. It can be seen that by increasing the barbituric acid content from CN-DCDA to CN-BA(20) that the C:N ratio decreases showing that the copolymerization creates more nitrogen deficient species with increased carbon content. This is due to the ring within barbituric acid containing a carbon in the usual position of a nitrogen in a typical carbon nitride melem repeating unit. This was expected as this has previously been reported.^{50,92,111–113,117,119,121}

For the carbon nitrides calcined at different temperatures, there appears to be an increase in C:N ratio with increasing temperature (CN-500 < CN-DCDA < CN-600), this has previously been reported and is said to be due to greater extent of polymerisation and loss of NH₃ during the process at elevated temperatures.^{47,148} Also it can be seen that with increased calcination temperature or with extended calcination periods that the hydrogen content decreases, this is another indication of higher degree of polymerisation.^{26,40,47,55,98,118,121,143,148,161}

Initially, the idea behind altering ratios of urea and thiourea precursors (CN-UT series) was to produce sulphur doped carbon nitrides, however from elemental analysis (and also XPS (3.3.1.6)), no sulphur was detected, or it was below the detection limit of the equipment. The presence of sulphur in thiourea based carbon nitrides synthesised in air has previously been reported⁷¹, but other studies were also unable to detect any, stating that any sulphur likely transformed into H₂S or sulphurous oxides which were released during calcination.¹³⁵

There is some variation in composition when varying the urea and thiourea content, but no specific trend can be drawn. Also, there is very little difference in C:N ratios when different precursors are used or when calcination time is varied.

3.3.1.2 Surface Area Measurement

N₂ adsorption-desorption isotherms were measured (Figure 32) and the Brunauer-Emmett-Teller (BET) surface areas of each material has been calculated (Table 9). According to the International Union of Pure and Applied Chemistry (IUPAC) surface area and pore size classification, the carbon nitrides all show type IV isotherms with type H3 hysteresis loops,

which are characteristic of mesoporous materials consisting of platelet-like particle aggregates, forming slit shaped pores.^{162,163}

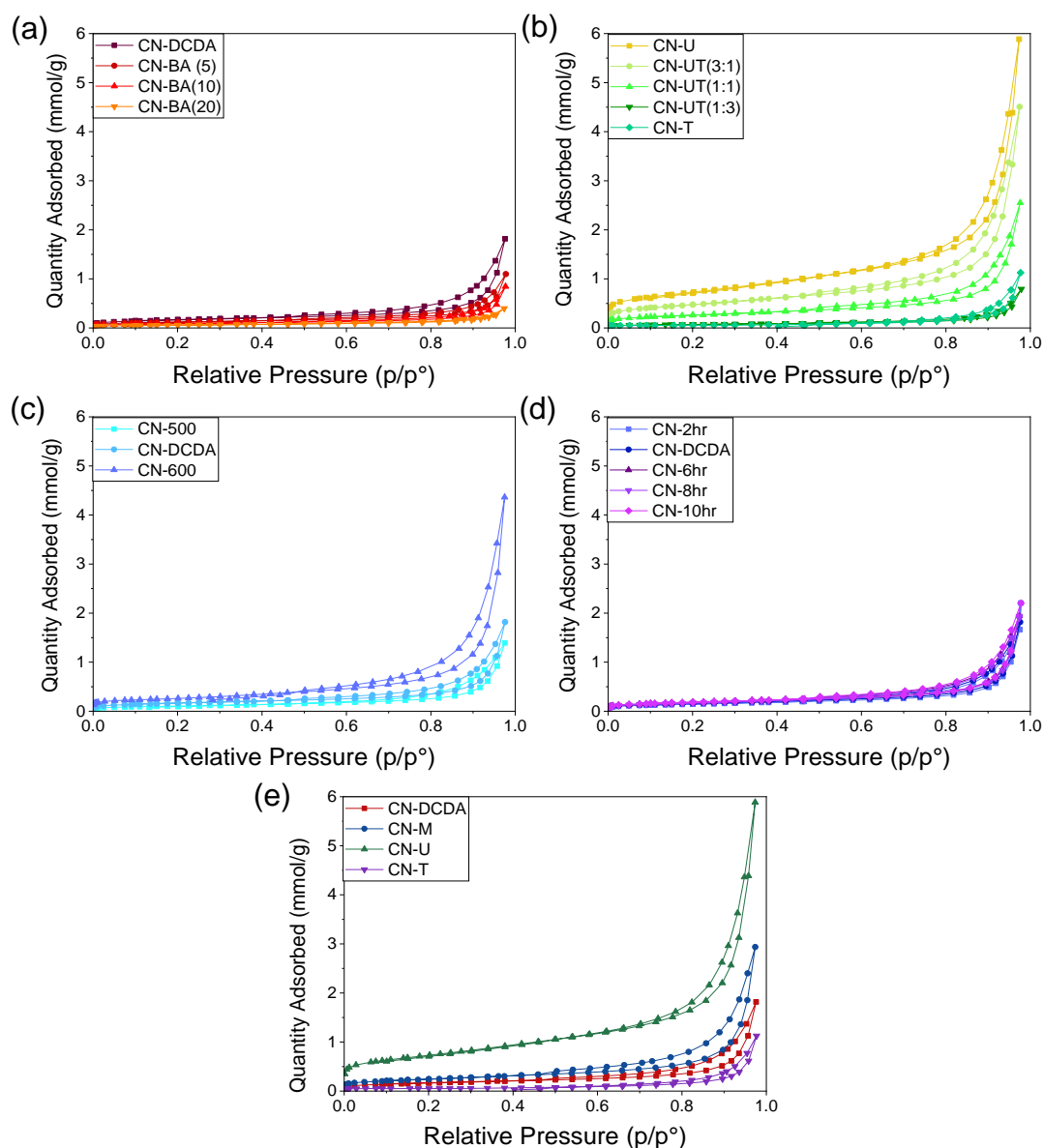


Figure 32 - N_2 adsorption/desorption isotherms of (a) CN-BA, (b) CN-UT, (c) CN-Temp, (d) CN-Time and (e) CN-Precursor series.

Most materials have quite low surface areas, which are very typical for bulk carbon nitrides synthesised via thermal condensation.^{26,50,57,64,153} Despite the mostly low surface areas exhibited by the materials, there are some variations and trends. Across the CN-BA series, there is a decrease in surface area with increasing barbituric acid content (CN-DCDA > CN-BA(5) > CN-BA(10) > CN-BA(20)). By varying the precursor used, the carbon nitride produced can have quite different surface areas. The material with the highest surface area is CN-U with

a surface area of 57.50 m²g⁻¹, whilst CN-T has the smallest of 3.72 m²g⁻¹ and across the CN-UT series there is a clear trend that with increasing thiourea content, the surface area decreases. There are also small variations with calcinations conditions, surface area increases with both increasing calcination time and calcination temperature.

Table 9 - Measured BET Surface area of each carbon nitride.

Material	Surface Area (m ² g ⁻¹) [a]	Error (±)[b]
CN-DCDA	12.81	0.06
CN-BA (5)	9.04	0.03
CN-BA(10)	6.79	0.03
CN-BA(20)	4.41	0.01
CN-M	19.08	0.04
CN-U	57.50	0.18
CN-UT(3:1)	37.22	0.12
CN-UT(1:1)	20.33	0.07
CN-UT(1:3)	5.46	0.05
CN-T	3.72	0.08
CN-500	8.52	0.01
CN-600	20.41	0.03
CN-2hr	11.32	0.05
CN-6hr	14.19	0.06
CN-8hr	13.44	0.04
CN-10hr	14.46	0.05

[a] BET surface area calculated over the pressure range (P/P₀) 0.05-0.3.

[b] Error in BET calculation.

3.3.1.3 Powder X-ray Diffraction (PXRD)

The PXRD patterns of all the carbon nitrides can be found in Figure 33. All materials exhibit two broad features at $2\Theta = \sim 13^\circ$ and $\sim 27^\circ$, these are characteristic peaks of carbon nitride and are consistent with their semi-amorphous nature. The patterns show that there is some long-range ordering due to the presence of the sharper peak at $2\Theta = \sim 27^\circ$ in most samples. The peak at $2\Theta = \sim 27^\circ$ is reported as the (002) plane (Figure 34 (a)) and is assigned as the interplanar distance of the stacked aromatic systems.^{7,40,167-}

170,41,42,60,65,154,164–166 The stacking distance of the carbon nitride sheets can be estimated using the Bragg equation ($n\lambda = 2d \sin \theta$) and ranges from 0.321 – 0.326 nm for the carbon nitrides presented in this work (Table 10).

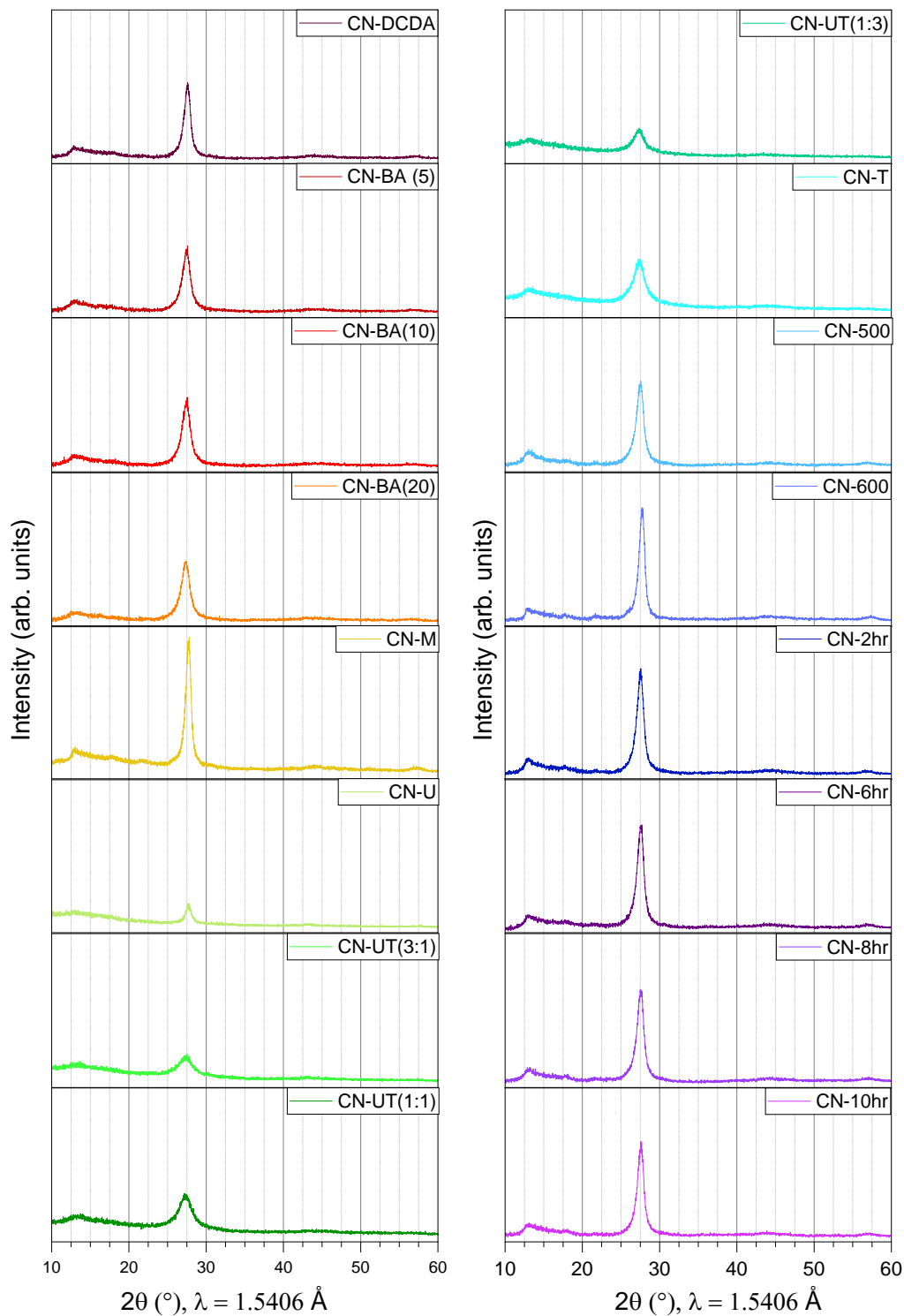


Figure 33 - PXR D patterns for each carbon nitride material.

Table 10 – Position of peaks in carbon nitride PXRD patterns and d-spacing values.

Material	(100) / (210)		(002)		
	2 Θ (°)	d-spacing (nm) ^[a]	2 Θ (°)	d-spacing (nm) ^[a]	FWHM ^[b]
CN-DCDA	12.9	0.688	27.6	0.323	0.969
CN-BA (5)	12.8	0.691	27.5	0.324	1.090
CN-BA(10)	12.9	0.688	27.5	0.325	1.215
CN-BA(20)	12.7	0.699	27.4	0.326	1.302
CN-M	12.9	0.685	27.7	0.322	0.837
CN-U	13.1	0.675	27.7	0.322	0.880
CN-UT(3:1)	13.2	0.673	27.5	0.325	2.077
CN-UT(1:1)	13.2	0.671	27.4	0.326	2.236
CN-UT(1:3)	13.4	0.661	27.4	0.325	1.711
CN-T	13.1	0.677	27.3	0.326	1.950
CN-500	13.0	0.682	27.5	0.324	1.091
CN-600	12.9	0.687	27.6	0.323	0.858
CN-2hr	13.1	0.678	27.6	0.323	1.029
CN-6hr	13.1	0.678	27.6	0.323	1.037
CN-8hr	13.0	0.680	27.5	0.324	1.003
CN-10hr	12.8	0.689	27.8	0.321	0.936

[a] d-spacing calculated using the Bragg-equation.

[b] Full width at half maximum.

Generally, the peak at $2\Theta = \sim 13^\circ$ is assigned to the in-plane structural packing motif of the carbon nitride heterocycles and in this work is determined to have a distance between 0.661 nm and 0.699 nm. These values are only slightly below that of the size of a single heptazine unit (0.713 nm), which has previously been attributed to a small tilt or buckling of the units to minimise repulsion between nitrogen lone pairs.^{6,26,50,63,64,74,142,170} Typically this peak has been assigned to the (100) plane in fully polymerised graphitic carbon nitride (Figure 34 (b)).^{42,60,65,154,165,167–170} However a paper published in 2013 by Tyborski *et al* utilized a combination of PXRD and DFT calculations to gain greater understanding of the 3D carbon nitride structure.¹⁶⁴ They found that the fully polymerised structures do not match completely with the observed patterns. Instead a structure similar to that of melon, a partially polymerised heptazine structure calculated by Lotsch *et al*⁷, was a much better fit, which meant that the peak at $2\Theta = \sim 13^\circ$

could be assigned to the (210) plane (Figure 34 (c)). Then in 2015, Fina *et al* approached this in similar way but also combined these methods with neutron scattering.⁴¹ They reached a similar conclusion but found that a more distorted structure with an offset between layers in an A-B stacking configuration was a better fit. However, due to the broadness of the peak it is unlikely that a single structure can be allocated, and these materials cannot be considered as an overall homogeneous phase, instead it is likely that numerous structures exist within the materials varying from melon type structures to more fully polymerised motifs.

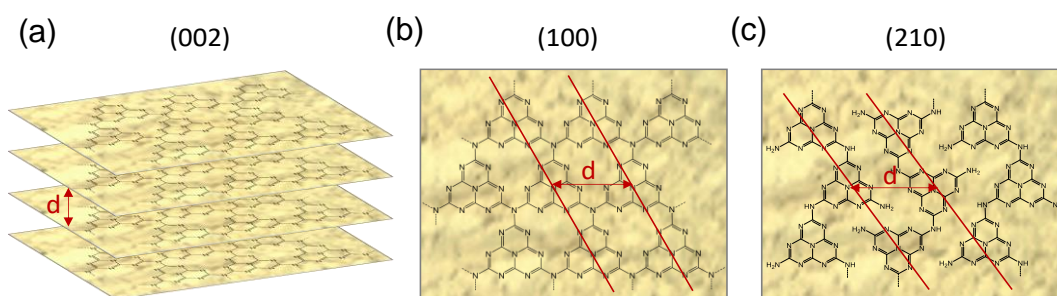


Figure 34 – Depiction of indexed planes in (a) and (b) fully polymerised carbon nitride and melon (c).⁴¹

From Table 10, it can be seen that the d-spacing values for the peak at $2\Theta = \sim 13^\circ$ decrease with increasing amounts of barbituric acid used in the synthesis of the carbon nitrides. This is generally considered to be due to the incorporation of the barbituric acid motif introducing C into the heptazine structure creating disturbance in the carbon nitride network and weakening the H-bonding network, disrupting long range ordering.^{50,112} Also for this series of materials, there appears to be a general shift in the $2\Theta = \sim 27^\circ$ peak to lower values, a decrease in intensity and increase in peak broadening (FWHM) indicating further disturbance in the graphitic structure.^{50,112}

When varying the ratio of urea: thiourea in the synthesis of the CN-UT materials, there does not appear to be an exact trend when increasing either urea or thiourea content, though there is a general decrease in the d-spacing for the peak at $2\Theta = \sim 13^\circ$ until the solely thiourea sample, CN-T, where it reaches its highest value for that series. For the peak at $2\Theta = \sim 27^\circ$, there is no particular shift or change in intensity that corresponds to the variation in ratios of precursors used. The materials within this series show the broadest peaks with the largest values for FWHM, indicating disturbance within the graphitic structure, with the exception of

CN-U which has the lowest value. Materials synthesised at different temperatures show slight differences in peak intensities and positions, but no specific trend can be drawn, only that the material synthesised at 600 °C has the highest intensity peak at $2\theta = \sim 27^\circ$ with the smallest d-spacing within that series, indicating a higher level of crystallinity.¹⁴³ This is also reflected in the values of FWHM which decreases with increasing temperature. Though there are some variations in the PXRD patterns of the samples calcined for different periods, no particular trend in peak positions or intensities is observed.

3.3.1.4 Scanning Electron Microscopy (SEM)

SEM was used to look at the morphologies of the CN-BA series of materials and the images can be seen in Figure 35. The images show that the materials display large particles composed of sheet like structures and there is little difference between each sample.

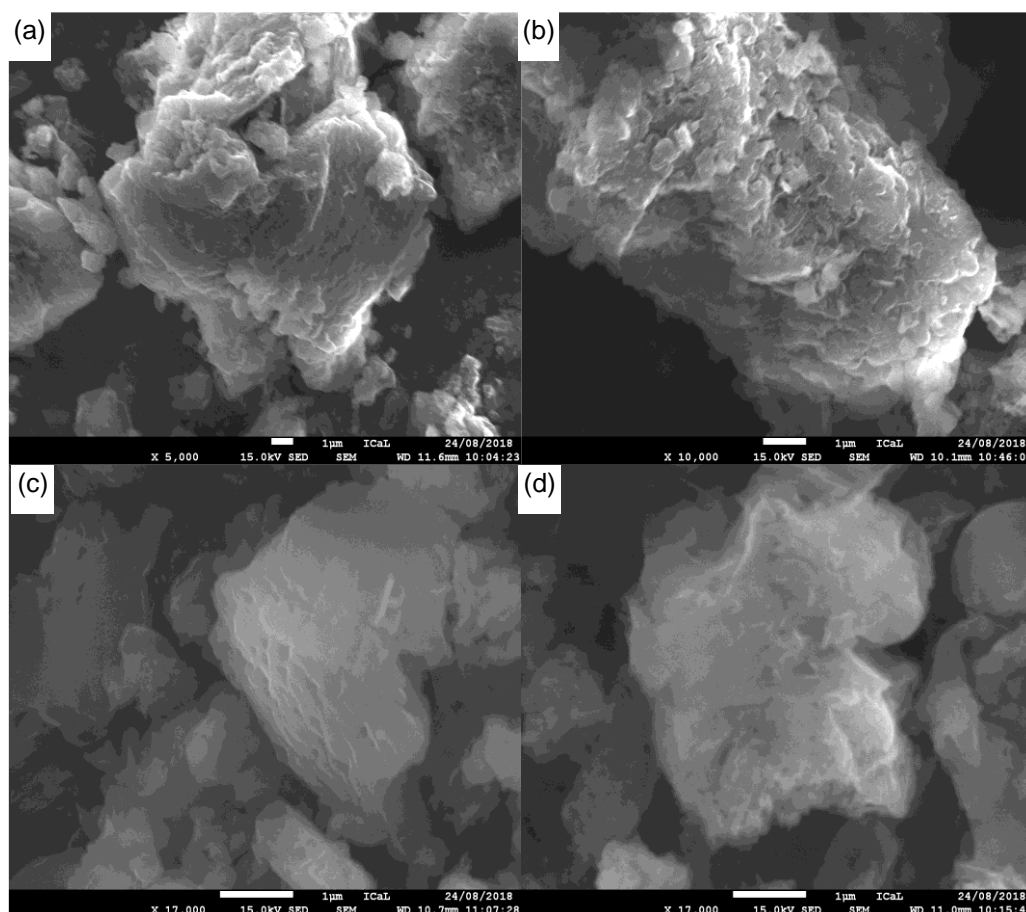


Figure 35 -SEM images of (a) CN-DCDA, (b) CN-BA(5), (c) CN-BA(10) and (d) CN-BA(20).

3.3.1.5 Diffuse Reflectance Infrared Fourier Transform Spectroscopy (DRIFTS)

DRIFTS was employed, in an attempt to understand the bonding and structure of the carbon nitrides. To obtain carbon nitride DRIFTS, 2 mg of the carbon nitride was diluted in 100 mg of KBr and the spectra presented in Figure 36 have been normalised by a single point in the baseline. Due to the nature of the measurement, differences in peak intensities should be considered carefully as measurements were performed without a reference sample to normalise the data to.

Within the literature, the majority of papers do not discuss in great detail carbon nitride IR assignments and if discussed generally refer to characteristic peaks in two or three regions: $\sim 3000\text{-}3500\text{ cm}^{-1}$, $\sim 1000\text{-}1700\text{ cm}^{-1}$ and $\sim 800\text{ cm}^{-1}$, attributed to amine groups, CN heterocycles and CN ring breathing modes, respectively.^{42,47,154,171–174,50,64,68,74,94,95,126,141} However, some reports do give a list of characteristic peaks within these regions^{66,67,160,175,176} and occasionally further assignment is given.^{7,25,177–185,71,75,137,138,143,149,166,168} Due to C-C, C-N and C-O stretches strongly coupling, they lie at similar wavenumbers, which means that peaks overlap and are often difficult to distinguish.^{74,166,174,186,187} This leads to wide discrepancies in the literature as to reported positions, intensities and assignments of peaks, likely arising from the wide range of precursors and synthetic procedures used in the materials synthesis. This means that at the moment we are unable to fully assign each of the peaks in the IR spectrum and can only speculate as to the potential species that could be present.

All carbon nitrides within this work showed the usual reported characteristic stretches at $\sim 3500\text{-}2800\text{ cm}^{-1}$, $\sim 1200\text{-}1700\text{ cm}^{-1}$ and $\sim 810\text{ cm}^{-1}$, usually assigned to amine groups, CN heterocycles and CN ring breathing modes, respectively, a full list of approximate peak positions and assignments can be found in Table 11.

The broad peaks $\sim 2900\text{-}3500\text{ cm}^{-1}$ are assigned to the overlap of stretching vibrations of -OH groups and -NH/-NH₂ vibrations implying the presence of surface amino groups. The presence of these amino groups further indicates incomplete polymerisation. The broadness of the bands is attributed to adsorbed water.^{66,71,94,126,137,160,188} As this broad region extends to

much lower wavenumbers than usual, this could indicate the presence of C-H stretches, which is a further indication of incomplete polymerisation, however this is difficult to definitively assign. The broad band has also previously been attributed to H-bonding or other interaction effects, but could be due to amine groups situated in different environments which may include triazine or heptazine rings but also incomplete ring structures.⁴⁰

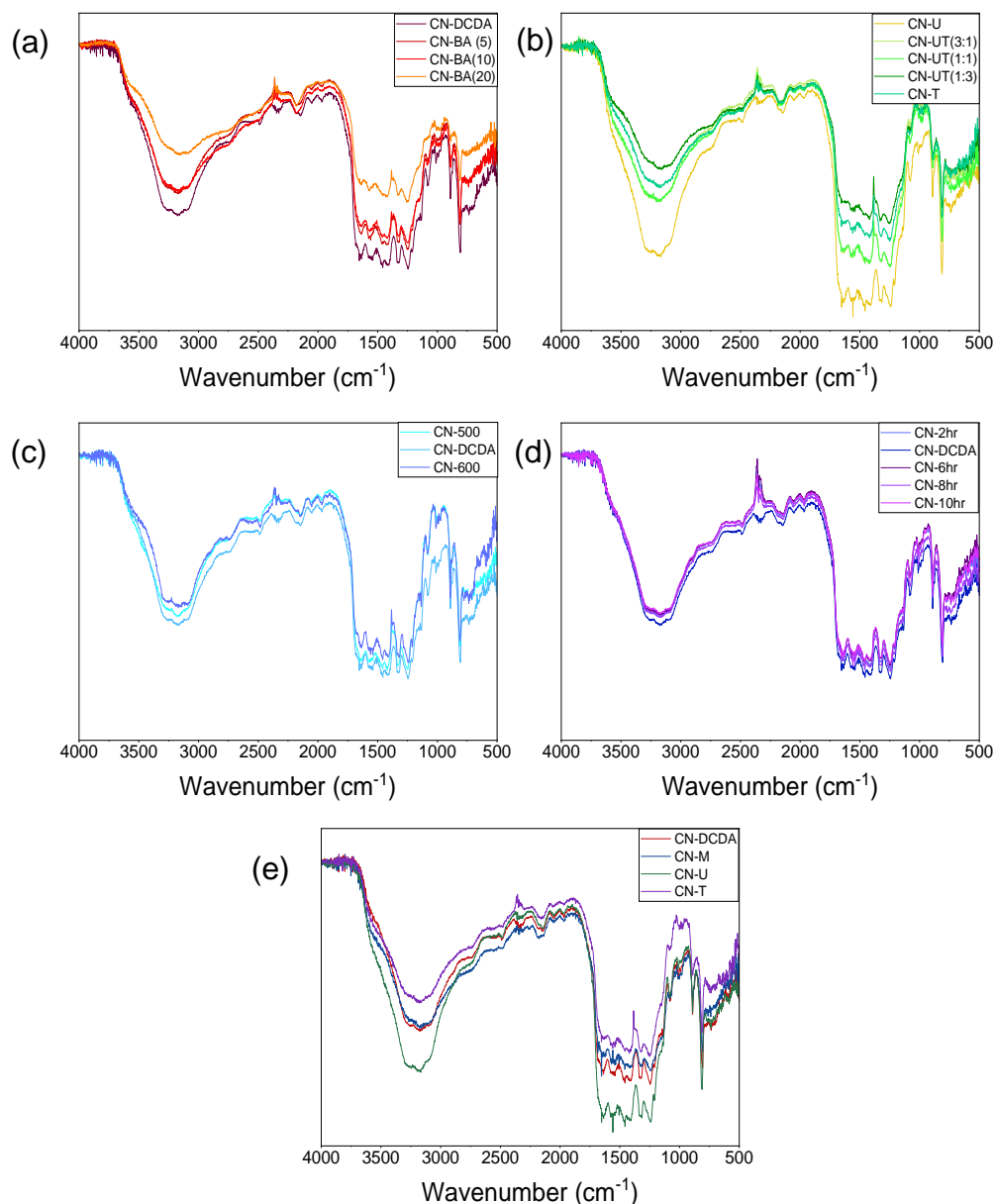


Figure 36 – DRIFTS of (a) CN-BA, (b) CN-UT, (c) CN-Temp, (d) CN-Time and (e)CN-Precursor series.

Table 11 – DRIFTS assignments.

Wavenumber Region (cm ⁻¹)	Approximate Wavenumber (cm ⁻¹) [a]	Assignment	References
~2400-3600	3560 (<i>sh</i>) 3260 (<i>ms, b</i>) 3175 (<i>ms, b</i>) 3100 (<i>ms, b</i>) 2750 (<i>sh</i>) 2509 (<i>sh</i>) 2485 (<i>w</i>)	-OH stretches -NH/-NH ₂ stretches <i>-CH stretches</i>	66,71,94,126,137,160,188
~2400-2200	-	Atmospheric CO ₂	63,71,168,184,188
~2100-2200	2180 (<i>w</i>) 2147 (<i>w</i>)	-C≡N stretches <i>-N=C=N- stretches</i>	25,75,180-185,18825
~1900-2100	2051 (<i>w</i>) 1969 (<i>w</i>)	<i>C=C=C, C=N=C, C=C=N</i>	188,189
~1200-1700	1642 (<i>s</i>) 1564 (<i>s</i>) 1460 (<i>s</i>) 1415 (<i>s</i>) 1330 (<i>s</i>) 1247 (<i>s</i>) 1210 (<i>sh</i>)	C-N heterocycle stretches including: C=N and C-N stretches C-NH-C and N(C) ₃ bridging units <i>-C(=O)-N-, C=C, C-OH, -C=C=N-, -C=N=N-, -C-O-C-</i>	7,25,74,75,94,95,126,137,138,141,14 3,149,42,154,160,166,168,171- 174,177,178,47,179- 185,188,190,191,50,192,193,63,64,6 6,68,71
~900-1200	1150 (<i>sh</i>) 1080 (<i>ms</i>) 1012 (<i>w</i>) 991 (<i>w</i>) 976 (<i>w</i>)	<i>C=C, C-H</i>	188,189
~890	891 (<i>ms</i>)	N-H deformation mode	71,149,168,188
~810	809 (<i>s</i>)	Out-of-plane bending mode of triazine/heptazine rings	7,25,74,75,94,95,126,137,138,141,14 3,149,42,154,160,166,168,171- 174,177,178,47,179- 185,188,50,63,64,66,68,71

[a] peak descriptions: s = strong, ms = medium strong, w = weak, b = broad, sh = shoulder
Potential assignments are italicised.

Within the ~1200-1700 cm⁻¹ there are a number of relatively sharp peaks, generally these are assigned as C-N heterocycles but some reports assign peaks to not only stretching vibrations of the C=N and C-N in the aromatic heptazine heterocycles^{138,177,179,182,184,190,191}, but also stretching vibrations of C-NH-C and N(C)₃ bridging units.^{137,143,166,185,192,193} This further

indicates a lower degree of polymerisation closer to that of melon than fully condensed graphitic carbon nitride due to defective condensation of the CN framework.

Due to multiple overlapping peaks, other oxygen containing species such as carbonyls and amide groups cannot be identified, despite their presence being indicated by CHN and XPS (3.3.1.1 and 3.3.1.6).

The peak at $\sim 810\text{ cm}^{-1}$ is assigned to the breathing mode of the triazine units and/or within the tri-s-triazine repeating units in the carbon nitride materials.^{63,64,184,188,66,74,94,126,166,180,181,183} A weak peak at $\sim 890\text{ cm}^{-1}$ can be assigned to the deformation mode of N-H.^{71,149,168,188} Another weak peak at $\sim 2100\text{-}2200\text{ cm}^{-1}$ is assigned to $\text{-C}\equiv\text{N}$ groups and is likely caused by incomplete polymerisation of DCDA in the majority of samples. However, it is also present in samples prepared with other precursors, in the cases of thiourea and urea. Synthesis of the carbon nitride likely proceeds via a dicyandiamide (DCDA) intermediate and for melamine, the material undergoes reorganisation to form heptazine rings, which if incomplete could lead to the formation of nitrile groups.^{2,6,11,36,44,47}

Across each of the series there does not appear to be any distinct differences in peak positions. The only shift that can be observed is a slight shift in position for the peak at $\sim 810\text{ cm}^{-1}$, which moves to slightly higher wavenumber for the CN-BA series which may be indicative of carbon being introduced into the rings and causing some distortion in the heterocycle. Also, within this series, with increasing amounts of barbituric acid used, peaks become broader and less defined, and the peaks centred at $\sim 810\text{ cm}^{-1}$ and $\sim 890\text{ cm}^{-1}$ decrease in intensity, which may also indicate increased disorder, due to incorporation of carbon into the structure.

3.3.1.6 X-ray Photoelectron Spectroscopy (XPS) Surface States

X-ray photoelectron spectroscopy (XPS) has been employed to elucidate the composition and chemical states at the surface of each of the prepared materials as XPS can be used to probe the top 1-10 nm of samples.⁴⁰ The full survey spectra for each carbon nitride can be seen in Figure 37, and indicate the presence of mainly C, N and a small amount of O at the surface of each of the materials.

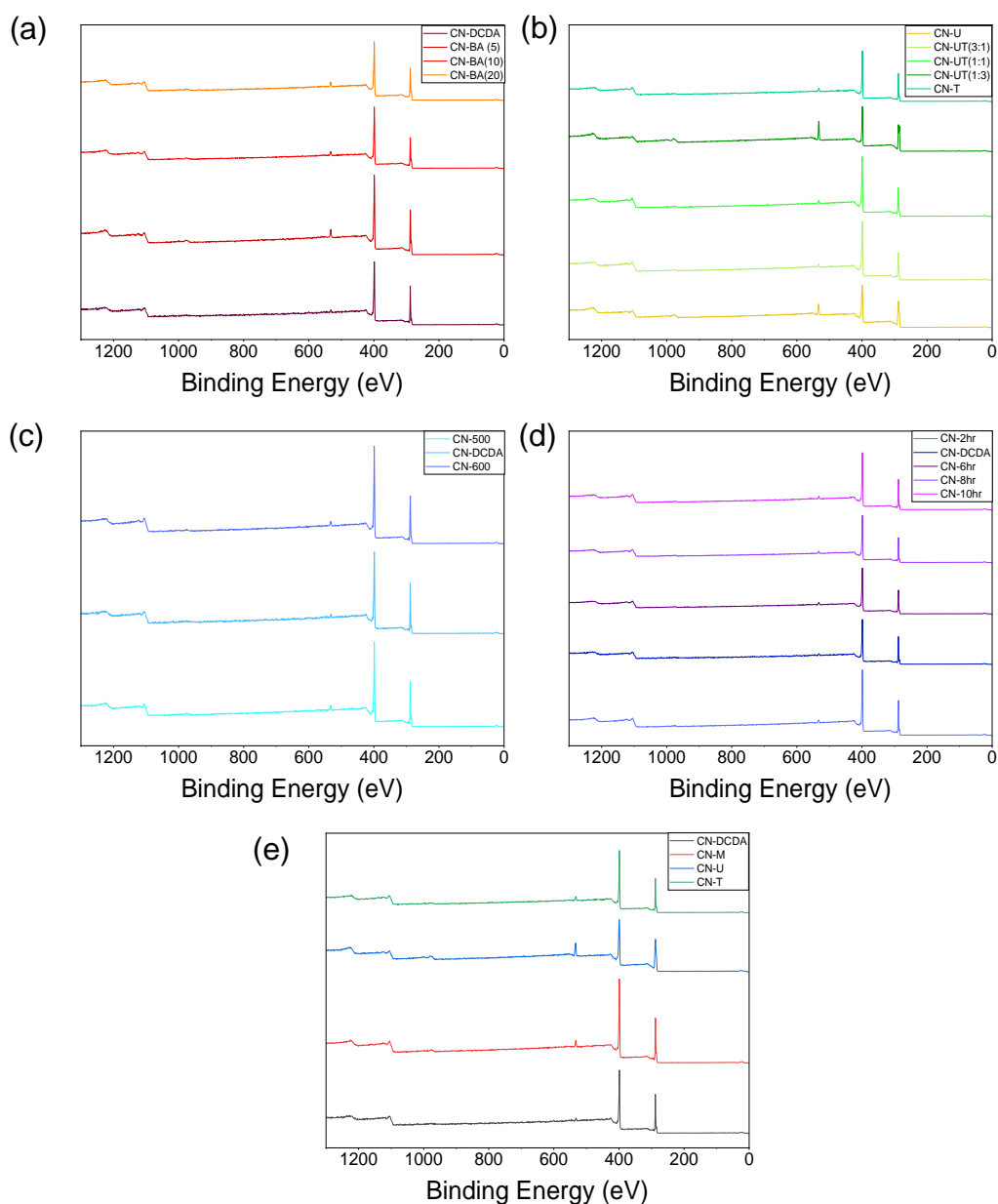


Figure 37 – XPS survey spectra of (a) CN-BA, (b) CN-UT, (c) CN-Temp, (d) CN-Time and (e) CN-Precursor series.

To gain understanding of the types of species present, high-resolution spectra of each region was measured and then fitted using Casa XPS software. The C1s and N1s spectra of the CN-BA series can be seen in Figure 39 and general assignments can be found in Table 12 and Table 13. The high-resolution spectra for other materials were not included in this chapter as they showed little difference when compared with the CN-DCDA sample but can be found in Appendix i.

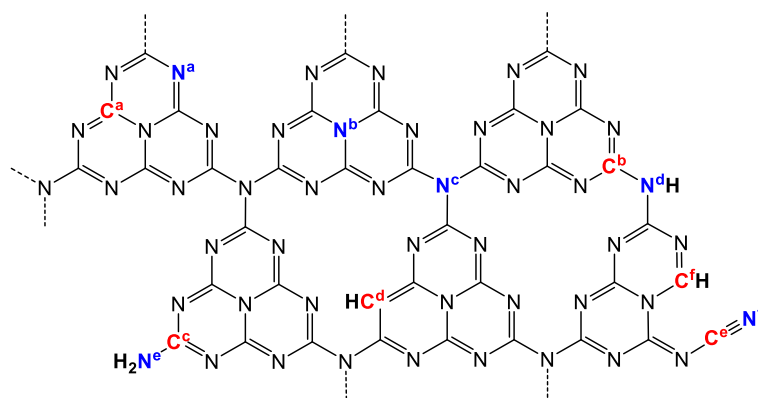


Figure 38 – Labeled representation of carbon nitride structure with potential and proposed defects.

Deconvolution of the high resolution N1s spectra (Figure 39) for all materials imply the existence of three N species. The peaks centred at ~398, ~399 and ~401 eV can be assigned to; the sp²-hybridised N (C-N=C) within the heptazine rings (N^a Figure 38), tertiary N (N-(C)₃) that bridge between and lie at the centre of the heptazine rings (N^b and N^c Figure 38) and N-Hx in primary and secondary amine groups (N^d and N^e Figure 38), respectively.^{40,55,117,120,121,124,126,138,156,168,177,194,60,195–202,66,67,71,74,75,95,112}

DRIFTS measurements indicated the presence of C≡N groups (N^f Figure 38), in XPS these groups are usually found at ~398 eV, which lies at a very close binding energy to sp²-hybridised N (C-N=C).¹⁹⁹ It is likely that from the N1s spectra we are unable to deconvolute the nitrile peak from the large aromatic N peak. The broad peak found at ~404 eV in the N1s spectra can be attributed to π excitations, charging effects or positive charge localisations in the heterocycles.^{25,55,122,126,138,156,168,194,200,202,203,60,66,67,71,112,117,120,121} A similar peak at ~ 293 eV in the C1s spectra is also assigned to these charge effects.

Table 12 – Deconvolution of N1s peak positions and assignments.

Peak Position (eV)	Assignment		Reference
398	N ^a and N ^f	(C-N=C)	40,55,117,120,121,124,126,138,156,168,177,200,60,201,202,66,67,71,74,75,95,112
399	N ^b and N ^c	N (N-(C) ₃)	40,55,112,117,120–122,124,126,138,156,168,60,177,200–202,66,67,71,74,75,95,96
401	N ^d and N ^e	N-Hx	40,55,112,117,120–122,124,126,138,143,156,60,168,177,200–202,66,67,71,74,75,95,96
404	π excitations and charging effects		25,55,122,126,138,156,168,200,202,203,60,66,67,71,112,117,120,121

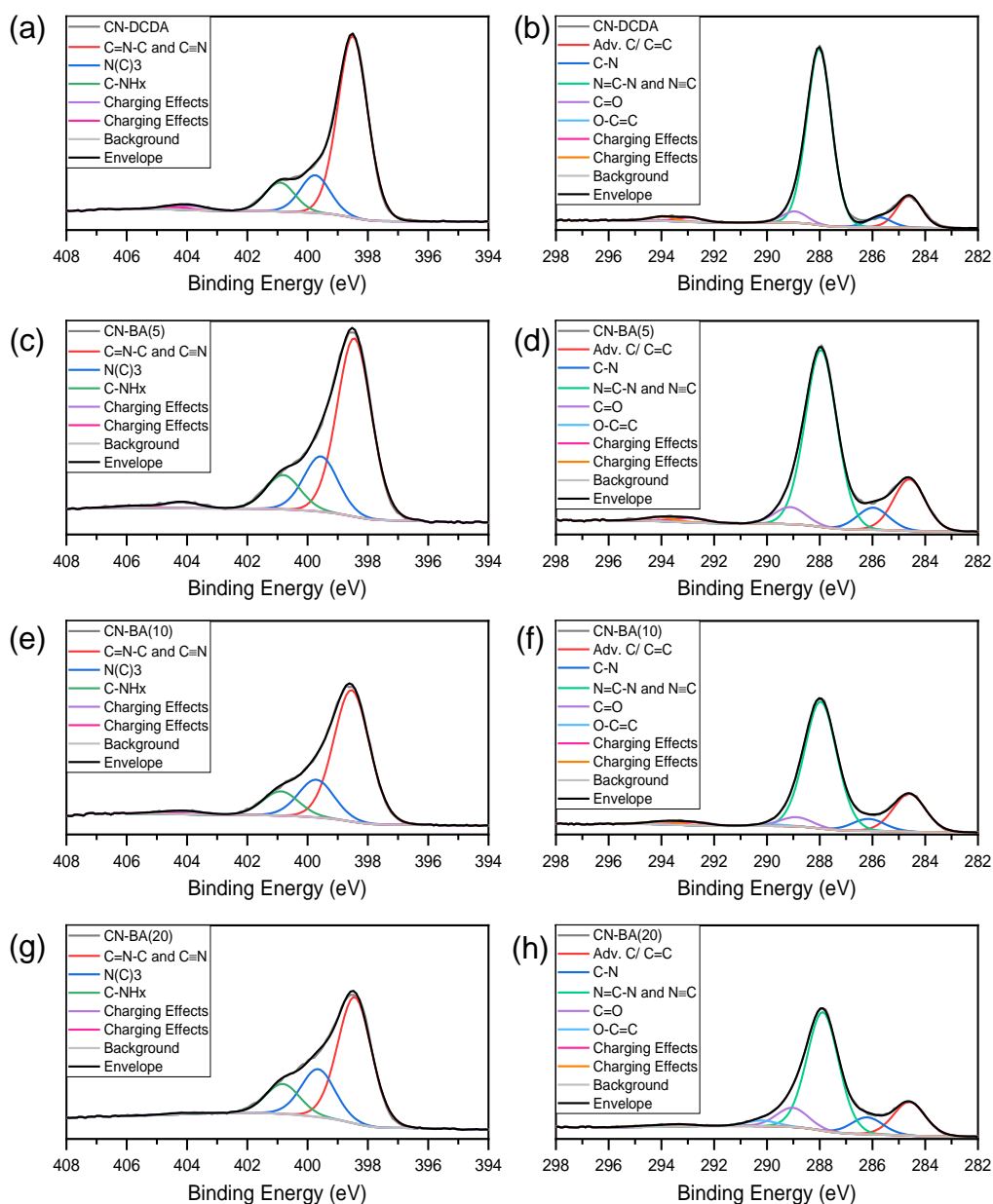


Figure 39 – High resolution deconvolution of N1s (left) and C1s (right) spectra for CN-DCDA ((a), (b)), CN-BA(5) ((c), (d)), CN-BA(10) ((e), (f)) and CN-BA(20) ((g), (h)).

Reports of the C1s spectra in the literature are much less consistent in terms of peak positions and assignments. Previous studies have fitted the spectra to only two peaks, referring only to the adventitious carbon and the sp^2 -hybridised carbon in the aromatic rings at ~ 284 eV and 288 eV respectively.^{59,67,207–210,71,94,112,120,122,204–206} However, in this work (Figure 39), the spectra could be deconvoluted to four peaks centred at 284.6, ~ 286 , ~ 288 and ~ 289 eV with the development of a fifth peak at ~ 290 eV, with increasing amounts of barbituric acid in samples CN-BA(10) and CN-BA(20). The first peak at 284.6 eV is assigned to adventitious carbon adsorbed onto the surface of the material and any sp^3 carbon formed during pyrolysis

including C-C, C=C and C-H species.^{40,73,195–202,74,75,95,115,120,121,168,194} From this XPS data it is not possible to differentiate between the adventitious and sp^3 carbon, despite DRIFTS indicating the potential presence of sp^3 carbon. The incorporation of C=C-H functionality (C^d Figure 38) that is added due to the use of barbituric acid within the precursor mixture, likely lies within this peak at 284.6 eV and cannot be deconvoluted. The most intense peak at ~288 eV is assigned to the N-C=N aromatic carbon in the heptazine ring (C^a Figure 38).^{40,73,195–202,74,75,95,115,120,121,168,194} Also, much like the N1s spectra, any $C\equiv N$ groups lie at a similar binding energy to the N-C=N carbon so cannot be deconvoluted.

Table 13 - Deconvolution of C1s peak positions and assignments.

Peak Position (eV)	Assignment		Reference
284.6	C^d and C^f	adventitious carbon (C-C, C=C, C-H, C=C-H)	40,73,201,202,74,75,95,115,120,121,168,200
286	C^b and C^c	C-NH _x	73,74,199–202,75,97,121,194–198
288	C^a and C^e	N-C=N, $C\equiv N$	40,73,195–202,74,75,95,115,120,121,168,194
289	C-O, C=O, N-C=O		55,74,75,97,115,125,211
290	O-C=O		195,199
293	π excitations and charging effects		73,203

The peak centred at ~286 eV has previously been reported as a number of different species including; C-O^{63,66,73,96,101,115,177} and N=CH-N^{113,124}, but in this work is attributed to C-N in the primary and secondary amine groups (C^b and C^c Figure 38).^{73,74,199–202,75,97,121,194–198} The peak at ~289 eV can be attributed to C-O/C=O^{198,199}, though the DRIFTS data appears to show no C=O stretches in the usual region of ~1700 cm^{-1} , it is more likely that this is due to amide groups and/or bound CO₂, as the carbonyl stretches in these groups are at lower wavenumbers and may be masked by the aromatic C-N stretches in the 1500-1700 cm^{-1} region. The peak at ~290 eV can be assigned to O-C=O^{195,199}, much like the amide groups, the carboxylate are probably difficult to distinguish from the aromatic C-N stretches in the DRIFTS. Also DRIFTS measurements look at the bulk material, XPS only looks at the surface, so any oxygen species may be at higher concentrations at the surface than in bulk, so are not strong enough to be observed by other techniques as the bulk swamps the signal. These oxygenated groups may in part be due to adsorbed water/CO₂, calcination in air leading to

oxygen containing intermediates or species and the incorporation of barbituric acid moieties containing three carbonyl groups.^{66,95,177}

As mentioned earlier the other carbon nitrides presented in this chapter showed very similar high resolution C1s and N1s spectra. This indicated that calcination time and temperature had very little effect on the surface states of the materials. Also XPS further indicated that using thiourea in precursor mixtures did not lead to sulphur doping as the S 2s or 2p peaks at 228 eV and 165 eV, respectively, were not observed, suggesting that all sulphur was released during calcination.^{95,138} By looking at the relative ratio of nitrogen species within the materials, the degree of polymerisation at the surface can be better understood. The carbon nitrides in this work, typically have ratios of C-N=C:N-(C)₃:N-H_x of 1:0.3:0.2, indicating that the materials are heptazine based and are likely to be mixed structures between melon and fully polymerised carbon nitrides. A fully condensed heptazine based material has a ratio of C-N=C:N-(C)₃ units of 1:0.33 and a melon structure would have N-(C)₃:N-H_x of 1:2.⁴⁰

3.3.1.7 Cross Polarisation (CP) Magic Angle Spinning (MAS) Solid State Nuclear Magnetic Resonance (SS NMR)

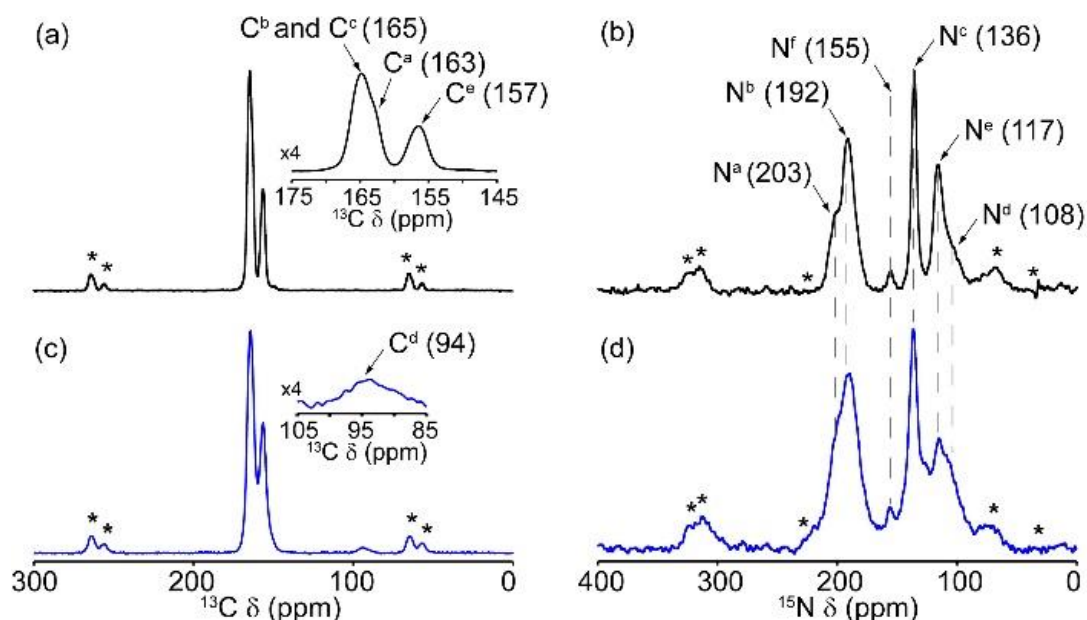


Figure 40 - (Left) ¹³C and (Right) ¹⁵N CP MAS spectra for CN-DCDA ((a),(b)) and CN-BA(20) ((c),(d)) with assignments with respect to the structure (e) and chemical shifts are given. Insets in (a) and (c) show the 175 – 145 and 105 – 85 ppm regions. Spinning sidebands are marked with asterisks (*) (Figure produced by Andrea Pugliese.)

^{13}C and ^{15}N CP MAS SS NMR was performed on two of the carbon nitride materials, CN-DCDA and CN-BA(20). These measurements were performed and analysed by Andrea Pugliese and are briefly discussed within the context of this thesis. Andrea's full analysis and assignments can be found in Figure 40, Table 14 and Table 15. Assignments have been given in reference to the structure assignments shown in Figure 38.

Table 14 - Table of assignments for ^{13}C CP MAS NMR spectra.^{7,43,180,212} (The standard error on the correspondent value)

Sample	δ (ppm)	Assignment	Width of the half-height (Hz)
CN-DCDA	157	C ^e	310 (5)
	163	C ^a	190 (20)
	165	C ^b and C ^c	320 (20)
CN-BA(20)	94	C ^d	650 (40)
	157	C ^e	540 (25)
	163	C ^a	440 (20)
	165	C ^b and C ^c	340 (10)

Table 15 – Table of assignments for ^{15}N CP MAS NMR spectra.^{7,43,180,213,214} (The standard error on the correspondent value)

Sample	δ (ppm)	Assignment	Width of the half-height (Hz)
CN-DCDA	108	N ^d	550 (40)
	117	N ^e	350 (15)
	136	N ^c	220 (20)
	155	N ^f	220 (30)
	192	N ^b	500 (10)
	203	N ^a	430 (10)
CN-BA(20)	108	N ^d	900 (15)
	117	N ^e	770 (50)
	136	N ^c	340 (15)
	155	N ^f	210 (25)
	192	N ^b	690 (40)
	203	N ^a	870 (45)

The ^{13}C NMR of both samples are similar to previous reports on DCDA and BA copolymerised samples.^{50,112,113,117,122} A new peak is observed at 94 ppm for the CN-BA(20) sample, which is not observed in the CN-DCDA material, indicating the existence of a new carbon environment. This can be assigned to protonated carbon confirming the incorporation of carbon into the carbon nitride structure, without disruption to the heptazine based structure.^{50,112,113,117,122} Also, CN-BA(20) ^{13}C NMR exhibits broader peaks which are indicative of lower level of crystallinity compared with CN-DCDA.¹¹³ However, the presence of carbonyl groups as indicated by XPS, or C-H as indicated by DRIFTS could not be confirmed, as they lie at a similar shift to the C-N heterocycle peaks and if present are likely below the detection limit of the NMR.

3.3.1.8 Ultraviolet-Visible-Near Infrared (UV-Vis-NIR) Spectroscopy

Optical properties of the as-prepared carbon nitrides were investigated using UV-vis diffuse reflectance spectroscopy (UV-Vis DRS). Band gap energies of the materials were determined by extrapolation of the absorption edge of the $(\alpha h\nu)^n$ Tauc plots, where n is equal to 2 for direct band gaps or $\frac{1}{2}$ for indirect band gaps (Figure 41) and values can be found in Table 16.

Usually, bulk carbon nitride materials are reported to give absorption spectra with a pronounced absorption edge at around 420 nm corresponding to a band gap of $\sim 2.7\text{eV}$, making the materials appear yellow in colour.^{2,6,50,51,215,216,12,24,26,30,31,36,38,45} Computational studies have determined that the bulk tri-s-triazines band gap is indirect in nature.^{23,49} Furthermore, within this work, the values for the indirect band gaps are closer to those expected via examination by eye of the material colours in Figure 31. The band gaps of the basic bulk carbon nitrides (CN-DCDA, CN-U, CN-T and CN-M) are within the expected range of those reported in the literature.^{26,55,60,71,95,134,142,152,153} When different precursors were used, the band gap varied from 2.55 eV to 2.93 eV (CN-U > CN-DCDA > CN-M > CN-T).

Varying the ratio of urea and thiourea precursors in the synthesis of the carbon nitrides has had some effect on the band gap. There does seem to be a general trend associated with the increase in the amount of thiourea used in the precursor mix, CN-U > CN-UT(3:1) \approx CN-UT(1:1) > CN-UT(1:3) \approx CN-T. This kind of general trend of decreasing in band gap associated with an increase in thiourea content has previously been reported.¹³⁵

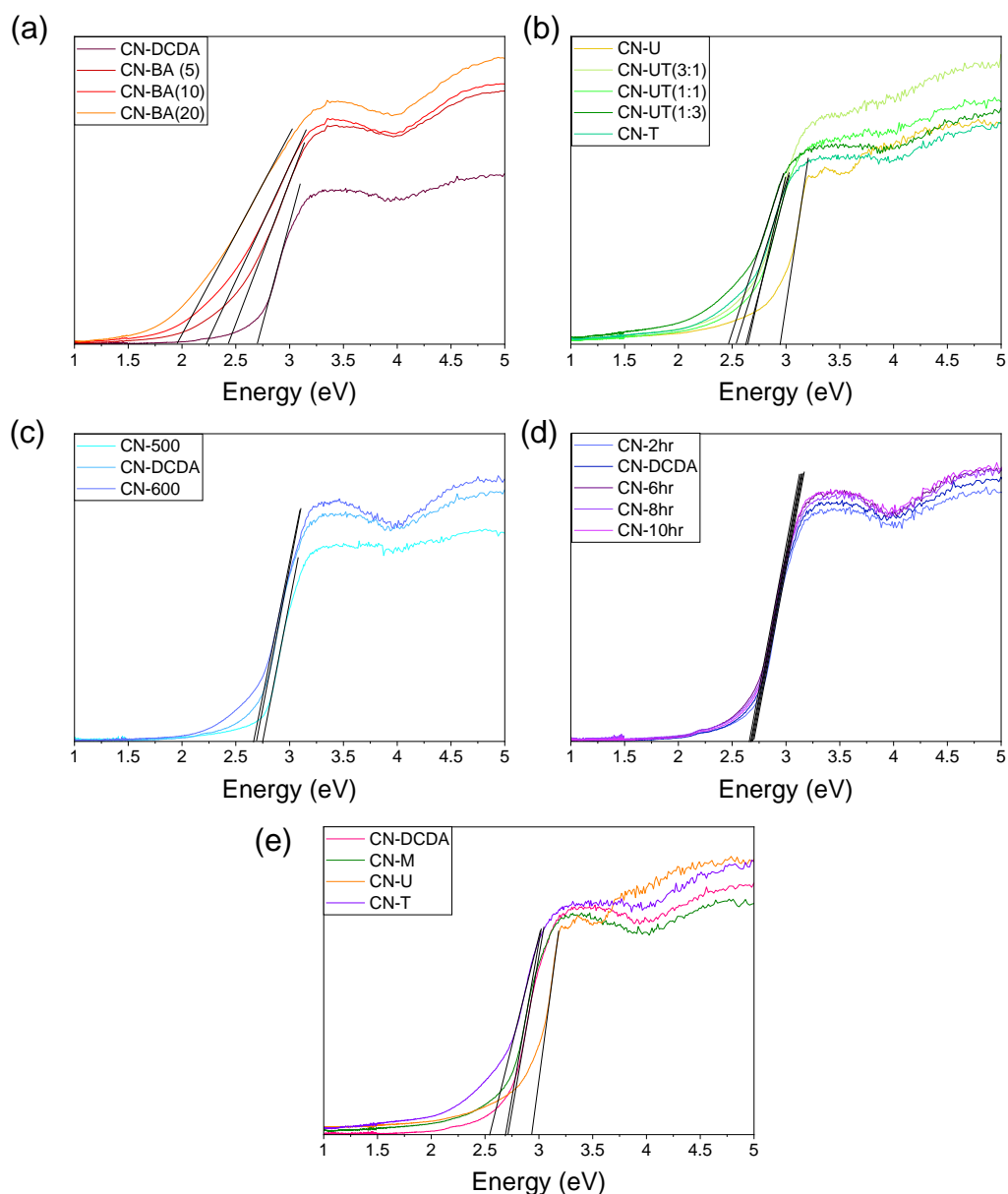


Figure 41 – Indirect Tauc Plots for (a) CN-BA, (b) CN-U:T, (c) CN-Temp, (d) CN-Time and (e) CN-Precursor series.

For the CN-BA series, it can be seen that with increasing amount of barbituric acid used, the band gap decreases significantly, from 2.69 eV for CN-DCDA down to 1.92 eV for CN-BA(20), which is reflected in the colour change across series (Figure 31) and agrees well with previous reports.^{50,91,125,92,111,112,115–117,119,122} It can also be seen that the light harvesting properties are enhanced as barbituric acid is incorporated into the structure. Materials synthesised under different calcination temperatures, show an extension of the absorption edge with increasing temperature, causing a small shift in the band gap from 2.76 eV (CN-500) to 2.64 eV (CN-

600), which has previously been reported.^{147,149–151} Once again, it can be seen that varying calcination time has had very little effect on the band gap of the materials

Table 16 – Indirect and direct band gaps for the carbon nitride materials obtained from Tauc plots.

Material	Band Gap (eV)	
	Indirect	Direct
CN-DCDA	2.69	2.90
CN-BA (5)	2.40	2.87
CN-BA(10)	2.21	2.80
CN-BA(20)	1.92	2.69
CN-M	2.67	2.87
CN-U	2.93	3.09
CN-UT(3:1)	2.62	2.90
CN-UT(1:1)	2.64	2.89
CN-UT(1:3)	2.49	2.79
CN-T	2.55	2.83
CN-500	2.76	2.94
CN-600	2.64	2.93
CN-2hr	2.72	2.91
CN-6hr	2.68	2.88
CN-8hr	2.69	2.90
CN-10hr	2.69	2.91

3.3.2 Photocatalytic Testing

3.3.2.1 Baseline Photocatalytic Activity

To determine baseline activity of the carbon nitride materials, they were initially tested for H₂ evolution under N₂ atmosphere in the presence of a hole scavenger. All carbon nitrides were tested on a scale of 2 mg of photocatalyst in 2 mL of hole scavenger in glass vials, purged with N₂ for 30 minutes then loaded onto the high throughput screening system (described in detail in Chapter 2) where they were exposed to illumination for about 4 hours. The high throughput set up consists of an array of white LEDs (~100 mWcm⁻²) allowing for testing of up

to 10 samples at once. In most cases only up to 5 different experiments were carried out at any one time to allow for testing in duplicate, due to the error in evolved gases found across positions during set-up development (see Chapter 2), hence the error bars in Figure 42. The holes scavenger used in these experiments was 10 mM ethylenediaminetetraacetic acid disodium salt (EDTA). The headspace of each experiment was then sampled and tested via GC injection to determine the quantity of gases evolved.

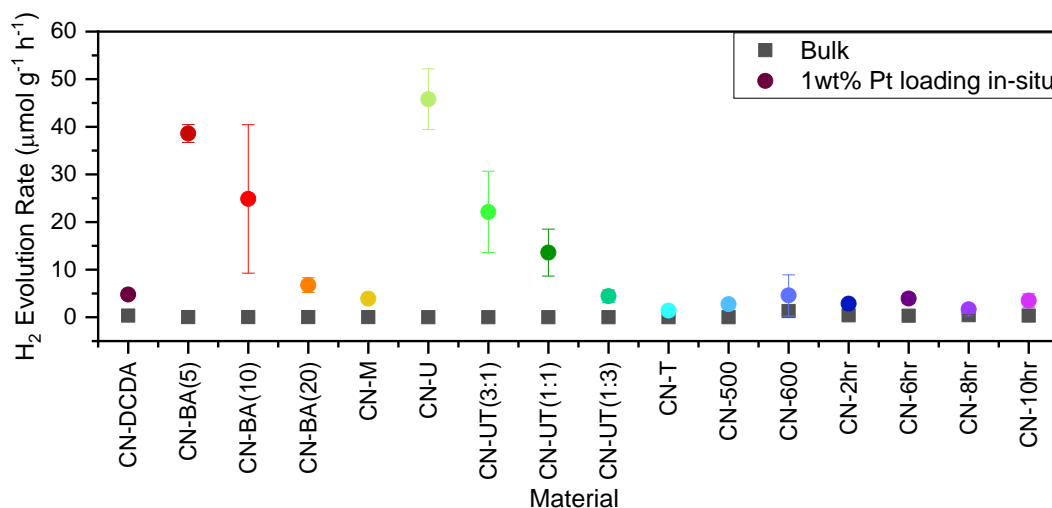


Figure 42 - Rate of H₂ evolved in μmol per gram of photocatalyst per hour for 2 mg of photocatalyst in 2 ml 10 mM EDTA with and without 1 μl H₂PtCl₆ (8 wt%) over 4 hours visible light irradiation at ~100 mWcm⁻² in a glass vial, tested on the screening set-up.

Baseline activity of the carbon nitride materials was determined and blank experiments showed no real activity, any gases evolved under these reaction conditions were due to scavenger degradation. The poor activity exhibited by these materials could be attributed to low surface area and high charge recombination rates. Due to this, samples were modified *in-situ* with a Pt co-catalyst (1 wt%) using chloroplatinic acid (H₂PtCl₆). This was done in the hopes of improving activity as Pt on the surface of a semiconductor can enhance charge separation, as well as lowering the overpotential for hydrogen formation from water at the surface of Pt.^{143,217,218} Results of photocatalytic H₂ evolution tests of the bulk and Pt modified materials can be found in Figure 42 and Table 17 and they show that addition of the Pt co-catalyst *in-situ* gives a large enhancement in photoactivity, as was expected.

Table 17 - Rate of H₂ evolved in μmol per gram of photocatalyst per hour for 2 mg of photocatalyst in 2 ml 10 mM EDTA with and without 1 μl H₂PtCl₆ (8 wt%) over 4 hours visible light irradiation at $\sim 100 \text{ mWcm}^{-2}$ in a glass vial, tested on the screening set-up.

Material	Rate of H ₂ evolution ($\mu\text{mol g}^{-1} \text{h}^{-1}$)	
	Bulk	1wt% Pt loading
CN-DCDA	0.359	4.773
CN-BA (5)	0.028	38.599
CN-BA(10)	0.024	24.854
CN-BA(20)	0.026	6.750
CN-M	0.026	3.900
CN-U	0	45.801
CN-UT(3:1)	0	22.126
CN-UT(1:1)	0	13.582
CN-UT(1:3)	0	4.444
CN-T	0	1.396
CN-500	0	2.758
CN-600	1.299	4.584
CN-2hr	0.410	2.865
CN-6hr	0.327	3.924
CN-8hr	0.419	1.663
CN-10hr	0.349	3.510

Variation in calcination time had a small effect on the photoactivity, but there appears to be no specific trend in photoactivity with the length of calcination time. As mentioned earlier there has been some discrepancies in the literature as to whether samples prepared at 550 or 600 are the better photocatalysts. Within these screening experiments it has been found that they both show similar levels of photoactivity towards H₂ evolution when platinised. But overall, the variation in photoactivity for samples synthesised under different calcination conditions is small and within error of the measurements. On the other hand, without the use of a Pt co-catalyst CN-600 showed much higher activity than any of the other samples but considering the activity of the platinised sample showing a similar level of activity to the other samples, this could have been due to some kind of experimental error or impurity. To confirm this result, photocatalytic test of the blank material would need to be repeated.

Both the CN-BA and CN- UT series show much greater variations. For the CN-UT series, photoactivity is highest for the CN-U material, with an activity of $45.801 \mu\text{mol g}^{-1} \text{h}^{-1}$ which gradually decreases with increasing thiourea content down to $1.396 \mu\text{mol g}^{-1} \text{h}^{-1}$ for CN-T. Previously it has been suggested that by mixing thiourea with other precursors a heterojunction can be formed and leads to improvement in activity over the pure precursors.^{85,138–140} However, it can be seen that there is a decrease in activity across the series, so it is unlikely that a heterojunction has been formed. On the other hand, for the CN-BA series, the activity initially increases with the addition of barbituric acid, but as more is added activity decreases again. To gain some understanding of these trends, the photoactivities of these materials were plotted against band gap and surface area, as seen in Figure 43.

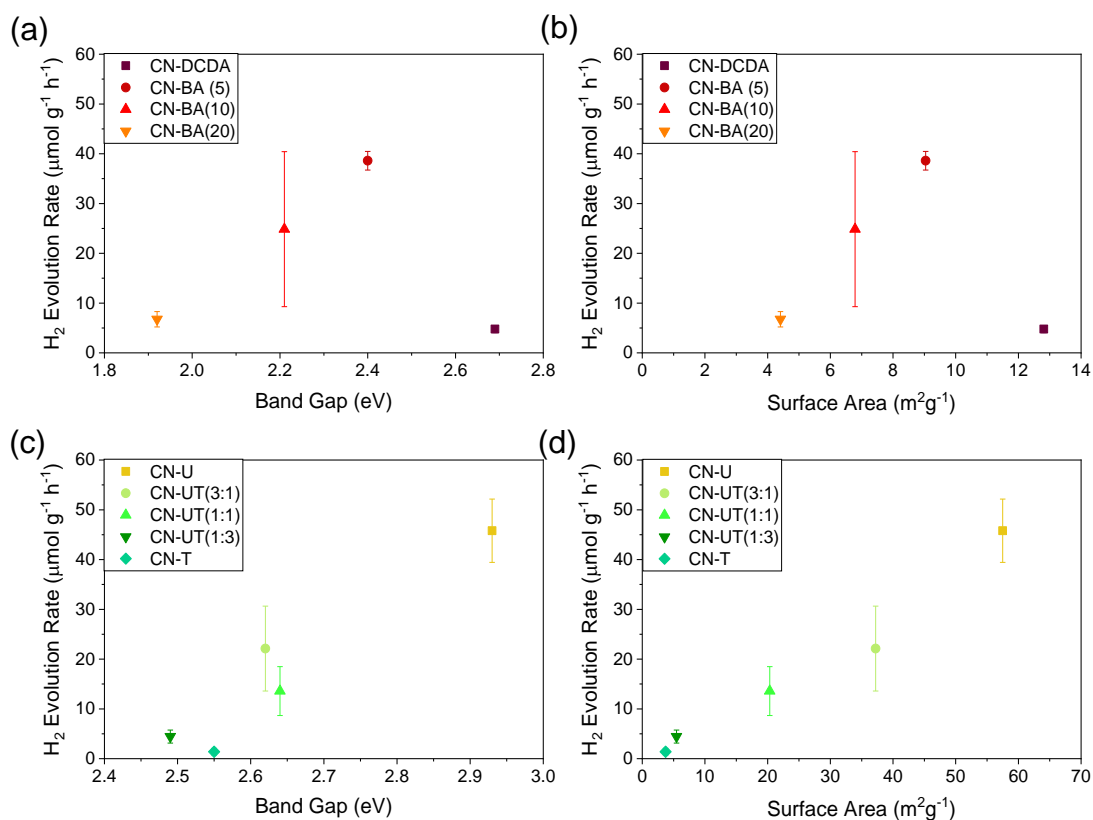


Figure 43 - Rate of H₂ evolution for the CN-BA ((a) and (b)) and CN-UT ((c) and (d)) vs band gap ((a) and (c)) and surface area ((b) and (d)).

As can be seen from Figure 43 (c) and (d), there is a strong correlation in the photoactivity of the materials in the CN-U:T series with both band gap and surface area. Normally an increase in band gap means a decrease in the portion of the light that the material can absorb and often

leads to a decrease in activity, but it also can mean a more negative conduction band with a greater driving force for the reduction reaction leading to an increase in activity. Additionally, an increase in surface area can give an increase in the number of active sites, increasing activity. Conversely the CN-BA series (Figure 43 (a) and (b)) shows no such trend with band gap or surface area. To understand the variation in photoactivity, further characterisation of the CN-BA series of materials is required and is discussed in the next section.

3.3.3 Time Resolved and Transient Studies

3.3.3.1 Steady-State Photoluminescence (PL) and Time-Resolved Emission Lifetime spectroscopy

PL and emission lifetime spectroscopy measurements were undertaken to understand the process of charge separation and transfer within the samples. PL emission is mainly associated with recombination of photogenerated charges or excitons and can be used to understand differences in charge recombination in different samples.^{63,74,112,138,159,168,219,220} However, care must be taken when comparing emission intensities as the measurements were performed without a solid-state emission standard.

The steady-state emission spectra of CN-BA series powders can be seen in Figure 44 (a). CN-DCDA shows a strong broad PL emission around 464 nm, which is typical for most bulk carbon nitrides.^{6,63,168,219,221,222} Upon the addition of barbituric acid this emission maxima then red shifts to 490 nm, which correspond with the decrease in the band gap.¹¹² Interestingly, as more barbituric acid is incorporated the PL emission shifts but only by a very small amount.

It appears that by increasing the amount of barbituric acid in the precursor mixture, that the PL emission is suppressed.¹¹² This is usually reported to indicate a reduction in charge recombination rates inferring enhanced charge lifetimes, but could also indicate disruption of the conjugated system, which could lead to low charge mobilities and therefore lower recombination rates.^{78,112,159,167,168,177}

Time resolved PL can give information on the lifetimes of free charges that lie near band edges, that recombine to emit light, rather than deep lying states.²²³ The radiative lifetimes for

each of the materials were determined by fitting the time-resolved fluorescence spectra to a 4-term exponential function corresponding to 4 emissive charge lifetimes (see Chapter 2 for details). The fitted spectra can be found in Figure 44 (b) and the charge carrier lifetimes can be found in Table 18.

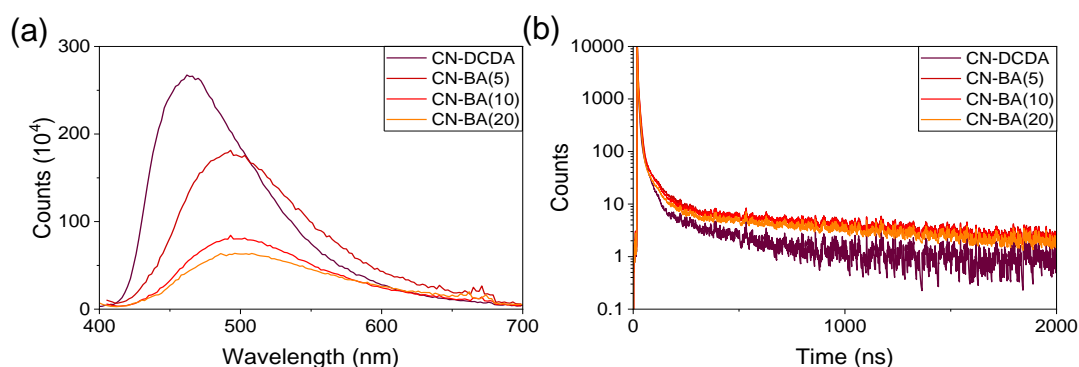


Figure 44 –(a) steady state PL emission spectra and (b) time-resolved emission spectra for CN-DCDA, CN-BA(5), CN-BA(10) and CN-BA(20). Excitation at 390 nm for steady-state PL emission. For time-resolved emission, excitation at 371 nm, monitoring emission at, 465, 485, 495 and 495 nm for CN-DCDA, CN-BA(5), CN-BA(10) and CN-BA(20), respectively.

Table 18 – Emission maxima and charge lifetimes for the CN-BA series.

Material	PL Emission Peak (nm)	$\tau_1^{[a]}$ (ns) (A ₁ (%))	τ_2 (ns) (A ₂ (%))	τ_3 (ns) (A ₃ (%))	τ_4 (ns) (A ₄ (%))	AWAL ^[b] (ns)
CN-DCDA	460	1.16 (75.87)	5.09 (22.76)	30.10 (1.32)	262.10 (0.05)	2.57
CN-BA(5)	491	1.45 (75.83)	7.81 (23.49)	60.96 (0.63)	1148.00 (0.05)	3.86
CN-BA(10)	495	1.32 (74.59)	7.06 (24.54)	49.30 (0.83)	1088.50 (0.05)	3.66
CN-BA(20)	498	1.18 (78.55)	6.90 (20.78)	50.56 (0.63)	1060.00 (0.04)	3.10

[a] Emission lifetimes determined by fitting time resolved emission spectra to a 4-component exponential, see section 2.3.9.

[b] Amplitude weighted average lifetimes (AWAL)

With the addition of barbituric acid in the CN-BA(5) sample, the charge carrier lifetimes are all significantly extended, especially that of the long charge lifetimes, which is almost 6 times longer than that of CN-DCDA. This increase in lifetime can improve the probability that charges

will be able to transfer to other species to perform redox reactions before they recombine.^{68,138} This enhancement in charge lifetimes could be due to disruption in conjugation due to the incorporation of extra carbon into the CN heterocycles or increased defect concentration, which can lead to lower charge mobility or can act as trap states extending lifetimes. It is also reflected in the enhanced photocatalytic activity of CN-BA(5) over the other materials in the series.

As more BA is incorporated, the produced carbon nitrides have enhanced lifetimes over the CN-DCDA, but lifetimes begin to decrease again. The reduction in the emission intensity, infers reduced recombination, likely due to enhanced lifetimes, but the lifetimes demonstrate that this is not the case. Instead, a fraction of the charge recombination must be occurring through less or non-radiative decay from the excited state, which may have been caused by localisation to new states introduced by the BA.^{75,111,124,202,224–226}

Previously it has been reported that these emissive states exist in the carbon nitride bulk and are in fact separate to the states responsible for photocatalysis at the surface.²²⁷ This was found by measuring the emission spectra and lifetimes of carbon nitride in the presence and absence of sacrificial donors. To further understand if these emissive states are linked to photocatalytic charge transfer, these measurements should be performed in the presence of scavengers.

3.3.3.2 Transient Absorption (TA) Spectroscopy

Much in the way that time resolved photoluminescence spectroscopy looks at the radiative lifetimes of charges, transient absorption spectroscopy is a powerful tool which can be used to understand photogenerated charges radiative, less-luminescent and non-emissive lifetimes over different time scales.^{153,228–232} A number of studies have utilised TA spectroscopy to gain insight into the nature and lifetime of photogenerated charges in carbon nitrides.^{118,153,234–236,223,227–233} TA spectra in this work were recorded in diffuse reflectance mode on powder samples in air, with an excitation wavelength of 355 nm on microsecond-second timescales, monitoring the visible (450-900 nm) region. Details of experimental set-up can be found in Chapter 2. The TAS spectra of the 4 materials in the CN-BA series can be found in Figure 45.

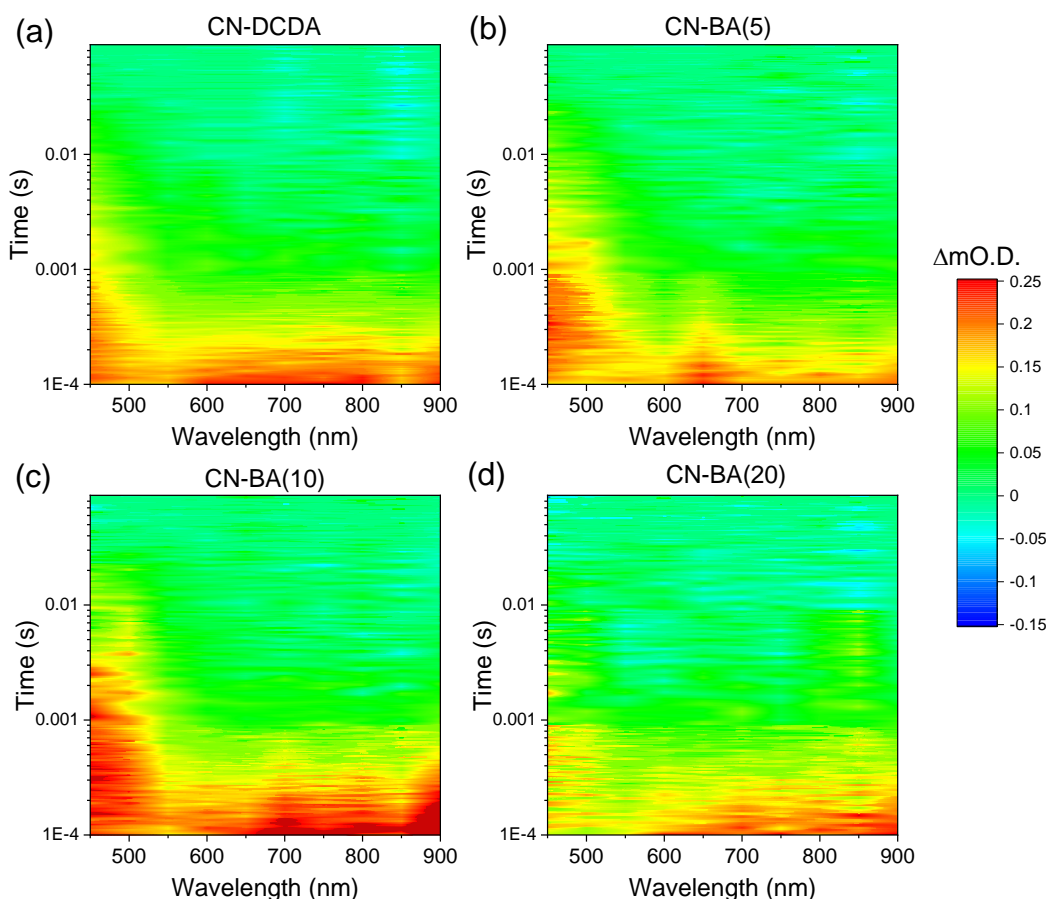


Figure 45 - TAS contour plots (0.1ms - 0.1 s) for (a) CN-DCDA, (b) CN-BA(5), (c) CN-BA(10) and (d) CN-BA(20).

As can be seen in Figure 45 , on timescales greater than 0.1 ms, 2 positive features emerge. Each of the spectra in Figure 46 show positive adsorption features at about 450 nm and 800 nm. It is generally reported that positive features which lie within the visible-near IR (400-3000 nm) region can be assigned to deeply trapped photogenerated electrons and/or holes or charge pairs, whilst features found in the mid IR regions (3000-10000 nm) are free or shallowly trapped charges.^{153,227,232,235,236} The longer lived broad positive feature at around 800 nm can be assigned to photogenerated electrons in deep trap states, in agreement with the literature.^{228–231,237,238} Previously it has been reported that a positive feature at ~510 nm in a carbon nitride material has been assigned to photogenerated holes, which could potentially be assigned to the positive feature at ~450 nm.²³⁸ However, to confirm these assignments, further measurements in the presence of electron and hole scavengers would be required.

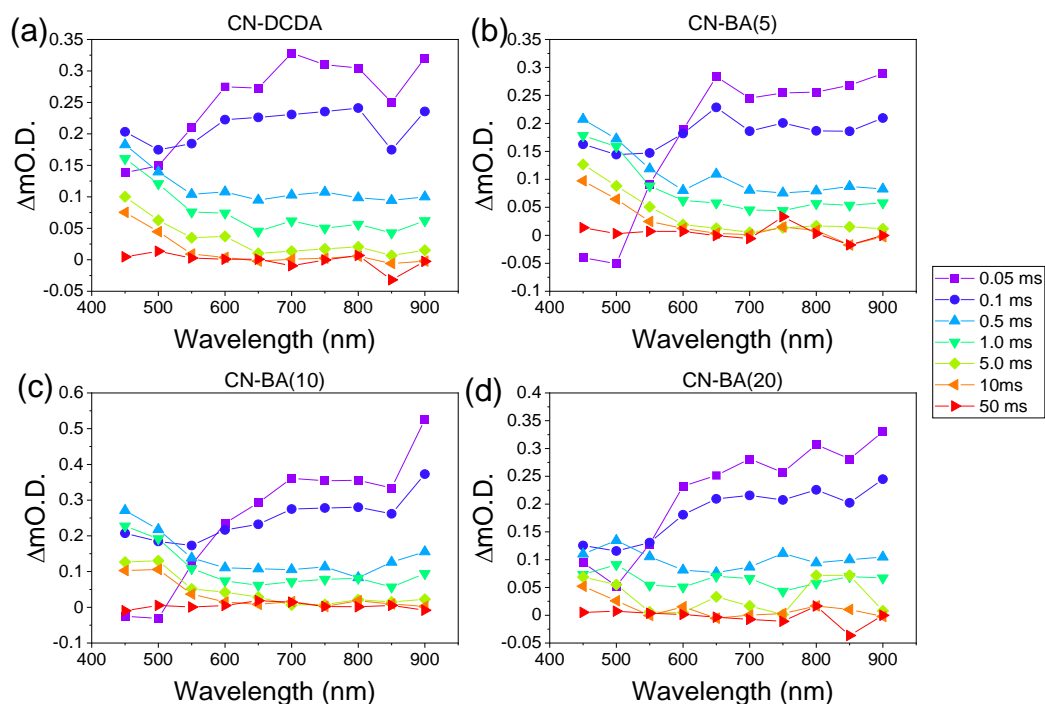


Figure 46 -TAS Spectra – wavelength vs the change in optical density at specific time scales (0.05ms to 50ms) for (a) CN-DCDA, (b) CN-BA(5), (c) CN-BA(10) and (d) CN-BA(20).

The lifetimes of the charges at each of these features can be determined by fitting the decay kinetic spectra (Figure 47) to exponential functions, the values of which can be found in Table 19. However, because of a strong negative feature, which is likely due to laser related scatter overlapping with the weak positive features Δ at around 450 nm, the lifetimes of the positive feature could only be fit from 0.1 ms onwards. Generally, the amplitude weighted average lifetime for each of the features (Table 19 and Figure 48) show that addition of barbituric acid into the structure, causes an initial increase in charge lifetime, but upon further addition the lifetimes decrease again, much like the PL emission lifetimes. This could be indicative of the formation of a greater concentration of defects, which act as recombination centres. Also, the trends in lifetimes for these three materials agree quite nicely with the photocatalytic activity for H₂ evolution.

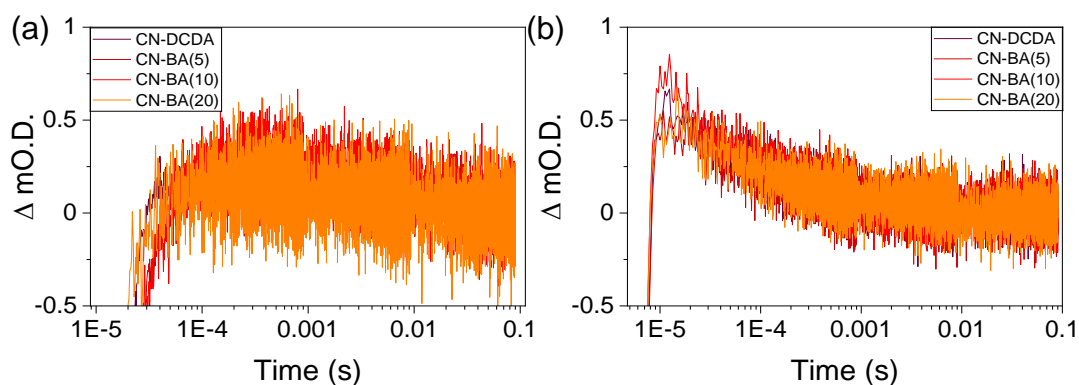


Figure 47 – Decay kinetics of CN-DCDA, CN-BA(5), CN-BA(10) and CN-BA(20) for (a) the positive feature at 450 nm and (b) the positive feature at 800 nm.

Table 19 – Charge lifetimes determined by exponential fit of the TA decay spectra.

Feature	Lifetime	Sample			
		CN-DCDA	CN-BA(5)	CN-BA(10)	CN-BA(20)
450 nm (positive)	$\tau_{1[a]}$ (ms) (A_1 (%))	0.75 (38.94)	1.75 (22.72)	2.96 (45.45)	22.93 (54.98)
	τ_2 (ms) (A_2 (%))	11.75 (61.06)	22.01 (77.28)	29.10 (54.55)	2.11 (45.02)
	AWAL ^[b] (ms)	7.47	17.41	17.22	13.56
800 nm (positive)	τ_1 (μ s) (A_1 (%))	13.42 (66.80)	31.33 (60.09)	18.65 (62.89)	31.99 (63.79)
	τ_2 (μ s) (A_2 (%))	145.88 (32.97)	296.51 (28.94)	174.18 (22.84)	253.57 (34.35)
	τ_3 (μ s) (A_3 (%))	5490.00 (0.23)	2370.00 (10.97)	1200.00 (14.27)	1210.00 (1.86)
	AWAL (μ s)	69.60	364.54	222.80	129.98

[a] Decay kinetics lifetimes determined by fitting time resolved emission spectra to a 2 or 3-component exponential, see section 2.3.10.

[b] Amplitude weighted average lifetimes (AWAL)

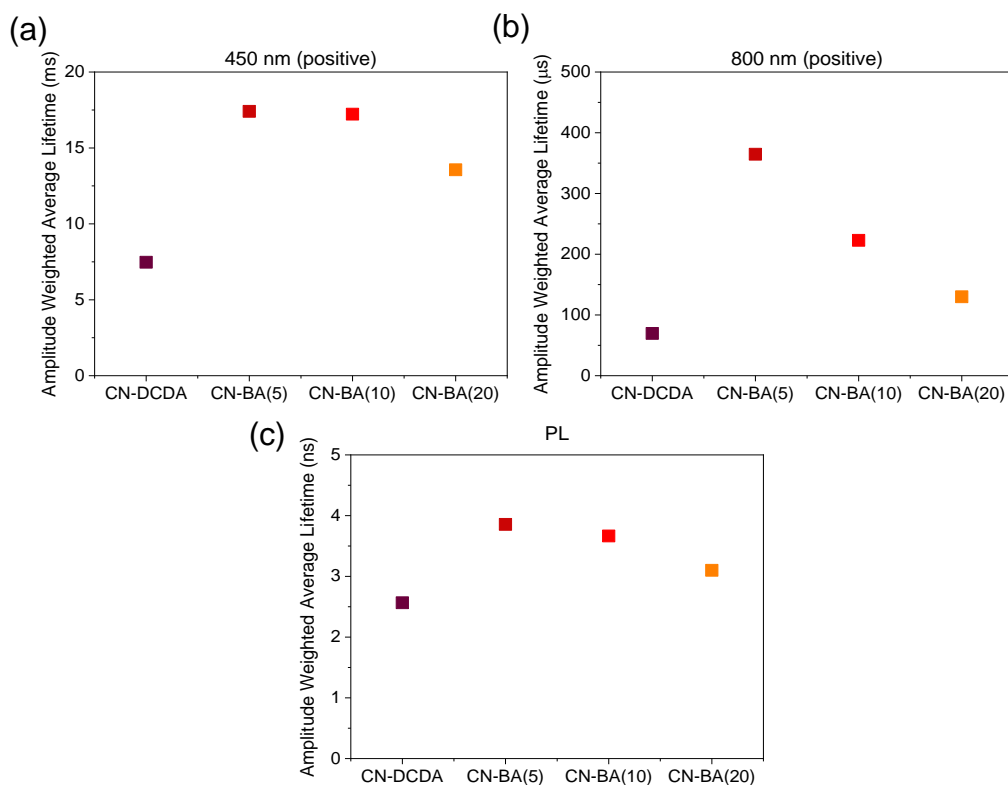


Figure 48 – Comparison of charge lifetimes of CN-DCDA, CN-BA(5), CN-BA(10) and CN-BA(20) for the (a) the positive feature at 450 nm, (b) the positive feature at 800 nm and (c) PL emission.

3.3.3.3 Raman Spectroscopy

Fourier Transform (FT) Raman Spectroscopy

Raman spectroscopy is a complementary method which can be used alongside infrared spectroscopy.^{186,188,189,239,240} Often in the literature, carbon nitride Raman spectroscopy uses lasers which lie within the UV or visible region and excite the material leading to strong emission which swamps the weaker Raman signal.²⁴⁰ FT-Raman usually utilises a near-IR laser (1064 nm) which greatly reduces this strong emission as the Raman probe is at a lower energy than the optical gap.^{189,241} FT and Kerr-gated (KG) Raman, along with time-resolved resonant Raman (TR³) experiments described later in this chapter, were recorded at the ULTRA laser facility (STFC Central laser Facility, Rutherford Appleton Laboratories) with the help of Dr Igor Sazanovich and Dr Gaia Neri. Further details of the KG Raman and TR³ experiment and the basics behind it can be found in Chapter 2.

The FT-Raman spectra for the CN-BA series of materials can be seen in Figure 49 and despite the use of a 1064 nm Raman probe they still show a significant level of emission. Therefore, the data is also presented following subtraction of a polynomial function, Figure 50.

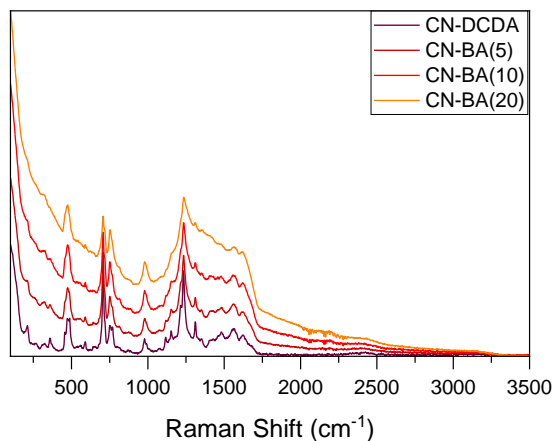


Figure 49 - FT Raman spectra of CN-DCDA, CN-BA(5), CN-BA(10) and CN-BA(20).

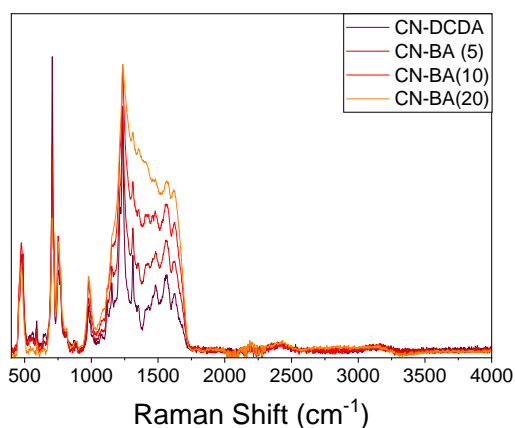


Figure 50 – Manually baselined FT Raman spectra of CN-DCDA, CN-BA(5), CN-BA(10) and CN-BA(20).

Carbon nitride Raman spectra are not reported as often as other characterisation measurements such as XPS and FTIR spectroscopy and when Raman spectra are shown, often peak positions and assignments are not reported, which makes definitive assignment here challenging. This is likely in part due to emission swamping the Raman signals on typical equipment but also due to strong overlapping of species in similar regions much like with IR spectroscopy. Table 20 lists the vibrational mode positions from Figure 50, alongside reported characteristic modes, assignments within the literature and potential assignments for those regions. Sometimes, a list of the characteristic peaks are reported for carbon nitride materials,

as can be seen in Table 20, and only occasionally are they given any further assignment.^{45,63,242–246}

Table 20 – Raman assignments for the CN-BA series of materials spectra in Figure 50.

Raman Shift Region (cm ⁻¹)	Approximate Raman Shift (cm ⁻¹) [a]	Reported Characteristic Shifts (cm ⁻¹)	Assignment
~400-700	475 (s) 558 (w) 590(s)	470 ^{45,63,242–246} 550 ^{45,242} 590 ^{242–246}	Unassigned
~600-900	650 (w) 706 (s) 753 (s)	705 ^{45,63,242–246} 750 ^{45,63,242–246}	In-plane bending of triazine/heptazine rings ^{189,211,241,242,246–249}
~900-1300	813 (w) 877 (w) 979(s) 1116 (s) 1153 (s) 1235 (s)	980 ^{242–246} 1150 ^{242,243,246} 1250 ^{45,63,242–246}	Symmetric N-breathing mode ^{55,189,211,241,246,247,249} sp ² C / C-N / C=N / N-C=N ^{45,131,188,189,245}
~1300-1700	1310 (s) 1353 (s) 1415 (w) 1480 (s) 1560 (s) 1619 (s)	1480 ^{45,242–246} 1570 ^{45,242,244} 1620 ^{45,63,242–246}	D and G Bands ^{55,102,105,142,208,246–250} sp ² C / C-N / C=N / N-C=N ^{75,188,189,245,251,252}
~2300	-	-	-C≡N / -N=C=N- ^{180,186,188,189,204,208,241,249,252}
~3200	-	-	NH _x / water ^{188,189}

[a] peak descriptions: s = strong, ms = medium, w = weak, vw = very weak, b = broad, sh = shoulder

Potential assignments for that region are italicised.

The vibrational modes at approximately 705 cm⁻¹ and 750 cm⁻¹ are typically assigned to the in-plane bending of C-N-C linkages within triazine or heptazine rings^{189,211,241,242,246–249} and the mode at 980 cm⁻¹ is attributed to the symmetric N-breathing mode within triazine or heptazine rings.^{55,189,211,241,246,247,249} Peaks within the 1300-1700 cm⁻¹ region are often said to resemble the D and G bands within graphitic materials.^{55,102,105,142,208,246–250} But it is likely that the modes which lie between 1100-1700 cm⁻¹ could be assigned to a range of things including; sp² C, C-N, C=N and N-C=N stretches.^{45,75,131,188,189,245,251,252}. Sometimes very broad and very weak

peaks at higher wavenumber are observed within the Raman spectra, around 2300 cm^{-1} , peaks are assigned to $-\text{C}\equiv\text{N}$ or $-\text{N}=\text{C}=\text{N}$ -^{180,186,188,189,204,208,241,249,252} and around 3400 cm^{-1} can be attributed to N-Hx groups or adsorbed water.^{188,189}

The CN-BA series all show the same vibrational modes, without any significant shift in position across the series. However, we do see clear differences between samples with a variation in intensity and width of peaks. As more barbituric acid is added, the peaks between 1100 and 1700 cm^{-1} become broader, decreasing the resolution of close lying vibrational modes and the intensity of the Raman scattering of these modes also increases from CN-DCDA down to CN-BA(20) (Figure 50). These modes are typically assigned to the ring (sp^2) modes and the increased scattering correlates with an expected increase in disorder of the carbon nitride structure due to the increased amount of barbituric acid being incorporated into the structure. Increased Raman scattering is sometimes used as an indicator of increased delocalisation of electrons within organic polymers, however further studies would be required to confirm this hypothesis.^{253,254} Interestingly the vibrational mode centred at 705 cm^{-1} , decreases in intensity with increasing BA content. A similar mode was also observed in the DRIFTS data (Figure 36) and was assigned to the disruption of the breathing modes of the triazine/ heptazine rings.

Time-Resolved Resonance Raman Spectroscopy (TR³)

TR³ can be used to obtain both chemical and structural information about a material in its excited state and can help to understand the role of different species or groups within the carbon nitride structure in photocatalysis and identify the vibrational spectra and lifetimes of sites where charge accumulation occurs.^{255–258} A number of different time-resolved spectroscopies have been employed for study of carbon nitride excited states, but so far no one has been able to provide evidence of the chemical nature of this excited state. TR³ can be used to measure the ground state Raman spectrum of a sample at different time delays after an appropriately timed excitation pulse. Subtraction of the ground state spectrum from the spectrum at each delay gives the difference spectrum. This should show how different peaks or groups evolve over time and should indicate the formation of new species due to the formation of photogenerated charges sitting on different groups in the carbon nitride structure.

To the best of our knowledge TR³ has not yet been employed for study of carbon nitride materials.

Although FT-Raman can be effective at reducing the effect of emission, it suffers from lower sensitivity as it does not allow for resonance enhancement and measurement of transient Raman spectra is extremely challenging using FT approaches.^{256,258,259} An alternative way to record Raman spectra of highly emissive materials is to make use of a Kerr-gate.^{240,256–258,260–264} Kerr-gated Raman spectroscopy uses the different timescales of Raman scattering and emission after an incident probe pulse on the sample to block emission. For the purposes of this thesis Raman scattering can be considered to be an effectively instantaneous process. In contrast, generation of an emissive state often occurs on the picosecond (ps) timescale and its radiative decay can persist for microseconds or longer. The Kerr-gate, which acts as an ultrafast gating system, can switch between open/closed to only allow the Raman signal to reach the detector.

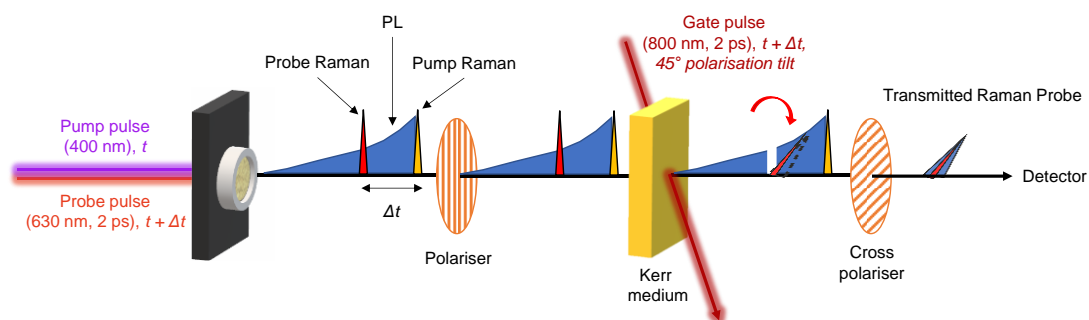


Figure 51 – Schematic representation of Kerr-gated TR³ Spectroscopy experimental set-up, adapted from the Central Laser Facility website <https://www.clf.stfc.ac.uk/Pages/Kerr-Gated-Raman-Spectroscopy.aspx> and applicable publications.^{240,264}

Figure 51 shows the scheme of a TR³ experiment that makes use of a Kerr-gate. In the time resolved experiment a laser pump pulse (400 nm in all the results discussed here) excites the sample which leads to both Raman scatter and emission from the sample. A 2nd laser pulse (Raman probe, here 630 nm unless stated otherwise) is then delivered to the sample at a time period after the pump laser (Δt). A probe wavelength of 630 nm was chosen as it was expected to overlap with the excited state of the carbon nitride materials, determined by TAS measurements (3.3.3.2). The Raman probe also causes Raman scattering (which are the desired photons for detection) and often emission. All scattered light and emission from the

sample is passed through a linear polariser and then the Kerr medium. Under intense illumination (here 800 nm is used) the Kerr medium transiently aligns and the CS₂ rotates the incident polarised light (scatter and emission from the sample) by 90°. When the Kerr medium is aligned, light can therefore be transmitted-through the cross-polariser to the detector. However, in the absence of the intense 800 nm light the Kerr medium rapidly (ps) relaxes. Therefore, using an appropriately timed, high intensity, laser pulse the Kerr-gate is effectively 'open' for only a short period of time, allowing the desired Raman signal to pass through and the longer-lived signal is blocked. Using the same apparatus, a ground state Kerr-gated Raman signal can be recorded by setting the experiment so that the Raman probe pulse arrives in advance of the pump laser pulse.

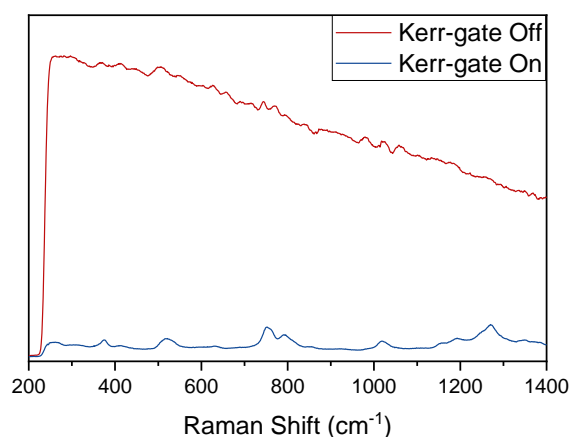


Figure 52 – CN-DCDA Raman spectra measured with and without the Kerr-gate.

Figure 52 shows the ground state Raman spectra for CN-DCDA with the Kerr-gate 'on' and 'off' and clearly shows that the Kerr-gate is very effective at removing the majority of the emission, providing clear ground state Raman spectra. Then we compared the ground state Raman spectra using both the KG apparatus and the commercial FT-Raman spectrometer to confirm that similar data was obtained (Figure 53).

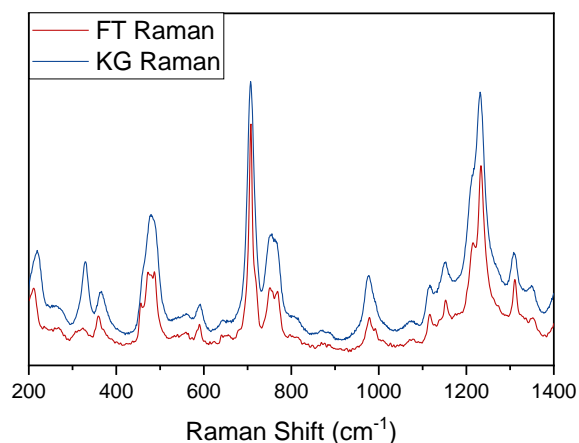


Figure 53 – Comparison of Raman spectra obtained for CN-DCDA via FT-Raman and TR³ experiments.

However, a small amount of emission was not removed by the KG and the presence of this complicates any TR³ experiment as emission arising from the pump (400 nm) and probe (630 nm) pulses will have different time dependencies. Attempts were made to manually subtract residual emission (by fitting to a polynomial function) after data acquisition. This was partially successful but as the overlap of the Raman probe wavelength (630 nm) with the ground state UV-vis spectrum increased with the barbituric acid containing samples, the possibility of manually introducing artefacts increases through the series of CN-BA(5), CN-BA(10) to CN-BA(20).

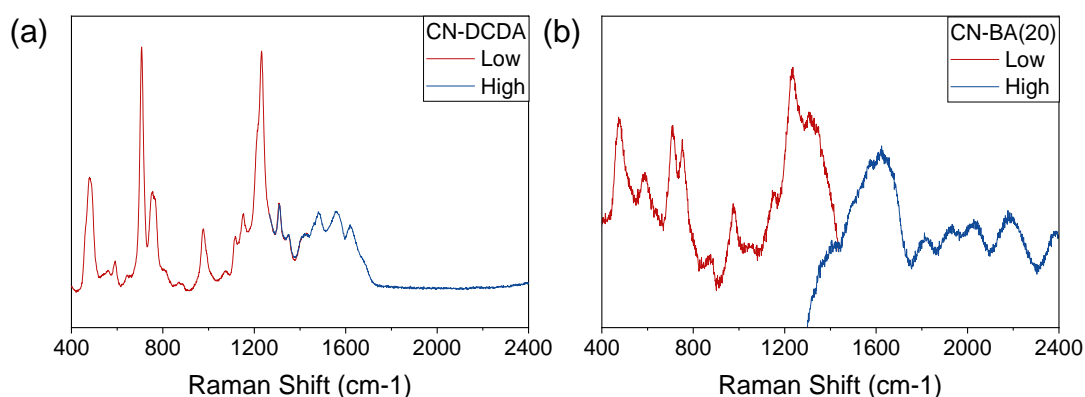


Figure 54 - KG Raman ground state spectra for (a) CN-DCDA and (b) CN-BA(20) over the low and high wavenumber window after emission subtraction and baselining.

A further complication is that the design of the KG experiment requires the Raman spectra to be measured over two spectral windows: 400-1440 cm⁻¹ and 1260-2400 cm⁻¹. Manual subtraction of a polynomial worked well for the low wavenumber window, but it was found that

the tendency to introduce artefacts was greater in the higher wavenumber window (Figure 54 (b)). As this is the first study we have initially focussed on the low (400 to 1300 cm^{-1}) wavenumber window of the TR^3 to avoid possible artefacts from the baselining process being mistaken for an excited state vibrational mode

Shown in Figure 55 is the difference spectrum for the TR^3 experiment of CN-DCDA, CN-BA(5), CN-BA(10) and CN-BA(20). From close analysis of the difference spectra, there does not appear to be the formation of any clear transient (positive) peaks. A bleaching (decrease) of the ground state Raman spectrum is however observed due to the formation of the excited state after exposure to an excitation pulse. As the sample returns to the ground state over time the sample signal recovers. As the TR^3 experiment monitors both emissive and non-emissive states that evolve over time after excitation it can provide complimentary information to emission spectroscopy, which by definition can only probe emissive excited states.

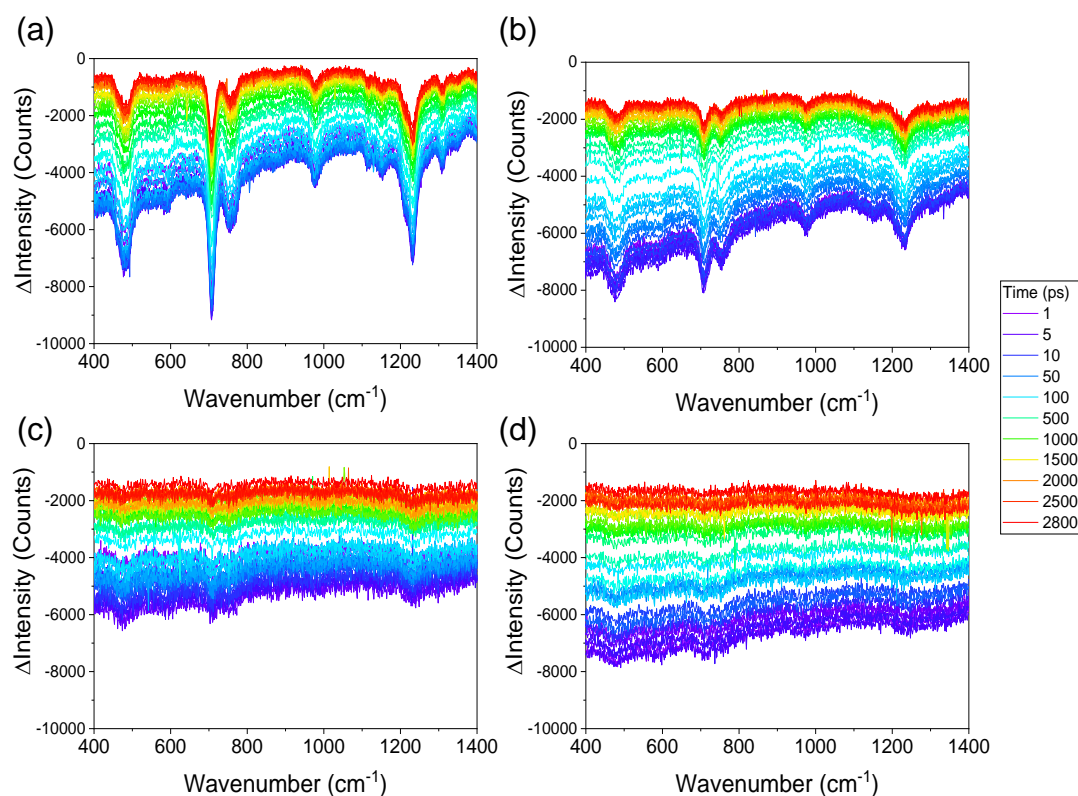


Figure 55 -Difference spectrum for (a) CN-DCDA, (b) CN-BA(5), (c) CN-BA(10) and (d) CN-BA(20) for time delays between 1 ps and 2800 ps.

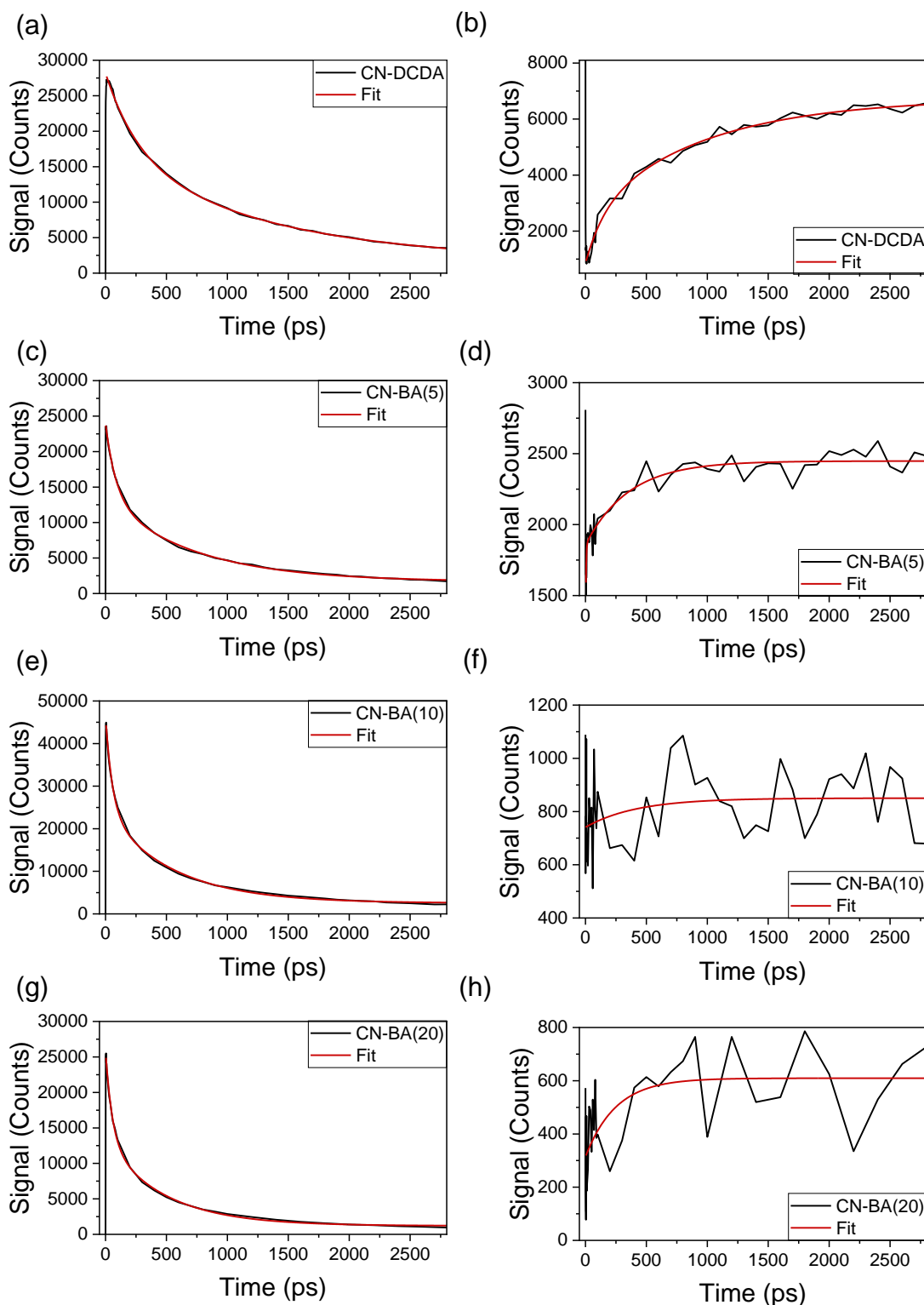


Figure 56 – Emission (left) and Raman bleach (right) kinetics for CN-DCDA ((a), (b)), CN-BA(5) ((c), (d)), CN-BA(10) ((e), (f)) and CN-BA(20) ((g), (h)).

Figure 56 show a series of spectra for the full range of BA samples. They show that as the BA content increases the magnitude of the TR³ bleaches decreases despite all samples being excited with the same intensity (400 nm) pump laser. This indicates that the excited states

formed at high BA concentrations have similar excited state Raman spectra to the ground state. In addition to being able to record the TR³ data, the Kerr-gated apparatus can also be used to obtain the ultrafast (ps time resolution) emission spectra. As the emission at each wavelength is fairly similar only the emission at 646 nm is explored in this work. The intensity of the emission recorded at 646 nm (see Figure 56) is roughly constant confirming that excited states are being generated with all samples.

To explore the lifetime of the emissive states the kinetics at 646 nm have been fitted to a sum of exponential functions (2 functions were found to be sufficient to achieve an adequate fit in this case), Figure 21. Across the series, the amplitude weighted average lifetime of emission (AWAL) decreases for the emission kinetics from CN-DCDA to CN-BA(20). This data, recorded on the picosecond timescale, is not in agreement with slower lifetime measurements determined by time-correlated single-photon counting PL (Figure 44, Table 18) and TAS (Figure 47, Table 19) measurements, which may be because it is tracking a different emissive state, a portion of which goes on to form the states seen in the conventional PL measurements, or that the short (~1 ps) intense laser pulse at 400 nm is giving rise to differing photophysical pathways.

The kinetics of the Raman bleach of the 480 cm⁻¹ vibrational mode for each sample can be seen in Figure 56. The bleach kinetics at each vibrational mode were similar, so only the 480 cm⁻¹ band is shown here. Comparison of the kinetics of the Raman bands, as more barbituric acid is added to the sample, was complicated by the relatively low signal:noise ratios at high barbituric acid concentrations. Despite this, two interesting features can be identified. Firstly, comparison of the emission and bleach kinetics of each sample clearly shows they are quite different, this indicates that the TR³ bleach data contains contributions from a non-emissive excited state. Secondly, as the barbituric acid goes from 0 to 5% we find that the lifetime of the TR³ bleach decreases significantly but between 5 and 10% it increases again. The change in lifetime of the TR³ state at 10 and 20% barbituric acid should be interpreted with caution, however it is interesting to note that the decrease in lifetime of the Raman bleach mode correlates with an increase in observed photocatalytic activity.

Table 21 – Emission and bleach lifetimes determined by exponential fit of the TR³ emission and bleach spectra.

Sample	Emission Kinetics		Bleach Kinetics	
CN-DCDA	$\tau_1^{[a]}$ (ps)	262	τ_1 (ps)	152
	(A_1 (%))	(41)	(A_1 (%))	(30)
	τ_2 (ps)	1279	τ_2 (ps)	957
	(A_2 (%))	(59)	(A_2 (%))	(70)
	AWAL ^[b] (ps)	859	AWAL (ps)	718
CN-BA(5)	τ_1 (ps)	87	τ_1 (ps)	4
	(A_1 (%))	(47)	(A_1 (%))	(56)
	τ_2 (ps)	729	τ_2 (ps)	354
	(A_2 (%))	(53)	(A_2 (%))	(44)
	AWAL (ps)	425	AWAL (ps)	158
CN-BA(10)	τ_1 (ps)	57	τ_1 (ps)	419
	(A_1 (%))	(51)		
	τ_2 (ps)	556		
	(A_2 (%))	(49)	(A_1 (%))	(100)
	AWAL (ps)	302		
CN-BA(20)	τ_1 (ps)	56	τ_1 (ps)	249
	(A_1 (%))	(52)		
	τ_2 (ps)	482		
	(A_2 (%))	(48)	(A_1 (%))	(100)
	AWAL (ps)	262		

[a] Emission and bleach kinetics lifetimes determined by fitting time resolved emission spectra to a 1 or 2-component exponential, see section 2.3.11.

[b] Amplitude weighted average lifetimes (AWAL)

In order to further explore these result experiments were attempted to measure TR³ spectra in the presence of solutions and hole scavengers (water, KCl, MeOH and TEOA), but unfortunately no change was observed and due to limited time at the Central Laser Facility, this was not studied further. Therefore, although these initial studies show that TR³ can be used to probe the kinetics of non-emissive states, it is unfortunately not possible to identify the chemical nature of the states as had been hoped. However, it does indicate that the carbon nitride structure is highly complex and that after excitation there are a plethora of new states,

which cannot be differentiated from the ground state due to broad Raman signals. Also, this could suggest that the charges are not accumulating on any specific group but are instead dispersed across the entire structure.

3.3.4 Band Structure Determination

Determining the band structure of materials can also help to understand trends in photocatalytic activity. A number of different combinations of methods have previously been used to determine the band structure of carbon nitride materials, mainly via the use of UV-Vis combined with either the Mott-Schottky method^{25,50,160,166,204,221,224,229,243,248,265,266,75,267–276,84,277,87,91,94,119,132,139}, XPS^{69,74,272,278–282,95,125,140,169,219,221,222,229}, or both^{75,80,94,125,229,271,272,275,283}.

3.3.4.1 Mott-Schottky (MS) Method

Across all the series of materials we can see larger differences in band gap and therefore electronic structure. Traditionally, the Mott-Schottky method has been used to find the flat band potential of materials to calculate the band structure of semiconductors, including carbon nitride.^{25,50,160,166,204,221,224,229,243,248,265,266,75,267–276,84,277,87,91,94,119,132,139} A number of methods were undertaken to produce uniform films, including chemical vapour deposition from DCDA and drop-casting/doctor-blading slurries of carbon nitride with different solvents and binders to obtain uniform, conductive and stable films.

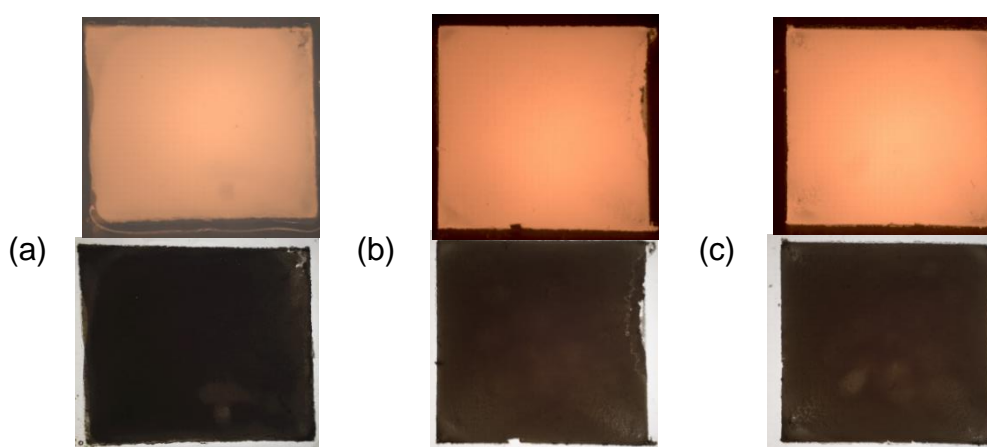


Figure 57 - Images of films prepared via drop-casting. (a) film 1, (b) film 2 and (c) film 3. Top: front lit. Bottom: back lit.

Finally, it was determined that drop-casting 200 μL slurries of CN-DCDA in acetone with Nafion (20 mg carbon nitride in 1 mL acetone and 50 μL Nafion (5 wt% solution)) led to the most reproducible and uniform films as can be seen from the images in Figure 57 taken on an optical microscope. These films were then used as the working electrodes for electrochemical measurements using the Mott-Schottky method, details of which can be found in Chapter 2.

Generally, the Mott-Schottky method is used to determine the flat band potential of carbon nitride materials and from this information band positions can be determined. Within the carbon nitride literature, some state that the flat band potential is the same as or very close to the conduction band position, so assume that they are the same thing.^{75,84,267,271,276,87,119,132,160,166,243,248,266} Others say that it is the fermi level which lies 0.1 - 0.2 V below the conduction band.^{265,274,275,283}

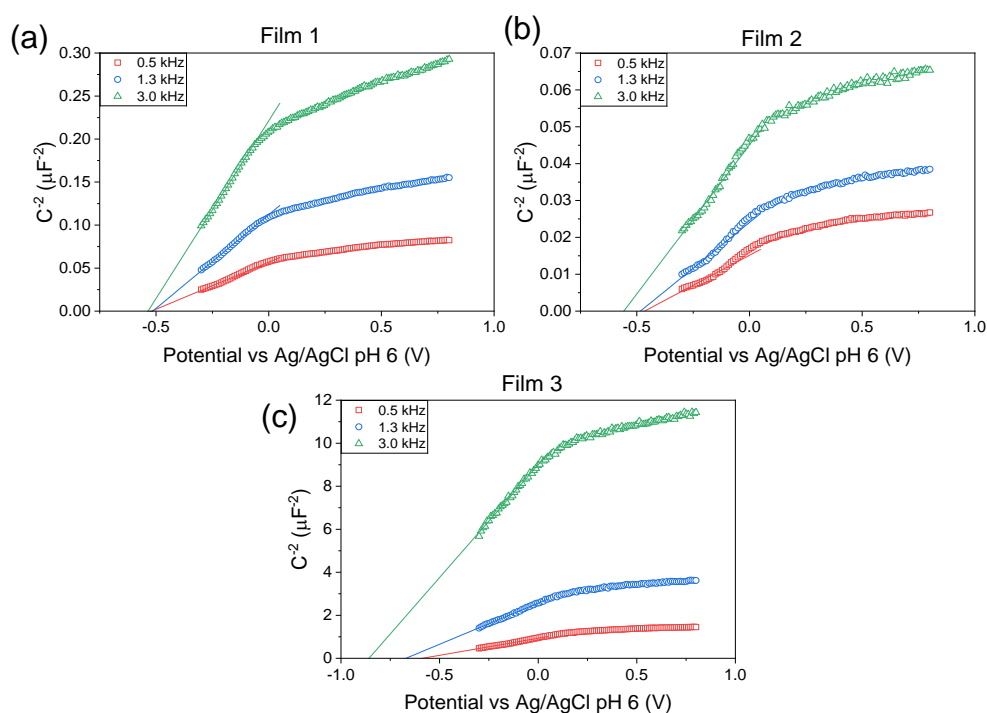


Figure 58 – Mott-Schottky plots for (a) film 1, (b) film 2 and (c) film 3 at 0.5 kHz, 1.3 kHz and 3 kHz. Measured in 3 electrode cell; carbon nitride film working electrode, Ag/AgCl reference electrode and Pt mesh counter electrode in 0.1M KCl under Ar atmosphere in the dark.

Figure 58 shows the MS plots for the carbon nitride films, each of which shows a positive slope, indicating n-type behaviour, typical of carbon nitride materials.^{25,50,269,271,272,277,84,91,139,166,204,266–268} To determine the flat band potential, the linear

portion of the plot is extrapolated to intersect the x-axis.⁸⁴ Normally, materials should show frequency independence for the x-axis intercept, so often MS plots are shown at frequencies ranging between 0.2 kHz and 3 kHz^{25,229,248,265,267,269,271–273}, but on occasion is shown at a single frequency^{87,119,139,166,204,266,270}. Figure 58 and Table 22 show that the x-intercept is frequency dependent, giving different values depending not only on the frequency but also the film used. The large variation in flat band potentials demonstrate that the MS method cannot be used for band structure determination of these materials.

Table 22 – Flat band potential at different frequencies for each film.

Film	Flat band potential (V) vs Ag/AgCl at pH 6		
	0.5 kHz	1.3 kHz	3.0 kHz
1	-0.520	-0.514	-0.536
2	-0.466	-0.484	-0.558
3	-0.587	-0.671	-0.868

3.3.4.2 XPS Band Structure

XPS can be used to measure the valence band maximum (VBM) of a material relative to its fermi level. In the literature, many have measured the VBM of carbon nitrides and directly used it to determine the materials band structure with no discussion on how this was done.^{69,74,278–280,95,125,169,219,221,222,229,272} Since the VBM is measured relative to the materials fermi level, to be able to compare materials, the fermi level must be determined by measuring the materials work function (WF) which can be done via XPS or UPS by measuring the secondary electron cut-off (SEC). A number of different methods have been used in the literature for determining the fermi level or work function including; the WF of the XPS analyser^{80,140,271,281,282}, measuring the WF of the material using XPS or UPS^{200,284}, or using the flat band potential from MS plots as the fermi level position^{275,283}. In this work the VBM and SEC of each material in the CN-BA series has been measured (Figure 59) and used to determine the WF and in combination with the UV-Vis band gap, the conduction and valence band positions (Table 23). The calculated band positions of each material relative to water splitting and CO₂ reduction redox potentials are depicted in Figure 60.

Table 23 – CN-BA series band gap, valence band maximum (VBM) relative to the fermi level, work function (WF) and conduction band (CB) and valence band (VB) position vs vacuum level.

Sample	Band Gap (eV)	XPS VBM (eV)	XPS WF (eV)	VB vs vacuum level (eV)	CB vs vacuum level (eV)
CN-DCDA	2.68	1.96	4.03	5.99	3.31
CN-BA(5)	2.40	1.55	4.03	5.58	3.18
CN-BA(10)	2.21	1.16	4.05	5.21	3.00
CN-BA(20)	1.92	1.77	4.06	5.83	3.91

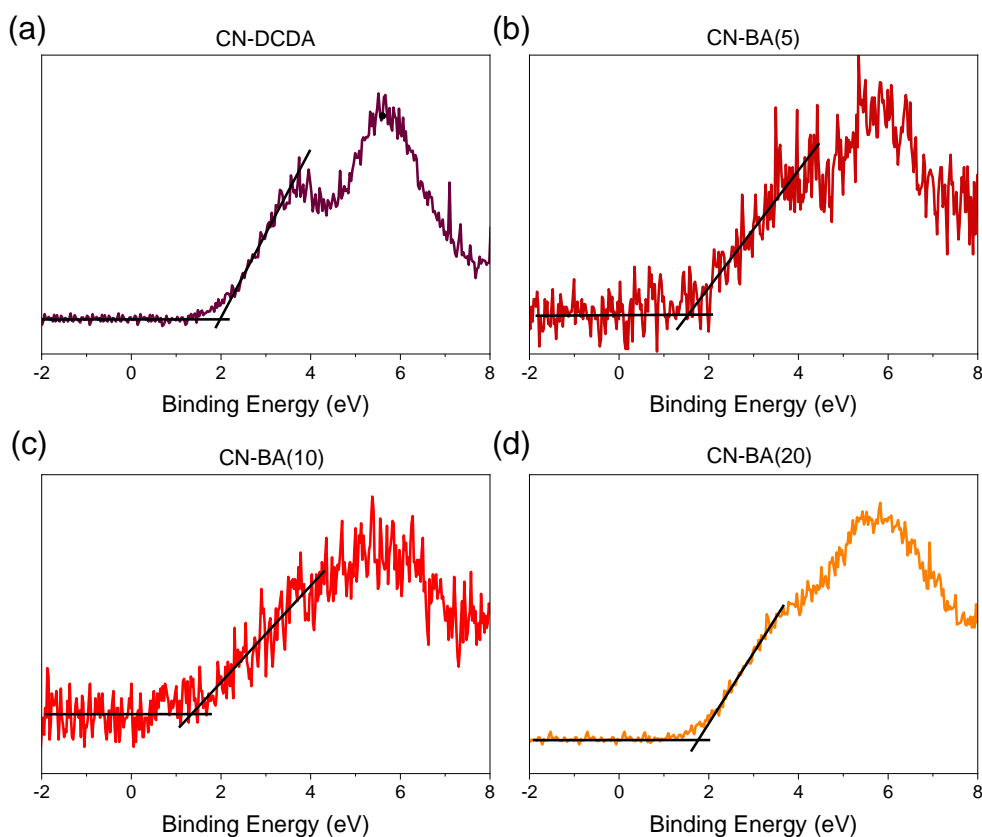


Figure 59 – XPS Valence band spectra for (a) CN-DCDA, (b) CN-BA(5), (c) CN-BA(10) and (d) CN-BA(20).

Across the CN-BA series, the band structures vary significantly and do not all seem to follow a trend with the amount of barbituric acid used in the precursor mixtures. The variation in band positions for CN-DCDA and CN-BA(20) agree well with the original paper that introduced copolymerisation of DCDA with barbituric acid in 2010.⁵⁰ The paper reported the band structures of the two materials showed contraction of the band positions with addition of

barbituric acid, which is also observed in this work. However, they did not report the band structures of the other materials within this series.

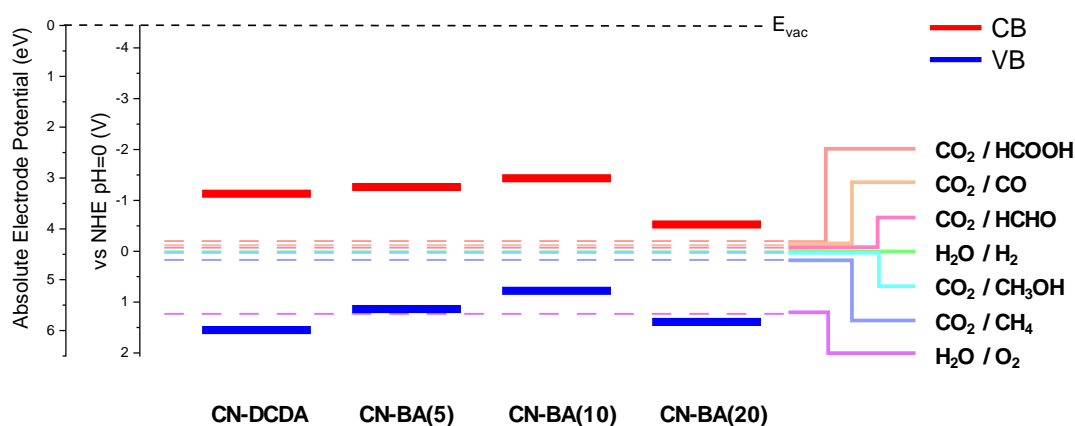


Figure 60 – Band structures of CN-DCDA, CN-BA(5), CN-BA(10) and CN-BA(20).

Initial addition of barbituric acid from CN-DCDA to CN-BA(5) appears to cause an upshift in the VB with only a small shift in the CB to more negative potentials, leading to a decreased band gap. This upshift in band positions continues for the CN-BA(10) sample, with further decrease in the band gap. However, when the largest amount of barbituric acid is used, both bands are shifted to more positive potentials. These changes in band structure can be used, alongside lifetimes data to understand the variation in photoactivity across the CN-BA series.

Moving across the CN-BA series, CN-DCDA has the largest band gap and shortest charge lifetimes, which lead to it having the lowest photocatalytic activity. Addition of a small amount of barbituric acid, decreases the band gap due to an upshift in both CB and VB positions of CN-BA(5), allowing the material to utilise more wavelengths of light to excite electrons to the CB, which then have a greater driving force for reduction reactions. Furthermore, CN-BA(5) is the material with the longest charge lifetimes, meaning the photogenerated charges are more likely to reach the adsorbed species co-catalyst or hole scavenger and participate in redox reactions before recombination can occur.

Further addition of barbituric acid leads to further decrease in the band gap and even an upshift in band positions of CN-BA(10), which would be expected to cause further enhancement in photocatalysis, however this is not the case, activity actually drops. This drop in activity is likely due to a reduction in the charge lifetimes and an upshift in VB position meaning that there is

a lower driving force to transfer to the hole scavenger. Despite having the smallest band gap, CN-BA(20) sees further decrease in photoactivity, which corresponds to decrease in charge lifetimes and down shift in band positions, lowering the driving force for the reduction reaction.

3.4 Conclusions and Future Work

Over 180 years of carbon nitride research, the actual structure of the material remains elusive and analysis of various characterisation data is still unclear or not discussed fully. Despite this, the literature still grows exponentially each year, as it is proven to be a useful material in a wide range of applications. In this work, we have attempted to gain more insight into the carbon nitride materials by creating and comparing a range of similar materials using a wide range of characterisation techniques.

Within this chapter, 16 carbon nitride materials have been synthesised using different precursors/calcination conditions, characterised using CHN, BET surface area, PXRD, SEM, DRIFTS, Raman, XPS, SS NMR and UV-Vis, with initial photocatalytic activity for H₂ evolution evaluated in the presence of a 1 wt% Pt co-catalyst and EDTA hole scavenger. Initial structural and electronic characterisation results agreed well with previous reported properties of carbon nitride. Although reports usually attempt to assign a single structure to the produced materials, the characterisation data shown in this chapter indicates the materials synthesised in this project are not a single homogeneous fully polymerised phase, but instead consist of numerous structures similar to that of melon, fully polymerised carbon nitride and systems that lie in between. Little difference in characterisation or photocatalytic activity was observed for materials synthesised under different calcination conditions and the series of materials synthesised with different ratios of urea and thiourea showed trends in photoactivity with surface area.

The most interesting series of materials was produced by copolymerisation of DCDA with different amounts of barbituric acid, which led to increased carbon content, decreased band gap, and enhanced photocatalysis. These materials showed no trend in observed photocatalytic activity with any of the initial characterisation data, including surface area and band gap. Further characterisation was required using time resolved techniques (Time-resolved PL, TAS and TR³) and band structure determination (UV-Vis and XPS), to gain greater understanding of variations in the photocatalytic activities obtained for these materials.

To the best of our knowledge this is the first report of KG Raman and TR³ of carbon nitride materials.

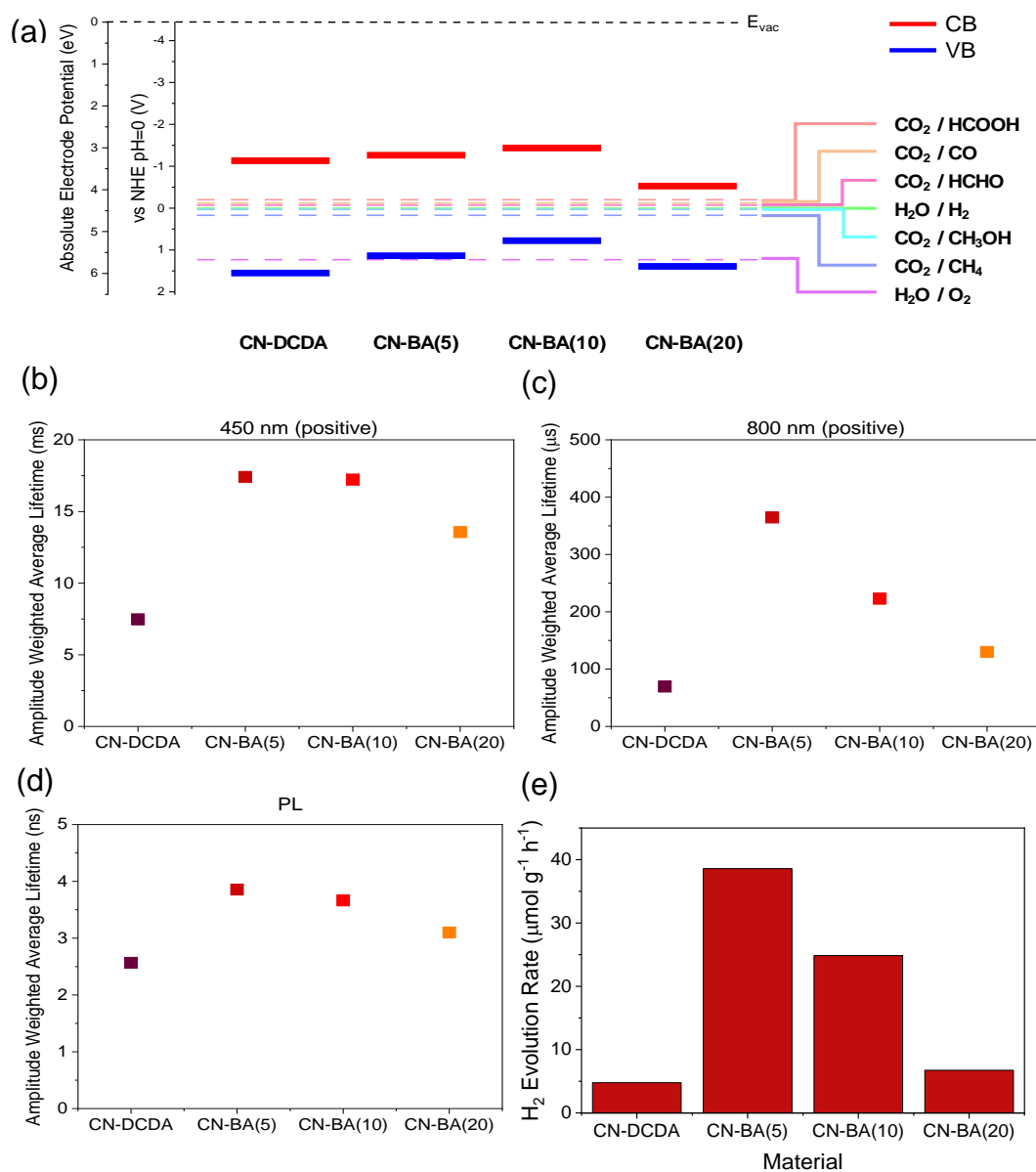


Figure 61 – The CN-BA series (a) Band structures, charge lifetimes, determined via TAS ((b), (c)) and (d) PL emission and (e) Photocatalytic activity for H₂ evolution.

Figure 61 summarises the data obtained for the band structure determination and time resolved measurements. The results showed that small amounts of barbituric acid gave extended charge lifetimes and a small upshift in conduction band position, giving increased photocatalytic activity. However, when larger amounts of barbituric acid were incorporated into the structure, charge lifetimes decreased and band positions shifted further, causing lower photoactivities. Decreased charge lifetimes and different band positions was likely caused by

the formation of defects, which potentially formed states within the band gap and acted as recombination centres, decreasing overall activity. Although, the incorporation of barbituric acid into the carbon nitride structure has been previously reported, the original study only determined 2 of the 4 materials band structures via the Mott-Schottky method, focussing on the 0% and 20% barbituric acid containing samples. In doing so, they only saw that there was a contraction of the band structure with both the CB and VB appearing to move closer together. Within this work, we see that there are shifts in each direction which can explain the variations in activity along with charge lifetimes which had not been previously explored.

Future work for these materials would be to perform more time resolved measurements in the presence of sacrificial donors to assign features observed in the time resolved measurements to electrons, holes or charge pairs. Work on the CN-BA series of materials continues in the next chapter, focussing on improving photocatalytic activity for both H₂ evolution and CO₂ reduction.

3.5 References

- 1 J. Liebig, *Ann. der Pharm.*, 1834, **10**, 1–47.
- 2 Y. Wang, X. Wang and M. Antonietti, *Angew. Chemie Int. Ed.*, 2012, **51**, 68–89.
- 3 T. Komatsu and T. Nakamura, *J. Mater. Chem.*, 2001, **11**, 474–478.
- 4 Y. Luo, Y. Yan, S. Zheng, H. Xue and H. Pang, *J. Mater. Chem. A*, 2019, **7**, 901–924.
- 5 C. Prasad, H. Tang and I. Bahadur, *J. Mol. Liq.*, 2019, **281**, 634–654.
- 6 A. Thomas, A. Fischer, F. Goettmann, M. Antonietti, J.-O. Müller, R. Schlögl and J. M. Carlsson, *J. Mater. Chem.*, 2008, **18**, 4893.
- 7 B. V. Lotsch, M. Döblinger, J. Sehnert, L. Seyfarth, J. Senker, O. Oeckler and W. Schnick, *Chem. - A Eur. J.*, 2007, **13**, 4969–4980.
- 8 W.-J. Ong, L.-L. Tan, Y. H. Ng, S.-T. Yong and S.-P. Chai, *Chem. Rev.*, 2016, **116**, 7159–7329.
- 9 E. Kroke and M. Schwarz, *Coord. Chem. Rev.*, 2004, **248**, 493–532.
- 10 E. Kroke, M. Schwarz, E. Horath-Bordon, P. Kroll, B. Noll and A. D. Norman, *New J. Chem.*, 2002, **26**, 508–512.
- 11 B. V. Lotsch and W. Schnick, *Chem. - A Eur. J.*, 2007, **13**, 4956–4968.
- 12 X. Wang, S. Blechert and M. Antonietti, *ACS Catal.*, 2012, **2**, 1596–1606.
- 13 L. Pauling and J. H. Sturdivant, *Proc. Natl. Acad. Sci.*, 1937, **23**, 615–620.
- 14 C. E. Redemann and H. J. Lucas, *J. Am. Chem. Soc.*, 1940, **62**, 842–846.
- 15 A. Y. Liu and M. L. Cohen, *Science (80-.)*, 1989, **245**, 841–842.
- 16 L. R. Shaginyan, *Powder Metall. Met. Ceram.*, 1998, **37**, 648–658.
- 17 T. Malkow, *Mater. Sci. Eng. A*, 2001, **302**, 311–324.
- 18 P. F. McMillan, *Curr. Opin. Solid State Mater. Sci.*, 1999, **4**, 171–178.
- 19 J. V. Badding, *Adv. Mater.*, 1997, **9**, 877–886.
- 20 S. Matsumoto, E. Q. Xie and F. Izumi, *Diam. Relat. Mater.*, 1999, **8**, 1175–1182.
- 21 D. M. Teter and R. J. Hemley, *Science (80-.)*, 1996, **271**, 53–55.
- 22 M. Deifallah, P. F. McMillan and F. Corà, *J. Phys. Chem. C*, 2008, **112**, 5447–5453.
- 23 Y. Xu and S. P. Gao, *Int. J. Hydrogen Energy*, 2012, **37**, 11072–11080.
- 24 J. Zhu, P. Xiao, H. Li and S. A. C. Carabineiro, *ACS Appl. Mater. Interfaces*, 2014, **6**, 16449–16465.
- 25 S. Yang, Y. Gong, J. Zhang, L. Zhan, L. Ma, Z. Fang, R. Vajtai, X. Wang and P. M. Ajayan, *Adv. Mater.*, 2013, **25**, 2452–2456.
- 26 X. Wang, K. Maeda, A. Thomas, K. Takanabe, G. Xin, J. M. Carlsson, K. Domen and M. Antonietti, *Nat. Mater.*, 2009, **8**, 76–80.
- 27 Z. Sun, H. Wang, Z. Wu and L. Wang, *Catal. Today*, 2018, **300**, 160–172.
- 28 M. M. Kandy, *Sustain. Energy Fuels*, 2020, **4**, 469–484.
- 29 W. K. Darkwah and K. A. Oswald, *Nanoscale Res. Lett.*, 2019, **14**, 234.
- 30 Y. Li, T. Kong and S. Shen, *Small*, 2019, **15**, 1900772.
- 31 Y. Fang and X. Wang, *Chem. Commun.*, 2018, **54**, 5674–5687.
- 32 M. Shen, L. Zhang and J. Shi, *Nanotechnology*, 2018, **29**, 412001.
- 33 Y. Chen, G. Jia, Y. Hu, G. Fan, Y. H. Tsang, Z. Li and Z. Zou, *Sustain. Energy Fuels*, 2017, **1**, 1875–1898.
- 34 R. Kuriki and K. Maeda, *Phys. Chem. Chem. Phys.*, 2017, **19**, 4938–4950.
- 35 S. Cao, J. Low, J. Yu and M. Jaroniec, *Adv. Mater.*, 2015, **27**, 2150–2176.
- 36 Y. Zheng, L. Lin, B. Wang and X. Wang, *Angew. Chemie Int. Ed.*, 2015, **54**, 12868–12884.
- 37 S. Cao and J. Yu, *J. Phys. Chem. Lett.*, 2014, **5**, 2101–2107.
- 38 S. Ye, R. Wang, M.-Z. Wu and Y.-P. Yuan, *Appl. Surf. Sci.*, 2015, **358**, 15–27.
- 39 G. Dong, Y. Zhang, Q. Pan and J. Qiu, *J. Photochem. Photobiol. C Photochem. Rev.*, 2014, **20**, 33–50.
- 40 T. S. Miller, A. B. Jorge, T. M. Suter, A. Sella, F. Corà and P. F. McMillan, *Phys. Chem. Chem. Phys.*, 2017, **19**, 15613–15638.
- 41 F. Fina, S. K. Callear, G. M. Carins and J. T. S. Irvine, *Chem. Mater.*, 2015, **27**, 2612–2618.
- 42 M. J. Bojdys, J. O. Müller, M. Antonietti and A. Thomas, *Chem. - A Eur. J.*, 2008, **14**, 8177–8182.
- 43 B. Jürgens, E. Irran, J. Senker, P. Kroll, H. Müller and W. Schnick, *J. Am. Chem. Soc.*, 2003, **125**, 10288–10300.

- 44 Y. Zheng, J. Liu, J. Liang, M. Jaroniec and S. Z. Qiao, *Energy Environ. Sci.*, 2012, **5**, 6717.
- 45 J. Wen, J. Xie, X. Chen and X. Li, *Appl. Surf. Sci.*, 2017, **391**, 72–123.
- 46 M. Volokh, G. Peng, J. Barrio and M. Shalom, *Angew. Chemie Int. Ed.*, 2019, **58**, 6138–6151.
- 47 S. C. Yan, Z. S. Li and Z. G. Zou, *Langmuir*, 2009, **25**, 10397–10401.
- 48 Y. Zhang, A. Thomas, M. Antonietti and X. Wang, *J. Am. Chem. Soc.*, 2009, **131**, 50–51.
- 49 H. Zhang, X. Zuo, H. Tang, G. Li and Z. Zhou, *Phys. Chem. Chem. Phys.*, 2015, **17**, 6280–6288.
- 50 J. Zhang, X. Chen, K. Takanahe, K. Maeda, K. Domen, J. D. Epping, X. Fu, M. Antonietti and X. Wang, *Angew. Chemie Int. Ed.*, 2010, **49**, 441–444.
- 51 K. R. Reddy, C. V. Reddy, M. N. Nadagouda, N. P. Shetti, S. Jaesool and T. M. Aminabhavi, *J. Environ. Manage.*, 2019, **238**, 25–40.
- 52 Y. Zhang and M. Antonietti, *Chem. - An Asian J.*, 2010, **5**, 1307–1311.
- 53 S. Chu, Y. Wang, Y. Guo, J. Feng, C. Wang, W. Luo, X. Fan and Z. Zou, *ACS Catal.*, 2013, **3**, 912–919.
- 54 X. Ma, Y. Lv, J. Xu, Y. Liu, R. Zhang and Y. Zhu, *J. Phys. Chem. C*, 2012, **116**, 23485–23493.
- 55 D. J. Martin, K. Qiu, S. A. Shevlin, A. D. Handoko, X. Chen, Z. Guo and J. Tang, *Angew. Chemie - Int. Ed.*, 2014, **53**, 9240–9245.
- 56 J. Ehrmaier, T. N. V. Karsili, A. L. Sobolewski and W. Domcke, *J. Phys. Chem. A*, 2017, **121**, 4754–4764.
- 57 X. Wang, K. Maeda, X. Chen, K. Takanahe, K. Domen, Y. Hou, X. Fu and M. Antonietti, *J. Am. Chem. Soc.*, 2009, **131**, 1680–1681.
- 58 F. Goettmann, A. Thomas and M. Antonietti, *Angew. Chemie - Int. Ed.*, 2007, **46**, 2717–2720.
- 59 G. Dong and L. Zhang, *J. Mater. Chem.*, 2012, **22**, 1160–1166.
- 60 J. Mao, T. Peng, X. Zhang, K. Li, L. Ye and L. Zan, *Catal. Sci. Technol.*, 2013, **3**, 1253.
- 61 Y. P. Yuan, S. W. Cao, Y. Sen Liao, L. S. Yin and C. Xue, *Appl. Catal. B Environ.*, 2013, **140–141**, 164–168.
- 62 K. Maeda, K. Sekizawa and O. Ishitani, *Chem. Commun.*, 2013, **49**, 10127.
- 63 Q. Xiang, J. Yu and M. Jaroniec, *J. Phys. Chem. C*, 2011, **115**, 7355–7363.
- 64 S. Min and G. Lu, *J. Phys. Chem. C*, 2012, **116**, 19644–19652.
- 65 J. Zhang, M. Zhang, L. Lin and X. Wang, *Angew. Chemie - Int. Ed.*, 2015, **54**, 6297–6301.
- 66 W.-J. Ong, L.-L. Tan, S.-P. Chai, S.-T. Yong and A. R. Mohamed, *Nano Energy*, 2015, **13**, 757–770.
- 67 L. K. Putri, W. J. Ong, W. S. Chang and S. P. Chai, *Catal. Sci. Technol.*, 2016, **6**, 744–754.
- 68 X. Li, G. Hartley, A. J. Ward, P. A. Young, A. F. Masters and T. Maschmeyer, *J. Phys. Chem. C*, 2015, **119**, 14938–14946.
- 69 G. Liu, P. Niu, C. Sun, S. C. Smith, Z. Chen, G. Q. Lu and H. M. Cheng, *J. Am. Chem. Soc.*, 2010, **132**, 11642–11648.
- 70 L. Ge, C. Han, X. Xiao, L. Guo and Y. Li, *Mater. Res. Bull.*, 2013, **48**, 3919–3925.
- 71 K. Wang, Q. Li, B. Liu, B. Cheng, W. Ho and J. Yu, *Appl. Catal. B Environ.*, 2015, **176–177**, 44–52.
- 72 N. D. Shcherban, S. M. Filonenko, M. L. Ovcharov, A. M. Mishura, M. A. Skoryk, A. Aho and D. Y. Murzin, *ChemistrySelect*, 2016, **1**, 4987–4993.
- 73 W. Li, Y. Hu, E. Rodríguez-Castellón and T. J. Bandosz, *J. Mater. Chem. A*, 2017, **5**, 16315–16325.
- 74 J. Li, B. Shen, Z. Hong, B. Lin, B. Gao and Y. Chen, *Chem. Commun.*, 2012, **48**, 12017.
- 75 J. Fu, B. Zhu, C. Jiang, B. Cheng, W. You and J. Yu, *Small*, 2017, **13**, 1603938.
- 76 Y. Wang, J. Zhang, X. Wang, M. Antonietti and H. Li, *Angew. Chemie Int. Ed.*, 2010, **49**, 3356–3359.
- 77 F. Raziq, Y. Qu, M. Humayun, A. Zada, H. Yu and L. Jing, *Appl. Catal. B Environ.*, 2017, **201**, 486–494.
- 78 G. Zhang, M. Zhang, X. Ye, X. Qiu, S. Lin and X. Wang, *Adv. Mater.*, 2014, **26**, 805–809.
- 79 Y. Zhang, T. Mori, J. Ye and M. Antonietti, *J. Am. Chem. Soc.*, 2010, **132**, 6294–6295.

- 80 B. Liu, L. Ye, R. Wang, J. Yang, Y. Zhang, R. Guan, L. Tian and X. Chen, *ACS Appl. Mater. Interfaces*, 2018, **10**, 4001–4009.
- 81 S. C. Yan, Z. S. Li and Z. G. Zou, *Langmuir*, 2010, **26**, 3894–3901.
- 82 N. Sagara, S. Kamimura, T. Tsubota and T. Ohno, *Appl. Catal. B Environ.*, 2016, **192**, 193–198.
- 83 Y. Wang, H. Li, J. Yao, X. Wang and M. Antonietti, *Chem. Sci.*, 2011, **2**, 446–450.
- 84 Q. Liang, M. Zhang, C. Liu, S. Xu and Z. Li, *Appl. Catal. A Gen.*, 2016, **519**, 107–115.
- 85 H. Qin, W. Lv, J. Bai, Y. Zhou, Y. Wen, Q. He, J. Tang, L. Wang and Q. Zhou, *J. Mater. Sci.*, 2019, **54**, 4811–4820.
- 86 L. Ye, D. Wu, K. H. Chu, B. Wang, H. Xie, H. Y. Yip and P. K. Wong, *Chem. Eng. J.*, 2016, **304**, 376–383.
- 87 X. Huang, W. Gu, S. Hu, Y. Hu, L. Zhou, J. Lei, L. Wang, Y. Liu and J. Zhang, *Catal. Sci. Technol.*, 2020, **10**, 3694–3700.
- 88 J. Zhang, G. Zhang, X. Chen, S. Lin, L. Möhlmann, G. Dołęga, G. Lipner, M. Antonietti, S. Blechert and X. Wang, *Angew. Chemie - Int. Ed.*, 2012, **51**, 3183–3187.
- 89 G. Zhang and X. Wang, *J. Catal.*, 2013, **307**, 246–253.
- 90 Y. Wang, S. Zhao, Y. Zhang, W. Chen, S. Yuan, Y. Zhou and Z. Huang, *Appl. Surf. Sci.*, 2019, **463**, 1–8.
- 91 X. Wei, H. Jiang and Z. Liu, *RSC Adv.*, 2016, **6**, 81372–81377.
- 92 M. Ning, Z. Chen, L. Li, Q. Meng, Z. Chen, Y. Zhang, M. Jin, Z. Zhang, M. Yuan, X. Wang and G. Zhou, *Electrochem. commun.*, 2018, **87**, 13–17.
- 93 Z. He, D. Wang, J. Tang, S. Song, J. Chen and X. Tao, *Environ. Sci. Pollut. Res.*, 2017, **24**, 8219–8229.
- 94 P. Xia, B. Zhu, J. Yu, S. Cao and M. Jaroniec, *J. Mater. Chem. A*, 2017, **5**, 3230–3238.
- 95 H. Wang, Z. Sun, Q. Li, Q. Tang and Z. Wu, *J. CO₂ Util.*, 2016, **14**, 143–151.
- 96 Q. Huang, J. Yu, S. Cao, C. Cui and B. Cheng, *Appl. Surf. Sci.*, 2015, **358**, 350–355.
- 97 B. Yue, Q. Li, H. Iwai, T. Kako and J. Ye, *Sci. Technol. Adv. Mater.*, 2011, **12**, 034401.
- 98 X. Wang, X. Chen, A. Thomas, X. Fu and M. Antonietti, *Adv. Mater.*, 2009, **21**, 1609–1612.
- 99 Y. Oh, J. O. Hwang, E. S. Lee, M. Yoon, V. D. Le, Y. H. Kim, D. H. Kim and S. O. Kim, *ACS Appl. Mater. Interfaces*, 2016, **8**, 25438–25443.
- 100 W. Yan, L. Yan and C. Jing, *Appl. Catal. B Environ.*, 2019, **244**, 475–485.
- 101 Z. Shu, Y. Wang, W. Wang, J. Zhou, T. Li, X. Liu, Y. Tan and Z. Zhao, *Int. J. Hydrogen Energy*, 2019, **44**, 748–756.
- 102 M. Zhang, X. Bai, D. Liu, J. Wang and Y. Zhu, *Appl. Catal. B Environ.*, 2015, **164**, 77–81.
- 103 J. Fan, H. Qin and S. Jiang, *Chem. Eng. J.*, 2019, **359**, 723–732.
- 104 H. Li, Y. Xia, T. Hu, Q. Deng, N. Du and W. Hou, *J. Mater. Chem. A*, 2018, **6**, 6238–6243.
- 105 Z. Zhu, X. Tang, T. Wang, W. Fan, Z. Liu, C. Li, P. Huo and Y. Yan, *Appl. Catal. B Environ.*, 2019, **241**, 319–328.
- 106 M. Xie, J. Tang, L. Kong, W. Lu, V. Natarajan, F. Zhu and J. Zhan, *Chem. Eng. J.*, 2019, **360**, 1213–1222.
- 107 W. Wu, Z. Ruan, J. Li, Y. Li, Y. Jiang, X. Xu, D. Li, Y. Yuan and K. Lin, *Nano-Micro Lett.*, 2019, **11**, 9.
- 108 Y. Wang, Y. Xu, Y. Wang, H. Qin, X. Li, Y. Zuo, S. Kang and L. Cui, *Catal. Commun.*, 2016, **74**, 75–79.
- 109 Y. Wang, Y. Wang, Y. Chen, C. Yin, Y. Zuo and L. F. Cui, *Mater. Lett.*, 2015, **139**, 70–72.
- 110 W. Niu and Y. Yang, *ACS Energy Lett.*, 2018, **3**, 2796–2815.
- 111 M. Shalom, M. Guttentag, C. Fettkenhauer, S. Inal, D. Neher, A. Llobet and M. Antonietti, *Chem. Mater.*, 2014, **26**, 5812–5818.
- 112 J. Qin, S. Wang, H. Ren, Y. Hou and X. Wang, *Appl. Catal. B Environ.*, 2015, **179**, 1–8.
- 113 E. Vorobyeva, Z. Chen, S. Mitchell, R. K. Leary, P. Midgley, J. M. Thomas, R. Hauert, E. Fako, N. López and J. Pérez-Ramírez, *J. Mater. Chem. A*, 2017, **5**, 16393–16403.
- 114 J. Ren, Y. Wu, Y. Dai, D. Sha, J. Pan, M. Chen, J. Wang, Q. Wang, N. Ye and X. Yan, *J. Mater. Sci. Mater. Electron.*, 2017, **28**, 641–651.
- 115 J. Barrio, L. Lin, X. Wang and M. Shalom, *ACS Sustain. Chem. Eng.*, 2018, **6**, 519–530.
- 116 L. Chen, Z. Song, X. Liu, L. Guo, M. Li and F. Fu, *Analyst*, 2018, **143**, 1609–1614.
- 117 L. Li, Q. Meng, H. Lv, L. Shui, Y. Zhang, Z. Zhang, Z. Chen, M. Yuan, R. Nötzel, X.

- Wang, J.-M. Liu and G. Zhou, *Appl. Surf. Sci.*, 2018, **428**, 739–747.
- 118 C. Tsounis, R. Kuriki, K. Shibata, J. J. M. Vequizo, D. Lu, A. Yamakata, O. Ishitani, R. Amal and K. Maeda, *ACS Sustain. Chem. Eng.*, 2018, **6**, 15333–15340.
- 119 C. Zhou, C. Lai, P. Xu, G. Zeng, D. Huang, Z. Li, C. Zhang, M. Cheng, L. Hu, J. Wan, F. Chen, W. Xiong and R. Deng, *ACS Sustain. Chem. Eng.*, 2018, **6**, 6941–6949.
- 120 C. Zhou, C. Lai, D. Huang, G. Zeng, C. Zhang, M. Cheng, L. Hu, J. Wan, W. Xiong, M. Wen, X. Wen and L. Qin, *Appl. Catal. B Environ.*, 2018, **220**, 202–210.
- 121 G. Li, Q. Wang, Y. Wu, Y. Li and L. Guo, *Spectrochim. Acta - Part A Mol. Biomol. Spectrosc.*, 2019, **215**, 307–312.
- 122 M. Li, S. Zhang, X. Liu, J. Han, X. Zhu, Q. Ge and H. Wang, *Eur. J. Inorg. Chem.*, 2019, **2019**, 2058–2064.
- 123 J. Li, D. Wu, J. Iocozzia, H. Du, X. Liu, Y. Yuan, W. Zhou, Z. Li, Z. Xue and Z. Lin, *Angew. Chemie Int. Ed.*, 2019, **58**, 1985–1989.
- 124 W. Tang, Y. Tian, B. Chen, Y. Xu, B. Li, X. Jing, J. Zhang and S. Xu, *ACS Appl. Mater. Interfaces*, 2020, **12**, 6396–6406.
- 125 Z. Teng, W. Cai, S. Liu, C. Wang, Q. Zhang, S. Chenliang and T. Ohno, *Appl. Catal. B Environ.*, 2020, **271**, 118917.
- 126 J. Tian, L. Zhang, X. Fan, Y. Zhou, M. Wang, R. Cheng, M. Li, X. Kan, X. Jin, Z. Liu, Y. Gao and J. Shi, *J. Mater. Chem. A*, 2016, **4**, 13814–13821.
- 127 Y. Guo, F. Kong, C. Wang, S. Chu, J. Yang, Y. Wang and Z. Zou, *J. Mater. Chem. A*, 2013, **1**, 5142.
- 128 J. Zhang, M. Zhang, S. Lin, X. Fu and X. Wang, *J. Catal.*, 2014, **310**, 24–30.
- 129 M. Zhang and X. Wang, *Energy Environ. Sci.*, 2014, **7**, 1902.
- 130 W. Ho, Z. Zhang, W. Lin, S. Huang, X. Zhang, X. Wang and Y. Huang, *ACS Appl. Mater. Interfaces*, 2015, **7**, 5497–5505.
- 131 M. Zhang, Y. Duan, H. Jia, F. Wang, L. Wang, Z. Su and C. Wang, *Catal. Sci. Technol.*, 2017, **7**, 452–458.
- 132 Z. Lin, S. Wang, Y. Miao, J. Yuan, Y. Liu, S. Xu and S. Cao, *Int. J. Hydrogen Energy*, 2020, **45**, 6341–6351.
- 133 C. Yang, B. Wang, L. Zhang, L. Yin and X. Wang, *Angew. Chemie - Int. Ed.*, 2017, **56**, 6627–6631.
- 134 F. Dong, Y. Sun, L. Wu, M. Fu and Z. Wu, *Catal. Sci. Technol.*, 2012, **2**, 1332.
- 135 Y. Zhang, H. Gong, G. Li, H. Zeng, L. Zhong, K. Liu, H. Cao and H. Yan, *Int. J. Hydrogen Energy*, 2017, **42**, 143–151.
- 136 G. Zhang, J. Zhang, M. Zhang and X. Wang, *J. Mater. Chem.*, 2012, **22**, 8083.
- 137 J. Hong, X. Xia, Y. Wang and R. Xu, *J. Mater. Chem.*, 2012, **22**, 15006–15012.
- 138 F. Dong, Z. Zhao, T. Xiong, Z. Ni, W. Zhang, Y. Sun and W. K. Ho, *ACS Appl. Mater. Interfaces*, 2013, **5**, 11392–11401.
- 139 M. Zhou, Z. Hou, L. Zhang, Y. Liu, Q. Gao and X. Chen, *Sustain. Energy Fuels*, 2017, **1**, 317–323.
- 140 Y. Qin, Y. Ding and H. Tang, *J. Environ. Chem. Eng.*, 2016, **4**, 4374–4384.
- 141 F. Dong, L. Wu, Y. Sun, M. Fu, Z. Wu and S. C. Lee, *J. Mater. Chem.*, 2011, **21**, 15171.
- 142 A. B. Jorge, D. J. Martin, M. T. S. Dhanoa, A. S. Rahman, N. Makwana, J. Tang, A. Sella, F. Corà, S. Firth, J. A. Darr and P. F. McMillan, *J. Phys. Chem. C*, 2013, **117**, 7178–7185.
- 143 J. Xu, Y. Li, S. Peng, G. Lu and S. Li, *Phys. Chem. Chem. Phys.*, 2013, **15**, 7657.
- 144 Z. Mo, X. She, Y. Li, L. Liu, L. Huang, Z. Chen, Q. Zhang, H. Xu and H. Li, *RSC Adv.*, 2015, **5**, 101552–101562.
- 145 D. R. Paul, R. Sharma, S. P. Nehra and A. Sharma, *RSC Adv.*, 2019, **9**, 15381–15391.
- 146 S. Cui, R. Li, J. Pei, Y. Wen, Y. Li and X. Xing, *Mater. Chem. Phys.*, 2020, **247**, 122867.
- 147 L. Wang, Y. Hou, S. Xiao, F. Bi, L. Zhao, Y. Li, X. Zhang, G. Gai and X. Dong, *RSC Adv.*, 2019, **9**, 39304–39314.
- 148 K. Maeda, D. An, R. Kuriki, D. Lu and O. Ishitani, *Beilstein J. Org. Chem*, 2018, **14**, 1806–1812.
- 149 F. Dong, Z. Wang, Y. Sun, W. K. Ho and H. Zhang, *J. Colloid Interface Sci.*, 2013, **401**, 70–79.
- 150 M. Shalom, S. Inal, C. Fettkenhauer, D. Neher and M. Antonietti, *J. Am. Chem. Soc.*, 2013, **135**, 7118–7121.
- 151 Y. Wang, H. Wang, F. Chen, F. Cao, X. Zhao, S. Meng and Y. Cui, *Appl. Catal. B Environ.*, 2017, **206**, 417–425.

- 152 T. Ohno, N. Murakami, T. Koyanagi and Y. Yang, *J. CO2 Util.*, 2014, **6**, 17–25.
- 153 J. J. Walsh, C. Jiang, J. Tang and A. J. Cowan, *Phys. Chem. Chem. Phys.*, 2016, **18**, 24825–24829.
- 154 Y. Zheng, L. Lin, X. Ye, F. Guo and X. Wang, *Angew. Chemie - Int. Ed.*, 2014, **53**, 11926–11930.
- 155 M. Groenewolt and M. Antonietti, *Adv. Mater.*, 2005, **17**, 1789–1792.
- 156 W. Tu, Y. Xu, J. Wang, B. Zhang, T. Zhou, S. Yin, S. Wu, C. Li, Y. Huang, Y. Zhou, Z. Zou, J. Robertson, M. Kraft and R. Xu, *ACS Sustain. Chem. Eng.*, 2017, **5**, 7260–7268.
- 157 E. Wirnhier, M. Döblinger, D. Gunzelmann, J. Senker, B. V Lotsch and W. Schnick, *Chem. - A Eur. J.*, 2011, **17**, 3213–3221.
- 158 F. Goettmann, A. Fischer, M. Antonietti and A. Thomas, *Angew. Chemie Int. Ed.*, 2006, **45**, 4467–4471.
- 159 J. Zhang, M. Zhang, R.-Q. Sun and X. Wang, *Angew. Chemie Int. Ed.*, 2012, **51**, 10145–10149.
- 160 Y. Wang, J. Hong, W. Zhang and R. Xu, *Catal. Sci. Technol.*, 2013, **3**, 1703.
- 161 X. Li, J. Zhang, L. Shen, Y. Ma, W. Lei, Q. Cui and G. Zou, *Appl. Phys. A*, 2009, **94**, 387–392.
- 162 M. Thommes, K. Kaneko, A. V. Neimark, J. P. Olivier, F. Rodriguez-Reinoso, J. Rouquerol and K. S. W. Sing, *Pure Appl. Chem.*, 2015, **87**, 1051–1069.
- 163 K. S. W. Sing, D. H. Everett, R. A. W. Haul, L. Moscou, R. A. Pierotti, J. Rouquerol and T. Siemieniewska, *Pure Appl. Chem.*, 1985, **57**, 603–619.
- 164 T. Tyborski, C. Merschjann, S. Orthmann, F. Yang, M.-C. Lux-Steiner and T. Schedel-Niedrig, *J. Phys. Condens. Matter*, 2013, **25**, 395402.
- 165 S.-W. Cao, X.-F. Liu, Y.-P. Yuan, Z.-Y. Zhang, Y.-S. Liao, J. Fang, S. C. J. Loo, T. C. Sum and C. Xue, *Appl. Catal. B Environ.*, 2014, **147**, 940–946.
- 166 Y. Cao, Z. Zhang, J. Long, J. Liang, H. H. H. Lin, H. H. H. Lin and X. Wang, *J. Mater. Chem. A*, 2014, **2**, 17797–17807.
- 167 S. Bai, X. Wang, C. Hu, M. Xie, J. Jiang and Y. Xiong, *Chem. Commun.*, 2014, **50**, 6094–6097.
- 168 J. Yu, K. Wang, W. Xiao and B. Cheng, *Phys. Chem. Chem. Phys.*, 2014, **16**, 11492.
- 169 L. Shi, T. Wang, H. Zhang, K. Chang and J. Ye, *Adv. Funct. Mater.*, 2015, **25**, 5360–5367.
- 170 B. W. Sun, H. Y. Yu, Y. J. Yang, H. J. Li, C. Y. Zhai, D. J. Qian and M. Chen, *Phys. Chem. Chem. Phys.*, 2017, **19**, 26072–26084.
- 171 Z. Wang, Y. Huang, L. Chen, M. Chen, J. Cao, W. Ho and S. C. Lee, *J. Mater. Chem. A*, 2018, **6**, 972–981.
- 172 J. Bian, J. Li, S. Kalytchuk, Y. Wang, Q. Li, T. C. Lau, T. A. Niehaus, A. L. Rogach and R. Q. Zhang, *ChemPhysChem*, 2015, **16**, 954–959.
- 173 Y. Yang, Y. Y. Guo, F. Liu, X. Yuan, Y. Y. Guo, S. Zhang, W. Guo and M. Huo, *Appl. Catal. B Environ.*, 2013, **142–143**, 828–837.
- 174 H. J. Li, B. W. Sun, L. Sui, D. J. Qian and M. Chen, *Phys. Chem. Chem. Phys.*, 2015, **17**, 3309–3315.
- 175 H. Xu, J. Yan, Y. Xu, Y. Song, H. Li, J. Xia, C. Huang and H. Wan, *Appl. Catal. B Environ.*, 2013, **129**, 182–193.
- 176 D. Mitoraj and H. Kisch, *Chem. - A Eur. J.*, 2010, **16**, 261–269.
- 177 S. Zhou, Y. Liu, J. Li, Y. Wang, G. Jiang, Z. Zhao, D. Wang, A. Duan, J. Liu and Y. Wei, *Appl. Catal. B Environ.*, 2014, **158–159**, 20–29.
- 178 H. Li, S. Gan, H. Wang, D. Han and L. Niu, *Adv. Mater.*, 2015, **27**, 6906–6913.
- 179 S. Hwang, S. Lee and J. S. Yu, *Appl. Surf. Sci.*, 2007, **253**, 5656–5659.
- 180 V. W. Lau, I. Moudrakovski, T. Botari, S. Weinberger, M. B. Mesch, V. Duppel, J. Senker, V. Blum and B. V. Lotsch, *Nat. Commun.*, 2016, **7**, 12165.
- 181 R. C. Dante, P. Martín-Ramos, A. Correa-Guimaraes and J. Martín-Gil, *Mater. Chem. Phys.*, 2011, **130**, 1094–1102.
- 182 B. V Lotsch and W. Schnick, *Chem. Mater.*, 2006, **18**, 1891–1900.
- 183 H. Montigaud, B. Tanguy, G. Demazeau, I. Alves and S. Courjault, *J. Mater. Sci.*, 2000, **35**, 2547–2552.
- 184 B. V Lotsch and W. Schnick, *Chem. Mater.*, 2005, **17**, 3976–3982.
- 185 D. R. Miller, J. Wang and E. G. Gillan, *J. Mater. Chem.*, 2002, **12**, 2463–2469.
- 186 A. C. Ferrari, S. E. Rodil, J. Robertson, S. E. Rodil and J. Robertson, *Phys. Rev. B - Condens. Matter Mater. Phys.*, 2003, **67**, 155306.

- 187 B. Bouchet-Fabre, E. Marino, G. Lazar, K. Zellama, M. Clin, D. Ballutaud, F. Abel and C. Godet, *Thin Solid Films*, 2005, **482**, 167–171.
- 188 G. Socrates, *Infrared and Raman characteristic group frequencies. Tables and charts*, John Wiley & Sons Ltd, Chichester, Third., 2001.
- 189 P. Larkin, *Infrared and Raman spectroscopy*, Elsevier, Amsterdam, Second., 2018.
- 190 W. Yu, D. Xu and T. Peng, *J. Mater. Chem. A*, 2015, **3**, 19936–19947.
- 191 R. C. Dante, P. Martín-Ramos, A. Correa-Guimaraes and J. Martín-Gil, *Mater. Chem. Phys.*, 2011, **130**, 1094.
- 192 B. V. Lotsch, M. Döblinger, J. Sehnert, L. Seyfarth, J. Senker, O. Oeckler and W. Schnick, *Chem. - A Eur. J.*, 2007, **13**, 4969–4980.
- 193 E. Wirnhier, M. B. Mesch, J. Senker and W. Schnick, *Chem. - A Eur. J.*, 2013, **19**, 2041–2049.
- 194 X. Li, G. Hartley, A. J. Ward, P. A. Young, A. F. Masters and T. Maschmeyer, *J. Phys. Chem. C*, 2015, **119**, 14938.
- 195 M. Taheri, M. Ghiaci and A. Shchukarev, *Appl. Organomet. Chem.*, 2018, **32**, e4338.
- 196 X. Kang, Y. Kang, X. Hong, S. Sun, C. Zhen, C. Hu, G. Liu and H. Cheng, *Prog. Nat. Sci. Mater. Int.*, 2018, **28**, 183.
- 197 E. Vorobyeva, Z. Chen, S. Mitchell, R. K. Leary, P. Midgley, J. M. Thomas, R. Hauert, E. Fako, N. López and J. Pérez-Ramírez, *J. Mater. Chem. A*, 2017, **5**, 16393.
- 198 J. Wu, N. Li, X.-H. Zhang, H.-B. Fang, Y.-Z. Zheng and X. Tao, *Appl. Catal. B Environ.*, 2018, **226**, 61.
- 199 N. Hellgren, R. T. Haasch, S. Schmidt, L. Hultman and I. Petrov, *Carbon N. Y.*, 2016, **108**, 242.
- 200 J.-C. Wang, H.-C. Yao, Z.-Y. Fan, L. Zhang, J.-S. Wang, S.-Q. Zang and Z.-J. Li, *ACS Appl. Mater. Interfaces*, 2016, **8**, 3765–3775.
- 201 S. W. Cao, Y. P. Yuan, J. Fang, M. M. Shahjamali, F. Y. C. Boey, J. Barber, S. C. Joachim Loo and C. Xue, *Int. J. Hydrogen Energy*, 2013, **38**, 1258–1266.
- 202 W. Xing, G. Chen, C. Li, Z. Han, Y. Hu and Q. Meng, *Nanoscale*, 2018, **10**, 5239–5245.
- 203 J. F. Moulder, J. Chastain, W. F. Stickle, P. E. Sobol and K. D. Bomben, *Handbook of x-ray photoelectron spectroscopy: a reference book of standard spectra for identification and interpretation of XPS data*, Physical Electronics Division, Perkin-Elmer Corporation, 1992.
- 204 M. Z. Rahman, P. C. Tapping, T. W. Kee, R. Smernik, N. Spooner, J. Moffatt, Y. Tang, K. Davey and S. Z. Qiao, *Adv. Funct. Mater.*, 2017, **27**, 1702384.
- 205 T. Song, P. Zhang, J. Zeng, T. Wang, A. Ali and H. Zeng, *ChemCatChem*, 2017, **9**, 4035–4042.
- 206 M. Li, H. Wang, X. Li, S. Zhang, J. Han, A. F. Masters, T. Maschmeyer and X. Liu, *ChemCatChem*, 2018, **10**, 581–589.
- 207 G. Shi, L. Yang, Z. Liu, X. Chen, J. Zhou and Y. Yu, *Appl. Surf. Sci.*, 2018, **427**, 1165–1173.
- 208 G. Li, J. Shi, G. Zhang, Y. Fang, M. Anpo and X. Wang, *Res. Chem. Intermed.*, 2017, **43**, 5137–5152.
- 209 J. T. Yin, Z. Li, Y. Cai, Q. F. Zhang and W. Chen, *Chem. Commun.*, 2017, **53**, 9430–9433.
- 210 Y. Li, W. Ho, K. Lv, B. Zhu and S. C. Lee, *Appl. Surf. Sci.*, 2018, **430**, 380–389.
- 211 Z. Pan, P. Niu, M. Liu, G. Zhang, Z. Zhu and X. Wang, *ChemSusChem*, 2020, **13**, 888–892.
- 212 J. C. Sánchez-López, C. Donnet, F. Lefèbvre, C. Fernández-Ramos and A. Fernández, *J. Appl. Phys.*, 2001, **90**, 675–681.
- 213 D. L. B. Robert M. Silverstein, Francis X. Webster, David J. Kiemle, *Spectrometric Identification of Organic Compounds*, John Wiley & Sons, Ltd, Chichester, 8th edn., 2014.
- 214 S. A. Richards and J. C. Hollerton, *Essential Practical NMR for Organic Chemistry | Wiley*, John Wiley & Sons, Ltd, Chichester, First., 2011.
- 215 W. Iqbal, B. Yang, X. Zhao, M. Rauf, M. Waqas, Y. Gong, J. Zhang and Y. Mao, *Catal. Sci. Technol.*, 2018, **8**, 4576–4599.
- 216 J. Zhang, Y. Chen and X. Wang, *Energy Environ. Sci.*, 2015, **8**, 3092–3108.
- 217 G. Zhang, Z. A. Lan and X. Wang, *Chem. Sci.*, 2017, **8**, 5261–5274.
- 218 A. L. Linsebigler, G. Lu and J. T. Yates, *Chem. Rev.*, 1995, **95**, 735–758.
- 219 H. Shi, G. Chen, C. Zhang and Z. Zou, *ACS Catal.*, 2014, **4**, 3637–3643.

- 220 Z. Wang, Y. Huo, Y. Fan, R. Wu, H. Wu, F. Wang and X. Xu, *J. Photochem. Photobiol. A Chem.*, 2018, **358**, 61–69.
- 221 M. Li, L. Zhang, X. Fan, Y. Zhou, M. Wu and J. Shi, *J. Mater. Chem. A*, 2015, **3**, 5189–5196.
- 222 F. Dong, Z. Zhao, T. Xiong, Z. Ni, W. Zhang, Y. Sun and W.-K. K. Ho, *ACS Appl. Mater. Interfaces*, 2013, **5**, 11392–11401.
- 223 H. Shi, S. Long, J. Hou, L. Ye, Y. Sun, W. Ni, C. Song, K. Li, G. G. Gurzadyan and X. Guo, *Chem. – A Eur. J.*, 2019, **25**, 5028–5035.
- 224 M. S. Akple, T. Ishigaki and P. Madhusudan, *Environ. Sci. Pollut. Res.*, 2020, **27**, 22604–22618.
- 225 M. Shen, L. Zhang, M. Wang, J. Tian, X. Jin, L. Guo, L. Wang and J. Shi, *J. Mater. Chem. A*, 2019, **7**, 1556–1563.
- 226 Z. Zhang, J. Huang, M. Zhang, Q. Yuan and B. Dong, *Appl. Catal. B Environ.*, 2015, **163**, 298–305.
- 227 R. Kuriki, C. S. K. Ranasinghe, Y. Yamazaki, A. Yamakata, O. Ishitani and K. Maeda, *J. Phys. Chem. C*, 2018, **122**, 16795–16802.
- 228 R. Godin, Y. Wang, M. A. Zwijnenburg, J. Tang and J. R. Durrant, *J. Am. Chem. Soc.*, 2017, **139**, 5216–5224.
- 229 Q. Ruan, T. Miao, H. Wang and J. Tang, *J. Am. Chem. Soc.*, 2020, **142**, 2795–2802.
- 230 H. Kasap, R. Godin, C. Jeay-Bizot, D. S. Achilleos, X. Fang, J. R. Durrant and E. Reisner, *ACS Catal.*, 2018, **8**, 6914–6926.
- 231 H. Zhang, Y. Chen, R. Lu, R. Li and A. Yu, *Phys. Chem. Chem. Phys.*, 2016, **18**, 14904–14910.
- 232 K. Wada, C. S. K. Ranasinghe, R. Kuriki, A. Yamakata, O. Ishitani and K. Maeda, *ACS Appl. Mater. Interfaces*, 2017, **9**, 23869–23877.
- 233 H. Kasap, C. A. Caputo, B. C. M. M. Martindale, R. Godin, V. W. H. Lau, B. V. Lotsch, J. R. Durrant and E. Reisner, *J. Am. Chem. Soc.*, 2016, **138**, 9183–9192.
- 234 J. Liu, H. Shi, Q. Shen, C. Guo and G. Zhao, *Green Chem.*, 2017, **19**, 5900–5910.
- 235 R. Kuriki, H. Matsunaga, T. Nakashima, K. Wada, A. Yamakata, O. Ishitani and K. Maeda, *J. Am. Chem. Soc.*, 2016, **138**, 5159–5170.
- 236 K. Maeda, D. An, C. S. Kumara Ranasinghe, T. Uchiyama, R. Kuriki, T. Kanazawa, D. Lu, S. Nozawa, A. Yamakata, Y. Uchimoto and O. Ishitani, *J. Mater. Chem. A*, 2018, **6**, 9708–9715.
- 237 H. Sun, K. Wei, D. Wu, Z. Jiang, H. Zhao, T. Wang, Q. Zhang and P. K. Wong, *Appl. Catal. B Environ.*, 2020, **264**, 118480.
- 238 Y. Wang, X. Liu, X. Han, R. Godin, J. Chen, W. Zhou, C. Jiang, J. F. Thompson, K. B. Mustafa, S. A. Shevlin, J. R. Durrant, Z. Guo and J. Tang, *Nat. Commun.*, 2020, **11**, 2531.
- 239 J. Coates, *Interpretation of Infrared Spectra, A Practical Approach, Encyclopedia of Analytical Chemistry*, John Wiley & Sons, Ltd, Chichester, UK, 2006.
- 240 L. Cabo-Fernandez, A. R. Neale, F. Braga, I. V. Sazanovich, R. Kostecki and L. J. Hardwick, *Phys. Chem. Chem. Phys.*, 2019, **21**, 23833–23842.
- 241 P. F. McMillan, V. Lees, E. Quirico, G. Montagnac, A. Sella, B. Reynard, P. Simon, E. Bailey, M. Deifallah and F. Corà, *J. Solid State Chem.*, 2009, **182**, 2670–2677.
- 242 T. Komatsu, *Macromol. Chem. Phys.*, 2001, **202**, 19–25.
- 243 W. J. Ong, L. K. Putri, Y. C. Tan, L. L. Tan, N. Li, Y. H. Ng, X. Wen and S. P. Chai, *Nano Res.*, 2017, **10**, 1673–1696.
- 244 J. Ma, C. Wang and H. He, *Appl. Catal. B Environ.*, 2016, **184**, 28–34.
- 245 J. Jiang, L. Ou-Yang, L. Zhu, A. Zheng, J. Zou, X. Yi and H. Tang, *Carbon N. Y.*, 2014, **80**, 213–221.
- 246 W.-J. Ong, L.-L. Tan, S.-P. Chai and S.-T. Yong, *Dalt. Trans.*, 2015, **44**, 1249–1257.
- 247 S. Wan, M. Ou, X. Wang, Y. Wang, Y. Zeng, J. Ding, S. Zhang and Q. Zhong, *Dalt. Trans.*, 2019, **48**, 12070–12079.
- 248 T. Giannakopoulou, I. Papailias, N. Todorova, N. Boukos, Y. Liu, J. Yu and C. Trapalis, *Chem. Eng. J.*, 2017, **310**, 571–580.
- 249 Z. A. Lan, G. Zhang and X. Wang, *Appl. Catal. B Environ.*, 2016, **192**, 116–125.
- 250 J. Xu, L. Zhang, R. Shi and Y. Zhu, *J. Mater. Chem. A*, 2013, **1**, 14766.
- 251 A. Kumar, P. Kumar, R. Borkar, A. Bansiwala, N. Labhsetwar and S. L. Jain, *Carbon N. Y.*, 2017, **123**, 371–379.
- 252 E. Quirico, G. Montagnac, V. Lees, P. F. McMillan, C. Szopa, G. Cernogora, J. N.

- Rouzaud, P. Simon, J. M. Bernard, P. Coll, N. Fray, R. D. Minard, F. Raulin, B. Reynard and B. Schmitt, *Icarus*, 2008, **198**, 218–231.
- 253 S. Wood, J. R. Hollis and J.-S. Kim, *J. Phys. D. Appl. Phys.*, 2017, **50**, 073001.
- 254 A. E. Bragg, W. Yu, J. Zhou and T. Magnanelli, *J. Phys. Chem. Lett.*, 2016, **7**, 3990–4000.
- 255 A. C. Benniston, P. Matousek and A. W. Parker, *J. Raman Spectrosc.*, 2000, **31**, 503–507.
- 256 S. K. Sahoo, S. Umapathy and A. W. Parker, *Appl. Spectrosc.*, 2011, **65**, 1087–1115.
- 257 A. C. Benniston, P. Matousek, I. E. McCulloch, A. W. Parker and M. Towrie, *J. Phys. Chem. A*, 2003, **107**, 4347–4353.
- 258 N. Everall, T. A. Hahn, P. M. Atousek, A. W. Parker and M. I. Towrie, *Appl. Spectrosc.*, 2001, **55**, 1701–1708.
- 259 P. Matousek, M. Towrie and A. W. Parker, *J. Raman Spectrosc.*, 2002, **33**, 238–242.
- 260 K. Vikman, H. Iitti, P. Matousek, M. Towrie, A. W. Parker and T. Vuorinen, *Vib. Spectrosc.*, 2005, **37**, 123–131.
- 261 P. Matousek, M. Towrie, A. Stanley and A. W. Parker, *Appl. Spectrosc.*, 1999, **53**, 1485–1489.
- 262 P. Matousek, M. Towrie, C. Ma, W. M. Kwok, D. Phillips, W. T. Toner and A. W. Parker, *J. Raman Spectrosc.*, 2001, **32**, 983–988.
- 263 A. Vlček Jr., I. R. Farrell, D. J. Liard, P. Matousek, M. Towrie, A. W. Parker, D. C. Grills and M. W. George, *J. Chem. Soc. Dalton Trans.*, 2002, 701–712.
- 264 M. C. H. Prieto, P. Matousek, M. Towrie, A. W. Parker, M. Wright, A. W. Ritchie and N. Stone, *J. Biomed. Opt.*, 2005, **10**, 044006.
- 265 Q. Liu, L. Ai and J. Jiang, *J. Mater. Chem. A*, 2018, **6**, 4102–4110.
- 266 M. Jourshabani, Z. Shariatnia and A. Badiei, *J. Colloid Interface Sci.*, 2017, **507**, 59–73.
- 267 Y.-S. Jun, E. Z. Lee, X. Wang, W. H. Hong, G. D. Stucky and A. Thomas, *Adv. Funct. Mater.*, 2013, **23**, 3661–3667.
- 268 G. Dong, K. Zhao and L. Zhang, *Chem. Commun.*, 2012, **48**, 6178.
- 269 G. Zhang, Z.-A. Lan, L. Lin, S. Lin and X. Wang, *Chem. Sci.*, 2016, **7**, 3062–3066.
- 270 H. Lan, Y. Tang, X. Zhang, S. You, Q. Tang, X. An, H. Liu and J. Qu, *Chem. Eng. J.*, 2018, **345**, 138–146.
- 271 J. Yuan, X. Yi, Y. Tang, C. Liu and S. Luo, *ACS Appl. Mater. Interfaces*, 2020, **12**, 19607–19615.
- 272 C. Ye, J. X. Li, Z. J. Li, X. B. Li, X. B. Fan, L. P. Zhang, B. Chen, C. H. Tung and L. Z. Wu, *ACS Catal.*, 2015, **5**, 6973–6979.
- 273 G. Zhao, H. Pang, G. Liu, P. Li, H. Liu, H. Zhang, L. Shi and J. Ye, *Appl. Catal. B Environ.*, 2017, **200**, 141–149.
- 274 Y. Wang, L. Guo, Y. Zeng, H. Guo, S. Wan, M. Ou, S. Zhang and Q. Zhong, *ACS Appl. Mater. Interfaces*, 2019, **11**, 30673–30681.
- 275 Y. Yang, Z. Tang, B. Zhou, J. Shen, H. He, A. Ali, Q. Zhong, Y. Xiong, C. Gao, A. Alsaedi, T. Hayat, X. Wang, Y. Zhou and Z. Zou, *Appl. Catal. B Environ.*, 2020, **264**, 118470.
- 276 S. Liu, F. Chen, S. Li, X. Peng and Y. Xiong, *Appl. Catal. B Environ.*, 2017, **211**, 1–10.
- 277 G. Liu, G. Zhao, W. Zhou, Y. Liu, H. Pang, H. Zhang, D. Hao, X. Meng, P. Li, T. Kako and J. Ye, *Adv. Funct. Mater.*, 2016, **26**, 6822–6829.
- 278 P. Niu, Y. Yang, J. C. Yu, G. Liu and H. M. Cheng, *Chem. Commun.*, 2014, **50**, 10837–10840.
- 279 Y. He, L. Zhang, M. Fan, X. Wang, M. L. Walbridge, Q. Nong, Y. Wu and L. Zhao, *Sol. Energy Mater. Sol. Cells*, 2015, **137**, 175–184.
- 280 Y. He, Y. Wang, L. Zhang, B. Teng and M. Fan, *Appl. Catal. B Environ.*, 2015, **168–169**, 1–8.
- 281 K. Wang, J. Fu and Y. Zheng, *Appl. Catal. B Environ.*, 2019, **254**, 270–282.
- 282 X. Liu, P. Wang, H. Zhai, Q. Zhang, B. Huang, Z. Wang, Y. Liu, Y. Dai, X. Qin and X. Zhang, *Appl. Catal. B Environ.*, 2018, **232**, 521–530.
- 283 Y. Bai, L. Ye, L. Wang, X. Shi, P. Wang, W. Bai and P. K. Wong, *Appl. Catal. B Environ.*, 2016, **194**, 98–104.
- 284 F. Yang, M. Lublow, S. Orthmann, C. Merschjann, T. Tyborski, M. Rusu, S. Kubala, A. Thomas, R. Arrigo, M. Hävecker and T. Schedel-Niedrig, *ChemSusChem*, 2012, **5**, 1227–1232.

4

Carbon Nitride Hybrid Materials

4.1 Introduction

It is widely known that bulk carbon nitride (CN) synthesised via traditional calcination methods suffer from poor photoactivities.^{1,2,11,12,3-10} There are a great many approaches that have been reported in the literature for improving carbon nitride materials, including nanostructure control, electronic structure modification and the formation of heterostructures. Electronic structure modification was explored in Chapter 3, this chapter focuses on nanostructure control and heterostructure formation through addition of molecular co-catalysts.

4.1.1 Nanostructure Control

Modification of the carbon nitride structure and introducing nano-structuring have been proven as effective methodologies for improvement of photocatalytic activities. Prior to addition of the molecular electrocatalysts to make the hybrid structure it is also important to maximise surface area to increase the available sites for catalyst binding. Strategies involve either top-down (exfoliation) or bottom up (templating) approaches and can result in increased surface area, porosity and in some cases charge separation, which all can lead to enhanced photocatalytic activity.^{4,12-16}

4.1.1.1 Exfoliation (top-down)

One of the main reasons for poor photoactivity of bulk carbon nitride obtained from usual thermal condensation procedures is the very low surface areas.^{4,12-16} Exfoliation of bulk carbon nitride to form nanosheets is a generally simple and effective method for enhancing surface area. Typically, exfoliation can be performed in one of three ways, liquid, chemical and thermal exfoliation. These methods lead to the formation of carbon nitride nanosheets with relatively high surface areas^{17,18,27-33,19-26}, altered photo-absorption abilities^{17,18,21,24,26,27,31,33} and in some case has been reported to enhance charge mobility by reducing charge diffusion lengths^{18,24,28}.

Chemical Exfoliation

Chemical exfoliation involves the use of a strong acid to wash the carbon nitrides and form nanosheets.^{19-23,33} Washing in acid does not lead to chemical disintegration of carbon nitride, instead the acid can intercalate into the interlayer space between sheets, forcing them apart

and in some case lead to protonation of the materials. This method has previously been reported to form materials with surface areas up to $200 \text{ m}^2\text{g}^{-1}$ and nanosheets as thin as 0.4 nm, close to the theoretical monolayer carbon nitride thickness of 0.325 nm.²¹³³

Liquid Exfoliation

Liquid exfoliation employs intercalation of solvents to break up the large particles of carbon nitride into smaller particles or sheets.^{34–43} A number of solvents have been utilised including isopropyl alcohol (IPA), water, n-methyl-2-pyrrolidone (NMP), 1,3-butanediol, ethanol (EtOH), methanol (MeOH) and acetone, among others and have been shown via atomic force microscopy (AFM) to produce sheets with ~ 2 nm thickness.^{34,35,44,36–43} Yang *et al* performed exfoliation of carbon nitride in a range of solvents and found that nanosheets produced in IPA and NMP could produce suspensions that were stable for at least 2 days, after undergoing 10 hours of sonication and found that IPA suspensions showed no precipitation after 4 months under ambient conditions.³⁵ These nanosheets can be collected via centrifugation and removal of solvent, but this often leads to re-aggregation of the exfoliated sheets.

Thermal exfoliation

Performing a post-synthesis calcination step on bulk carbon nitride is known as thermal exfoliation. Typically, materials are heated to between 500 °C and 600 °C for several hours and the obtained materials have much higher surface areas and in some case reported to have >10 times larger surface areas over the bulk material.^{17,18,32,24–31} Mostly this step is performed in air^{28–31}, but there are some reports which show that when executed under a different atmosphere, other additional functionalities and structure can be incorporated.

A few groups have reported that by heating under a H₂ atmosphere can not only increase surface area but can also introduce extra hydrogen defects and nitrogen vacancies into the structure.^{17,45} Xia *et al* performed this calcination step under the flow of ammonia and found that the resultant high surface area materials were also endowed with extra amine functionality which was found to increase CO₂ adsorption and in turn photocatalytic CO₂ reduction.¹⁸ Fu *et al* found that heating bulk carbon nitride at 600 °C in the presence of air and under a N₂ flow led to the formation of O-doped carbon nitride nanotubes.²⁴ Thermal exfoliation is a very easy method but can lead to the formation of defects and often product yields are very low.³²

4.1.1.2 Templating (bottom-up)

Carbon nitride precursors can be combined with soft or hard templates, which can be removed during or post-synthesis. These techniques can often lead to the formation of large surface area materials with interesting nanostructures depending on the template used.^{4,12-16} Mesoporous carbon nitrides produced in this way have been found to contain open crystalline pores and large surface area, which can facilitate more efficient mass transfer and free-charge transport, along with enhanced light absorption due to large surface areas and multiple scattering effects.^{2,46}

Hard Template

Typically, the templating procedure involves the combination of silica templates and organic precursors in solution, then removal of solvent and calcination. The template can then be removed using HF or NH_4HF_2 .^{1,46,55-60,47-54} The silica template is often a colloidal suspension of microspheres or microstructures with high surface areas which can interact with amine and aromatic nitrogen groups within the carbon nitride backbone.^{4,12-16,61}

Utilising hard templates can be an effective way to produce these high surface area materials but due to the required removal of the silica template with hazardous chemicals, this method is not environmentally friendly and cannot be transferred to an industrial process.⁵⁰ Also it can leave a small amount of silica in the end product.⁶² Along with silica, there have been a few reports of the use of CaCO_3 ⁶³⁻⁶⁵, anodic aluminium oxide^{66,67} and clays such as smectitic saponite and montmorillonite⁶⁸ as hard templates for carbon nitride synthesis.

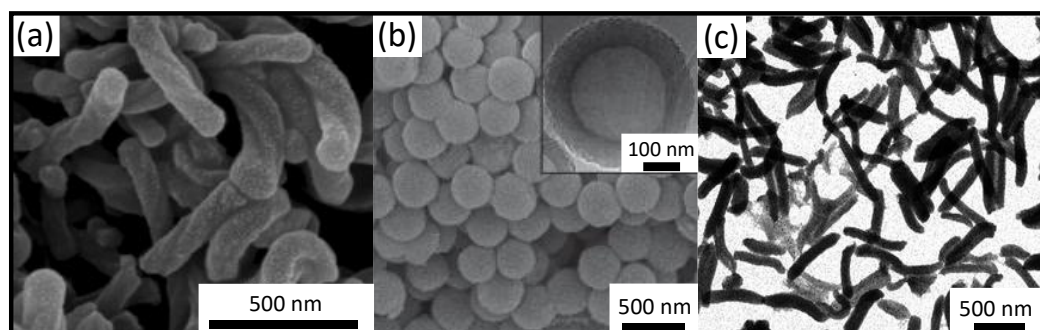


Figure 62 – Scanning electron microscopy (SEM) images of carbon nitrides synthesised using silica templates, (a) helical⁶², (b) hollow nanospheres⁵⁵ and (c) nanowires⁶⁹. Inset (b) transmission electron microscopy (TEM) image.

Soft Template

Using soft templates which do not use harsh chemicals required for template removal can be a good alternative to traditional hard templates as the soft template typically decomposes during the carbon nitride synthesis. But this method can also cause challenges as templates must be chosen based on thermal stability as they are required to decompose before the formation of the carbon nitride and can often lead to carbon doping.^{1,48,70,71}

In 2010, Zhang and co-workers first reported the synthesis of nanoporous carbon nitride using soft templates. They employed a total of 15 different non-ionic surfactants, amphiphilic block polymers and ionic liquids as soft templates for high surface area carbon nitrides.⁷² These carbon nitrides not only had enhanced surface area (reaching a maximum of 299 m²g⁻¹) over the bulk material, but also saw increased conductivity in some cases.

Self-Templating or Supramolecular Pre-Organisation

Nanostructured materials can also be synthesised without the use of an external template and does not require any post-synthesis treatments to remove the template. It relies on the use of noncovalent interactions to form ordered structures or precursor complexes, which can then be calcined to form higher surface area materials and can sometimes introduce interesting morphologies.^{57,58,80–83,70,73–79} Typically 2 or more carbon nitride precursors are combined in ethanol and the complex can be precipitated and then calcined for carbon nitride synthesis.

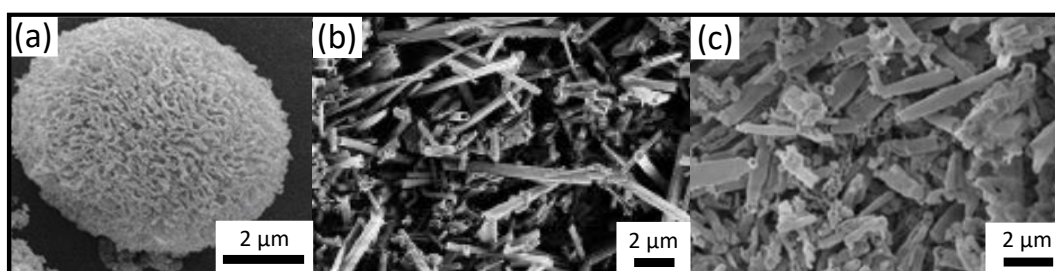


Figure 63 – SEM images of carbon nitrides produced using supramolecular self-assembly taken from references (a)⁸³, (b)⁷³ and (c)⁸².

4.1.2 Heterostructure formation

The formation of heterostructures, composites or heterojunctions of carbon nitride with other materials can often be vital for photocatalysis. There are a number of different methods which can result in enhanced light absorption or increased charge separation giving enhanced photocatalytic activity.

4.1.2.1 Metal Particles

A common method used for improvement of photocatalytic activity on carbon nitride is the attachment of noble metal particles to the surface of the semiconductor. Metal particles at the surface can act as effective electron trapping sites, enhancing charge separation or reducing the overpotential for photocatalytic reactions and enhance photocatalytic performance.^{2,5,11,71,84–89} Pt has been proven to be the most efficient co-catalyst for H₂ evolution and is widely used on carbon nitride for both water splitting and CO₂ reduction reactions.^{4,5,91–100,17,101–110,33,111–113,46,47,54,56,86,90}

Other metals such as Pd^{36,110,114} Au^{115–120} and Ag^{115,121,122} have also been employed as co-catalysts to improve photocatalytic activity to various carbon products. However, the scarcity of noble metals limits their use.^{3,4,9,123} Cheaper transition metals have also been explored such as Cu^{124–126}, Co^{127,128}, Ni^{5,89,129} along with bimetallic particles^{130–133}.

4.1.2.2 Dye-Sensitised

Carbon nitride is well known for having a band gap which typically lies at around 2.7 eV, which means that it can absorb wavelengths of light >460 nm.^{1,3,11,71,89,134–136} Though this lies within the visible region, it still only utilises a small fraction of visible light. Over the years, various dyes have been used to sensitise carbon nitride materials and extend light absorption further into the visible region.^{2,5,6,12,32} For the system to work well, the dye must have visible wavelength absorption and its lowest unoccupied molecular orbital (LUMO) must lie at a more negative potential than the carbon nitride conduction band (CB).⁶ This allows the photogenerated electrons to be injected into the CB of the carbon nitride enhancing charge separation and suppressing recombination.

In 2010, Takanabe *et al* published the first dye-sensitised carbon nitride.¹⁰³ They found that magnesium phthalocyanine combined with mesoporous carbon nitride gave enhanced absorption into visible range and enhanced photoactivity for H₂ evolution, but a Pt co-catalyst was required for H₂ evolution to occur. Since then a range of both organic and metal containing dyes have been used for increased light absorption and improved activity, such as; EosinY^{86,92,94,97,132,137,138}, Erythrosin B^{92,97,138}, Erythrosin Y⁹⁷, acriflavine¹³⁹, fluorescein^{92,97,138}, Rose Bengal⁹⁷, thiazole orange¹⁴⁰ and various phthalocyanines^{91,105,141,142}, among others.

4.1.2.3 Molecular co-catalysts

Molecular catalysts have been used for enhanced photoactivity towards both H₂ evolution and CO₂ reduction, acting as light absorbers or catalytic centres, capturing photogenerated electrons from semiconductors.^{5,6,89,143} For H₂ evolution a few metal complexes have been used as co-catalysts on carbon nitride, including [Ni(bis(1,5-R'-diphospha-3,7-R''-diazacyclooctane))] ²⁺ (NiP)^{144,145}, a Ni-thiourea-triethylamine complex¹⁴⁶, Co(dmgh)₂pyCl and similar cobaloximes^{147,148}.

The first molecular catalyst reported for photocatalytic CO₂ reduction was by Ishitani and co-workers in 2013.⁵¹ They reported the attachment of *cis,trans*-[Ru{4,4'-(CH₂PO₃H₂)₂-2,2'-bipyridine}(CO)₂Cl₂] (RuCP) (Figure 64 (a)) onto carbon nitride and found that the system was capable of photocatalytically reducing CO₂ to HCOOH as the major product (>80% selectivity) along with CO and H₂ in the presence of acetonitrile (MeCN) and triethanolamine (TEOA) (4:1 v/v) solutions under visible illumination (>400 nm). Over the years, Ru mono bipyridine and derivative co-catalysts have been the most studied molecular catalysts on carbon nitride for CO₂ reduction. The researchers involved in the preliminary paper have published many studies that focussed on improving on this initial photocatalytic activity and followed various strategies to do so which included improving the carbon nitride surface area⁶⁰, alteration of attachment groups^{149–155} (Figure 64 (a)) and formation of a binuclear system containing the catalyst (Ru bpy) and a photosensitiser unit (Ru tris-bpy) (Figure 64 (b))^{156,157}. They have also investigated altering the complexes metal centres^{158,159}, deposition of various materials (SiO₂, Ag, Ag₂O, TiO₂) to enhance catalyst loadings and in some cases charge separation^{153,156,158,159}, synthesis of carbon nitride at different temperatures¹⁵⁴ and via

copolymerisation of urea and phenyl urea for extended light absorption and enhanced charge lifetimes¹⁵⁵.

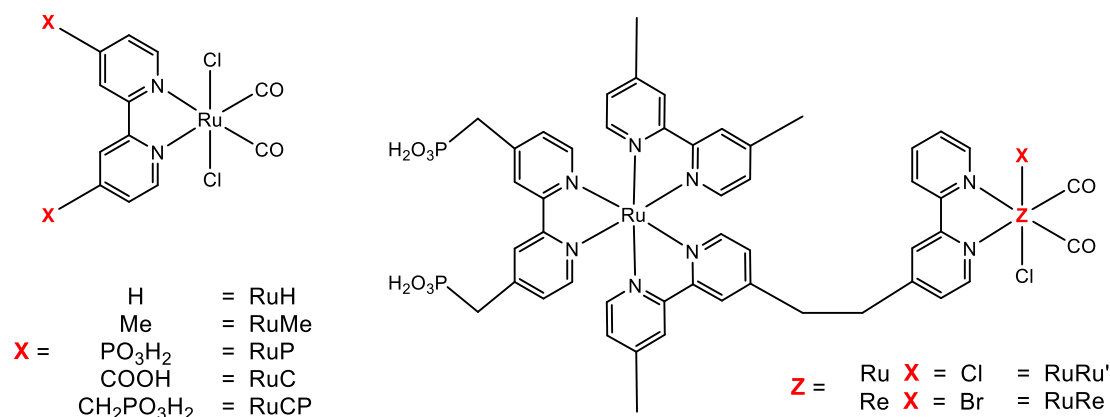


Figure 64 – Structures of Ru 2,2'-bipyridine catalyst used as co-catalysts on carbon nitrides for photocatalytic CO₂ reduction published by Ishitani, Maeda and co-workers.
51,60,157–159,149–156

Other molecular catalysts which have been studied as co-catalysts on carbon nitride for photocatalytic CO₂ reduction include complexes based on Co and Mn bipyridine^{160–164}, Co and Fe quaterpyridine^{165,166}, Co and Fe porphyrins^{167–170}, Co cyclam¹⁷¹, Co phthalocyanine¹⁷² and a heteroleptic Ir complex¹⁷³.

4.1.2.4 Semiconductor Heterojunctions

Semiconductor heterojunctions are typically categorised based on their electronic structure, particularly relative positions of conduction and valence bands.⁹ The 3 categories are type I (straddling alignment), type II (staggered alignment) and z-scheme (liquid phase, solid—state and direct).⁹ Depending on the carbon nitride used and the semiconductor that it is combined with, carbon nitride can be used in all types of heterojunctions as typically it has valence and conduction bands which straddle the water splitting and CO₂ reduction redox potentials.^{90,135,174} A number of semiconductors have been combined with carbon nitride for photocatalytic CO₂ reduction including; TiO₂^{41,175–181}, WO₃^{115,182,183}, Fe₂O₃^{184–186}, ZnO^{187–192}, CdS^{163,193–195}, BiVO₄^{196–198}, among others.^{25,199,208,200–207}

4.1.2.5 Metal-Organic Framework (MOF) Composites

Carbon nitride-MOF hybrid photocatalysts have been shown to have enhanced photoactivities towards CO₂ reduction over bulk carbon nitrides.^{37,209} Hybrid materials can be synthesised via

simple mixing or in-situ formation of MOFs on pre-prepared carbon nitride, forming good contacts between the carbon nitride and MOF allowing for efficient charge transfer across the junction due to π - π interactions between the carbon nitride and organic linkers.^{37,123,209–212} Along with enhanced charge separation the hybrids have extended light absorption and higher surface areas improving photocatalytic activities.^{37,123,210–214} Also MOFs can be used to capture and concentrate CO₂.^{27,123} MOFs that have been used in carbon nitride composites include ZIF-9^{27,123}, UiO-66^{37,214}, MIL-101²¹¹ and ZIF-67²¹³.

4.1.2.6 Carbon Based Systems

For photocatalytic CO₂ reduction, the main carbon based materials which have been used in composites with carbon nitride are reduced graphene oxide (RGO), carbon quantum/nanodots and carbon nanotubes.^{23,215–219} The materials often act as co-catalysts, aiding in charge separation acting as the catalytic centres for CO₂ reduction. RGO has also been proven as an effective redox mediator in Z-scheme systems containing carbon nitride and other semiconductor towards CO₂ reduction.^{220–222}

4.2 Aim of Work

Within the last chapter, 16 carbon nitrides were synthesised, characterised and initial photocatalytic activity for H₂ evolution was evaluated. The aim of this chapter is to take those materials, attach molecular catalysts to their surface and test for CO₂ reduction. The molecular catalysts chosen for study in this work, shown in Figure 65, are Ni^{II}(1,4,8,11-tetraazacyclotetradecane), (NiCyc), Ni^{II}(1,4,8,11-tetraazacyclotetradecane-6-carboxylic acid) (NiCycC), Ni^{II}([(1,4,8,11-tetraazacyclotetradecan-1-yl)methylene]phosphonic acid) (NiCycP) and Fe^{III} tetra(4-carboxylphenyl)porphyrin (FeTCPP).

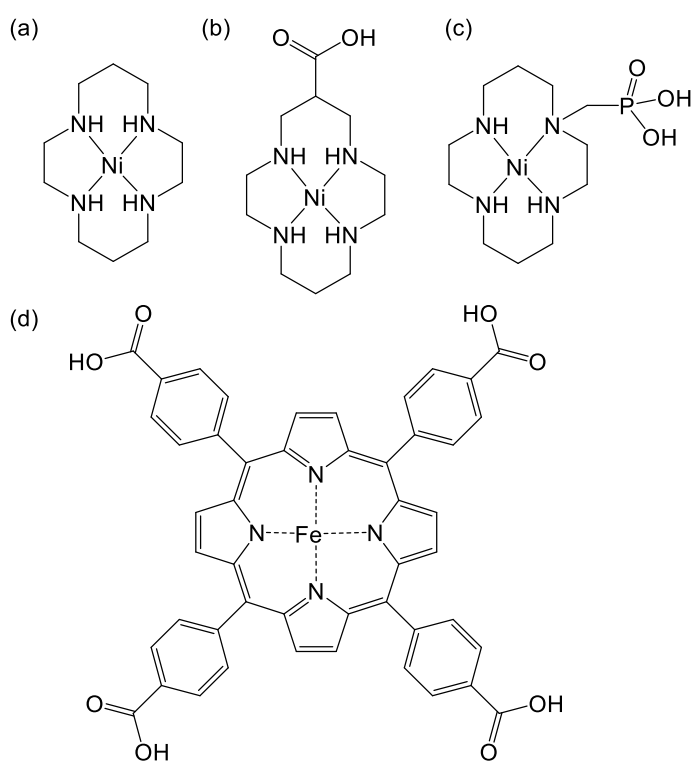


Figure 65 – Molecular catalyst used within this project. (a) Ni^{II}(1,4,8,11-tetraazacyclotetradecane), (NiCyc), (b) Ni^{II}(1,4,8,11-tetraazacyclotetradecane-6-carboxylic acid) (NiCycC), (c) Ni^{II}([(1,4,8,11-tetraazacyclotetradecan-1-yl)methylene]phosphonic acid) (NiCycP) and (d) Fe^{III} tetra(4-carboxylphenyl)porphyrin (FeTCPP)

Ni tetraazacyclotetradecane (cyclam) catalysts were chosen for study as they have previously been shown to electrochemically reduce CO₂ to CO.^{223,224} NiCycP has also been immobilised on to the surface of ZnSe quantum dots and dye-sensitised ZrO₂ particles and has been shown to photocatalytically reduce CO₂, producing CO and H₂ under visible illumination.^{225,226} The Ni^{III/II} couples for NiCyc, NiCycC and NiCycP are at -1.3V vs NHE at pH 5²²⁴, -1.33 V vs NHE

pH 5²²⁴ and -1.23 V vs NHE pH 4²²⁶, respectively, which should mean that charge transfer to the catalyst should be possible for most of the carbon nitrides presented in this work.

It is well known that most carbon nitrides contain amine functionalities and it has been reported that these groups could act as hydrogen bonding motifs, interacting with carboxylic and phosphonic acid functionalities on molecular catalyst anchoring them to the surface.^{143,158} Furthermore, there are many reports of the successful attachments of both dyes and molecular catalysts onto the carbon nitride surface with phosphonic and carboxylic acid groups.^{51,60,153–159,144,145,147–152} Although NiCyc has no anchoring groups it has been found to reduce CO₂ under illumination when in solution with Ru bpy dye in solution^{227–229}, so charge transfer could occur if the NiCyc is in solution and in close proximity to the carbon nitride. In 2020, it was reported that a Co cyclam catalyst was immobilised onto the surfaces of carbon nitride, TiO₂ and N-Ta₂O₅ for photocatalytic CO₂ reduction.¹⁷¹ The paper showed that the systems were capable of reducing CO₂ to CO under UV and/or visible illumination and was confirmed via isotopic labelling infrared studies. The highest activities obtained under visible illumination (>360 nm and >420 nm) were observed for the complexes attached to the carbon nitride material. So far there have been no reports of any Ni cyclam catalysts attached to carbon nitrides for photocatalytic CO₂ reduction.

Both carbon nitride and porphyrin materials contain π conjugated planar layers, meaning the FeTCPP can attach to carbon nitride via π - π stacking.^{6,89,96,168,169,230} Furthermore, the carboxylic acid groups can form hydrogen bonds with the amino groups on the carbon nitride.¹⁶⁸ The ligand TCPP has previously been used on carbon nitride, acting as a dye enhancing visible light absorption and in turn photocatalytic H₂ evolution.^{96,230} The TCPP porphyrin has also been metalated with Co, Zn, Cu and Fe and used in combination with carbon nitride for a number of photocatalytic applications.^{168,169,231–234}

In 2018, He and co-workers reported the combination of carbon nitride with FeTCPP for use as a photocatalyst for CO₂ reduction.¹⁶⁸ They found that the CN/FeTCPP hybrid was capable of reducing CO₂ to CO with 98% selectivity when the photocatalytic experiment was performed in acetonitrile/water/triethanolamine (3:1:1, v:v:v) under visible illumination (420 nm < λ > 780 nm) with an intensity of 220 mWcm⁻². They investigated different FeTCPP loadings onto

carbon nitride, attached via mechanical mixing in ethanolic solution but did not give full procedure details or quantify the FeTCPP loading. Blank experiments were performed and indicated that the carbon nitride, FeTCPP, light and CO₂ were all required for CO to be produced, but they did not perform isotopic labelling experiments to confirm the origin of the produced CO. Within this work, they also reported the redox couples for Fe^{III/II}, Fe^{II/I} and Fe^{I/0} are 0.031 V, -0.61 V and -1.3 V vs NHE, measured under Ar in dimethylformamide (DMF) and stated that it is capable of accepting electrons from carbon nitride.

By the time that this paper was published, immobilisation of FeTCPP onto the carbon nitrides was already well underway in this project and initial photocatalytic experiments were being performed. Within this paper they focussed on catalyst loadings on a single carbon nitride, whilst this project has focused on attachment to a range of different carbon nitrides and testing these hybrid systems for photocatalytic CO₂ reduction in aqueous solution.

Very recently these researchers published another paper in which they combined carbon nitride/FeTCPP hybrid catalyst with carbon dots for enhanced photocatalytic CO₂ reduction.¹⁶⁹ The carbon dots were produced via thermal pyrolysis of citric acid and urea powders, similar to methods of co-polymerisation which generally lead to carbon doping. They found that carbon dots gave enhanced light absorption, interfacial charge separation and promoted electron transfer leading to these enhanced activities.

The materials synthesised and characterised in Chapter 3; CN-BA, CN-Precursor, CN-UT, CN-Temp and CN-Time, have been combined with the chosen catalysts. Each of these molecular catalysts should, in some way, be able to interact with the carbon nitride materials synthesised in this work and in most cases the carbon nitrides band structure should allow for electron transfer to the co-catalyst. After initial testing, only the CN-BA series were carried forward for further modification and testing.

4.3 Results and Discussion

4.3.1 Initial Attachment and Screening of Co-catalysts

Immobilisation of NiCycP on ZnSe quantum dots and ZrO₂ particles has previously been performed by soaking the semiconductors in NiCycP/ethanol solutions for several hours.^{225,226} Soaking experiments were performed on a selection of the carbon nitrides, but diffuse reflectance infrared Fourier transform spectroscopy (DRIFTS) and inductively coupled plasma optical emission spectrometry (ICP OES) could not confirm the attachment of the NiCycP on the carbon nitrides. Details of soaking and stripping procedures can be found in Chapter 2, in sections 2.2 Modification of Materials and 2.1.1 General Methods, respectively. This may have been due to the quantity attached to the surface being lower than the detection limit of the equipment, likely because of the carbon nitrides low surface areas. In light of this, it was decided to have all Ni cyclam catalysts remain in solution for the photocatalysis experiments, this would ensure that some co-catalyst might be in contact with the carbon nitride surface throughout the experiments, also the Ni cyclam catalysts only weakly absorb visible light, so do not act as internal filters.^{223–225} Ni cyclams were kept in solution at a concentration of 1mM and catalysts were left to soak for 24 hours, prior to purging and illumination.

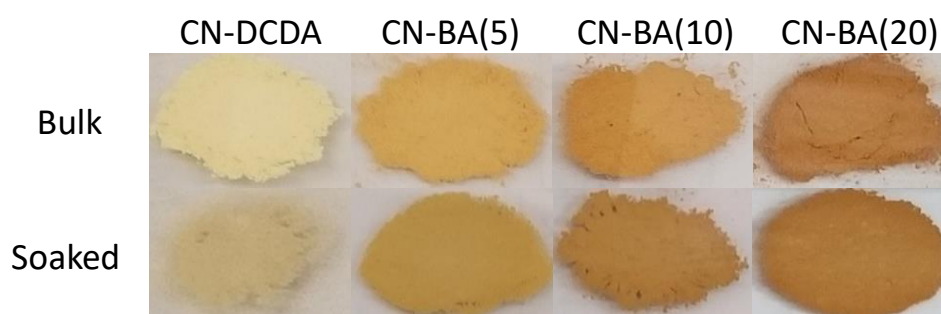


Figure 66 – Images of the CN-BA series of materials pre- and post-soaking in FeTCCP solutions; CN-DCDA, CN-BA(5), CN-BA(10) and CN-BA(20).

For investigation of CN/FeTCCP hybrids, each of the carbon nitrides was pre-soaked in 90 μ M FeTCCP ethanolic solution for 24 hours, washed three times with ethanol and dried at 60 $^{\circ}$ C overnight. Unfortunately, there was not enough of the CN-UT series of materials for the soaking experiments, so initial screening of these materials with FeTCCP were not performed.

To check for attachment of FeTCPP onto the carbon nitride surfaces, initial characterisation of the soaked CN-BA series was carried out. The images in Figure 66 show the CN-BA series materials pre- and post-soaking in FeTCPP solutions for 24 hours and show that most of the materials show a slight colour change after soaking.

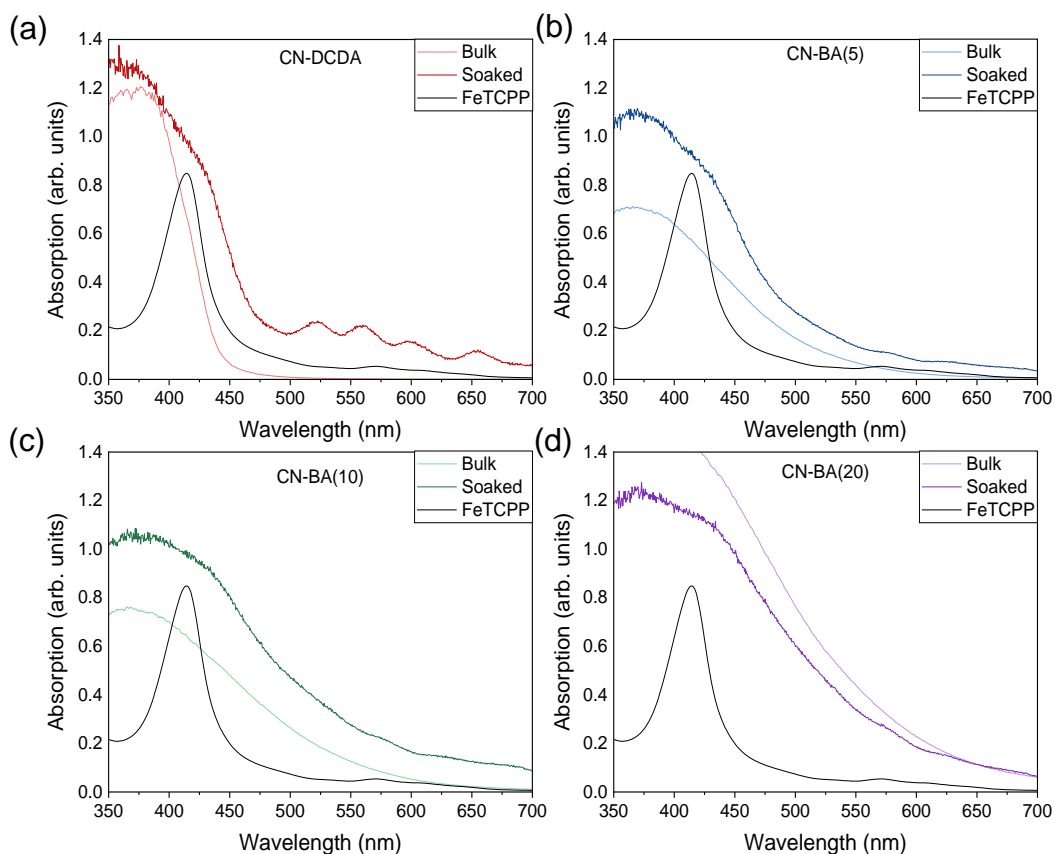


Figure 67 – UV-Vis diffuse reflectance spectra (Kubelka-Munk) of (a) CN-DCDA, (b) CN-BA(5), (c) CN-BA(10) and (d) CN-BA(20) pre- and post-soaking in FeTCPP solution and UV-Vis spectra of 90 μ M FeTCPP ethanolic solution for comparison.

Though apparent from the images, that some FeTCPP had attached to the carbon nitrides ultraviolet-visible diffuse reflectance spectroscopy (UV-Vis DRS) and DRIFTS were employed to further confirm the presence of FeTCPP on the carbon nitride surface. UV-Vis spectra of the soaked bulk samples and the FeTCPP in ethanolic solution can be found in Figure 67 and show that after soaking, CN-DCDA, CN-BA(5) and CN-BA(10) have enhanced light absorption, with CN-DCDA showing peaks that can be assigned to the FeTCPP complex. Figure 67 (a) shows a strong Soret band appearing at 420 nm and weak Q- bands at 532, 572, 618 and 645 nm, attributed to π - π^* transitions, characteristic of Fe porphyrin complexes.^{168,231,235,236} Upon soaking onto the carbon nitride, these peaks appear to shift by 5

nm to lower wavelengths, which can be attributed π - π stacking of the FeTCPP on the carbon nitride.^{96,231,233,235}

Comparison of the DRIFTS spectra of the bulk and soaked samples in Figure 68 do not show any new peaks which could be identified as FeTCPP on the soaked samples. This is likely due to the quantity of FeTCPP on the samples being small and the characteristic stretches for the FeTCPP being masked by the vibrational modes of the carbon nitride. Further characterisation of these samples was not carried out as they were for screening experiments. A more detailed analysis was performed on the exfoliated samples later on in this chapter.

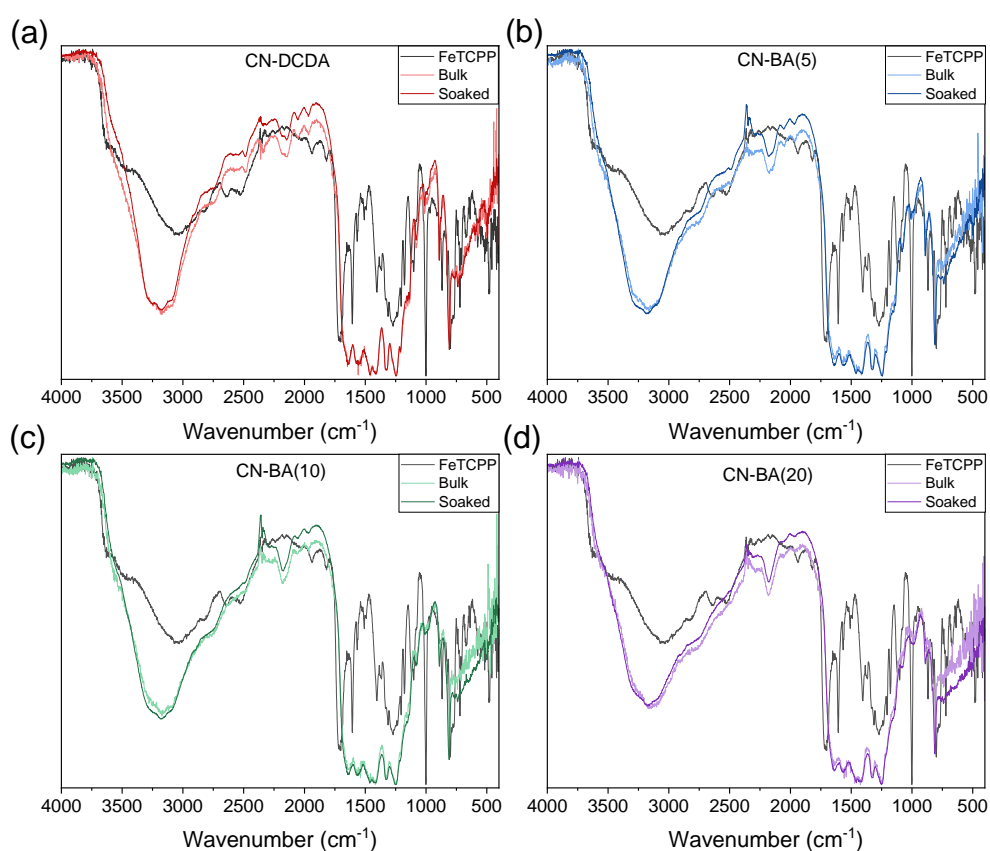


Figure 68 – DRIFTS spectra of (a) CN-DCDA, (b) CN-BA(5), (c) CN-BA(10) and (d) CN-BA(20) pre- and post-soaking in FeTCPP solution.

Screening experiments of the carbon nitrides for photocatalytic CO₂ reduction in the presence of molecular catalysts were performed on the high throughput set-up which consists of an array of white LEDs at ~100 mWcm⁻² and allows testing of up to 10 samples at a time (described in detail in Chapter 2). All carbon nitrides were tested on a scale of 2 mg of photocatalyst in 2 mL of 10 mM ethylenediaminetetraacetic acid disodium salt (EDTA) hole

scavenger in glass vials, purged with CO₂ for 30 minutes then illuminated for 4 hours, using the high throughput system. Gases evolved were sampled at the end of the 4 hours of illumination and quantified via gas chromatography (GC). The quantities of CO and H₂ evolved after photocatalytic screening experiments can be seen in Figure 69 and show that out of the chosen catalysts, that the FeTCCP soaked samples appear to be the highest performing hybrids, producing significantly more CO, than the Ni cyclam hybrids, which all show similarly low levels of activity. The low activities may be a result of low levels of the catalyst attaching or in close proximity to the carbon nitride surfaces, due to low surface areas, leading to poor charge transfer to the catalyst and low levels of activity.

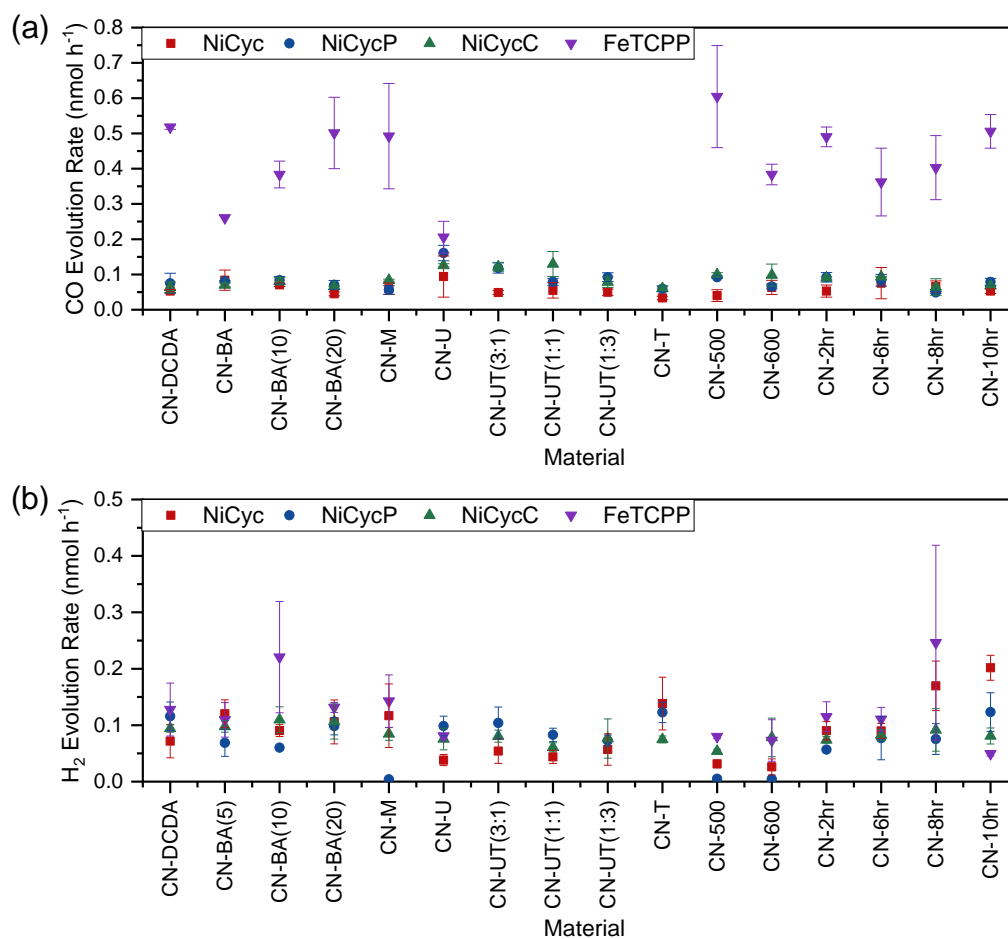


Figure 69 - Rate of (a) CO and (b) H₂ evolved in nmol per hour for 2 mg of photocatalyst in 2 ml 10 mM EDTA over 4 hours visible light irradiation at ~100 mWcm⁻² in a glass vial, tested on the screening set-up. NiCyc, NiCycC and NiCycP were used as co-catalysts in solution at 1 mM concentration and samples were left to soak in the dark for 24 hours prior to purging and illumination.

Since the CN/FeTCCP hybrids showed the highest activity, the CN-DCDA/FeTCCP sample was carried forward for further study. A range of experiments, including blank studies without

the presence of CO₂ or catalyst components and variation of the solvent mixtures used, were performed to confirm the CO being produced was due to photocatalytic CO₂ reduction over the CN-DCDA/FeTCPP catalyst, the results of which can be found in Figure 70. Initially, the results seemed positive as the CN-DCDA/FeTCPP in 10mM EDTA showed higher CO evolution under CO₂ than under N₂, also greater levels of activity were observed for the combined hybrid over the singular components. However, tests in different solutions mixtures and co-catalysts show that the activity that was observed was not true CO₂ reduction, as most experiments gave similar levels of CO under N₂ and CO₂. As with the Ni cyclam catalyst, the likely cause of lack of activity is due to low levels of catalyst attachment arising from low surface areas. The next step was to investigate increasing the surface areas of these materials.

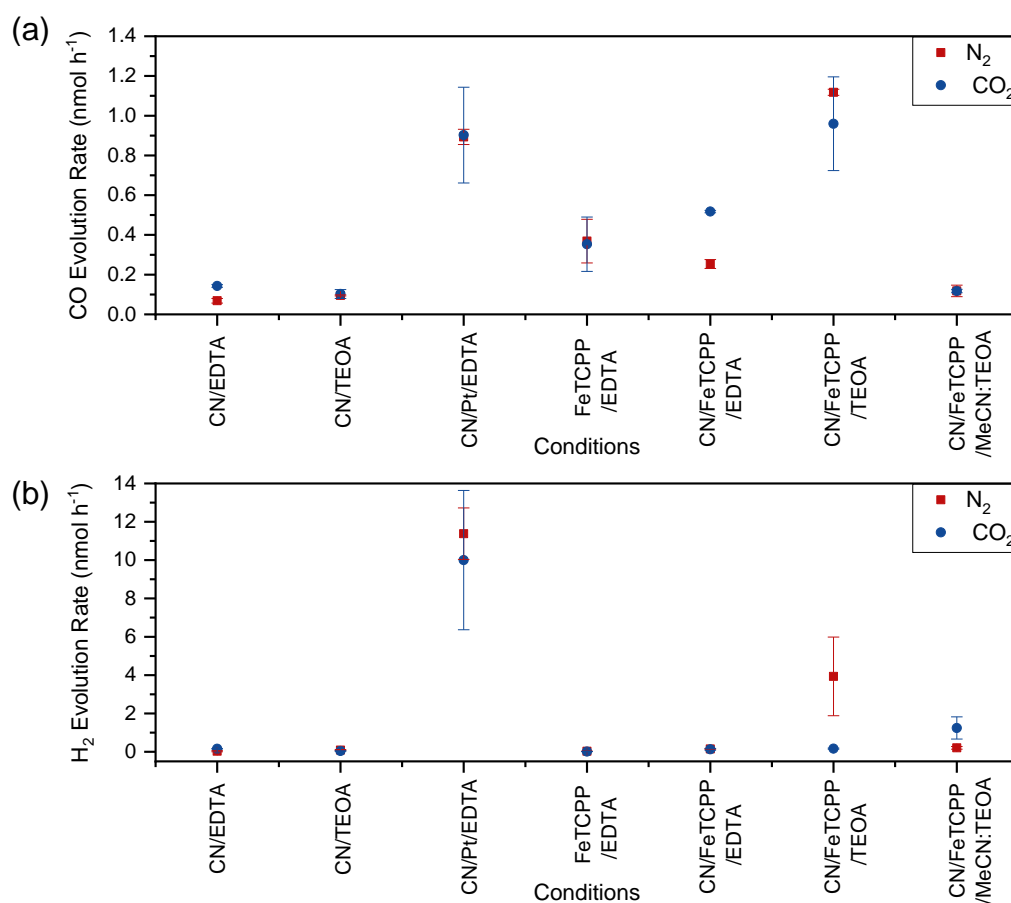


Figure 70 - Rate of (a) CO and (b) H₂ evolved in nmol per hour for 2 mg of photocatalyst in 2 ml of solution over 4 hours visible light irradiation at ~100 mWcm⁻² in a glass vial, tested on the screening set-up. Solution used; EDTA (10 mM EDTA in water), TEOA (10 % v/v TEOA in water) and MeCN:TEOA (4:1 v:v).

4.3.2 Exfoliation of Carbon nitrides

Increasing the surface areas of carbon nitrides can be done using a range of methods, including exfoliation of the bulk material and synthesis using templates.^{1,17,26–33,46,47,18,48–57,19,58–60,70,71,20–25} Exfoliation of the bulk materials was attempted via ultrasonication and acid washing, but due to the ultrasonic probe eroding and excessive washing procedures, thermal exfoliation was chosen to prepare higher surface area materials. In the last chapter, it was found that, of all the materials synthesised within this work, the CN-BA series showed the greatest variation and most interesting trends in electronic structure, charge lifetimes and photocatalytic activity, so these materials were chosen for further study. For exfoliation of the bulk carbon nitrides, a larger quantity of each material was required, so the CN-BA series was re-synthesised and re-characterised and showed little difference when compared with the original series. High surface area (HSA) materials were prepared by loading 400 mg of bulk carbon nitride into an open alumina crucible and calcining at 500 °C for 2 hours in air. Typically, when thermally exfoliating bulk materials, high surface area materials were obtained in 30–50% yields.

4.3.2.1 Characterisation

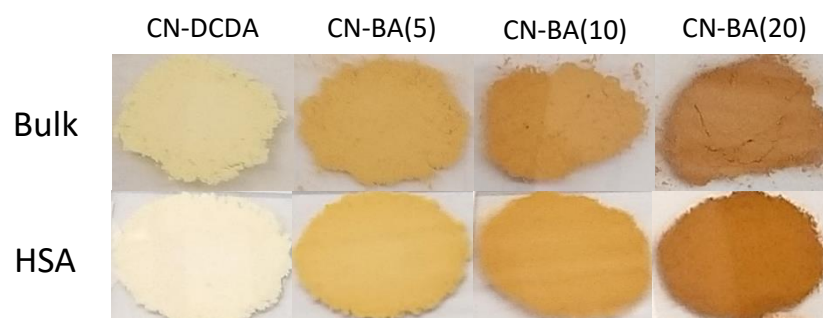


Figure 71 – Images of the bulk and high surface area materials.

Images of the bulk and exfoliated CN-BA series materials can be found in Figure 71. Elemental analysis (CHN) was conducted on the bulk and exfoliated materials and the results are summarised in Table 24. After exfoliation, the materials show the same trends in composition across the series, that are observed in the bulk, that with increasing barbituric acid content, the C:N ratios increase, due to higher carbon content. By calcining the materials in air, it appears that the oxygen content of the materials increases, indicating the possible addition of

oxygenated species to the carbon nitride surface. It can also be seen that after exfoliation each of the high surface area materials has lower nitrogen content than the corresponding bulk material implying the formation of nitrogen vacancies.¹⁷ Comparison of the relative differences in normalised composition between bulk and high surface area materials, CN-DCDA shows the smallest change. The barbituric acid materials show greater variation which may be due to greater structural change.

Table 24 – Elemental compositions, calculated C:N molar ratios and normalised composition of each carbon nitride.

Material	Measured Mass (%)			C:N (molar ratio)	Composition (Normalised)
	C	H	N		
CN-DCDA	34.92	1.56	61.25	0.665	C _{0.32} H _{0.17} N _{0.48} O _{0.02}
HSA- CN-DCDA	34.18	1.57	59.58	0.669	C _{0.31} H _{0.17} N _{0.47} O _{0.05}
CN-BA (5)	35.27	1.75	60.76	0.677	C _{0.32} H _{0.19} N _{0.47} O _{0.02}
HSA- CN-BA(5)	34.43	1.76	57.01	0.704	C _{0.31} H _{0.19} N _{0.44} O _{0.07}
CN-BA(10)	35.93	1.75	60.48	0.693	C _{0.33} H _{0.19} N _{0.47} O _{0.01}
HSA- CN-BA(10)	35.33	1.83	55.37	0.744	C _{0.31} H _{0.19} N _{0.42} O _{0.07}
CN-BA(20)	37.23	1.80	59.27	0.733	C _{0.34} H _{0.19} N _{0.46} O _{0.01}
HSA- CN-BA(20)	37.56	1.88	50.68	0.864	C _{0.33} H _{0.20} N _{0.38} O _{0.10}

To confirm that the exfoliation procedure, did in fact increase the surface area of the materials, the N₂ adsorption/desorption isotherms were measured (Figure 72) and the Brunauer-Emmett-Teller (BET) surface areas of each material has been calculated (Table 25). Each of the materials, bulk and exfoliated, show type IV isotherms with type H3 hysteresis loops, according to International Union of Pure and Applied Chemistry (IUPAC) surface area and pore size classifications.^{237,238} Upon thermal exfoliation, it is clear to see that the surface areas of the bulk materials are greatly enhanced, ranging from ~13 - 22 times higher.

As to why there is such a large variation in surface areas of the materials, is not fully understood. Materials were all placed in the same sized crucibles, placed in the same position in the same furnace, calcined at the same temperatures using the same heating and cooling rates. Also, the exfoliation step was performed on the same bulk material, multiple times and this wide variation in surface area was still observed, indicating that it is not sample based.

The most likely explanation would be variation in the ramping rate of the furnace when cooling down. This was not studied further.

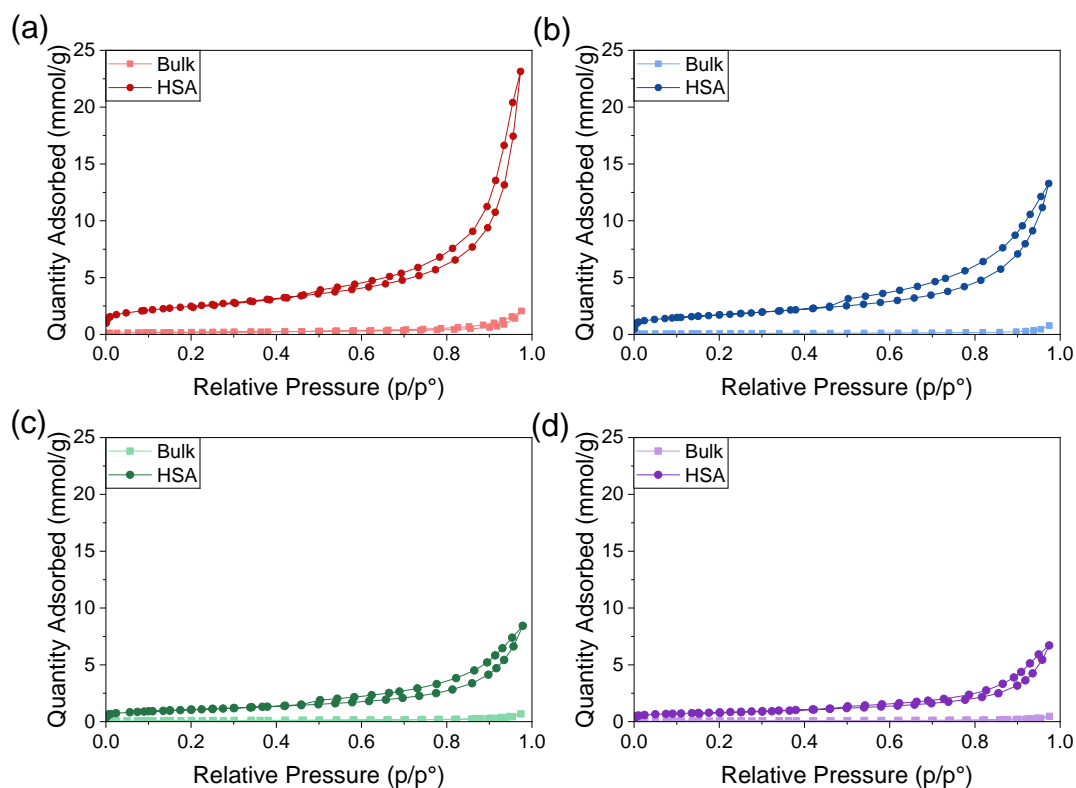


Figure 72 - N_2 adsorption/desorption isotherms of bulk and high surface area carbon nitrides. (a) CN-DCDA, (b) CN-BA(5), (c) CN-BA(10) and (d) CN-BA(20)

Table 25 - Measured BET Surface area of the bulk and HSA carbon nitrides.

Material	Surface Area (m^2g^{-1})	
	Bulk	HSA
CN-DCDA	14.70	192.54 (± 26.52) ^[b]
CN-BA(5)	6.38	135.45 (± 28.05)
CN-BA(10)	6.60	82.40 (± 10.66)
CN-BA(20)	4.41	63.78 (± 1.61)

[a] BET surface area calculated over the pressure range (P/P_0) 0.05-0.3.

[b] Standard deviation of the BET surface area of the high surface area material repeat synthesis.

DRIFTS spectra of the bulk and high surface area materials, all show characteristic carbon nitride stretches (Figure 73), indicating that the basic carbon nitride structure is retained. Once the material undergoes thermal exfoliation, the materials DRIFTS spectra show a broadening of the peaks in the $2800\text{--}3400\text{ cm}^{-1}$ region. This is likely due to enhanced surface area leading

to greater adsorption of water onto the sample. Furthermore, peaks become sharper in the CN heterocycle region, perhaps indicating greater crystallinity or higher degree of ordering upon a second calcination step, with the exception of CN-DCDA(20) where the peaks become less defined, indicating greater disorder. Overall, across the series, there can be seen no new peaks after exfoliation which could be attributed to incorporation of oxygenated species. These species are likely in too small amounts at the surface of the carbon nitrides to be distinguished from the bulk material.

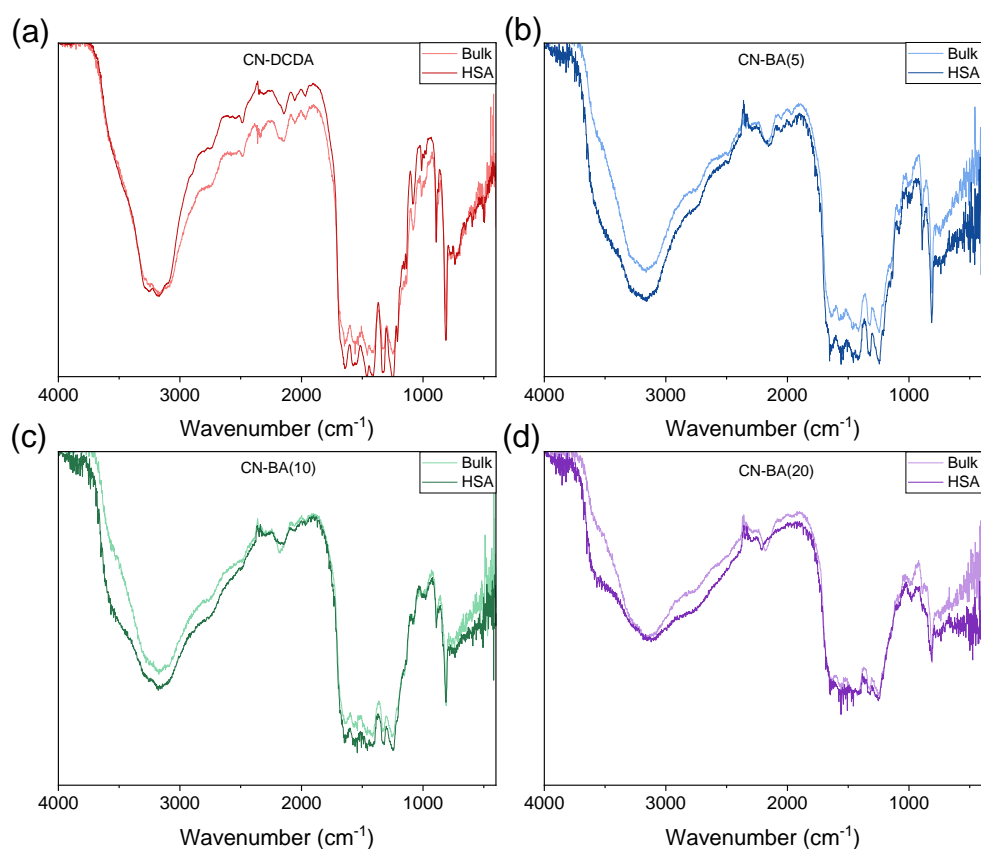


Figure 73 – DRIFTS spectra of bulk and high surface area carbon nitrides. (a) CN-DCDA, (b) CN-BA(5), (c) CN-BA(10) and (d) CN-BA(20).

The UV-Vis spectra of the materials (Figure 74) show that after exfoliation, the materials show a slight blue-shift in the adsorption edge, increasing the indirect band gap (Table 26) for all samples, except CN-BA(20) which instead sees a small decrease in its band gap. It has previously been observed that exfoliation of materials leads to an increase in band gap, attributed to quantum size effects of ultrathin structures leading to shifts in conduction and valence band positions in opposite directions.^{18,27,30}

Table 26 – Band gaps of the bulk and high surface area carbon nitriles.

Material	Band Gap (eV) ^[a]	
	Bulk	HSA
CN-DCDA	2.66	2.73
CN-BA(5)	2.09	2.21
CN-BA(10)	1.96	2.00
CN-BA(20)	1.85	1.74

[a] Determined from extrapolation of indirect Tauc plot.

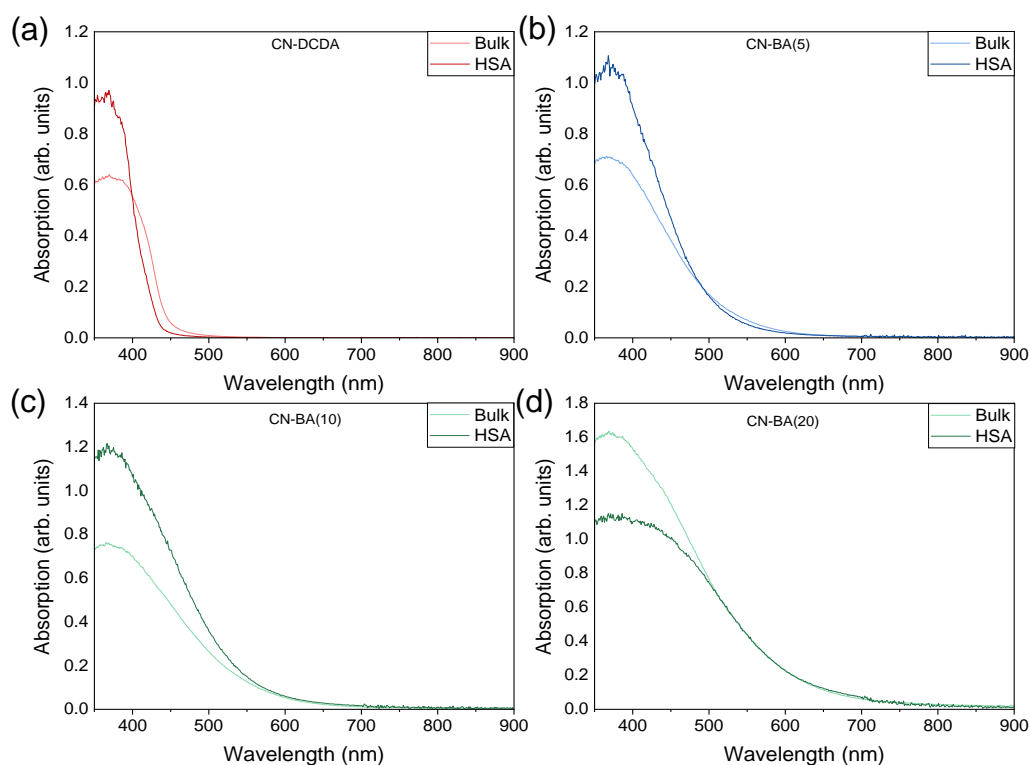


Figure 74 – UV-Vis diffuse reflectance spectra (Kubelka-Munk) of bulk and high surface area carbon nitriles. (a) CN-DCDA, (b) CN-BA(5), (c) CN-BA(10) and (d) CN-BA(20).

To understand the effect that increasing surface area has on charge separation and transfer, the steady state and time-resolved photoluminescence (PL) emission spectra were measured (Figure 75). The steady state PL emission spectra show that even with an increase in surface area, the trends across the series are maintained. With increasing barbituric acid content there is a red shift in the emission peak maxima and the emission intensity is suppressed. After exfoliation, the PL peak blue-shifted and a shoulder developed at shorter wavelengths, this shift is consistent with the blue shift observed in the UV-vis data. Also, there is a general decrease in PL emission intensity, with exception of CN-DCDA which sees a slight increase.

But due to the measurement being performed without a solid-state emission standard, care must be taken when comparing emission intensities. The PL emission suppression is indicative of a reduction in charge recombination via a radiative pathway and is often interpreted as an increase in charge lifetimes.

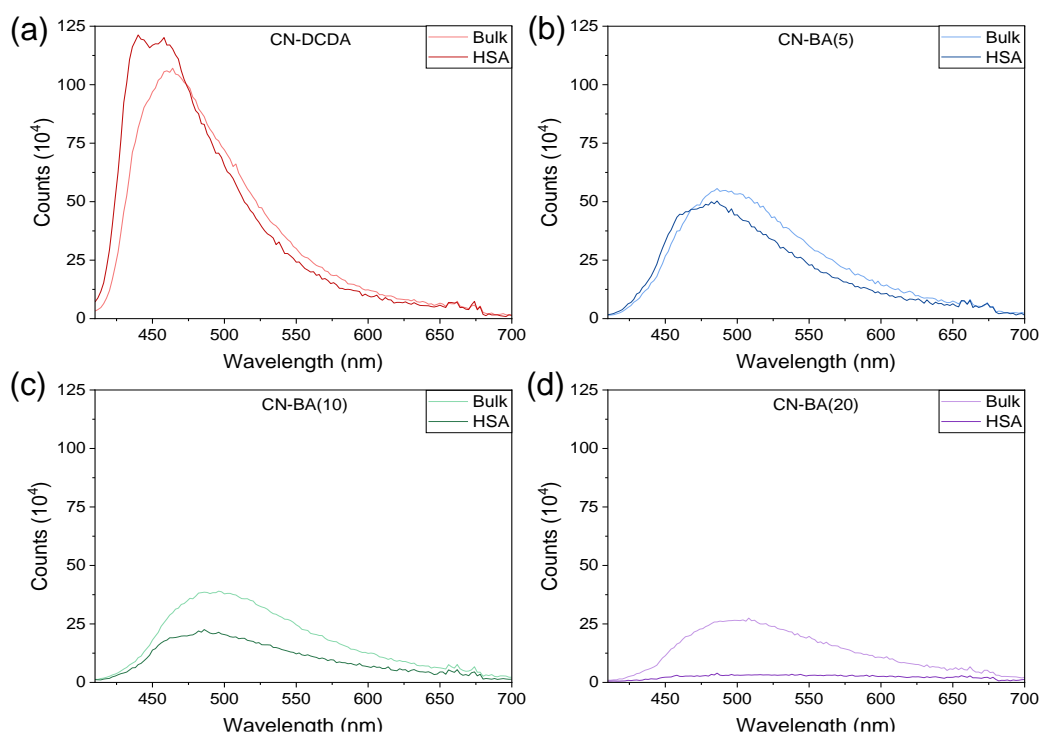


Figure 75 – Steady state PL emission spectra for bulk and high surface area carbon nitrides. (a) CN-DCDA, (b) CN-BA(5), (c) CN-BA(10) and (d) CN-BA(20). Excitation at 390 nm.

Table 27 – Steady state PL emission peak positions of the bulk and high surface area materials.

Material	PL Emission Peak (nm)	
	Bulk	HSA
CN-DCDA	464	458, 440
CN-BA(5)	486	482, 464
CN-BA(10)	490	486, 464
CN-BA(20)	496	488

Radiative lifetimes for each of the materials over the nanosecond to microsecond timescale were determined by fitting the time-resolved emission spectra (Figure 76) to a 4-term exponential function, values of which can be seen in Table 28. Again, the trends across the

series are maintained, with lifetimes initially increasing from CN-DCDA to CN-BA(5), but with higher levels of barbituric acid used, the lifetimes begin to decrease again.

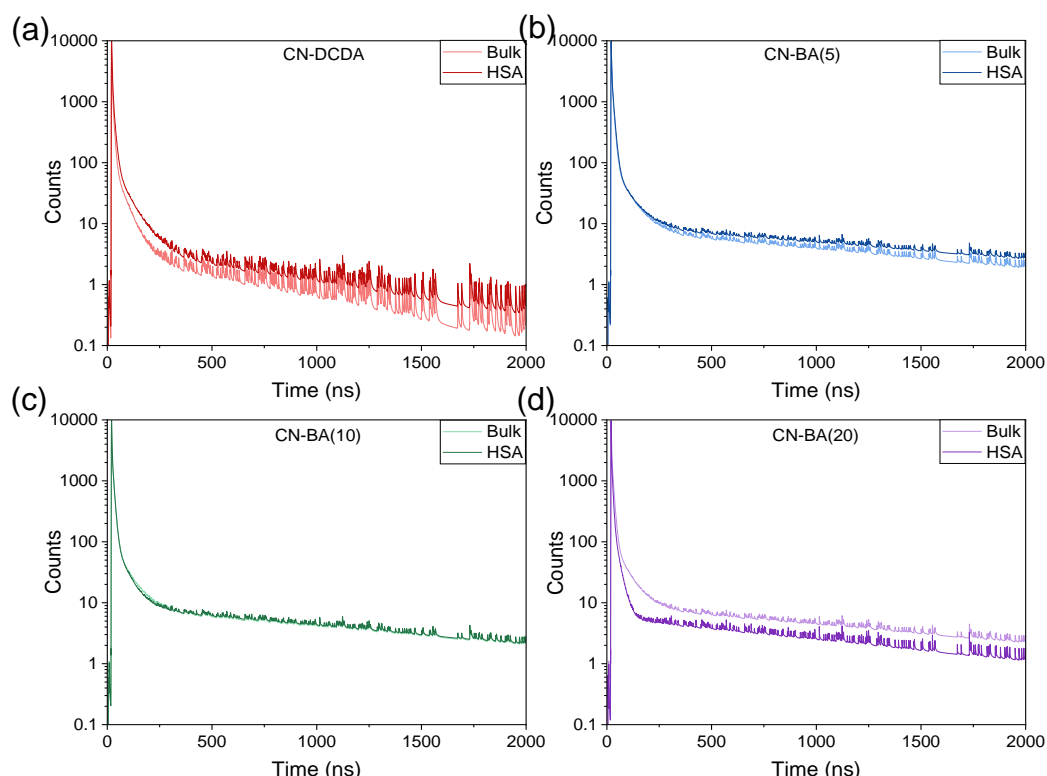


Figure 76 – Time-resolved emission spectra for bulk and high surface area carbon nitrides. (a) CN-DCDA, (b) CN-BA(5), (c) CN-BA(10) and (d) CN-BA(20). Excitation at 371 nm monitoring emission at, 465, 485, 495 and 495 nm for CN-DCDA, CN-BA(5), CN-BA(10) and CN-BA(20), respectively

However, it appears that after increasing the surface area of the materials, the effect on the charge lifetimes varies between samples. Samples CN-DCDA and CN-BA(5) see an increase in each of the lifetimes, with very little variation in amplitude. This increase in charge lifetimes has previously been assumed to be due to improved electron transport, band structure change induced by the quantum confinement effect or the strong capture ability of states at the surface.^{18,30} Increases in charge lifetimes improves the probability that the charges will take part in photocatalytic reactions before recombination can occur and will likely result in enhanced photocatalytic activities.^{45,239} Despite samples CN-BA(10) and CN-BA(20) showing emission suppression after exfoliation, indicative of reduced recombination, implying enhanced charge lifetimes, CN-BA(10) shows little change in charge lifetimes and CN-BA(20) sees lifetimes half of that of the bulk. Suppression of the PL emission and no change/decrease in lifetimes is likely due to the decay of photogenerated charges via non-emissive pathways.

Decrease in charge lifetimes has previously been observed for higher surface area materials.^{17,24,48}

Table 28 – Radiative lifetimes for bulk and high surface area carbon nitrides.

Material	$\tau_1^{[a]}$ (ns) (A_1 (%))	τ_2 (ns) (A_2 (%))	τ_3 (ns) (A_3 (%))	τ_4 (ns) (A_4 (%))	AWAL ^[b] (ns)
CN-DCDA	1.58 (0.81)	6.80 (0.18)	46.01 (0.01)	603.33 (0.0002)	2.98
HSA-CN-DCDA	2.40 (0.81)	9.29 (0.18)	61.90 (0.01)	760.50 (0.0003)	4.36
CN-BA (5)	1.71 (0.74)	8.40 (0.25)	64.48 (0.01)	1373.00 (0.0006)	4.68
HSA-CN-BA(5)	1.72 (0.74)	9.20 (0.26)	66.01 (0.01)	1588.10 (0.0007)	5.15
CN-BA(10)	1.63 (0.75)	8.38 (0.25)	61.42 (0.01)	1437.20 (0.0006)	4.61
HSA-CN-BA(10)	1.44 (0.74)	8.16 (0.25)	51.62 (0.01)	1407.40 (0.0006)	4.45
CN-BA(20)	1.49 (0.74)	8.10 (0.25)	59.05 (0.01)	1424.00 (0.0006)	4.48
HSA-CN-BA(20)	0.66 (0.78)	5.11 (0.21)	22.21 (0.02)	1224.70 (0.0003)	2.38

[a] Emission lifetimes determined by fitting time resolved emission spectra to a 4-component exponential, see section 2.3.9.

[b] Amplitude weighted average lifetimes (AWAL)

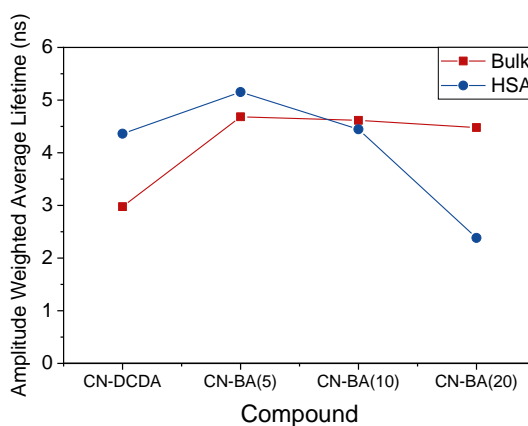


Figure 77 – Amplitude weighted average lifetimes for bulk and high surface area carbon nitrides; CN-DCDA, CN-BA(5), CN-BA(10) and CN-BA(20).

4.3.2.2 Photocatalytic Activity

Both the bulk and high surface area materials were tested for H₂ evolution on the high throughput screening set-up in the presence of EDTA hole scavenger and H₂PtCl₆ for in-situ Pt deposition (1 wt% loading). The rates of H₂ evolved after 4 hours of illumination is presented in Figure 78 and shows that after thermal exfoliation, the materials have greatly enhanced photocatalytic activity, with HSA-CN-BA(5) achieving the highest activity of 234 $\mu\text{mol g}^{-1} \text{h}^{-1}$ for H₂ evolution. The high surface area materials have activities 16, 6, 7.5 and 9 times larger than the bulk materials for CN-DCDA, CN-BA(5), CN-BA(10) and CN-BA(20), respectively. Enhancement in photocatalytic activity can be mostly attributed to increase in surface area providing higher amounts of catalytic sites for Pt deposition and H₂ evolution, along with improved charge lifetimes for samples CN-DCDA and CN-BA(5). Furthermore, the trend in activity across the CN-BA series is maintained even after undergoing exfoliation, combined with the small changes in band gap it is likely that the variation in band structure across the series has not been altered much to that of the bulk materials.

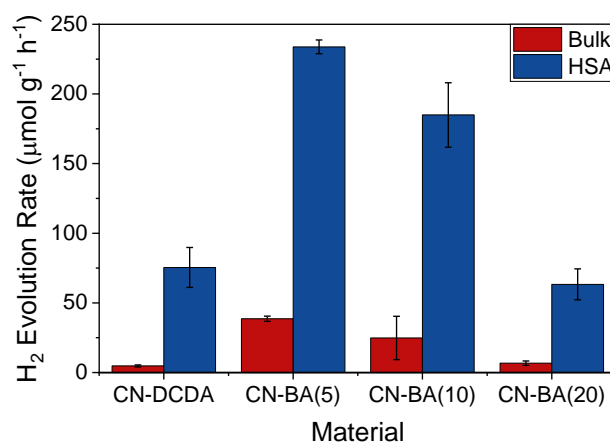


Figure 78 - Rate of H₂ evolved in μmol per gram of photocatalyst per hour for 2 mg of photocatalyst in 2 ml 10 mM EDTA with 1 μl H₂PtCl₆ (8 wt%) over 4 hours visible light irradiation at $\sim 100 \text{ mWcm}^{-2}$ in a glass vial, tested on the screening set-up.

Due to the great increase in surface area and the large variation in surface area between materials, the H₂ evolution when normalised to surface area and the rate of H₂ evolution per surface area is shown in Figure 79. The variation in photoactivity trends across the series is very similar for the bulk and high surface area materials, further indicating that the band structure of the materials has not been greatly affected by the exfoliation. When normalised to

surface area, CN-BA(5), CN-BA(10) and CN-BA(20) show lower rates for the higher surface area materials than the corresponding bulk samples. The enhancement in H₂ evolution rate per surface area for CN-DCDA when exfoliated may arise from the enhancement in charge lifetimes. Whereas the decrease in activity for the samples could be attributed to a number of factors. The barbituric acid materials all see larger differences in composition after exfoliation than the CN-DCDA material, this could indicate the formation of a greater number of defects, which are in too small amounts to be detected via DRIFTS. These defects could act as recombination centres, which provide non-emissive decay pathways for photogenerated charges, hence the PL emission suppression, ultimately resulting in slightly decreased activity.

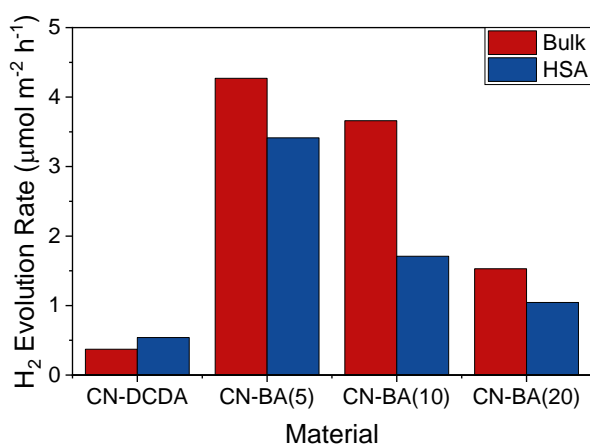


Figure 79 - Rate of H₂ evolved in μmol per m² per hour for 2 mg of photocatalyst in 2 ml 10 mM EDTA with 1 μl H₂PtCl₆ (8 wt%) over 4 hours visible light irradiation at ~100 mWcm⁻² in a glass vial, tested on the screening set-up.

4.3.3 Attachment of Co-catalysts to High Surface Area

Materials

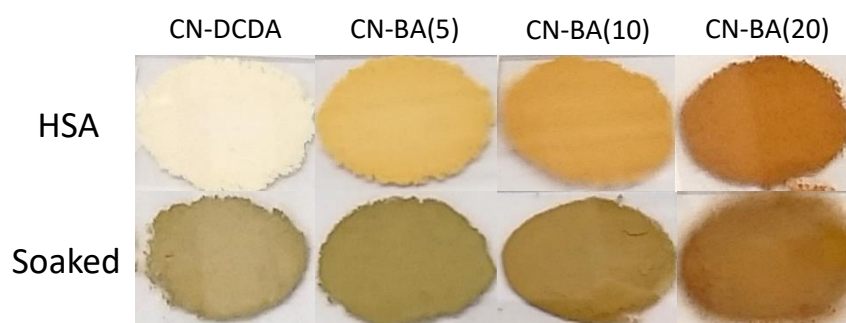


Figure 80 - Images of the high surface area materials pre- and post-soaking in FeTCP solutions; HSA-CN-DCDA, HSA-CN-BA(5), HSA-CN-BA(10) and HSA-CN-BA(20).

For attachment of FeTCPP on to the high surface area materials, the same procedure for soaking the bulk materials was followed, each of the carbon nitrides was pre-soaked in 90 μM FeTCPP ethanolic solution for 24 hours, washed three times with ethanol and dried at 60 $^{\circ}\text{C}$ overnight. Figure 80 shows images of the materials before and after soaking in FeTCPP solutions and clearly shows an obvious colour change for all materials, indicating attachment of the molecular catalyst on to the carbon nitrides surface.

4.3.3.1 Characterisation

The quantity of the molecular catalyst loaded onto each of the high surface area carbon nitrides was determined by UV-Vis and ICP. UV-Vis spectra of the FeTCPP solutions pre- and post-soaking are shown in Figure 81 and show characteristic porphyrin bands, with a strong Soret band appearing at 420 nm and weak Q- bands at 532, 572, 618 and 645 nm, attributed to π - π^* transitions.^{168,231,235,236}

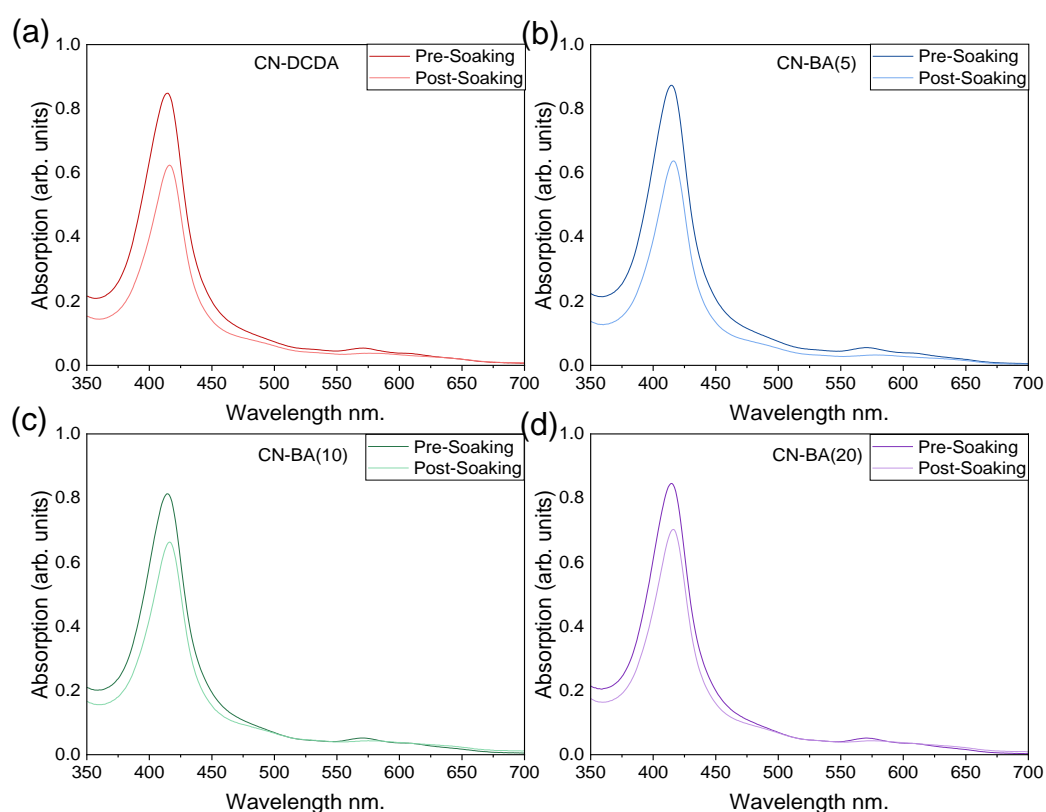


Figure 81 – UV-Vis spectra of 90 μM FeTCPP ethanolic solution prior to and after high surface area carbon nitride soaking over 24 hours.

The maximum loading of FeTCPP prior to washing was estimated from the most intense peak at 420 nm using the Beer-Lambert equation (Table 29). In comparison to the FeTCPP loadings

determined by ICP, the values are very close, which indicates that extra washing steps did not lead to desorption of the catalyst from the carbon nitride surface, at any appreciable level. Despite the large difference in surface area, the materials show similar levels of FeTCPP loading.

Table 29 – Estimated theoretical and experimental FeTCPP loadings on high surface area carbon nitrides.

Material	Maximum theoretical loading ^[a] (µg FeTCPP/ mg CN)	Loading of FeTCPP ICP (µg FeTCPP/ mg CN)	Loading of FeTCPP UV-Vis ^[b] (µg FeTCPP/ mg CN)	Loading FeTCPP ICP (wt%)
HSA-CN-DCDA	93.8	21	20.9	2.1
HSA-CN-BA(5)	65.7	19	21.4	1.9
HSA-CN-BA(10)	40.1	14	14.6	1.4
HSA-CN-BA(20)	31.1	14	13.4	1.4

[a] Maximum theoretical loading estimated using carbon nitride surface area and the distance between opposite carboxylic acid groups assumed to be the diameter of the FeTCPP molecule.

[b] Estimated using the Beer-Lambert equation.

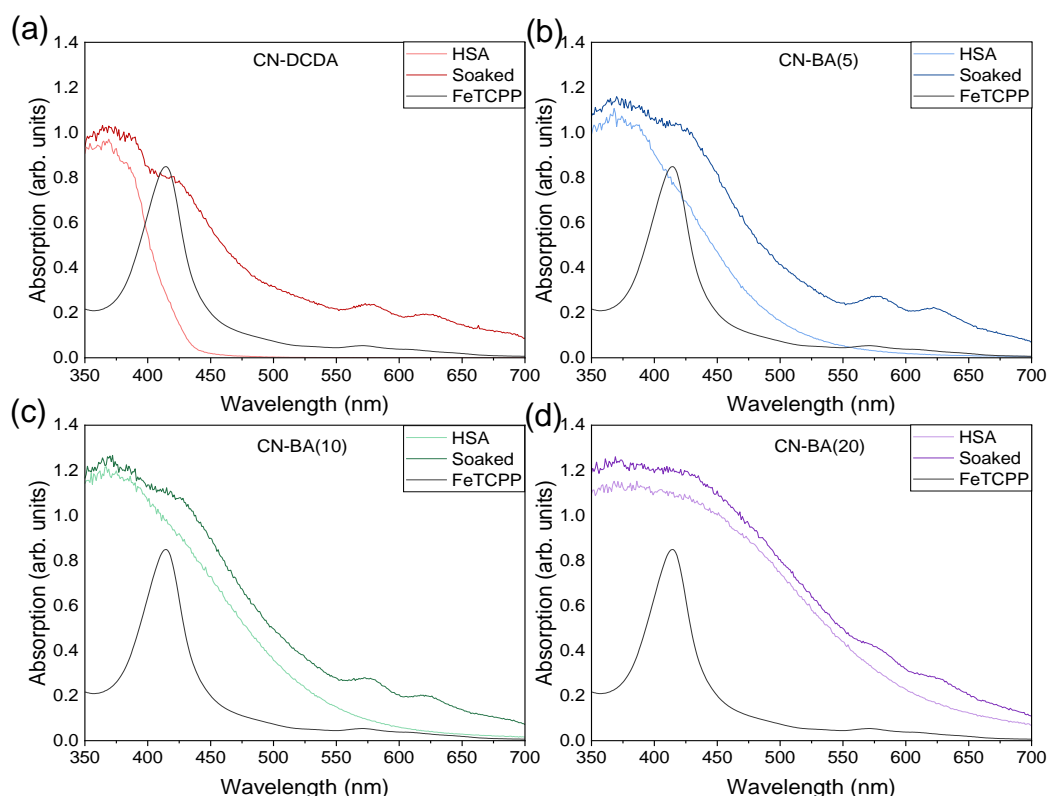


Figure 82 - UV-Vis diffuse reflectance spectra (Kubelka-Munk) of (a) HSA-CN-DCDA, (b) HSA-CN-BA(5), (c) HSA-CN-BA(10) and (d) HSA-CN-BA(20) pre- and post- soaking in FeTCPP solution and UV-Vis spectra of 90 µM FeTCPP ethanolic solution for comparison.

The UV-vis spectra the carbon nitrides before and after soaking (Figure 82) show extended absorption into the visible range, with clear peaks at 420 nm, 577 nm and 623 nm which can be assigned to the FeTCPP complex. These peaks have been shifted ~ 5 nm from the peaks found for FeTCPP in ethanol, which can be attributed π - π stacking of the FeTCPP on the carbon nitride.^{96,231,233,235} Comparison of the DRIFTS spectra before and after soaking do not show the emergence of new peaks that can be assigned to FeTCPP. It appears that the loading of FeTCPP is still too low to be distinguished from the carbon nitride material. Even subtracting the carbon nitride as a baseline does not help to identify new peaks.

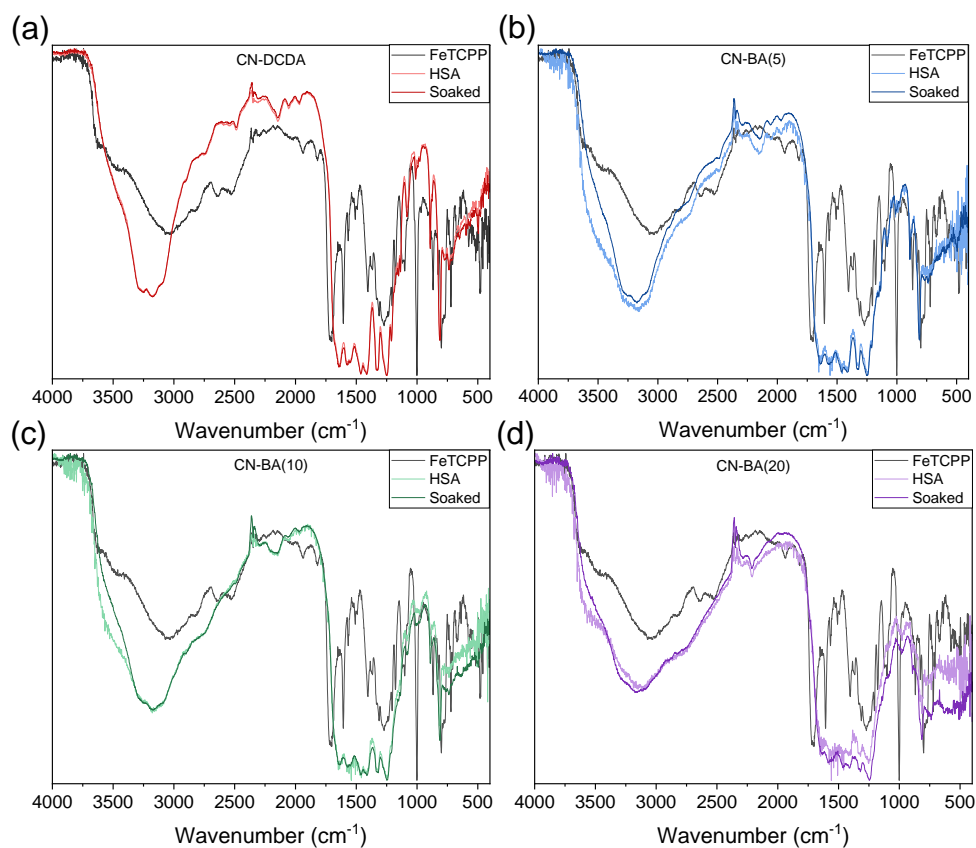


Figure 83 - DRIFTS spectra of (a) HSA-CN-DCDA, (b) HSA-CN-BA(5), (c) HSA-CN-BA(10) and (d) HSA-CN-BA(20) pre- and post- soaking in FeTCPP solution

To understand the charge transfer from the carbon nitride to the FeTCPP catalyst the PL emission and time-resolved emission spectra were measured for each sample. The PL emission spectra for each of the materials show a large reduction in emission intensity after FeTCPP soaking. The suppression of the emission upon addition of the co-catalyst is indicative of reduced recombination, likely arising from charge transfer from the carbon nitride to the co-catalyst.^{36,100,168–170,201,240}

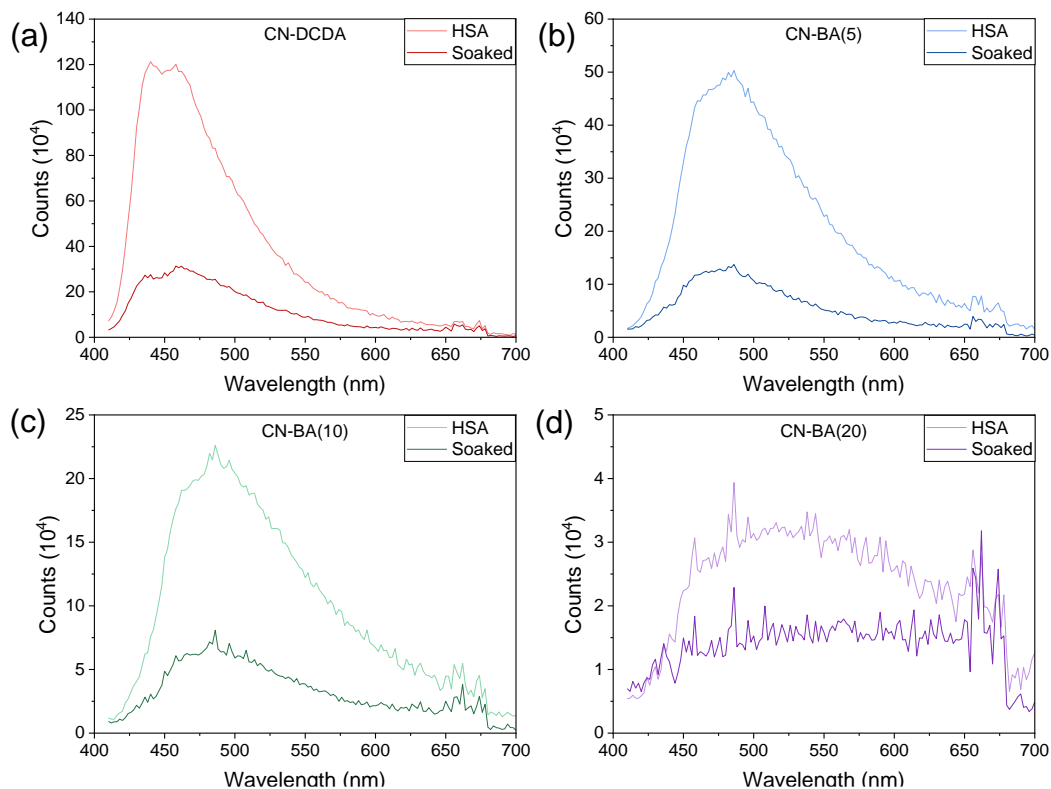


Figure 84 - Steady state PL emission spectra for carbon nitrides pre- and post-soaking. (a) CN-DCDA, (b) CN-BA(5), (c) CN-BA(10) and (d) CN-BA(20). Excitation at 390 nm.

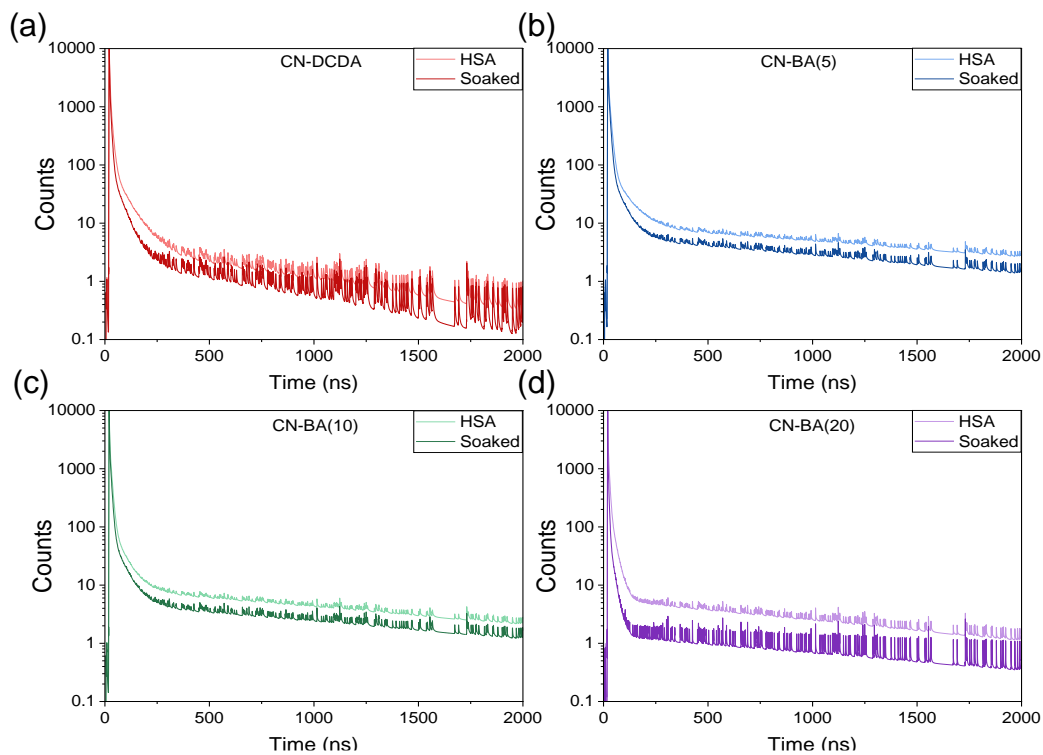


Figure 85 – Time-resolved emission spectra for carbon nitrides pre- and post-soaking. (a) CN-DCDA, (b) CN-BA(5), (c) CN-BA(10) and (d) CN-BA(20). Excitation at 371 nm monitoring emission at 465, 485, 495 and 495 nm for CN-DCDA, CN-BA(5), CN-BA(10) and CN-BA(20), respectively.

Time-resolved emission spectra were measured for each of the high surface area hybrid materials and compared with those of the blank carbon nitride materials (Figure 85). The lifetimes of charges were determined by fitting the spectra to a 4-term exponential, values of which can be found in Table 30. Suppression of the PL emission again would indicate enhancement in charge lifetimes, however, as was observed for some of the bulk and high surface area materials, the charge lifetimes decrease. All of the soaked materials show a shortening of charges lifetimes. This is due to photogenerated charges transferring to the co-catalyst and decay of the photogenerated charges occurs on the FeTCPP via a non-radiative pathway, leaving a higher concentration of holes in the carbon nitride which were able to combine with electrons at a faster rate.^{168,169,201,217} To understand charge transfer between the carbon nitride and FeTCPP better, other time resolved techniques would need to be explored.

Table 30 - Radiative lifetimes for carbon nitriles pre- and post-soaking.

Material	$\tau_1^{[a]}$ (ns) (A_1 (%))	τ_2 (ns) (A_2 (%))	τ_3 (ns) (A_3 (%))	τ_4 (ns) (A_4 (%))	AWAL ^[b] (ns)
HSA-CN-DCDA	2.40 (0.81)	9.29 (0.18)	61.90 (0.01)	760.50 (0.0003)	4.36
HSA-CN-DCDA/FeTCPP	1.43 (0.77)	5.93 (0.22)	42.63 (0.01)	619.52 (0.0002)	2.81
HSA-CN-BA(5)	1.72 (0.74)	9.20 (0.26)	66.01 (0.01)	1588.10 (0.0007)	5.15
HSA-CN-BA(5)/FeTCPP	1.20 (0.77)	7.07 (0.22)	46.10 (0.01)	1354.10 (0.0004)	3.34
CN-BA(10)	1.63 (0.75)	8.38 (0.25)	61.42 (0.01)	1437.20 (0.0006)	4.61
HSA-CN-BA(10)/FeTCPP	1.04 (0.80)	6.82 (0.20)	49.94 (0.01)	1413.10 (0.0003)	2.86
HSA-CN-BA(20)	0.66 (0.78)	5.11 (0.21)	22.21 (0.02)	1224.70 (0.0003)	2.38
HSA-CN-BA(20)/FeTCPP	0.34 (0.89)	3.37 (0.10)	18.21 (0.01)	1448.80 (0.0001)	0.85

[a] Emission lifetimes determined by fitting time resolved emission spectra to a 4-component exponential, see section 2.3.9.

[b] Amplitude weighted average lifetimes (AWAL)

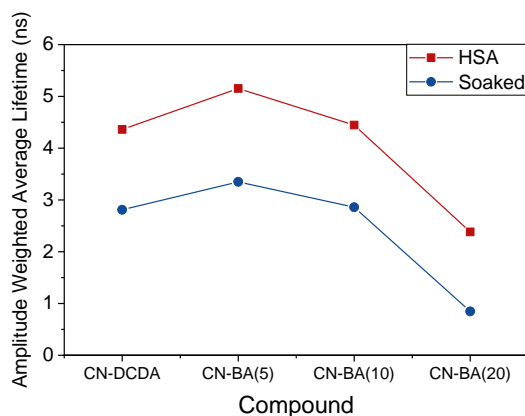


Figure 86 - Amplitude weighted average lifetimes for carbon nitrides pre- and post-soaking; CN-DCDA, CN-BA(5), CN-BA(10) and CN-BA(20).

4.3.3.2 Photocatalytic Activity

To evaluate the hybrid materials photocatalytic activity towards CO₂ reduction, experiments were performed on the Xe lamp set up. Typically, 4 mg of hybrid photocatalyst was loaded into a 4 mL quartz cuvette plus headspace, with 4 mL of hole scavenger, then purged with N₂ or CO₂ for 30 minutes prior to being placed under UV-Vis illumination for 4 hours on the Xe lamp set up. The Xe lamp was equipped with a water filter, to block IR irradiation and a 375 nm long pass filter to block some UV irradiation. Due to issues which arose from using EDTA as the hole scavenger for CO₂ reduction under UV-Vis illumination, (discussed in detail in Chapter 5), TEOA was chosen for photocatalytic CO₂ reduction experiments and was kept at a concentration of 10% volume in water.

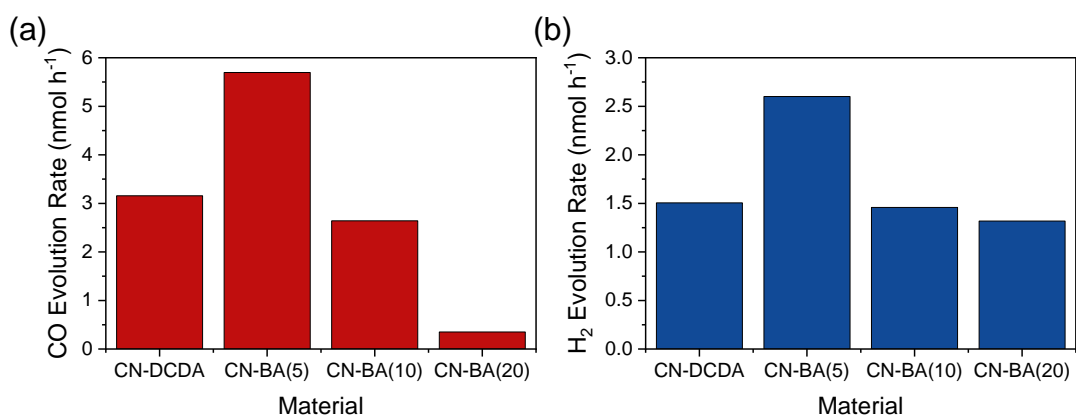


Figure 87 - Rate of (a) CO and (b) H₂ evolution in nmol per hour for 4 mg photocatalyst in 4 ml 10% TEOA (v/v) in water. Samples were purged with CO₂ and placed under UV-Vis illumination at ~100 mWcm⁻² in a quartz-cuvette, for 4 hours on the 300 W Xe lamp set-up. The Xe lamp was equipped with a water filter and a 375 nm long pass filter.

The results for photocatalytic CO₂ reduction over the carbon nitride/FeTCCP hybrid materials can be found in Figure 87 and show that all materials were capable of reducing CO₂ to CO under UV-Vis illumination (>375 nm) in the presence of TEOA as a hole scavenger over 4 hours of illumination. The highest rate of CO evolution was obtained by HSA-CN-BA(5)/FeTCCP, with a rate of 5.696 nmol h⁻¹. No liquid products were detected, but if present were below the detection limit of the ion chromatograph.

To confirm if the observed CO evolution was produced via photocatalytic CO₂ reduction, a number of control experiments were performed, including testing under N₂, without the hybrid catalyst, with the single components of the hybrid catalyst and with the carbon nitride in an FeTCCP solution, without soaking. The results of the experiments are shown in Figure 88, Table 32 and Table 33), details of the experiments can be found in Table 31. Figure 88 shows that in the absence of CO₂ and catalysts, only very small quantities of CO are evolved, much smaller than the levels of CO produced with most of the hybrid catalysts under CO₂, strongly indicating that the CO evolved is due to photocatalytic CO₂ reduction over the hybrid materials.

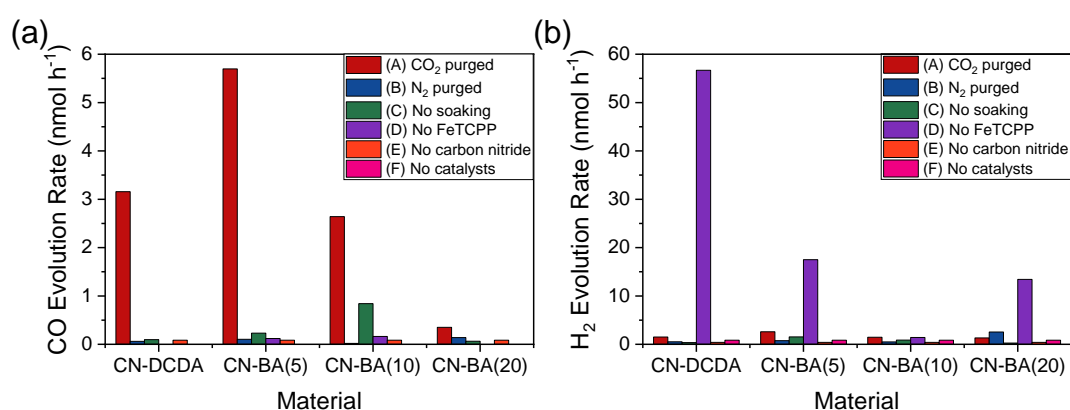


Figure 88 - Rate of (a) CO and (b) H₂ evolution in nmol per hour for 4 mg photocatalyst in 4 ml 10% TEOA (v/v) in water. Samples were purged with N₂ or CO₂ and placed under UV-Vis illumination at ~100 mWcm⁻² in a quartz-cuvette, for 4 hours on the 300 W Xe lamp set-up. The Xe lamp was equipped with a water filter and a 375 nm long pass filter. Conditions for experiments give in Table 31.

Experiments were also performed with 4 mg of carbon nitride or 25 μM FeTCCP in 10% TEOA solution. This concentration of FeTCCP is equivalent to 22 μg of molecular catalyst per mg of carbon nitride, which is close to the FeTCCP loading on the carbon nitriles determined by ICP and UV-Vis (Table 29). Again, these tests produced much lower quantities of CO, showing that both the carbon nitride and FeTCCP co-catalyst are required for CO₂ reduction to occur.

It is also worth noting, that the carbon nitride in 10% TEOA under CO₂ without the addition of co-catalyst, though did not produce significant levels CO, did produce H₂ above the levels of the other experiments, without the aid of a co-catalyst, for samples HSA-CN-DCDA, HSA-CN-BA(5) and HSA-CN-BA(20). This is likely due to enhanced surface areas providing a greater number surface sites for catalysis to occur. As to why CN-BA(10) did not show improved activity is not known and further experiments would be needed to confirm these results, but this was not studied further as the main goal was to study CO₂ reduction over the hybrid catalyst. To determine if the attachment of the FeTCPP onto the surface was necessary for CO₂ reduction to occur, 4 mg of carbon nitride was placed in in 4 mL 25 μM FeTCPP in 10% TEOA in water. The photocatalytic experiment under a CO₂ atmosphere was found again to produce much lower amounts of CO, indicating that soaking is required for attachment and efficient electron transfer between the semiconductor and molecular co-catalyst.

Table 31 - Conditions for experiments shown in Figure 88.

Experiment	Label	CN	FeTCPP	Hole Scavenger	Atmosphere
CN/FeTCPP/10%TEOA/CO ₂	A	✓	✓	✓	CO ₂
CN/FeTCPP/10%TEOA/N ₂	B	✓	✓	✓	N ₂
CN/10%TEOA(25 μM FeTCPP)/CO ₂	C	✓	✓	✓	CO ₂
CN/10%TEOA/CO ₂	D	✓	✗	✓	CO ₂
FeTCPP/10%TEOA/CO ₂	E	✗	✓	✓	CO ₂
10%TEOA/CO ₂	F	✗	✗	✓	CO ₂

Table 32 – Rates of CO evolution for each of the CN/FeTCPP hybrid materials under different testing conditions.

Experiment	CO Evolution (nmol h ⁻¹)			
	CN-DCDA	CN-BA(5)	CN-BA(10)	CN-BA(20)
CN/FeTCPP/10%TEOA/CO ₂	3.156	5.696	2.641	0.350
CN/FeTCPP/10%TEOA/N ₂	0.061	0.103	0.019	0.139
CN/10%TEOA(25 μM FeTCPP)/CO ₂	0.096	0.231	0.840	0.063
CN/10%TEOA/CO ₂	0	0.121	0.163	0
FeTCPP/10%TEOA/CO ₂	0.085			
10%TEOA/CO ₂	0			

Table 33 - Rates of H₂ evolution for each of the CN/FeTCPP hybrid materials under different testing conditions.

Experiment	H ₂ Evolution (nmol h ⁻¹)			
	CN-DCDA	CN-BA(5)	CN-BA(10)	CN-BA(20)
CN/FeTCPP/10%TEOA/CO ₂	1.505	2.601	1.458	1.318
CN/FeTCPP/10%TEOA/N ₂	0.524	0.744	0.498	2.543
CN/10%TEOA(25 μM FeTCPP)/CO ₂	0.344	1.536	0.875	0.267
CN/10%TEOA/CO ₂	56.670	17.509	1.404	13.436
FeTCPP/10%TEOA/CO ₂	0.410			
10%TEOA/CO ₂	0.851			

Measuring the photocatalytic activity under specific wavelengths of light can be used to elucidate the photoresponse of the CN/FeTCPP hybrid. For the wavelength dependency measurements, the HSA-CN-DCDA/FeTCPP sample was chosen as it had the clearest separation between the carbon nitride band edge and the strongest FeTCPP band. Figure 89 shows the response of HSA-CN-DCDA/FeTCPP for CO evolution under 365, 395 and 420 nm monochromatic illumination over a 24-hour period, overlaid with UV-Vis spectra of HSA-CN-DCDA, HSA-CN-DCDA/FeTCPP and FeTCPP in ethanolic solution. The response of HSA-CN-DCDA/FeTCPP at different wavelengths matches well with the recorded UV-vis spectra of the carbon nitride, confirming that CO reduction was initiated by excitation of the carbon nitride.

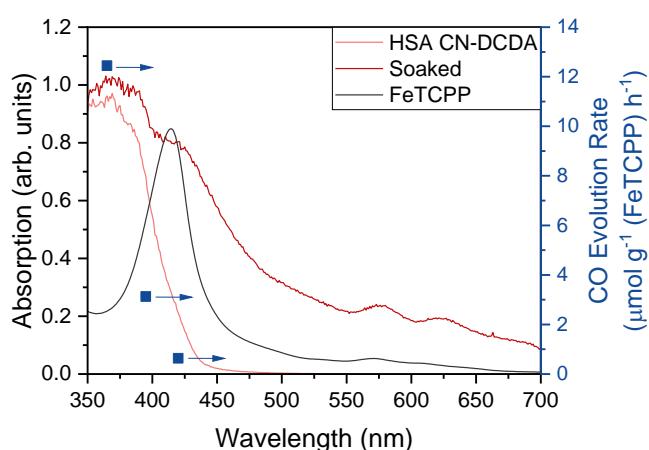


Figure 89 - UV-Vis diffuse reflectance spectra (Kubelka-Munk) of HSA-CN-DCDA pre- and post-soaking in FeTCPP solution and UV-Vis spectra of 90 μM FeTCPP ethanolic solution overlaid with Rate of CO evolution in μmol per gram of FeTCPP per hour for 2 mg photocatalyst in 2 ml 10% TEOA (v/v) in water. Samples were purged with CO₂ and placed under monochromatic illumination (365, 395 and 420 nm) at ~0.16 mWcm⁻² in a quartz-cuvette, for 24 hours on a 150 W Xe lamp with monochromator.

Normalisation of the photocatalytic activity for the hybrid materials in 10% TEOA under CO₂ to the FeTCPP loading is shown in Table 34 and Figure 90. Across the series the photocatalytic activities for CO₂ reduction appear to follow closely the trends observed for the high surface area and bulk materials for H₂ evolution in the presence of a Pt co-catalyst. From the similar trends in activity, band gap and radiative lifetimes, it is likely that the materials follow the same trends in band structure as was observed in Chapter 3. But to confirm, the band structures of the high surface area materials would need to be measured.

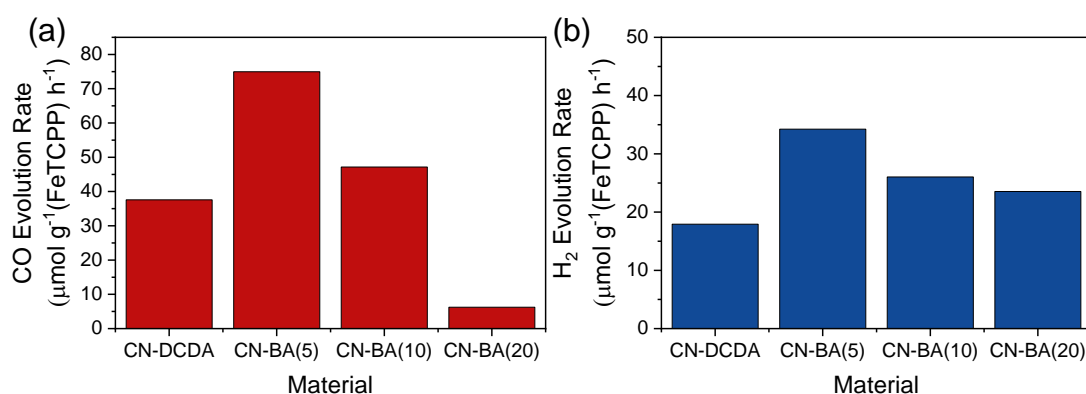


Figure 90 - Rate of (a) CO and (b) H₂ evolution in μmol per gram of FeTCPP per hour for 4 mg photocatalyst in 4 ml 10% TEOA (v/v) in water. Samples were purged with CO₂ and placed under UV-Vis illumination at ~100 mWcm⁻² in a quartz-cuvette, for 4 hours on the 300 W Xe lamp set-up. The Xe lamp was equipped with a water filter and a 375 nm long pass filter.

Table 34 – Rate of CO and H₂ evolution for FeTCPP materials.

Sample	Rate of Evolution (nmol h ⁻¹)		Rate of Evolution (μmol g ⁻¹ (FeTCPP) h ⁻¹)		Selectivity (%)	
	CO	H ₂	CO	H ₂	CO	H ₂
CN-DCDA	3.156	1.505	37.567	17.914	67.71	32.29
CN-BA(5)	5.696	2.601	74.952	34.227	68.65	31.35
CN-BA(10)	2.641	1.458	47.164	26.037	64.43	35.57
CN-BA(20)	0.350	1.318	6.253	23.537	20.99	79.01

It has been determined electrocatalytically that the Fe species required for CO₂ reduction to occur using Fe-porphyrin catalysts, is Fe⁰.^{241–248} For photocatalytic CO₂ reduction to occur over the CN/FeTCPP hybrids, the conduction band of the carbon nitride must lie at a more negative potential to allow for electron transfer to the Fe porphyrin to form the Fe⁰ species that is required. Comparison of the band structures obtained for the bulk materials in Chapter 3 and

the reported redox couples for FeTCPP in DMF can be found in Figure 91. Although one is found under vacuum and the other was determined in an organic solvent and the actual values would differ in solution and at different pH, they can still help to understand the differences in activity, but care must be taken, when making comparisons.

Figure 91 shows that samples CN-DCDA, CN-BA(5) and CN-BA(10) have CB that lie at a more negative potential than the $\text{Fe}^{I/0}$ redox couple, which means that electrons can transfer to the FeTCPP co-catalyst resulting in the formation of Fe^0 , which is required for CO_2 reduction. However, CN-BA(20) has a CB which lies at a much more positive potential than the other materials and appears to lie below that of the $\text{Fe}^{I/0}$ redox couple. This means that the excited electron which lies in the conduction band does not have enough energy to transfer over to the FeTCPP and form the Fe^0 species required, so CO_2 reduction is unlikely to occur over that hybrid material. This is confirmed by comparison of the CO and H_2 evolution under CO_2 and N_2 in Table 32 and Table 33 as the level of CO produced under CO_2 and N_2 are very close.

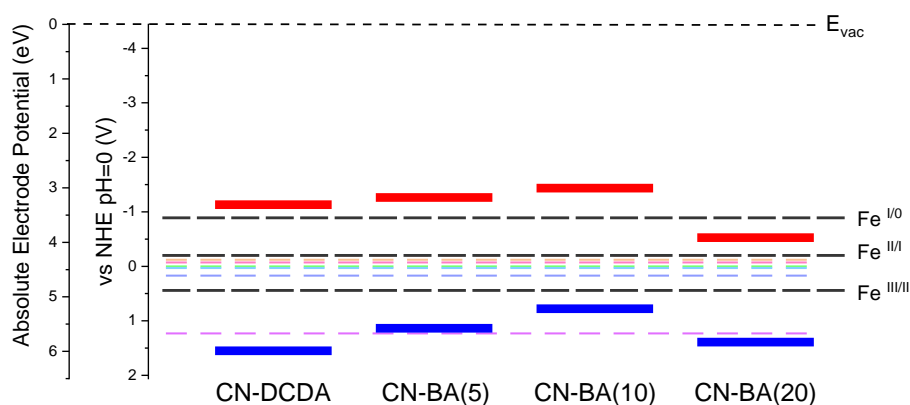


Figure 91 – Band structures of CN-DCDA, CN-BA(5), CN-BA(10) and CN-BA(20), taken from Chapter 3 compared with the Fe redox couples in DMF taken from reference ¹⁶⁸.

It is important to note that 24 hours after the photocatalysis experiments were performed that for the experiments which had been purged with N_2 , the solution had changed from colourless to green/blue and the powders had reverted to their original colour due to the FeTCPP dissolving into the solution. This colour change was not observed immediately after the 4-hour photocatalysis experiment, but there may have been a small amount of FeTCPP which had detached during the experiment. This was observed for all materials but was most pronounced for the HSA-CN-DCDA sample, the detachment was less noticeable on the other samples and

was not found to occur for samples purged with CO₂. This is thought to be due to the differences in pH when purging with CO₂ and N₂, the N₂ purged samples were found to have a pH ~10.8, whereas the CO₂ were found to have a pH of ~7.8. Further experiments altering the pH of solutions, specifically adjusting the pH of the N₂ experiment to that found for the CO₂ purged solutions, are required to ensure that difference in pH did not greatly affect the photoactivity observed in the blank studies.

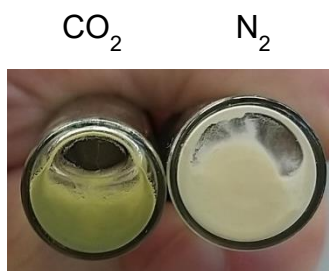


Figure 92 – Images of HSA-CN-DCDA/FeTCCP in 10% TEOA purged with CO₂ (left) and N₂ (right) 24 hours after photocatalysis experiment and storage in air.

As mentioned in the aim of work section, the combination of carbon nitride and FeTCCP as a co-catalyst for photocatalytic CO₂ reduction has previously been reported.¹⁶⁸ Within the paper, they reported much higher quantities of CO produced over their CN/FeTCCP hybrids, ranging between 1 and 6.5 mmol of CO per weight of FeTCCP used in the experiment and found the highest activity, when normalised to FeTCCP, was obtained using the lowest loading. The testing conditions used within this paper are quite different to those used in this project, photocatalysis experiments were illuminated at ~220 mWcm⁻² (420 nm < λ < 780 nm) for 6 hours and performed in solutions of MeCN, water and TEOA (3:1:1, v:v:v). Also, the reported photocatalytic procedure states that 50 mg of carbon nitride and a certain amount of FeTCCP (0.1, 0.25, 0.5, 1 or 2 mg) were placed in 100 mL of MeCN:water:TEOA (3:1:1, v:v:v) and left stirring for an unspecified amount of time before purging and put under illumination, indicating that the FeTCCP remains in solution throughout the experiment. This means that the FeTCCP was at a concentration of between 1-23 μM, lower than concentrations used in the experiments presented here. Furthermore, very little characterisation of the CN/FeTCCP hybrid is presented and the actual quantity of FeTCCP loaded onto the carbon nitride is not explored.

There are a number of potential reasons for the comparably low photoactivity, these include, solvent mixture, light source and FeTCCP loading. Quite often photocatalytic CO₂ reduction performed on a suspension is done so using organic media, this is because of the relatively low solubility of CO₂ in water and H₂ evolution can compete with CO₂ reduction in aqueous solution. However, the work presented here was performed in 10% TEOA in water and the three hybrids capable of reducing CO₂ to CO showed greater than 60% selectivities towards CO production. The light sources and filters used in this work provided illumination >375 nm and blocked IR irradiation, whereas the wavelengths used in the paper were between 420 and 780 nm, also the light intensity used in the paper is more than double that used within this work. This will have a great effect on the photocatalytic activity and also may lead to heating of the experiment which can further enhance activities. The loading of FeTCCP in this work cannot be compared directly with those in the paper, but from the procedures described in the paper, it is likely that the loading of FeTCCP onto the carbon nitride is much lower. High loadings of any co-catalyst can lead to low activities due to blockage of light reaching the photoabsorber, which might be the case for FeTCCP on carbon nitride.

An experiment using the same solvent conditions from the paper was performed with HSA-CN-BA(5)/FeTCCP. It was noticed that when the experiment was started that the solution separated, forming two distinct layers; an MeCN layer above a water, TEOA and HSA-CN-BA(5)/FeTCCP suspension layer, despite stirring. The experiment was continued and was found that within the first few minutes that visible gas bubbling in the solution was occurring, however the level of gases produced were quite low, relative to the gas bubbling that was observed. Also, it was noticed that when placed in the dark, the sample continued to bubble for at least a minute in the absence of light. It was then noticed that the bubbling was only occurring when the sample was stirring. To ensure that the activity that was being observed was not mechanocatalytic or a light assisted process, the sample was left in the dark for the last hour of the experiment, however it was found that the gas quantities did not increase in the absence of light. Within the first 3 hours of the experiment it was found that the rate of evolution for H₂ and CO were, 5.326 nmol h⁻¹ and 1.538 nmol h⁻¹, which is in fact lower than the activities obtained in 10% TEOA solutions for CO production and gives enhanced H₂ evolution. As to why the solution separated into two layers or why visible bubbling was

observed was not explored further as the main aim of this work was to test the hybrid catalysts in water in the presence of a hole scavenger.

The final experiment which is required to provide definitive proof that the CO evolved over the course of the photocatalysis tests is directly from CO₂ reduction is an isotopically labelled experiment. For the isotopic labelling experiment, 10 mg of HSA-CN-BA(5) was placed in 10 mL 10% TEOA in water, first purged with N₂, for removal of O₂, for 30 minutes and then purged with ¹³CO₂ for several minutes. The system was then put under illumination (>375 nm and ~200 mWcm⁻²) for 24 hours before testing the headspace via FTIR. The system was scaled up, with a higher light intensity and longer illuminations times to give the system the best chance to produce as much gas as possible to make it easier to detect via FTIR. For comparison, this experiment was also performed in the presence of ¹²CO₂, to confirm the shift in peak positions between ¹²CO and ¹³CO. The ¹²CO₂ experiment showed that the system produced 1.064 μmol of H₂ and 0.083 μmol of CO. The difference in selectivities between H₂ and CO likely result in the variation in purging leading to different pH and different species being present during the photocatalysis. Whereas when the system was purged with ¹³CO₂ it produced 0.071 μmol of H₂ and 0.157 μmol of CO. As to why there was a shift in the selectivities compared with the ¹²CO₂ is unknown as both systems were prepared and purged in the same way for the same amount of time.

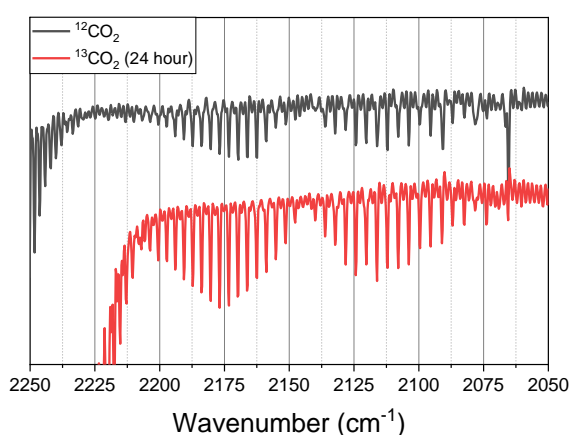


Figure 93 – FTIR spectra of gas samples taken from photocatalytic experiments purged with ¹²CO₂ or ¹³CO₂. Conditions of the photocatalytic test; for 10 mg HSA-CN-BA(5)/FeTCPP in 10 ml 10% TEOA (v/v) in water. Samples were purged with N₂ for 30 minutes then ¹²CO₂ or ¹³CO₂ for 2 minutes and placed under UV-Vis illumination at ~200 mWcm⁻² in a quartz-cuvette, for 24 hours on the 300 W Xe lamp set-up. The Xe lamp was equipped a 375 nm long pass filter.

Figure 93 shows the results of the FTIR isotopic labelling experiments when purged under $^{12}\text{CO}_2$ and $^{13}\text{CO}_2$, specifically looking at the CO stretching region. A positive result should show that the CO bands shifted to lower wavenumbers with the Q-branch shifted from $\sim 2150\text{ cm}^{-1}$ under $^{12}\text{CO}_2$ to $\sim 2100\text{ cm}^{-1}$ under $^{13}\text{CO}_2$. However, the data presented in Figure 93 shows a small shift of $\sim 4\text{ cm}^{-1}$ to higher wavenumber of the CO stretch.

A similar positive shift in the CO stretch has previously been reported during $^{13}\text{CO}_2$ studies by our group.²⁴⁹ The apparent positive shift in stretching frequency of the Q-branch was found to be due to the presence of both ^{13}CO and ^{12}CO , with the overlapped spectra complicating analysis. By subtracting a scaled ^{12}CO signal away from the ^{13}CO signal, they were able to determine that $\sim 30\%$ of the FTIR signal of the $^{13}\text{CO}_2$ experiment was due to ^{12}CO . The source of the ^{12}CO was tentatively attributed to long irradiation times leading to breakdown of the hole scavenger, ascorbate. Shorter periods of illumination saw only minimal amounts of CO evolved in the absence of CO_2 and was found that longer illumination led to a rapid rise in the CO levels. Subtraction of the ^{12}CO from the ^{13}CO was attempted with the data presented here, however no actual ^{13}CO signal could be identified and is likely swamped by the ^{12}CO signal. It is postulated that the source of the ^{12}CO is from TEOA and is thought to be due to degradation of the scavenger forming $^{12}\text{CO}_2$ which was preferentially reduced at the catalysts surface over $^{13}\text{CO}_2$, which is further away in solution. The small amount of CO produced when experiments were performed under a N_2 atmosphere could be due to TEOA oxidation forming CO_2 as it is consumed for electron donation when performing H_2 evolution. However, TEOA is a widely used scavenger in CO_2 reduction and previous studies have found positive results for isotopically labelled experiments when using TEOA as the hole scavenger. It may take some time to form the $^{12}\text{CO}_2$ required for subsequent reduction, which may be swamping the FTIR signal. Shorter illumination times could lead to the formation of ^{13}CO which might be easier to identify via FTIR. To test this, HSA-CN-BA(5) was tested under typical conditions on a scale of 4 mg of photocatalyst to 4 mL 10% TEOA under Xe lamp illuminations with a water filter and 375 nm long pass filter at an intensity of 100 mWcm^{-2} for a much shorter period (4 hours). After 4 hours of illumination, this experiment produced $0.109\text{ }\mu\text{mol}$ of H_2 and $0.030\text{ }\mu\text{mol}$ of CO.

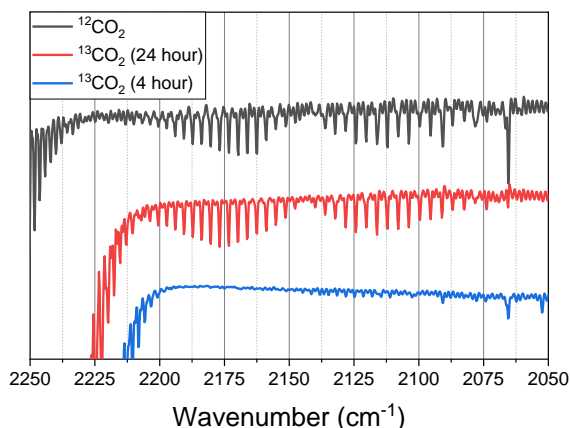


Figure 94 – FTIR spectra of gas samples taken from the 4 hour photocatalytic experiment purged with $^{13}\text{CO}_2$ compared with the $^{12}\text{CO}_2$ and 24 hour $^{13}\text{CO}_2$ experiments. Conditions of the 4 hour photocatalytic test; for 4 mg HSA-CN-BA(5)/FeTCPP in 10 ml 10% TEOA (v/v) in water. Samples were purged with N_2 for 30 minutes then $^{13}\text{CO}_2$ for 2 minutes and placed under UV-Vis illumination at $\sim 100 \text{ mWcm}^{-2}$ in a quartz-cuvette, for 4 hours on the 300 W Xe lamp set-up. The Xe lamp was equipped a 375 nm long pass filter and water filter.

Figure 94 shows the FTIR of the sampled headspace and shows the small CO doublet centred $\sim 2100 \text{ cm}^{-1}$ confirming the presence of ^{13}CO . This proves that the CO produced in the first 4 hours of illumination is due to reductions of the purged $^{13}\text{CO}_2$ gas. Over longer illumination periods the majority of the CO is formed from the reduction of $^{12}\text{CO}_2$ likely produced via the degradation of the TEOA. For evidence of TEOA degradation leading to subsequent CO_2 reduction, this experiment would have to be repeated in the presence of $^{12}\text{CO}_2$ and ^{13}C labelled TEOA.

When performing the isotopic labelling experiments, it was also noticed that a significant amount of methane was produced after both 4 and 24 hours of illumination (0.015 and 0.25 μmol respectively) which was not observed for the other experiments under 4 hours of illumination, when purged with solely CO_2 . The quantities of methane detected in the 4-hour experiments were low ($\sim 1\text{-}4 \text{ nmol}$), but of a quantity that is typically observed for manual injections in a GC, no matter the type or scale of experiment and is due to air in the needle and air getting into the injection port when injecting so this was not initially studied any further. To understand why an unusual amount of CH_4 was produced during the 24-hour isotopic labelling experiments, a time course experiment was performed, and the results can be found in Figure 95.

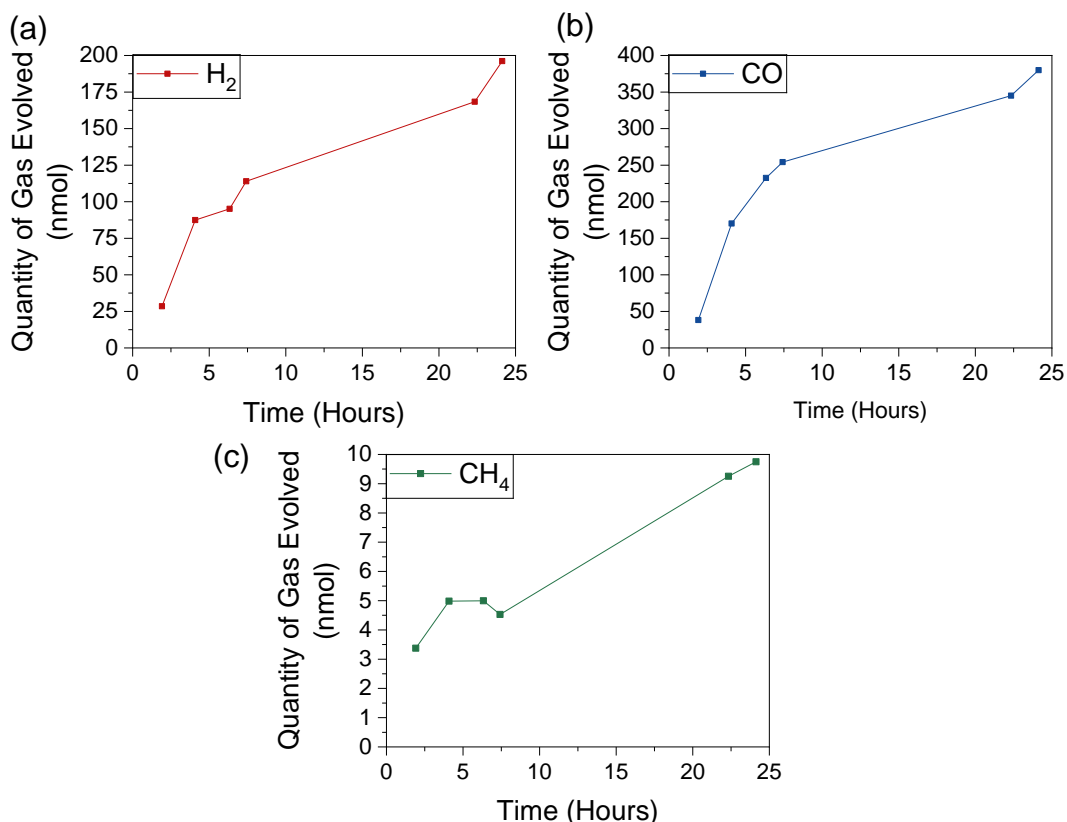


Figure 95 – Quantity of (a) H₂, (b) CO and (c) CH₄ evolved in nmol for 4 mg HSA-CN-BA(5)/FeTCPP in 4 mL 10% TEOA (v/v) in water. Sample was purged with CO₂ and placed under UV-Vis illumination at ~100 mWcm⁻² in a quartz-cuvette, for ~24 hours on the 300 W Xe lamp set-up. The Xe lamp was equipped with a 375 nm long pass filter.

Figure 95 shows that within the first 6 hours of the experiment H₂ and CO evolution increases steadily then starts to slow. Within this time the level of CH₄ detected is at a level that is typical for most manual injections. However, approaching the 24-hour mark H₂ and CO production has significantly slowed, whilst the CH₄ detected is almost double that which is usually detected.

This slowing rate in the production of H₂ and CO, and the subsequent increase in CH₄ levels is indicative of CO reduction to CH₄. This has previously been observed on other Fe porphyrin catalysts, which have been tested for photocatalytic CO₂ reduction in the presence of a photosensitiser and a hole scavenger in acetonitrile.^{250,251} They found that the systems were capable of CO₂ reduction to CO, which was subsequently reduced further leading to CH₄ production. Isotopic labelling experiments also confirmed their findings. It is likely that the CH₄ produced in the isotopic labelling experiments over the standard photocatalysis experiments shown within this thesis is due to the difference in pH caused by the different methods for

purging. Standard experiments were purged for a full 30 minutes prior to illumination, so resulted in a much lower pH in comparison to the isotopically labelled experiments which were first purged with nitrogen and then only purged with CO₂ for 2 minutes.

4.4 Conclusions and Future work

Within this chapter 16 carbon nitrides were screened for use with three Ni cyclams and an Fe porphyrin complex as co-catalysts for photocatalytic CO₂ reduction. Initial screening experiments found that none of the bulk carbon nitride hybrid catalysts were capable of CO₂ reduction. This was believed to be due to bulk materials having very low surface areas and low catalyst attachment.

The CN-BA series of materials was carried forward to undergo exfoliation and were found to have markedly increased surface areas which led to large enhancements in photocatalytic activities for H₂ evolution. The trend in activities across the series were still maintained after exfoliation, indicating that the trend in band structure across the series remained mostly unchanged.

Attachment of the FeTCPP onto the high surface area carbon nitrides was successful and loadings were quantified via UV-Vis DRS and ICP. The hybrid materials were tested for photocatalytic CO₂ reduction and 3 of the 4 hybrid materials were found to produce CO and H₂, with >60% selectivity towards CO production in mainly aqueous solutions. The material with the highest activity was found to be HSA-CN-BA(5)/FeTCPP. The variation in activity for this series of materials could mostly be explained by variations in band structure and charge lifetimes, especially the lack of activity observed by HSA-CN-BA(20)/FeTCPP due to incompatible band positions and redox potentials. This highlights the importance of understanding the band structures and electronic structures of all components of hybrid materials and determination of the band structures of the materials should be standard practice. Control experiments all indicated that the carbon nitride-FeTCPP hybrid catalyst, hole scavenger and CO₂ were required for CO₂ reduction.

Isotopic labelling experiments initially showed the production of only ¹²CO over 24 hours of illumination at 200 mWcm⁻². However, an experiment performed on a smaller scale at lower light intensities (~100mWcm⁻²), illuminated for only 4 hours, showed the production of ¹³CO confirming that the hybrid catalysts were reducing the CO₂ that the experiment was purged with. These results indicate that somewhere between 4 and 24 hours, that the TEOA hole

scavenger is likely being consumed and forming $^{12}\text{CO}_2$ which is then going on to be reduced, forming larger amounts of ^{12}CO which initially swamped the FTIR signal. This chapter highlights the importance of thorough blank and isotopic labelled experiments for confirmation of photocatalytic CO_2 reduction.

Future work for these materials would be to continue with characterisation of both the exfoliated materials and corresponding FeTCPP hybrids to confirm their band structures. Furthermore, time resolved studies with and without a sacrificial donor present could be performed to further understand charge transport and separation in the hybrid materials. The ultimate goal would be to combine these materials with a water oxidation system and potentially a redox mediator, to be able to perform CO_2 reduction coupled with overall water splitting without the need for any charge scavengers.

4.5 References

- 1 Y. Wang, X. Wang and M. Antonietti, *Angew. Chemie Int. Ed.*, 2012, **51**, 68–89.
- 2 S. Cao and J. Yu, *J. Phys. Chem. Lett.*, 2014, **5**, 2101–2107.
- 3 S. Ye, R. Wang, M.-Z. Wu and Y.-P. Yuan, *Appl. Surf. Sci.*, 2015, **358**, 15–27.
- 4 S. Cao, J. Low, J. Yu and M. Jaroniec, *Adv. Mater.*, 2015, **27**, 2150–2176.
- 5 W.-J. Ong, L.-L. Tan, Y. H. Ng, S.-T. Yong and S.-P. Chai, *Chem. Rev.*, 2016, **116**, 7159–7329.
- 6 N. Zhang, L. Wen, J. Yan and Y. Liu, *Chem. Pap.*, 2020, **74**, 389–406.
- 7 M. M. Kandy, *Sustain. Energy Fuels*, 2020, **4**, 469–484.
- 8 B. He, Y. Wang, Q. Zhai, P. Qiu, G. Dong, X. Liu, Y. Chen and Z. Li, *Nanoscale*, 2020, **12**, 8636–8646.
- 9 W. K. Darkwah and K. A. Oswald, *Nanoscale Res. Lett.*, 2019, **14**, 234.
- 10 M. Z. Rahman and C. B. Mullins, *Acc. Chem. Res.*, 2019, **52**, 248–257.
- 11 Y. Fang and X. Wang, *Chem. Commun.*, 2018, **54**, 5674–5687.
- 12 J. Wen, J. Xie, X. Chen and X. Li, *Appl. Surf. Sci.*, 2017, **391**, 72–123.
- 13 Y. Zheng, J. Liu, J. Liang, M. Jaroniec and S. Z. Qiao, *Energy Environ. Sci.*, 2012, **5**, 6717.
- 14 W. Iqbal, B. Yang, X. Zhao, M. Rauf, M. Waqas, Y. Gong, J. Zhang and Y. Mao, *Catal. Sci. Technol.*, 2018, **8**, 4576–4599.
- 15 S. N. Talapaneni, G. Singh, I. Y. Kim, K. AlBahily, A. H. Al-Muhtaseb, A. S. Karakoti, E. Tavakkoli and A. Vinu, *Adv. Mater.*, 2019, **32**, 1904635.
- 16 W. Niu and Y. Yang, *ACS Energy Lett.*, 2018, **3**, 2796–2815.
- 17 W. Tu, Y. Xu, J. Wang, B. Zhang, T. Zhou, S. Yin, S. Wu, C. Li, Y. Huang, Y. Zhou, Z. Zou, J. Robertson, M. Kraft and R. Xu, *ACS Sustain. Chem. Eng.*, 2017, **5**, 7260–7268.
- 18 P. Xia, B. Zhu, J. Yu, S. Cao and M. Jaroniec, *J. Mater. Chem. A*, 2017, **5**, 3230–3238.
- 19 K. L. Corp and C. W. Schlenker, *J. Am. Chem. Soc.*, 2017, **139**, 7904–7912.
- 20 L. K. Putri, W. J. Ong, W. S. Chang and S. P. Chai, *Catal. Sci. Technol.*, 2016, **6**, 744–754.
- 21 Y. Zhang, A. Thomas, M. Antonietti and X. Wang, *J. Am. Chem. Soc.*, 2009, **131**, 50–51.
- 22 J. Jiang, L. Ou-Yang, L. Zhu, A. Zheng, J. Zou, X. Yi and H. Tang, *Carbon N. Y.*, 2014, **80**, 213–221.
- 23 W.-J. Ong, L.-L. Tan, S.-P. Chai, S.-T. Yong and A. R. Mohamed, *Nano Energy*, 2015, **13**, 757–770.
- 24 J. Fu, B. Zhu, C. Jiang, B. Cheng, W. You and J. Yu, *Small*, 2017, **13**, 1603938.
- 25 F. Raziq, Y. Qu, M. Humayun, A. Zada, H. Yu and L. Jing, *Appl. Catal. B Environ.*, 2017, **201**, 486–494.
- 26 P. Niu, Y. Yang, J. C. Yu, G. Liu and H. M. Cheng, *Chem. Commun.*, 2014, **50**, 10837–10840.
- 27 H. Zhou, P. Li, J. Liu, Z. Chen, L. Liu, D. Dontsova, R. Yan, T. Fan, D. Zhang and J. Ye, *Nano Energy*, 2016, **25**, 128–135.
- 28 X. Wu, J. Cheng, X. Li, Y. Li and K. Lv, *Appl. Surf. Sci.*, 2019, **465**, 1037–1046.
- 29 Y. Wang, X. Liu, X. Han, R. Godin, J. Chen, W. Zhou, C. Jiang, J. F. Thompson, K. B. Mustafa, S. A. Shevlin, J. R. Durrant, Z. Guo and J. Tang, *Nat. Commun.*, 2020, **11**, 2531.
- 30 P. Niu, L. Zhang, G. Liu and H. M. Cheng, *Adv. Funct. Mater.*, 2012, **22**, 4763–4770.
- 31 J. T. Yin, Z. Li, Y. Cai, Q. F. Zhang and W. Chen, *Chem. Commun.*, 2017, **53**, 9430–9433.
- 32 J. Zhang, Y. Chen and X. Wang, *Energy Environ. Sci.*, 2015, **8**, 3092–3108.
- 33 J. Xu, L. Zhang, R. Shi and Y. Zhu, *J. Mater. Chem. A*, 2013, **1**, 14766.
- 34 H. J. Li, B. W. Sun, L. Sui, D. J. Qian and M. Chen, *Phys. Chem. Chem. Phys.*, 2015, **17**, 3309–3315.
- 35 S. Yang, Y. Gong, J. Zhang, L. Zhan, L. Ma, Z. Fang, R. Vajtai, X. Wang and P. M. Ajayan, *Adv. Mater.*, 2013, **25**, 2452–2456.
- 36 S. Bai, X. Wang, C. Hu, M. Xie, J. Jiang and Y. Xiong, *Chem. Commun.*, 2014, **50**, 6094–6097.
- 37 L. Shi, T. Wang, H. Zhang, K. Chang and J. Ye, *Adv. Funct. Mater.*, 2015, **25**, 5360–5367.

- 38 X. She, H. Xu, Y. Xu, J. Yan, J. Xia, L. Xu, Y. Song, Y. Jiang, Q. Zhang and H. Li, *J. Mater. Chem. A*, 2014, **2**, 2563–2570.
- 39 H. Zhao, H. Yu, X. Quan, S. Chen, Y. Zhang, H. Zhao and H. Wang, *Appl. Catal. B Environ.*, 2014, **152–153**, 46–50.
- 40 D. Xu, B. Cheng, W. Wang, C. Jiang and J. Yu, *Appl. Catal. B Environ.*, 2018, **231**, 368–380.
- 41 A. Crake, K. C. Christoforidis, R. Godin, B. Moss, A. Kafizas, S. Zafeiratos, J. R. Durrant and C. Petit, *Appl. Catal. B Environ.*, 2019, **242**, 369–378.
- 42 J. Zhang, Y. Wang, J. Jin, J. Zhang, Z. Lin, F. Huang and J. Yu, *ACS Appl. Mater. Interfaces*, 2013, **5**, 10317–10324.
- 43 Q. Lin, L. Li, S. Liang, M. Liu, J. Bi and L. Wu, *Appl. Catal. B Environ.*, 2015, **163**, 135–142.
- 44 X. Zhang, X. Xie, H. Wang, J. Zhang, B. Pan and Y. Xie, *J. Am. Chem. Soc.*, 2013, **135**, 18–21.
- 45 X. Li, G. Hartley, A. J. Ward, P. A. Young, A. F. Masters and T. Maschmeyer, *J. Phys. Chem. C*, 2015, **119**, 14938–14946.
- 46 X. Wang, K. Maeda, X. Chen, K. Takanabe, K. Domen, Y. Hou, X. Fu and M. Antonietti, *J. Am. Chem. Soc.*, 2009, **131**, 1680–1681.
- 47 X. Chen, Y.-S. Jun, K. Takanabe, K. Maeda, K. Domen, X. Fu, M. Antonietti and X. Wang, *Inoue, Y. Energy Environ. Sci.*, 2009, **21**, 1523.
- 48 X. Wang, S. Blechert and M. Antonietti, *ACS Catal.*, 2012, **2**, 1596–1606.
- 49 M. Groenewolt and M. Antonietti, *Adv. Mater.*, 2005, **17**, 1789–1792.
- 50 Y. Wang, J. Zhang, X. Wang, M. Antonietti and H. Li, *Angew. Chemie Int. Ed.*, 2010, **49**, 3356–3359.
- 51 K. Maeda, K. Sekizawa and O. Ishitani, *Chem. Commun.*, 2013, **49**, 10127.
- 52 A. Vinu, K. Ariga, T. Mori, T. Nakanishi, S. Hishita, D. Golberg and Y. Bando, *Adv. Mater.*, 2005, **17**, 1648–1652.
- 53 S. Hwang, S. Lee and J. S. Yu, *Appl. Surf. Sci.*, 2007, **253**, 5656–5659.
- 54 J. Hong, X. Xia, Y. Wang and R. Xu, *J. Mater. Chem.*, 2012, **22**, 15006–15012.
- 55 J. Sun, J. Zhang, M. Zhang, M. Antonietti, X. Fu and X. Wang, *Nat. Commun.*, 2012, **3**, 1139.
- 56 Y.-S. Jun, J. Park, S. U. Lee, A. Thomas, W. H. Hong and G. D. Stucky, *Angew. Chemie Int. Ed.*, 2013, **52**, 11083–11087.
- 57 Y.-S. Jun, E. Z. Lee, X. Wang, W. H. Hong, G. D. Stucky and A. Thomas, *Adv. Funct. Mater.*, 2013, **23**, 3661–3667.
- 58 M. Shalom, S. Inal, C. Fettkenhauer, D. Neher and M. Antonietti, *J. Am. Chem. Soc.*, 2013, **135**, 7118–7121.
- 59 M. Ovcharov, N. Shcherban, S. Filonenko, A. Mishura, M. Skoryk, V. Shvalagin and V. Granchak, *Mater. Sci. Eng. B Solid-State Mater. Adv. Technol.*, 2015, **202**, 1–7.
- 60 K. Maeda, R. Kuriki, M. Zhang, X. Wang and O. Ishitani, *J. Mater. Chem. A*, 2014, **2**, 15146–15151.
- 61 A. Thomas, A. Fischer, F. Goettmann, M. Antonietti, J.-O. Müller, R. Schlögl and J. M. Carlsson, *J. Mater. Chem.*, 2008, **18**, 4893.
- 62 Y. Zheng, L. Lin, X. Ye, F. Guo and X. Wang, *Angew. Chemie - Int. Ed.*, 2014, **53**, 11926–11930.
- 63 J. Wang, C. Zhang, Y. Shen, Z. Zhou, J. Yu, Y. Li, W. Wei, S. Liu and Y. Zhang, *J. Mater. Chem. A*, 2015, **3**, 5126–5131.
- 64 I. Papailias, N. Todorova, T. Giannakopoulou, J. Yu, D. Dimotikali and C. Trapalis, *Catal. Today*, 2017, **280**, 37–44.
- 65 D. Chen, J. Yang and H. Ding, *Appl. Surf. Sci.*, 2017, **391**, 384–391.
- 66 X.-H. H. Li, J. Zhang, X. Chen, A. Fischer, A. Thomas, M. Antonietti and X. Wang, *Chem. Mater*, 2011, **23**, 4344–4348.
- 67 S. W. Bian, Z. Ma and W. G. Song, *J. Phys. Chem. C*, 2009, **113**, 8668–8672.
- 68 G. Jiang, C.-H. Zhou, X. Xia, F. Yang, D. Tong, W. Yu and S. Liu, *Mater. Lett.*, 2010, **64**, 2718–2721.
- 69 X. H. Li, X. Wang and M. Antonietti, *Chem. Sci.*, 2012, **3**, 2170–2174.
- 70 Y. Zheng, L. Lin, B. Wang and X. Wang, *Angew. Chemie Int. Ed.*, 2015, **54**, 12868–12884.
- 71 J. Zhu, P. Xiao, H. Li and S. A. C. Carabineiro, *ACS Appl. Mater. Interfaces*, 2014, **6**, 16449–16465.

- 72 Y. Wang, X. Wang, M. Antonietti and Y. Zhang, *ChemSusChem*, 2010, **3**, 435–439.
- 73 T. Jordan, N. Fechler, J. Xu, T. J. K. Brenner, M. Antonietti and M. Shalom, *ChemCatChem*, 2015, **7**, 2826–2830.
- 74 J. Gao, Y. Zhou, Z. Li, S. Yan, N. Wang and Z. Zou, *Nanoscale*, 2012, **4**, 3687–3692.
- 75 M. K. Bhunia, K. Yamauchi and K. Takanahe, *Angew. Chemie Int. Ed.*, 2014, **53**, 11001–11005.
- 76 Y. Ishida, L. Chabanne, M. Antonietti and M. Shalom, *Langmuir*, 2014, **30**, 447–451.
- 77 C. Zhou, C. Lai, P. Xu, G. Zeng, D. Huang, Z. Li, C. Zhang, M. Cheng, L. Hu, J. Wan, F. Chen, W. Xiong and R. Deng, *ACS Sustain. Chem. Eng.*, 2018, **6**, 6941–6949.
- 78 S. Wan, Q. Zhong, M. Ou and S. Zhang, *RSC Adv.*, 2016, **6**, 101208–101215.
- 79 W. Tang, Y. Tian, B. Chen, Y. Xu, B. Li, X. Jing, J. Zhang and S. Xu, *ACS Appl. Mater. Interfaces*, 2020, **12**, 6396–6406.
- 80 M. Shalom, M. Guttentag, C. Fettkenhauer, S. Inal, D. Neher, A. Llobet and M. Antonietti, *Chem. Mater.*, 2014, **26**, 5812–5818.
- 81 C. Zhou, C. Lai, D. Huang, G. Zeng, C. Zhang, M. Cheng, L. Hu, J. Wan, W. Xiong, M. Wen, X. Wen and L. Qin, *Appl. Catal. B Environ.*, 2018, **220**, 202–210.
- 82 J. Barrio, L. Lin, X. Wang and M. Shalom, *ACS Sustain. Chem. Eng.*, 2018, **6**, 519–530.
- 83 F. Li, D. Zhang and Q. Xiang, *Chem. Commun.*, 2020, **56**, 2443–2446.
- 84 Z. Zhao, Y. Sun and F. Dong, *Nanoscale*, 2015, **7**, 15–37.
- 85 Q. Han, N. Chen, J. Zhang and L. Qu, *Mater. Horizons*, 2017, **4**, 832–850.
- 86 J. Xu, Y. Li, S. Peng, G. Lu and S. Li, *Phys. Chem. Chem. Phys.*, 2013, **15**, 7657.
- 87 G. Zhang, Z. A. Lan and X. Wang, *Chem. Sci.*, 2017, **8**, 5261–5274.
- 88 A. L. Linsebigler, G. Lu and J. T. Yates, *Chem. Rev.*, 1995, **95**, 735–758.
- 89 Y. Li, T. Kong and S. Shen, *Small*, 2019, **15**, 1900772.
- 90 X. Wang, K. Maeda, A. Thomas, K. Takanahe, G. Xin, J. M. Carlsson, K. Domen and M. Antonietti, *Nat. Mater.*, 2009, **8**, 76–80.
- 91 L. Yu, X. Zhang, C. Zhuang, L. Lin, R. Li and T. Peng, *Phys. Chem. Chem. Phys.*, 2014, **16**, 4106–4114.
- 92 P. Wang, Z. Guan, Q. Li and J. Yang, *J. Mater. Sci.*, 2018, **53**, 774–786.
- 93 Z. Pan, Y. Zheng, F. Guo, P. Niu and X. Wang, *ChemSusChem*, 2017, **10**, 87–90.
- 94 Y. Xue, Y. Lei, X. Liu, Y. Li, W. Deng, F. Wang and S. Min, *New J. Chem.*, 2018, **42**, 14083–14086.
- 95 G. Zhang, Z.-A. Lan, L. Lin, S. Lin and X. Wang, *Chem. Sci.*, 2016, **7**, 3062–3066.
- 96 S. Mei, J. Gao, Y. Zhang, J. Yang, Y. Wu, X. Wang, R. Zhao, X. Zhai, C. Hao, R. Li and J. Yan, *J. Colloid Interface Sci.*, 2017, **506**, 58–65.
- 97 Y. Wang, J. Hong, W. Zhang and R. Xu, *Catal. Sci. Technol.*, 2013, **3**, 1703.
- 98 D. Zheng, X.-N. Cao and X. Wang, *Angew. Chemie Int. Ed.*, 2016, **55**, 11512–11516.
- 99 S. Chen, C. Wang, B. R. Bunes, Y. Li, C. Wang and L. Zang, *Appl. Catal. A Gen.*, 2015, **498**, 63–68.
- 100 Q. Xiang, J. Yu and M. Jaroniec, *J. Phys. Chem. C*, 2011, **115**, 7355–7363.
- 101 M. Z. Rahman, P. C. Tapping, T. W. Kee, R. Smernik, N. Spooner, J. Moffatt, Y. Tang, K. Davey and S. Z. Qiao, *Adv. Funct. Mater.*, 2017, **27**, 1702384.
- 102 Y. Zheng, J. Wang, J. Zhang, T. Peng and R. Li, *Dalt. Trans.*, 2017, **46**, 8219–8228.
- 103 K. Takanahe, K. Kamata, X. Wang, M. Antonietti, J. Kubota and K. Domen, *Phys. Chem. Chem. Phys.*, 2010, **12**, 13020–13025.
- 104 V. W. Lau, V. W. Yu, F. Ehrat, T. Botari, I. Moudrakovski, T. Simon, V. Duppel, E. Medina, J. K. Stolarczyk, J. Feldmann, V. Blum and B. V. Lotsch, *Adv. Energy Mater.*, 2017, **7**, 1602251.
- 105 X. Zhang, L. Yu, R. Li, T. Peng and X. Li, *Catal. Sci. Technol.*, 2014, **4**, 3251–3260.
- 106 V. W. Lau, I. Moudrakovski, T. Botari, S. Weinberger, M. B. Mesch, V. Duppel, J. Senker, V. Blum and B. V. Lotsch, *Nat. Commun.*, 2016, **7**, 12165.
- 107 M. Zhang, Y. Duan, H. Jia, F. Wang, L. Wang, Z. Su and C. Wang, *Catal. Sci. Technol.*, 2017, **7**, 452–458.
- 108 Y. Cao, Z. Zhang, J. Long, J. Liang, H. H. H. Lin, H. H. H. Lin and X. Wang, *J. Mater. Chem. A*, 2014, **2**, 17797–17807.
- 109 J. Yu, K. Wang, W. Xiao and B. Cheng, *Phys. Chem. Chem. Phys.*, 2014, **16**, 11492.
- 110 G. Gao, Y. Jiao, E. R. Waclawik and A. Du, *J. Am. Chem. Soc.*, 2016, **138**, 6292–6297.
- 111 W.-J. Ong, L.-L. Tan, S.-P. Chai and S.-T. Yong, *Dalt. Trans.*, 2015, **44**, 1249–1257.
- 112 Y. Yang, Z. Tang, B. Zhou, J. Shen, H. He, A. Ali, Q. Zhong, Y. Xiong, C. Gao, A.

- Alsaedi, T. Hayat, X. Wang, Y. Zhou and Z. Zou, *Appl. Catal. B Environ.*, 2020, **264**, 118470.
- 113 K. Wang, Q. Li, B. Liu, B. Cheng, W. Ho and J. Yu, *Appl. Catal. B Environ.*, 2015, **176–177**, 44–52.
- 114 R. Zhang, Z. Huang, C. Li, Y. Zuo and Y. Zhou, *Appl. Surf. Sci.*, 2019, **475**, 953–960.
- 115 T. Ohno, N. Murakami, T. Koyanagi and Y. Yang, *J. CO₂ Util.*, 2014, **6**, 17–25.
- 116 Y. Di, X. Wang, A. Thomas and M. Antonietti, *ChemCatChem*, 2010, **2**, 834–838.
- 117 Y. Guo, H. Jia, J. Yang, H. Yin, Z. Yang, J. Wang and B. Yang, *Phys. Chem. Chem. Phys.*, 2018, **20**, 22296–22307.
- 118 W. Cheng, H. Su, F. Tang, W. Che, Y. Huang, X. Zheng, T. Yao, J. Liu, F. Hu, Y. Jiang, Q. Liu and S. Wei, *J. Mater. Chem. A*, 2017, **5**, 19649–19655.
- 119 S. Patnaik, S. Martha, G. Madras and K. Parida, *Phys. Chem. Chem. Phys.*, 2016, **18**, 28502–28514.
- 120 F. Li, H. Zhou, J. Fan and Q. Xiang, *J. Colloid Interface Sci.*, 2020, **570**, 11–19.
- 121 X. Bai, R. Zong, C. Li, D. Liu, Y. Liu and Y. Zhu, *Appl. Catal. B Environ.*, 2014, **147**, 82–91.
- 122 Y. Yang, Y. Y. Guo, F. Liu, X. Yuan, Y. Y. Guo, S. Zhang, W. Guo and M. Huo, *Appl. Catal. B Environ.*, 2013, **142–143**, 828–837.
- 123 S. Wang, J. Lin and X. Wang, *Phys. Chem. Chem. Phys.*, 2014, **16**, 14656.
- 124 M. Fan, C. Song, T. Chen, X. Yan, D. Xu, W. Gu, W. Shi and L. Xiao, *RSC Adv.*, 2016, **6**, 34633–34640.
- 125 H. Shi, S. Long, J. Hou, L. Ye, Y. Sun, W. Ni, C. Song, K. Li, G. G. Gurzadyan and X. Guo, *Chem. – A Eur. J.*, 2019, **25**, 5028–5035.
- 126 G. Shi, L. Yang, Z. Liu, X. Chen, J. Zhou and Y. Yu, *Appl. Surf. Sci.*, 2018, **427**, 1165–1173.
- 127 Y. Cao, S. Chen, Q. Luo, H. Yan, Y. Lin, W. Liu, L. Cao, J. Lu, J. Yang, T. Yao and S. Wei, *Angew. Chemie - Int. Ed.*, 2017, **56**, 12191–12196.
- 128 P. Huang, J. Huang, S. A. Pantovich, A. D. Carl, T. G. Fenton, C. A. Caputo, R. L. Grimm, A. I. Frenkel and G. Li, *J. Am. Chem. Soc.*, 2018, **140**, 16042–16047.
- 129 L. Kong, Y. Dong, P. Jiang, G. Wang, H. Zhang and N. Zhao, *J. Mater. Chem. A*, 2016, **4**, 9998–10007.
- 130 X. Zhao, B. Luo, R. Long, C. Wang and Y. Xiong, *J. Mater. Chem. A*, 2015, **3**, 4134–4138.
- 131 C. Han, Y. Lu, J. Zhang, L. Ge, Y. Li, C. Chen, Y. Xin, L. Wu and S. Fang, *J. Mater. Chem. A*, 2015, **3**, 23274–23282.
- 132 P. Wang, L. Zong, Z. Guan, Q. Li and J. Yang, *Nanoscale Res. Lett.*, 2018, **13**, 33.
- 133 C. Han, L. Wu, L. Ge, Y. Li and Z. Zhao, *Carbon N. Y.*, 2015, **92**, 31–40.
- 134 H. Zhang, X. Zuo, H. Tang, G. Li and Z. Zhou, *Phys. Chem. Chem. Phys.*, 2015, **17**, 6280–6288.
- 135 J. Zhang, X. Chen, K. Takanebe, K. Maeda, K. Domen, J. D. Epping, X. Fu, M. Antonietti and X. Wang, *Angew. Chemie Int. Ed.*, 2010, **49**, 441–444.
- 136 K. R. Reddy, C. V. Reddy, M. N. Nadagouda, N. P. Shetti, S. Jaesool and T. M. Aminabhavi, *J. Environ. Manage.*, 2019, **238**, 25–40.
- 137 S. Min and G. Lu, *J. Phys. Chem. C*, 2012, **116**, 19644–19652.
- 138 H. Zhang, S. Li, R. Lu and A. Yu, *ACS Appl. Mater. Interfaces*, 2015, **7**, 21868–21874.
- 139 J. Dong, M. Wang, X. Li, L. Chen, Y. He and L. Sun, *ChemSusChem*, 2012, **5**, 2133–2138.
- 140 K. Mori, T. Itoh, H. Kakudo, T. Iwamoto, Y. Masui, M. Onaka and H. Yamashita, *Phys. Chem. Chem. Phys.*, 2015, **17**, 24086–24091.
- 141 Y. Guo, S. Song, Y. Zheng, R. Li and T. Peng, *Dalt. Trans.*, 2016, **45**, 14071–14079.
- 142 S. Song, Y. Guo, T. Peng, J. Zhang and R. Li, *RSC Adv.*, 2016, **6**, 77366–77374.
- 143 R. Kuriki and K. Maeda, *Phys. Chem. Chem. Phys.*, 2017, **19**, 4938–4950.
- 144 H. Kasap, R. Godin, C. Jeay-Bizot, D. S. Achilleos, X. Fang, J. R. Durrant and E. Reisner, *ACS Catal.*, 2018, **8**, 6914–6926.
- 145 H. Kasap, C. A. Caputo, B. C. M. M. Martindale, R. Godin, V. W. H. Lau, B. V. Lotsch, J. R. Durrant and E. Reisner, *J. Am. Chem. Soc.*, 2016, **138**, 9183–9192.
- 146 D. Wang, Y. Zhang and W. Chen, *Chem. Commun.*, 2014, **50**, 1754.
- 147 X. W. Song, H. M. Wen, C. B. Ma, H. H. Cui, H. Chen and C. N. Chen, *RSC Adv.*, 2014, **4**, 18853–18861.
- 148 S. W. Cao, X. F. Liu, Y. P. Yuan, Z. Y. Zhang, J. Fang, S. C. J. Loo, J. Barber, T. C.

- Sum and C. Xue, *Phys. Chem. Chem. Phys.*, 2013, **15**, 18363–18366.
- 149 R. Kuriki, K. Sekizawa, O. Ishitani and K. Maeda, *Angew. Chemie Int. Ed.*, 2015, **54**, 2406–2409.
- 150 K. Maeda, R. Kuriki and O. Ishitani, *Chem. Lett.*, 2016, **45**, 182–184.
- 151 R. Kuriki, O. Ishitani and K. Maeda, *ACS Appl. Mater. Interfaces*, 2016, **8**, 6011–6018.
- 152 R. Kuriki, C. S. K. Ranasinghe, Y. Yamazaki, A. Yamakata, O. Ishitani and K. Maeda, *J. Phys. Chem. C*, 2018, **122**, 16795–16802.
- 153 K. Maeda, D. An, C. S. Kumara Ranasinghe, T. Uchiyama, R. Kuriki, T. Kanazawa, D. Lu, S. Nozawa, A. Yamakata, Y. Uchimoto and O. Ishitani, *J. Mater. Chem. A*, 2018, **6**, 9708–9715.
- 154 K. Maeda, D. An, R. Kuriki, D. Lu and O. Ishitani, *Beilstein J. Org. Chem*, 2018, **14**, 1806–1812.
- 155 C. Tsounis, R. Kuriki, K. Shibata, J. J. M. Vequizo, D. Lu, A. Yamakata, O. Ishitani, R. Amal and K. Maeda, *ACS Sustain. Chem. Eng.*, 2018, **6**, 15333–15340.
- 156 R. Kuriki, H. Matsunaga, T. Nakashima, K. Wada, A. Yamakata, O. Ishitani and K. Maeda, *J. Am. Chem. Soc.*, 2016, **138**, 5159–5170.
- 157 R. Kuriki, M. Yamamoto, K. Higuchi, Y. Yamamoto, M. Akatsuka, D. Lu, S. Yagi, T. Yoshida, O. Ishitani and K. Maeda, *Angew. Chemie*, 2017, **129**, 4945–4949.
- 158 K. Wada, M. Eguchi, O. Ishitani and K. Maeda, *ChemSusChem*, 2017, **10**, 287–295.
- 159 K. Wada, C. S. K. Ranasinghe, R. Kuriki, A. Yamakata, O. Ishitani and K. Maeda, *ACS Appl. Mater. Interfaces*, 2017, **9**, 23869–23877.
- 160 J. Lin, Z. Pan and X. Wang, *ACS Sustain. Chem. Eng.*, 2014, **2**, 353–358.
- 161 J. J. Walsh, C. Jiang, J. Tang and A. J. Cowan, *Phys. Chem. Chem. Phys.*, 2016, **18**, 24825–24829.
- 162 Z. Pan, P. Niu, M. Liu, G. Zhang, Z. Zhu and X. Wang, *ChemSusChem*, 2020, **13**, 888–892.
- 163 N.-N. Vu, S. Kaliaguine and T.-O. Do, *ACS Appl. Energy Mater.*, 2020, **3**, 6422–6433.
- 164 X. Ma, C. Hu and Z. Bian, *Inorg. Chem. Commun.*, 2020, **117**, 107951.
- 165 C. Cometto, R. Kuriki, L. Chen, K. Maeda, T. C. Lau, O. Ishitani and M. Robert, *J. Am. Chem. Soc.*, 2018, **140**, 7437–7440.
- 166 B. Ma, G. Chen, C. Fave, L. Chen, R. Kuriki, K. Maeda, O. Ishitani, T. C. Lau, J. Bonin and M. Robert, *J. Am. Chem. Soc.*, 2020, **142**, 6188–6195.
- 167 J. Liu, H. Shi, Q. Shen, C. Guo and G. Zhao, *Green Chem.*, 2017, **19**, 5900–5910.
- 168 L. Lin, C. Hou, X. Zhang, Y. Wang, Y. Chen and T. He, *Appl. Catal. B Environ.*, 2018, **221**, 312–319.
- 169 X. Zhang, L. Lin, D. Qu, J. Yang, Y. Weng, Z. Wang, Z. Sun, Y. Chen and T. He, *Appl. Catal. B Environ.*, 2020, **265**, 118595.
- 170 G. Zhao, H. Pang, G. Liu, P. Li, H. Liu, H. Zhang, L. Shi and J. Ye, *Appl. Catal. B Environ.*, 2017, **200**, 141–149.
- 171 P. Huang, S. A. Pantovich, N. O. Okolie, N. A. Deskins and G. Li, *ChemPhotoChem*, 2020, **4**, 420–426.
- 172 S. Roy and E. Reisner, *Angew. Chemie Int. Ed.*, 2019, **58**, 12180–12184.
- 173 A. Kumar, P. Kumar, R. Borkar, A. Bansiwala, N. Labhsetwar and S. L. Jain, *Carbon N. Y.*, 2017, **123**, 371–379.
- 174 Y. Zhang and M. Antonietti, *Chem. - An Asian J.*, 2010, **5**, 1307–1311.
- 175 S. Zhou, Y. Liu, J. Li, Y. Wang, G. Jiang, Z. Zhao, D. Wang, A. Duan, J. Liu and Y. Wei, *Appl. Catal. B Environ.*, 2014, **158–159**, 20–29.
- 176 D. O. Adekoya, M. Tahir and N. A. S. Amin, *J. CO₂ Util.*, 2017, **18**, 261–274.
- 177 N. T. Thanh Truc, L. Giang Bach, N. Thi Hanh, T. D. Pham, N. Thi Phuong Le Chi, D. T. Tran, M. V. Nguyen and V. N. Nguyen, *J. Colloid Interface Sci.*, 2019, **540**, 1–8.
- 178 J. Wu, Y. Feng, B. E. Logan, C. Dai, X. Han, D. Li and J. Liu, *ACS Sustain. Chem. Eng.*, 2019, **7**, 15289–15296.
- 179 R. Sun, X. Jiang, M. Zhang, Y. Ma, X. Jiang, Z. Liu, Y. Wang, J. Yang, M. Xie and W. Han, *J. Catal.*, 2019, **378**, 192–200.
- 180 H. Wang, H. Li, Z. Chen, J. Li, X. Li, P. Huo and Q. Wang, *Solid State Sci.*, 2020, **100**, 106099.
- 181 Q. Wang, L. Zhang, Y. Guo, M. Shen, M. Wang, B. Li and J. Shi, *Chem. Eng. J.*, 2020, **396**, 125347.
- 182 S. Huang, Y. Long, S. Ruan and Y. J. Zeng, *ACS Omega*, 2019, **4**, 15593–15599.
- 183 X. Li, X. Song, C. Ma, Y. Cheng, D. Shen, S. Zhang, W. Liu, P. Huo and H. Wang, *ACS*

- Appl. Nano Mater.*, 2020, **3**, 1298–1306.
- 184 Z. Jiang, W. Wan, H. Li, S. Yuan, H. Zhao and P. K. Wong, *Adv. Mater.*, 2018, **30**, 1706108.
- 185 J. Wang, C. Qin, H. Wang, M. Chu, A. Zada, X. Zhang, J. Li, F. Raziq, Y. Qu and L. Jing, *Appl. Catal. B Environ.*, 2018, **221**, 459–466.
- 186 B. Duan and L. Mei, *J. Colloid Interface Sci.*, 2020, **575**, 265–273.
- 187 W. Yu, D. Xu and T. Peng, *J. Mater. Chem. A*, 2015, **3**, 19936–19947.
- 188 Y. He, Y. Wang, L. Zhang, B. Teng and M. Fan, *Appl. Catal. B Environ.*, 2015, **168–169**, 1–8.
- 189 Q. Guo, L. Fu, T. Yan, W. Tian, D. Ma, J. Li, Y. Jiang and X. Wang, *Appl. Surf. Sci.*, 2020, **509**, 144773.
- 190 Z. Zhu, C. Chen and R. Wu, *J. Chinese Chem. Soc.*, 2020, **67**, 1654–1660.
- 191 L. Zhu, H. Li, Q. Xu, D. Xiong and P. Xia, *J. Colloid Interface Sci.*, 2020, **564**, 303–312.
- 192 N. Nie, L. Zhang, J. Fu, B. Cheng and J. Yu, *Appl. Surf. Sci.*, 2018, **441**, 12–22.
- 193 X. Yang, W. Xin, X. Yin and X. Shao, *Chem. Phys. Lett.*, 2016, **651**, 127–132.
- 194 M. Zhou, S. Wang, P. Yang, C. Huang and X. Wang, *ACS Catal.*, 2018, **8**, 4928–4936.
- 195 X. Li, M. Edelmannová, P. Huo and K. Kočí, *J. Mater. Sci.*, 2020, **55**, 3299–3313.
- 196 Q. Xie, W. He, S. Liu, C. Li, J. Zhang and P. K. Wong, *Chinese J. Catal.*, 2020, **41**, 140–153.
- 197 R. A. Rather, M. Khan and I. M. C. Lo, *J. Catal.*, 2018, **366**, 28–36.
- 198 M. Lu, Q. Li, C. Zhang, X. Fan, L. Li, Y. Dong, G. Chen and H. Shi, *Carbon N. Y.*, 2020, **160**, 342–352.
- 199 C. Han, R. Zhang, Y. Ye, L. Wang, Z. Ma, F. Su, H. Xie, Y. Zhou, P. K. Wong and L. Ye, *J. Mater. Chem. A*, 2019, **7**, 9726–9735.
- 200 Y. He, L. Zhang, M. Fan, X. Wang, M. L. Walbridge, Q. Nong, Y. Wu and L. Zhao, *Sol. Energy Mater. Sol. Cells*, 2015, **137**, 175–184.
- 201 S.-W. Cao, X.-F. Liu, Y.-P. Yuan, Z.-Y. Zhang, Y.-S. Liao, J. Fang, S. C. J. Loo, T. C. Sum and C. Xue, *Appl. Catal. B Environ.*, 2014, **147**, 940–946.
- 202 H. Shi, G. Chen, C. Zhang and Z. Zou, *ACS Catal.*, 2014, **4**, 3637–3643.
- 203 M. Li, L. Zhang, X. Fan, Y. Zhou, M. Wu and J. Shi, *J. Mater. Chem. A*, 2015, **3**, 5189–5196.
- 204 Y. He, L. Zhang, B. Teng and M. Fan, *Environ. Sci. Technol.*, 2015, **49**, 649–656.
- 205 Y. Bai, L. Ye, L. Wang, X. Shi, P. Wang, W. Bai and P. K. Wong, *Appl. Catal. B Environ.*, 2016, **194**, 98–104.
- 206 M. Li, L. Zhang, M. Wu, Y. Du, X. Fan, M. Wang, L. Zhang, Q. Kong and J. Shi, *Nano Energy*, 2016, **19**, 145–155.
- 207 J.-C. Wang, H.-C. Yao, Z.-Y. Fan, L. Zhang, J.-S. Wang, S.-Q. Zang and Z.-J. Li, *ACS Appl. Mater. Interfaces*, 2016, **8**, 3765–3775.
- 208 M. Li, L. Zhang, X. Fan, M. Wu, M. Wang, R. Cheng, L. Zhang, H. Yao and J. Shi, *Appl. Catal. B Environ.*, 2017, **201**, 629–635.
- 209 C. C. Wang, X. H. Yi and P. Wang, *Appl. Catal. B Environ.*, 2019, **247**, 24–48.
- 210 Q. Chen, S. Li, H. Xu, G. Wang, Y. Qu, P. Zhu and D. Wang, *Chinese J. Catal.*, 2020, **41**, 514–523.
- 211 X.-Y. Dao, X.-F. Xie, J.-H. Guo, X.-Y. Zhang, Y.-S. Kang and W.-Y. Sun, *Cite This ACS Appl. Energy Mater*, 2020, **2020**, 3946–3954.
- 212 Y. Wang, W. Zhen, Y. Zeng, S. Wan, H. Guo, S. Zhang and Q. Zhong, *J. Mater. Chem. A*, 2020, **8**, 6034–6040.
- 213 Y. Meng, L. Zhang, H. Jiu, Q. Zhang, H. Zhang, W. Ren, Y. Sun and D. Li, *Mater. Sci. Semicond. Process.*, 2019, **95**, 35–41.
- 214 Y. Wang, L. Guo, Y. Zeng, H. Guo, S. Wan, M. Ou, S. Zhang and Q. Zhong, *ACS Appl. Mater. Interfaces*, 2019, **11**, 30673–30681.
- 215 Y. Wang, Q. Cai, M. Yao, S. Kang, Z. Ge and X. Li, *ACS Sustain. Chem. Eng.*, 2018, **6**, 2529–2534.
- 216 Q. Li, S. Wang, Z. Sun, Q. Tang, Y. Liu, L. Wang, H. Wang and Z. Wu, *Nano Res.*, 2019, **12**, 2749–2759.
- 217 W. J. Ong, L. K. Putri, Y. C. Tan, L. L. Tan, N. Li, Y. H. Ng, X. Wen and S. P. Chai, *Nano Res.*, 2017, **10**, 1673–1696.
- 218 W. J. Ong, L. L. Tan, S. P. Chai and S. T. Yong, *Chem. Commun.*, 2015, **51**, 858–861.
- 219 M. Tahir, B. Tahir, M. G. M. Nawawi, M. Hussain and A. Muhammad, *Appl. Surf. Sci.*, 2019, **485**, 450–461.

- 220 Y. Yang, J. Wu, T. Xiao, Z. Tang, J. Shen, H. Li, Y. Zhou and Z. Zou, *Appl. Catal. B Environ.*, 2019, **255**, 117771.
- 221 A. Bafaqeer, M. Tahir, A. A. Khan and N. A. S. Amin, *Ind. Eng. Chem. Res.*, 2019, **58**, 8612–8624.
- 222 W. K. Jo, S. Kumar, S. Eslava and S. Tonda, *Appl. Catal. B Environ.*, 2018, **239**, 586–598.
- 223 G. Neri, J. J. Walsh, C. Wilson, A. Reynal, J. Y. C. Lim, X. Li, A. J. P. White, N. J. Long, J. R. Durrant and A. J. Cowan, *Phys. Chem. Chem. Phys.*, 2015, **17**, 1562–1566.
- 224 G. Neri, I. M. Aldous, J. J. Walsh, L. J. Hardwick and A. J. Cowan, *Chem. Sci.*, 2016, **7**, 1521–1526.
- 225 G. Neri, M. Forster, J. J. Walsh, C. M. Robertson, T. J. Whittles, P. Farràs and A. J. Cowan, *Chem. Commun.*, 2016, **52**, 14200–14203.
- 226 M. F. Kuehnel, C. D. Sahm, G. Neri, J. R. Lee, K. L. Orchard, A. J. Cowan and E. Reisner, *Chem. Sci.*, 2018, **9**, 2501–2509.
- 227 C. A. Craig, L. O. Spreer, J. W. Otvos and M. Calvin, *J. Phys. Chem.*, 1990, **94**, 7957–7960.
- 228 K. Mochizuki, S. Manaka, I. Takeda and T. Kondo, *Inorg. Chem.*, 1996, **35**, 5132–5136.
- 229 M. A. Méndez, P. Voyame and H. H. Girault, *Angew. Chemie Int. Ed.*, 2011, **50**, 7391–7394.
- 230 E. S. Da Silva, N. M. Moura, M. G. P. M. S. Neves, A. Coutinho, M. Prieto, C. G. Silva and J. L. Faria, *Appl. Catal. B Environ.*, 2018, **221**, 56–69.
- 231 W. Li, X. He, R. Ge, M. Zhu, L. Feng and Y. Li, *Sustain. Mater. Technol.*, 2019, **22**, e00114.
- 232 K. Zhu, M. Zhang, X. Feng, L. Qin, S.-Z. Kang and X. Li, *Appl. Catal. B Environ.*, 2020, **268**, 118434.
- 233 D. Chen, K. Wang, W. Hong, R. Zong, W. Yao and Y. Zhu, *Appl. Catal. B Environ.*, 2015, **166–167**, 366–373.
- 234 Z. Ma, C. Zeng, L. Hu, Q. Zhao, Q. Yang, J. Niu, B. Yao and Y. He, *Appl. Surf. Sci.*, 2019, **484**, 489–500.
- 235 F. Shao, L. Mi, Z. Tian, C. Zheng, Y. Zhang, Q. Li and S. Liu, *ACS Appl. Mater. Interfaces*, 2019, **11**, 44922–44930.
- 236 P. Chanhom, N. Charoenlap, C. Manipuntee and N. Insin, *J. Magn. Magn. Mater.*, 2019, **475**, 602–610.
- 237 M. Thommes, K. Kaneko, A. V. Neimark, J. P. Olivier, F. Rodriguez-Reinoso, J. Rouquerol and K. S. W. Sing, *Pure Appl. Chem.*, 2015, **87**, 1051–1069.
- 238 K. S. W. Sing, D. H. Everett, R. A. W. Haul, L. Moscou, R. A. Pierotti, J. Rouquerol and T. Siemieniowska, *Pure Appl. Chem.*, 1985, **57**, 603–619.
- 239 F. Dong, Z. Zhao, T. Xiong, Z. Ni, W. Zhang, Y. Sun and W. K. Ho, *ACS Appl. Mater. Interfaces*, 2013, **5**, 11392–11401.
- 240 J. Li, B. Shen, Z. Hong, B. Lin, B. Gao and Y. Chen, *Chem. Commun.*, 2012, **48**, 12017.
- 241 I. Azcarate, C. Costentin, M. Robert and J. M. Savéant, *J. Phys. Chem. C*, 2016, **120**, 28951–28960.
- 242 C. Costentin, G. Passard, M. Robert and J. M. Savéant, *J. Am. Chem. Soc.*, 2014, **136**, 11821–11829.
- 243 I. Azcarate, C. Costentin, M. Robert and J.-M. Savéant, *J. Am. Chem. Soc.*, 2016, **138**, 16639–16644.
- 244 C. Costentin, S. Drouet, G. Passard, M. Robert and J.-M. Savéant, *J. Am. Chem. Soc.*, 2013, **135**, 9023–9031.
- 245 C. Costentin, S. Drouet, M. Robert and J.-M. Savéant, *Science (80-.)*, 2012, **338**, 90–94.
- 246 C. Costentin, M. Robert, J. M. Savéant and A. Tatin, *Proc. Natl. Acad. Sci. U. S. A.*, 2015, **112**, 6882–6886.
- 247 I. Bhugun, D. Lexa and J.-M. Saveant, *J. Am. Chem. Soc.*, 1994, **116**, 5015–5016.
- 248 M. Hammouche, D. Lexa, J. M. Savéant and M. Mometeau, *J. Electroanal. Chem. Interfacial Electrochem.*, 1988, **249**, 347–351.
- 249 G. Neri, M. Forster, J. J. Walsh, C. M. Robertson, T. J. Whittles, P. Farràs and A. J. Cowan, *Chem. Commun.*, 2016, **52**, 14200–14203.
- 250 H. Rao, C.-H. Lim, J. Bonin, G. M. Miyake and M. Robert, *J. Am. Chem. Soc.*, 2018, **140**, 17830–17834.
- 251 H. Rao, L. C. Schmidt, J. Bonin and M. Robert, *Nature*, 2017, **548**, 74–77.

5

Metal Oxides and Hybrid Materials

5.1 Introduction

Copper(I)-based metal oxides appear to be promising materials for water splitting and CO₂ reduction. They have a wide range of bandgap sizes. (~1.2 eV to >3.0 eV), are made from earth-abundant metals and are relatively stable under aqueous conditions in comparison to other metal semiconductors such as CdS.¹⁻⁹ Furthermore, Cu(I) sites have been proposed to stabilise CO₂ reduction reaction intermediates.¹⁰

Cu₂O has been widely studied for use in catalysis as electrodes, photoelectrodes and photocatalysts.^{3,6,8,9,11-15} It has been reported to be a p-type semiconductor with a band gap of ~2.1 eV and a band structure which allows it to perform both the reduction and oxidation reactions required for overall water splitting and CO₂ reduction. Nevertheless, one issue that continues to have a detrimental effect on its use as both photoelectrodes and photocatalysts, is its stability. Cu₂O is susceptible to photodecomposition in aqueous solution as photogenerated electrons reduce Cu^I to Cu metal, causing it to deactivate.^{8,15,16} The reduction potential for Cu^I to Cu metal is more positive than that of the CO₂ and water splitting redox potentials, and lies within the Cu₂O band gap, meaning that Cu(I) oxides are easily reduced and difficult to stabilise.^{15,17} But it has been proposed that the addition of a second metal into the structure, with empty d orbitals, can increase the Cu-O bond strength and also adding other metal orbitals into the conduction band that are less readily reduced, enhancing stability.^{1,17,19}

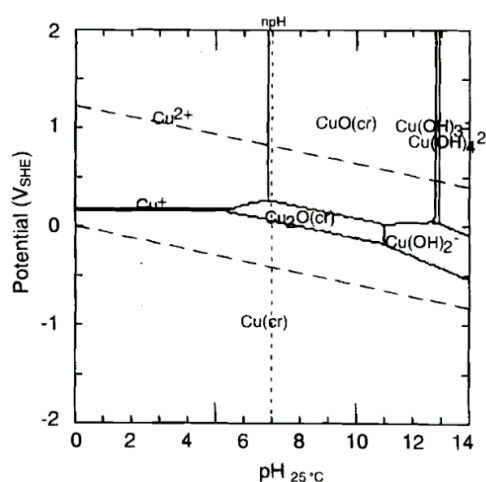


Figure 96 - Pourbaix Diagram for copper at 25 °C, taken from reference ¹⁸. The dashed lines represent water redox potentials showing the stability area of water.

5.2 Aim of Work

The main aim of this work is to synthesise and characterise materials for use as photocatalysts for CO₂ reduction. Materials chosen for study in this chapter have either not been tested or only briefly studied for CO₂ reduction, often as photoelectrodes rather than photocatalysts. The reported band structures of the delafossite and niobate materials studied within this chapter are shown in Figure 97, and they have been targeted due to the relative simplicity of their solid-state synthesis, previous reported photoelectrochemical activity and positions of conduction bands (CB) and valence bands (VB).

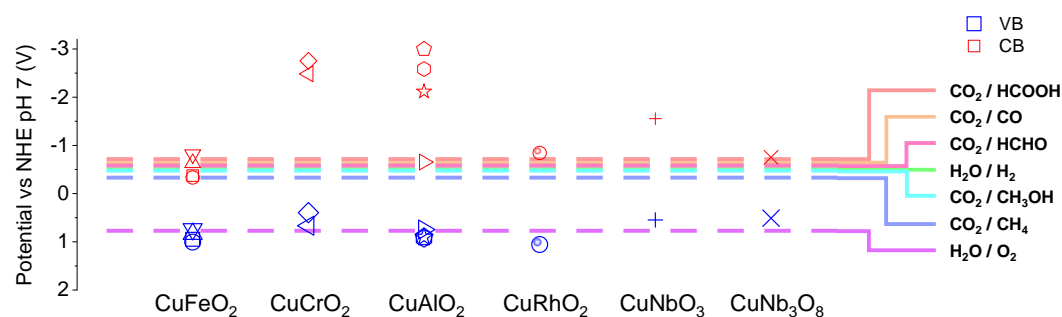


Figure 97 - Band structures of materials studied within this work. Band positions are estimated from reported values. The symbols used for the conduction and valence bands are to differentiate between references.^{1,19,28–32,20–27}

The band positions in Figure 97 were estimated from literature values and converted to a common reference electrode (normal hydrogen electrode (NHE)) and pH. All materials are reported to have CB negative enough to facilitate H₂ evolution and CO₂ reduction, as evidenced by previously reported activity. In the literature, a range of values have been reported for the band positions of CuFeO₂ and CuAlO₂. For CuAlO₂ there is great dispute over the exact value of the band gap, but several reports^{28,29,33} have shown the VB to lie at a similar position with the only large discrepancy being over the CB position. Nevertheless, as can be seen from Figure 97, all CB positions should allow for the reduction reactions to occur. Whilst there is more consistency in reported band gap for CuFeO₂,^{20,24–26} the exact band positions vary slightly and due to the small band gap, small variations in band positions can mean the difference between having a large enough driving force to reduce H₂O/CO₂ and not. However, experimentally CuFeO₂ has been shown to both photoelectrochemically and photocatalytically perform water splitting and CO₂ reduction.^{25,34–41}

5.2.1 Materials and Previous Activity

5.2.1.1 Delafossite Materials

Delafossite materials are ternary metal oxides which have the structure of the mineral delafossite, CuFeO_2 , named after mineralogist Gabriel Delafosse. They have the general formula ABO_2 where A is a monovalent cation, Pt, Pd, Ag or Cu and B a trivalent cation, Al, Co, Cr, Fe, Ga, In, Ni, Rh, Sc or Y. They crystallise into a layered structure where monovalent A atoms are coordinated to two O atoms in linear O-A-O bonds and edge shared $\text{B}^{\text{III}}\text{O}_6$ octahedra. Depending on stacking of these layers, compounds crystallise in hexagonal or rhombohedral space groups (Figure 98).^{1,42-48} Interest in these materials has developed over the years due to their diverse reported properties relating to magnetism, thermoelectrics, electronics (transparent conducting oxides, solar cells, batteries) and catalysis (electro-, photo- and photoelectro-). Generally, Pt and Pd based delafossites have shown metallic behaviour whilst Cu and Ag delafossites are reported to be semiconductors.⁴²⁻⁴⁸ Cu(I) containing delafossites studied within this project have the formula CuMO_2 , where the metal cation M is Al, Cr, Fe or Rh and were chosen based on reported properties and activities.

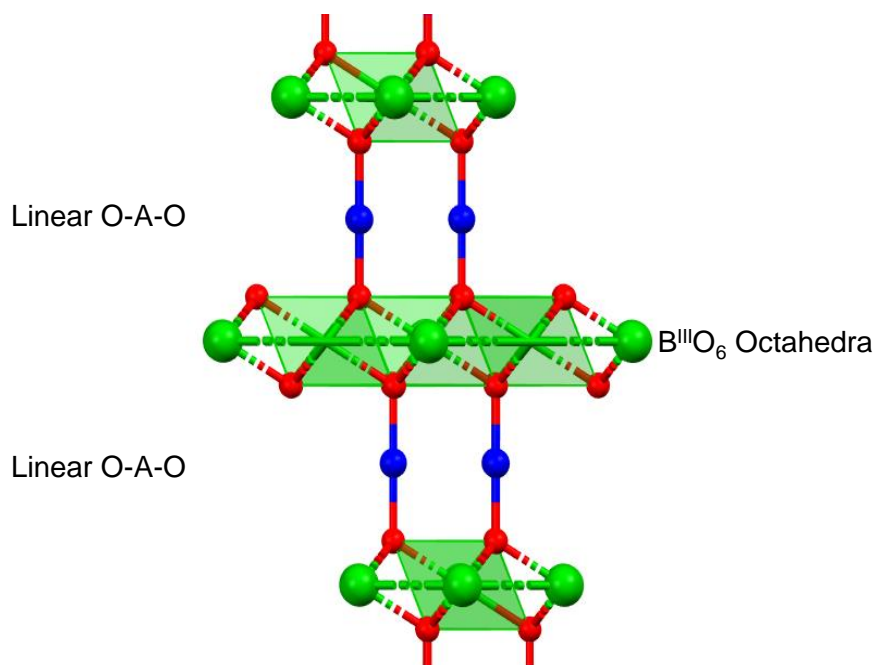


Figure 98 – Depiction of delafossite structure.¹

CuFeO₂

CuFeO₂ is a p-type semiconductor with a reported direct band gap ranging between 1.28 and 1.55 eV.^{24–26,49,50} Computationally, it has been determined that the VB is mainly composed of Cu-3d states, while the CB has mainly Fe 3d character, which should aid in stability over Cu₂O.^{51–53} In 2005 it was first reported by Trari and co-workers for photocatalytic H₂ production using S₂O₃²⁻ oxidation to scavenge holes.⁵⁴ The best activity was found for CuFeO₂ in Na₂S₂O₃ at pH 13.60 at 50°C. Interestingly they found that activity increased with decreasing specific area and that addition of carbon or Cu₂O co-catalysts reduced activity. H₂ evolution rates steadily slowed after 20 minutes, until it reached a plateau after about 120 minutes, this was ascribed to competing reduction reactions of hole scavenger products. Later, CuFeO₂ was investigated for photocatalytic removal of toxic metal ions in solution (Zn, Cu, Cd, Ag, Ni, Pb and Hg).²⁴ It was found that under illumination all metal ions (with the exception of Hg) deposited onto the surface of the CuFeO₂ and H₂ evolution followed after deposition. Depending on the metal ion used, the H₂ activity increased steadily until it reached a plateau between 20 and 60 minutes.

In 2008, a CuFeO₂/SnO₂ heterojunction was studied for H₂ evolution where the CuFeO₂ acted as a sensitiser for the SnO₂.⁴⁹ CuFeO₂ was synthesised using different precursors salts which led to variations in surface area and therefore photoactivity. The highest activity was observed when using CuFeO₂ synthesised using nitrate salt precursors, which had the highest surface area, but activity was found to plateau after 20 minutes of UV-Vis irradiation, again likely due to scavenger products being reduced, competing with H₂ production and increased charge recombination due to increased partial pressure of H₂ lowering band bending at the interface.

The first report of CuFeO₂ used for CO₂ reduction was in 2013.³⁴ Gu *et al* reported the use of a Mg doped CuFeO₂ for both photoelectrochemical and photocatalytic CO₂ reduction. Formate was produced via photoelectrochemical reduction of CO₂ with a faradaic efficiency of 10% at -0.9 V vs SCE. Faradaic losses were attributed to H₂ production due to the formation of bubbles at the surface of the electrode but was not quantified. Bulk electrolysis under N₂ and labelled ¹³CO₂ confirmed the carbon source to be the CO₂. Photocatalytic CO₂ reduction experiments also yielded formate. Post-illumination characterisation revealed the formation of

Cu⁰ metal at the surface of the electrode after 24 hours of illumination but was not detectable after shorter illumination times around 8 hours. This paper was the first and only report of the use of CuFeO₂ for photocatalytic CO₂ reduction and the paper only briefly mentions its testing and presents no data. Also, this material has never been tested for CO₂ reduction in the presence of a molecular catalyst.

In 2015, Kang *et al* reported a CuFeO₂/CuO photoelectrode capable of complete CO₂ reduction and water splitting without an external bias for over 1 week, producing formate with over 90% selectivity.³⁵ When tested separately, CuFeO₂, CuO and Cu₂O generated lower amounts of formate and no oxygen evolution was observed. The source of carbon in the formate was confirmed to be the CO₂ via isotopic labelling experiments. Two years later, the same authors reported that the initial CuFeO₂/CuO electrodes could be regenerated by a thermal treatment and found that the electrode was capable of producing formate for 35 days with weekly oxidative annealing.²⁵

Yehezkeli *et al* constructed and tested cells containing CdS/NiO_x photoanodes and CuFeO₂/CuO or NiO/CdTe photocathodes for photoelectrochemical CO₂ reduction in 2016.³⁶ They tested both configurations in the presence and absence of bias, then with and without CpRh(bpy)Cl₂ as a co-catalyst. Without the co-catalyst the CuFeO₂/CuO electrode generated more formate than the NiO/CdTe electrode, both with and without an applied bias. However, when using the CpRh(bpy)Cl₂ co-catalyst, though activity improved for both electrodes, NiO/CdTe showed a much greater performance than CuFeO₂/CuO and even produced micromolar amounts of methanol. This difference in activity was potentially attributed to different CO₂ reduction pathways occurring at each electrode. It was stated that on the CuFeO₂/CuO electrode CO₂ reduction occurs via destabilisation of CO₂ whereas on NiO/CdTe it proceeds via direct electron transfer to CO₂.

In 2017, Baker and co-workers reported a CuFeO₂/CuO photocathode for CO₂ reduction to acetate.³⁷ They also reported that by changing the Cu:Fe ratios of the electrode the CO₂ reduction product could be controlled: higher Cu concentrations (Fe:Cu of 0.1) lead to formate as the major product whereas Fe:Cu of 1.3 leads to the production of only acetate. However,

it was discovered that acetate formation occurred only within the first 10 minutes of reaction, and due to dissolution of Fe^{3+} from the surface, activity ceased.

Kang *et al*, continued work on the $\text{CuFeO}_2/\text{CuO}$ electrodes and in 2019 reported photoelectrochemical CO_2 reduction and water splitting to produce C1-C6 aliphatic acid anions and O_2 with conversion efficiencies close to 3% under simulated sunlight without any sacrificial donors or an electrical bias.³⁸ By adding Pt to the $\text{CuFeO}_2/\text{CuO}$ electrodes and adjusting the electrode configuration, they were able to tune activity towards various aliphatic acids, whilst also producing O_2 over 30 hours. These electrodes had good stability for 7 days, after which they underwent chemical reduction but again after thermal treatment, activity returned to a similar level and could be used for at least 5 weeks. An enhancement in the overall energy efficiencies of CO_2 reduction to formate could be seen when Cl^- was added to solution, however O_2 evolution ceased. This was attributed to chlorine having a comparable reduction potential to that of oxygen, but Cl^- oxidation requires fewer electrons so occurs faster, causing O_2 evolution to stop. The presence of Cl^- was also found to stabilise the $\text{CuFeO}_2/\text{CuO}$ electrodes inhibiting structural changes.

There have been further reports of CuFeO_2 being used in photoelectrochemical CO_2 reduction, but experiments required an applied bias for catalysis to occur. Later in 2019, Yuan *et al* reported a Li doped CuFeO_2 electrode and a $\text{CuFeO}_2/\text{CuO}$ electrode both able to produce methanol and ethanol with an external bias.^{39,40} They reported a similar observation to a report by Yang *et al* in 2017, where lower concentration of Cu led to C2 products on $\text{CuFeO}_2/\text{CuO}$ electrodes, in this case ethanol over methanol.^{37,39} Earlier in 2019 another group reported the use of a p-n heterojunction of CuFeO_2 deposited onto Nb doped TiO_2 nanotube arrays for photoelectrochemical CO_2 reduction to ethanol and formaldehyde when under illumination and an applied bias.⁴¹ The material has also been tested for photocatalytic and photoelectrochemical removal of organic and inorganic pollutants^{41,52,55,56} and photoelectrochemical water splitting.^{20,26,57-60}

CuCrO_2

CuCrO_2 is a p-type semiconductor that has been reported to have a direct band gap ranging between 1.25 and 3.46 eV.^{27,61,70-75,62-69} Early reports of CuCrO_2 stated that it was a narrow

band gap semiconductor but it has been reported to have a band gap ranging between 1.25 and 3.2 eV.^{61–69} In 2014 Ma *et al* stated that the absorption bands at 450 nm and 600 nm (2.76 eV and 2.07 eV, respectively) in the UV-vis diffuse reflectance spectra could be assigned to localised d-d transitions of Cr³⁺ and would not lead to charge separation and photocatalysis, so concluded that the UV-Vis spectra cannot be used to deduce the band structure.⁷⁶ Later, a paper published in 2015 by Díaz-García *et al* investigated the optical band gap of CuCrO₂ in greater depth.²¹ They determined from both UV-Vis and incident photon-to-current efficiency (IPCE) measurements that the true band gap, which leads to charge separation and photocatalysis is 3.15 eV as no photocurrents were generated for wavelengths greater than 430nm. Since the Díaz-García paper, direct band gaps for CuCrO₂ have been reported ranging between 2.82 and 3.46 eV.^{27,70–75} Also it has been determined via DFT calculations that the valence and conduction bands are made up of Cu 3d and Cr 3d mixed with O 2p states, respectively, which should give enhanced stability over Cu₂O.⁷⁶

In terms of solar fuels generation there have been a number of reports for its use as both a photocatalyst and photoelectrode. In 2006, CuCrO₂ was reported as a photocatalyst for H₂ evolution in various sulphur containing scavengers and the highest H₂ evolution rate was attained when it was coupled to n-Cu₂O in the presence of a sulphide scavenger.⁶² In 2013, Zhang *et al* studied mesoporous Mg doped CuCrO₂ and tested it for photocatalytic H₂ evolution in Na₂S solution under visible illumination for up to 60 hours.⁷⁷ They found improved activity over the bulk and undoped materials, which was ascribed to greater crystallinity and higher electronic conductivity, leading to reduced charge recombination. However, it was found that under UV-Vis illumination, undoped mesoporous CuCrO₂ produced similar quantities of H₂ to the doped version and after prolonged illumination (>10 hours) activity decreased due to photocorrosion. The presence of Mg however appeared to stabilise the material and after 128 hours the material showed no reduction of Cu(I) to Cu metal. Later in that year, Liu *et al* prepared CuCrO₂/WO₃ and CuCrO₂/ZnO photocatalyst composites for H₂ evolution in water and found that the composites had improved activity over the bulk CuCrO₂ catalyst due to the formation of the p-n heterojunction.⁷⁸ Other groups have also reported that the formation of this p-n heterojunction between CuCrO₂ and other n-type metal oxides (TiO₂ and SnO₂) has led to improved photocatalytic activity.^{74,79} In 2014 Ma *et al* studied its use as a photocatalyst towards

H₂ production in the presence of various co-catalyst (Pt, Pd, Rh, Ir, Au and Ru) with ethanol as a hole scavenger. They determined that Pt was the best co-catalyst for H₂ evolution over CuCrO₂.⁷⁶

As of yet, CuCrO₂ has not been reported for photocatalytic CO₂ reduction, but in 2018, Varga *et al* tested it as a photocathode.⁷³ They detected both gaseous (H₂, CO and CH₄) and liquid products (HCOOH and CH₃OH), with H₂ as the major product after the 240 minutes photoelectrochemical experiment. Control and isotopic labelling experiments confirmed the origin of the products and verified that CO₂ reduction was occurring.

CuCrO₂ has also found use as a photocatalyst for the removal and degradation of organic and inorganic water contaminants.^{63–65,71,74,79–81} There have been a number of studies for its use in other electronic and opto-electronic devices, including photoelectrodes^{66,76} towards water splitting,^{21,72,82,83} anodes in lithium-ion batteries,^{84–86} hole transport materials in perovskite solar cells,^{87,88} dye sensitised solar cells^{47,72,84,89,90} and as transparent conductive oxides.^{69,70,91,92}

CuAlO₂

CuAlO₂ is a p-type semiconductor with excellent chemical stability over the whole pH range, which has led to its use in a range of applications including photocatalysis,^{93–97} photoelectrochemistry,^{29,33,98} electrochemistry,⁹⁹ dye-sensitised solar cells,^{47,100,101} optoelectronics^{102,103} and transparent conductive oxides^{28,104–106} among others. Within the literature there is great inconsistency as to the nature and value of the band gap of CuAlO₂. Experimental values for the indirect band gap vary from 1.46 to 2.99 eV^{29,96,107–111} and for the direct band gap values range from 3.01 to 3.9 eV.^{22,28,104,106,109–112} Computational studies have not shed much light on the matter, with reports ranging from 1.8 to 2.99 eV^{113–117} and 3.07 to 3.53 eV^{114–118} for indirect and direct band gaps respectively. No definitive answer has yet been reached as to the value of the optical band gap, quite often papers report both band gaps and highlight the band gap that most suits the application, for example when used as a photocatalyst or photoelectrode typically the smaller indirect band gap is chosen, whereas the larger direct band gap is preferred for transparent conductive oxides.

With respect to photocatalytic fuel production, CuAlO_2 has only been employed as a photocatalyst for H_2 evolution, never CO_2 reduction. It was first tested for photocatalytic H_2 evolution in the presence of a sulphide electron donor in 2005, but activity was found to plateau within the first 40 minutes of illumination, due to reduction of the hole scavenger oxidation product competing with H_2 evolution.⁹³ In 2007, the same group reported a $\text{CuAlO}_2/\text{TiO}_2$ heterojunction photocatalyst for H_2 evolution, by mixing different weights of both materials in a suspension.⁹⁴ CuAlO_2 was used as a small band gap semiconductor, coupled to the large band gap TiO_2 , with improved photocatalytic activity compared to the previous report where CuAlO_2 was used alone. Activity was only improved up to a certain weight of TiO_2 in the suspension and then it dropped off. This was ascribed to loss of generated charges due to the high resistivity of TiO_2 rather than the fact that more concentrated solutions would be blocking light from penetrating further into the suspension. They observed the same plateau in activity with this heterojunction. In 2009, CuAlO_2 was tested for thermal photocatalytic generation of H_2 in water without a scavenger between 187-237 °C, in which boiling the water acted as a method of stirring.⁹⁵ The group reported both the direct and indirect band gaps (3.01 eV and 1.87 eV respectively). They did not report any drop-in activity and found the process and catalyst to be stable for run times of 1 hour to several. It has also been employed as a photocatalyst for removal of inorganic pollutants.^{96,97}

CuRhO₂

Of all the Cu(I) delafossites, CuRhO_2 is one of the least studied. Though never reported as a photocatalyst for H_2 evolution or CO_2 reduction, it has been used as a photoelectrode for H_2 evolution. In 2014, it was reported as a 'self-healing' photoelectrode for water reduction.¹⁹ The band structure of the material was determined along with its ability to produce H_2 from air-saturated basic solutions. Under Ar purged experiments the electrodes were found to be unstable due to reduction of Cu(I) at the surface of the electrode, this was found not to occur when O_2 was present as the O_2 could scavenge electrons and prevent reduction, 'healing' the electrode.¹⁹ It has also been studied for use as an anode for water electrolysis.^{99,119} There have been a number of doping studies, but these works have been towards improving properties related to magnetism and thermoelectrics. Dopant studies include Al, Ag, Mg, Co and Mn.¹²⁰⁻¹²⁴ Mg substitution has been found to decrease resistivity whilst still maintaining

thermopower and mobility for use as a thermoelectric material. Ag was not found to improve any properties.¹²¹ Doping with Co or Mn has shown to enhance the magnetic properties of the materials.^{123,124} It has also been determined via DFT calculations that the CB is dominated by Rh 4d mixed with O 2p states and the VB is mainly Cu 3d in character with some mixing of Rh 4d and O 2p.¹⁹

5.2.1.2 Copper Niobate Materials

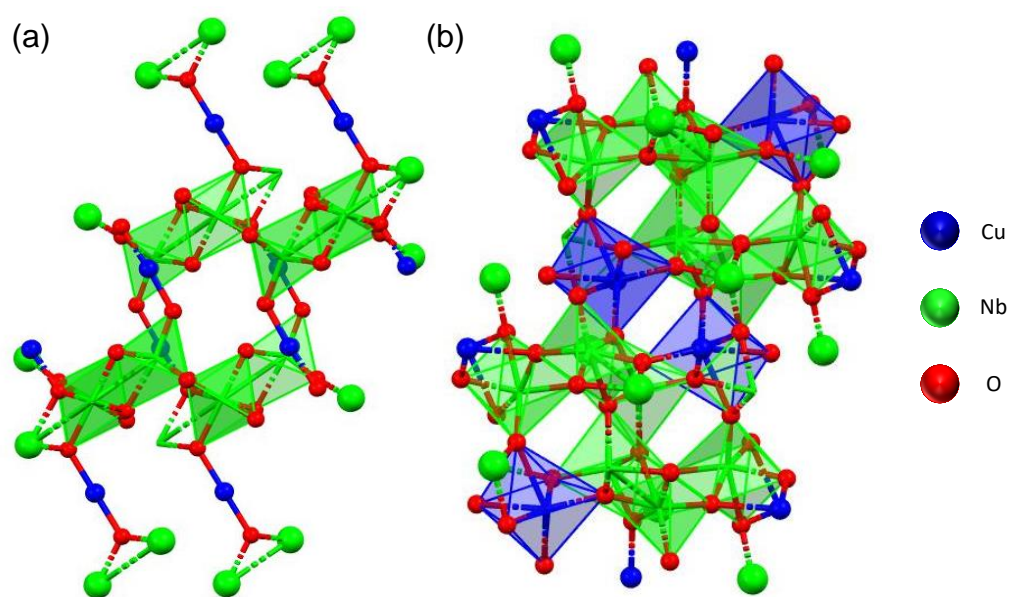


Figure 99 -Crystal structures of (a) CuNbO_3 and (b) CuNb_3O_8 .¹²⁵

The copper niobate compounds that have been studied within this project are CuNbO_3 and CuNb_3O_8 . Compared with the delafossites, there has been far less work published on these materials. There are only a handful of papers on their photocatalytic activity towards H_2 evolution and so far, there have been no reports on the use of either material for CO_2 reduction.

CuNbO_3 was first reported in 1965 by L. Shick *et al.*¹²⁶ Since then, it has been studied for use as a target for the fabrication of Cu-Nb-O transparent conductive oxide films and as a precursor for the formation of LiNbO_3 towards reversible lithium intercalation, before its use as a photoelectrode in 2011.^{127–129} Joshi *et al.* found that the CuNbO_3 electrodes exhibited relatively stable photocurrent over a few hours of illumination, owed to electrons being excited into Nb d orbitals, which make up the CB, rather than Cu based orbitals.¹²⁹ The group then went on to synthesise $\text{CuNb}_{1-x}\text{Ta}_x\text{O}_3$ ($0 < x \leq 0.25$) solid solutions to determine its effect on the

photocatalytic and photoelectrochemical properties.²³ When tested as a photocatalyst suspension, they found that as the amount of Ta increased, the materials photocatalytic activity towards H₂ evolution under UV-Vis irradiation decreased. This was attributed to Ta causing distortions in the CuNbO₃ crystal structure leading to a decrease in charge mobility. They also stated that the largest amount of hydrogen was produced in the first 1-2 hours of irradiation and after that activity either slowed or stopped. This was put down to changes in the particles surface as no bulk decomposition was seen via PXRD. CuNbO₃ has also been investigated for use in non-linear optics and ethanol steam reforming.^{130,131}

CuNb₃O₈ is a p-type semiconductor which was first reported in 1977 by Wahlström *et al.*,¹²⁶ but was only fully investigated and its electrochemical properties studied by Joshi *et al.* in 2012.³² The material was synthesised via solid state methods and tested as a polycrystalline film electrode, showing promise towards application in photoelectrochemical fuel production. It showed stability over a few hours of testing. In the paper they reported DFT calculations stating the nature of the band gap and calculated its band structure theoretically via DFT and experimentally using the Mott-Schottky method. They also determined, that like CuNbO₃, the VB consists mainly of Cu 3d states with some O 2p mixing, whilst the CB consists mainly of Nb d orbitals.

In 2013 the same group reported the activity of CuNb₃O₈ for H₂ evolution in the presence of a Pt co-catalyst and methanol hole scavenger, but found after 2 hours of illumination, the rate of H₂ production slowed significantly.¹³² They later investigated how an additional heating step leads to Cu extrusion, forming CuO island on the surface, which they proposed could help drive charge separation within the material.¹³³ Also it has been found that forming a rod-like heterojunction of H₃ONb₃O₈-CuNb₃O₈ (HN-CN) gave improved photocatalytic activity, which was attributed to the formation of a p-n heterostructure promoting charge separation. Note that without the presence of Pt there was no photoactivity observed.¹³⁴ CuNb₃O₈ has also been studied for use in non-linear optics.¹³⁵

5.2.2 This Work

Unfortunately, a number of these materials, though more stable than Cu_2O , still undergo photocorrosion.^{23,34,35,38,77} One method to reduce this is by combination of the semiconductor with a co-catalyst, as noble metal and molecular co-catalyst act as electron traps on the semiconductor surface. By drawing the electrons out of the semiconductor conduction band, the co-catalyst can prevent materials, such as Cu(I) based metal oxides, from self-reducing, improving overall stability. One of the major benefits of using a molecular co-catalyst is that the specific binding of the complex allows for reduction to specific products.

The molecular catalyst selected for study in this project is [Ni([(1,4,8,11-tetraazacyclotetradecan-1-yl)methylene]phosphonic acid)] (NiCycP) and is shown in Figure 100. NiCycP is an electrocatalyst which has previously been used as a co-catalyst on ZnSe and dye sensitised ZrO_2 for photocatalytic CO_2 reduction and has been reported to produce CO and H_2 under visible illumination.^{136,137} Phosphonate groups on molecular catalysts or dyes have been proven as an anchoring group, stabilising the attachment of species to the semiconductor surface.^{138–143} This stable anchoring group is required when working with water soluble catalysts in an aqueous environment. Phosphonates can bind to a wide variety of metal ions, ranging from monovalent to tetravalent and even higher oxidation states in some cases. The mode of binding of phosphonate ligands depends not only on the degree of protonation but also the nature of the organic chain linked to the phosphorus and the soaking conditions. The presence of three oxygen atoms in the phosphonate group can lead to a variety of different binding modes, some of which are depicted in Figure 100, including mono-, bi- and tridentate, in combination with other electrostatic and hydrogen bonding interactions. Also, these groups can bind to single or multiple metal atoms bringing about a complex range of binding modes. The phosphonate anchoring group has previously been used for attachment of molecular catalysts and dyes on Cu delafossite surfaces.^{72,144} NiCycP has an onset potential for electrocatalytic CO_2 reduction at -0.95 V vs NHE at pH 4, therefore charge transfer from the semiconductor to the catalyst should be possible with most of the catalysts chosen for study.

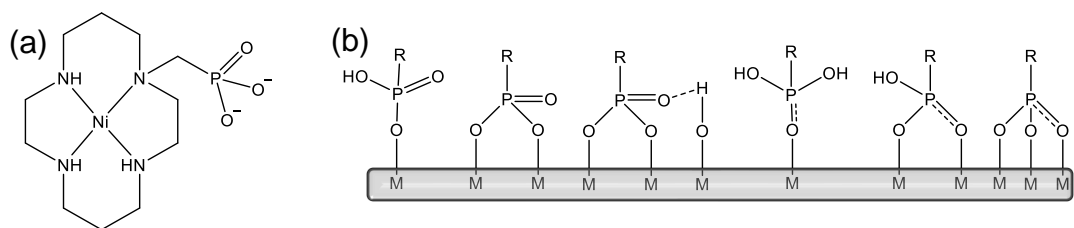


Figure 100 – (a) NiCycP structure and (b) phosphonate binding modes to a metal oxide surface. ^{138–143}

To fully evaluate these materials for photocatalytic CO₂ reduction, low surface area materials were generated via known solid state methods. The materials were then characterised using powder X-ray diffraction, UV-Vis spectroscopy, surface area measurements, scanning electron microscopy and energy dispersive X-ray spectroscopy. Baseline activity was assessed by initially screening for photocatalytic H₂ evolution in the absence and presence of Pt co-catalyst and were then combined with NiCycP and tested for CO₂ reduction. The plan was to then continue to synthesise higher purity materials with larger surface areas.

5.3 Results and Discussion

5.3.1 Synthesis and Characterisation

The synthesis of CuFeO_2 , CuCrO_2 , CuAlO_2 , CuRhO_2 , CuNbO_3 and CuNb_3O_8 have all been previously reported. Materials were synthesised via solid state methods, details of which can be found in the experimental section (Chapter 2).

5.3.1.1 Powder X-ray Diffraction (PXRD)

PXRD patterns for CuFeO_2 , CuCrO_2 , CuAlO_2 , CuRhO_2 , CuNbO_3 and CuNb_3O_8 can be found in Figure 101. They indicate the formation of single phases for two of the six metal oxides synthesised within this project, CuCrO_2 and CuAlO_2 . For the other materials, CuFeO_2 , CuRhO_2 and CuNbO_3 , only one impurity phase was identified in each, and CuNb_3O_8 was found to contain two impurity phases. All impurity phases have been highlighted as stars above the patterns in Figure 101 and in some cases may arise from errors in weighing of the precursors. In the case of CuNbO_3 , a 20% excess of Cu_2O was used in the synthesis, followed by an acid wash, and it likely was not enough to remove all excess Cu. Also, it has previously been reported that for the synthesis of CuNb_3O_8 an excess of 15% Cu_2O is required to obtain a high purity material without the Nb_2O_5 impurity phase, this was only realised after synthesis.¹³³

Of the impurities present in the synthesised materials, Cu_4O_3 and NbO_2 have not been reported to be photoactive. In the case of CuNbO_3 , the Cu metal has the potential to act as a co-catalyst on the surface enhancing charge separation and Cu has been found to improve photoactivity towards H_2 evolution and CO_2 reduction on a number of semiconductors.¹⁴⁵ In the case of the CuO impurity in CuRhO_2 , CuO had previously been shown to improve photoelectrochemical CO_2 reduction on CuFeO_2 electrodes.^{25,35-40} Nb_2O_5 has been reported to be photoactive for a range of reactions.¹⁴⁶⁻¹⁴⁹ As an impurity it could potentially enhance the photocatalysis by forming a heterojunction with CuNb_3O_8 , aiding charge separation.

Despite the lack of purity of the metal oxide samples presented here, they were carried forward to screen the materials to determine a baseline activity towards CO_2 reduction, as most of these materials have not been reported for photocatalytic CO_2 reduction or only briefly

explored. Once initial photoactivity was evaluated, the plan was to synthesise higher purity and higher surface area materials.

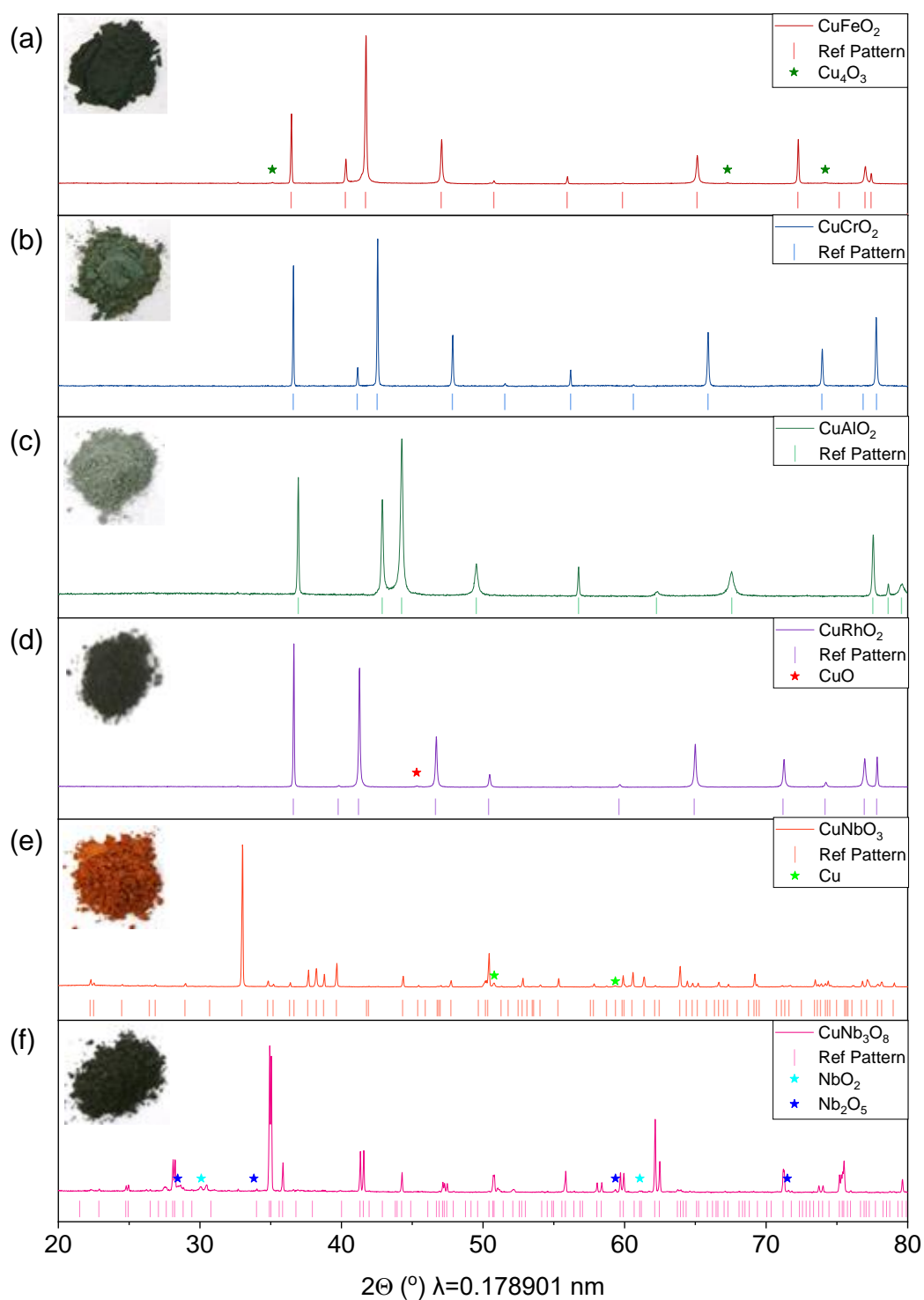


Figure 101 - PXRD patterns of (a) CuFeO_2 , (b) CuCrO_2 , (c) CuAlO_2 , (d) CuRhO_2 , (e) CuNbO_3 and (f) CuNb_3O_8 . Reference patterns (vertical lines) and impurities (stars) are given for comparison. Inset: photographs of the powders.

5.3.1.2 Ultraviolet-Visible-Near Infrared (UV-Vis-NIR) Spectroscopy

The optical band gap of each material was estimated directly from Tauc plots in Figure 102 and values can be found in Table 35. The direct band gap of 1.32 eV for CuFeO₂ agrees well with literature values.^{24–26,49,50} In the literature the direct band gap of CuCrO₂ has been reported to range between 2.82 and 3.46 eV, which agree well with the direct band gap of 3.44 eV determined in this work.^{27,70–75} The other features in the Tauc plot (Figure 102(b)) are d-d transitions that do not result in photocatalysis.⁷⁶ As discussed in the introduction, there have been no conclusive reports as to the exact value of the band gap of CuAlO₂, with reports ranging from 1.46 to 3.9 eV.^{22,28,111,112,29,96,104,106–110} In this work, both the direct and indirect band gaps are quite high and since only the direct value agrees with the literature, the band gap for CuAlO₂ is determined to be 3.49 eV. Only one paper in the literature has studied the optical properties of CuRhO₂ and it reports a band gap of 1.9 eV, which is in good agreement with the value of 1.71 eV obtained for the direct band gap in the work reported here.¹⁹ The large variation in band gap for these delafossite materials is due to which orbitals the CB and VB are composed of. Each of the materials VB are composed of Cu 3d states, whereas the CB are mainly composed of either Fe, Cr, Al, or Rh element states, which is shown quite well in the band structure diagram shown in Figure 97.

Table 35 - Experimentally determined band gaps compared with reported values.

Material	Band Gap (eV)		Literature (eV)	
	Direct	Indirect	Direct	Indirect
CuFeO ₂	1.32	1.03	1.28-1.55 ^{24–26,49,50}	1.05-1.47 ^{20,25}
CuCrO ₂	1.83, 2.33, 3.44	1.34, 1.60	2.82-3.46 ^{27,70–75}	1.28-2.12 ^{61,62,66}
CuAlO ₂	3.49	3.31	3.01-3.9 ^{22,28,104,106,109–112}	1.46-2.99 ^{29,96,107–111}
CuRhO ₂	1.71 , 2.27	1.09, 1.34	1.90 ¹⁹	
CuNbO ₃	2.08	1.83	2.10 ¹⁷	1.89 ²³
CuNb ₃ O ₈	1.45, 2.00	1.20	1.47 ³²	1.26 ³²

*Values in bold are to highlight the optical band gaps of each material determined in this project.

The band gaps of the copper niobate materials have previously been studied both experimentally and computationally and the band gaps have been found to be direct in nature

for CuNbO_3 and indirect for CuNb_3O_8 .^{17,32} The results for both materials found here are in good agreement with the literature. CuNbO_3 is reported to have a band gap of 2.10 eV and the material synthesised in this project has been found to have a direct band gap of 2.08 eV.¹⁷ For CuNb_3O_8 , the reported and obtained values of 1.26 eV and 1.20 eV for the indirect band gap, respectively, are quite close.³² As the band gaps determined within this project are in good agreement with those in the literature the band structures of these materials were not further studied.

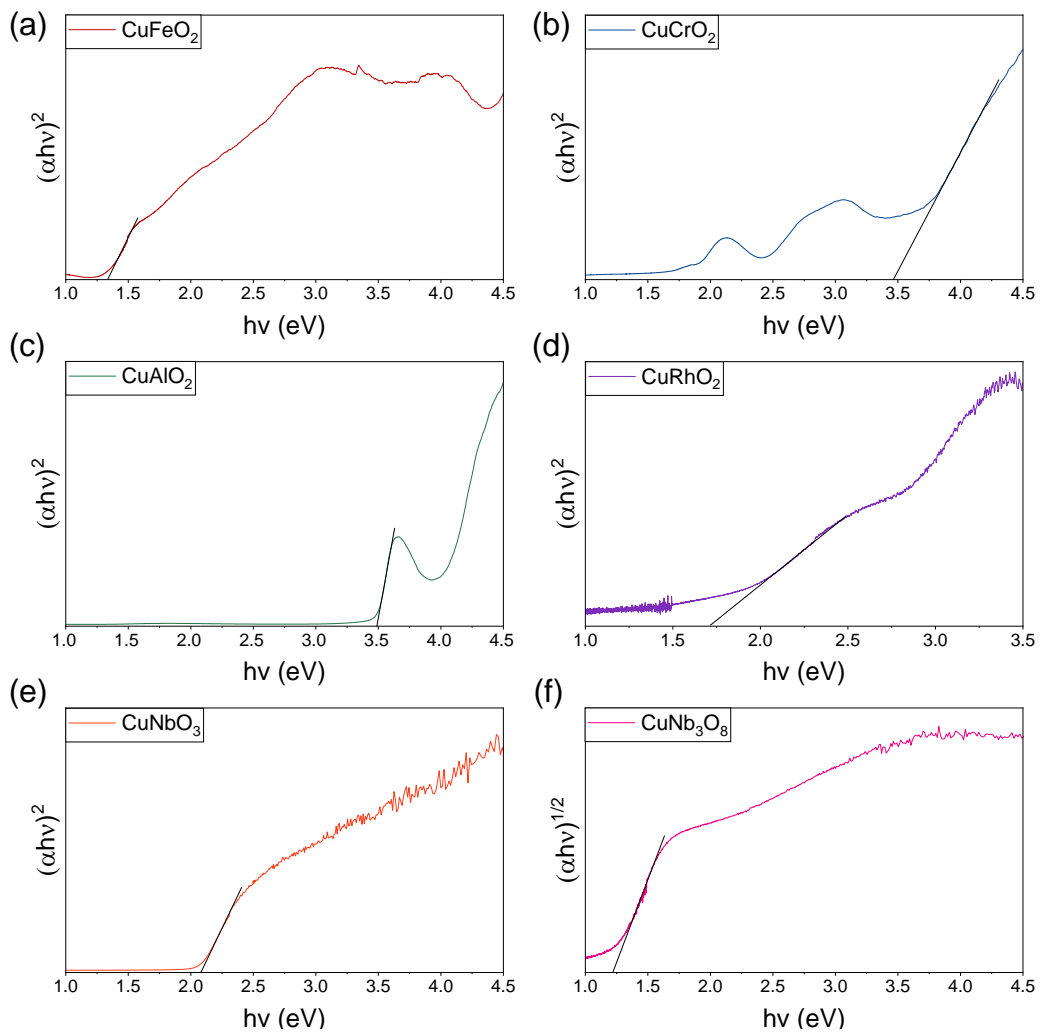


Figure 102 - Tauc plots depicting the direct or indirect band gaps of materials (a) CuFeO_2 (direct), (b) CuCrO_2 (direct), (c) CuAlO_2 (direct), (d) CuRhO_2 (direct), (e) CuNbO_3 (direct) and (f) CuNb_3O_8 (indirect).

5.3.1.3 Surface Area Measurement

The Brunauer-Emmett-Teller (BET) surface areas for all the metal oxides were calculated from the N₂ adsorption-desorption isotherms (Figure 103) and values can be found in Table 36. The measured BET surface areas for all materials are quite low, ranging between 0.086-3.067 m²g⁻¹, but this is expected considering all materials were synthesised via solid state methods with long calcination times. According to the International Union of Pure and Applied Chemistry (IUPAC) surface area and pore size classification, all materials show type II isotherms, typical of non-porous materials.¹⁵⁰

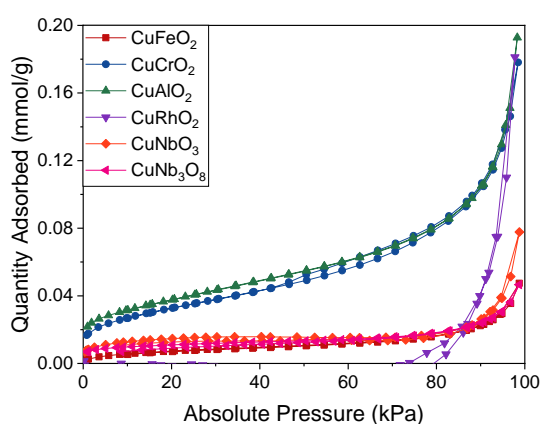


Figure 103 - N₂ adsorption/desorption isotherms of (a) CuFeO₂, (b) CuCrO₂, (c) CuAlO₂, (d) CuRhO₂, (e) CuNbO₃ and (f) CuNb₃O₈.

Table 36 - Measured BET surface area of (a) CuFeO₂, (b) CuCrO₂, (c) CuAlO₂, (d) CuRhO₂, (e) CuNbO₃ and (f) CuNb₃O₈.

Material	Surface Area (m ² g ⁻¹) [a]	Error (±) [b]
CuFeO ₂	0.63	0.01
CuCrO ₂	2.70	0.01
CuAlO ₂	3.07	0.1
CuRhO ₂	0.09	0.29
CuNbO ₃	1.10	0.02
CuNb ₃ O ₈	0.82	0.01

[a] BET surface area calculated over the pressure range (P/P₀) 0.05-0.3.

[b] Error in BET calculation.

For the delafossite materials, there is correlation between calcination time and surface area: CuRhO₂, CuFeO₂, CuCrO₂ and CuAlO₂ were calcined for 48, 36, 20 and 10 hours,

respectively. Notably, the surface area of CuRhO₂ was found to be very low, but it does have a relatively large error. This is believed to be due to the small quantity of material used for the measurement. A larger quantity could not be used as only a small amount of material was synthesised due to cost of the Rh₂O₃ precursor.

5.3.1.4 Scanning Electron Microscopy (SEM) and Energy-Dispersive X-ray Spectroscopy (EDX)

SEM was used to understand the morphologies and particles sizes of each of the materials (Figure 104 and Table 37). All materials, except CuNb₃O₈, exhibit irregular particle shapes with a widely dispersed particle size, indicative of a low degree of uniformity between the particles. The CuAlO₂ and CuNbO₃ samples show smaller platelet-like particles, which is reflected in the BET surface areas (Table 37) and SEM average particle area (Table 37). Any larger particles appear to be clusters of agglomerated microstructures (Figure 104 (h), (i), (n) and (o)). CuNb₃O₈ images (Figure 104 (m-o)) display smaller, more spherical particles and some clustered needle-like particles which are likely to be the Nb oxide impurity phase (confirmed by EDX). Particle area estimated from SEM images is a very rough estimate as in some images it is difficult to distinguish between particles due to large particle overlap.

Table 37 - Average particle area estimated by SEM and range for each of the materials.

Material	Average Particle Area (µm ²)	Particle Area Range (µm ²)	Standard deviation (µm ²)
CuFeO ₂	82.59	0.51 – 1238.13	181.05
CuCrO ₂	41.81	0.51 - 1230.73	121.58
CuAlO ₂	13.94	0.11 – 660.70	45.46
CuRhO ₂	17.13	0.51 – 1739.67	68.37
CuNbO ₃	20.04	0.51 – 684.07	41.82
CuNb ₃ O ₈	1.67	0.10 – 304.95	9.85

Note: Particle area was estimated from 100 µm windows using ImageJ software with the exception of CuNb₃O₈ which was estimated from a 50 µm window.

To investigate element distribution in each of the samples, SEM EDX mapping was performed. Figure 105 shows two different magnifications of SEM EDX overlay maps for each material and tables of composition for each image. For CuFeO₂ (Figure 105 (a-c)) SEM EDX showed a relatively even distribution of Cu and Fe on the particles over the 50 µm window, however

when zooming into a single particle, Cu rich regions can be seen. This is to be expected as a second phase of Cu_4O_3 was found within the PXRD, however the EDX Cu:Fe ratio of the 50 μm and 10 μm regions, 1.08 and 1.06 respectively, indicate the material to be slightly Fe rich. The presence of Si can also be seen in the images in Figure 105 (b) and (j) and the tables in Figure 105 (c), (f), (l) and (o), this likely arises from the synthesis of the materials, where an agate pestle and mortar were used to grind the precursors and the final product. Furthermore, quartz tubes were used in the synthesis of CuNbO_3 and CuNb_3O_8 .

CuCrO_2 also shows an even distribution of metals, confirmed by the EDX Cu:Cr ratios being very close to 1 (Figure 105 (f)). Though the PXRD of CuAlO_2 showed no impurity phases, Figure 105 (g) and (h) show Cu rich areas, but this is likely to be an effect of shadowing. Shadowing can occur in EDX analysis because the detector lies off centre from the sample (towards the top of each image), meaning that lower energy X-rays (such as Al and O) are not energetic enough to pass through the particle to the detector, creating a shadow. Figure 105 (i) show that this region is apparently high in Al, as evidenced by the Cu:Al ratio of 1.21, but the image does not show any particles or regions that are high in Al.

The SEM EDX also shows the presence of some metals that should not be in that specific sample but are in the other materials studied in this work. This can be seen in CuAlO_2 where Nb is observed (Figure 105 (g-i)) and in CuRhO_2 where Al is seen (Figure 105 (j-l)) and likely stem from all materials being measured on the same stub, leading to some cross-contamination. Figure 105 (j-l) shows the SEM EDX of CuRhO_2 ; from the images and the Cu:Rh ratios it can be seen that the material is Cu rich, with Cu:Rh ratios less than 1 and clearly defined Cu particles can be seen, which are likely to be CuO as confirmed by PXRD. A similar observation can be made of CuNbO_3 (Figure 105 (m-o)), with Cu rich particles and Cu:Nb ratios less than 1 and its PXRD confirms the presence of a Cu phase. PXRD of CuNb_3O_8 confirmed the presence of two Nb oxide phases, however due to the stoichiometry of the material it is difficult to view any Nb rich particles in the EDX mapping, but on closer examination, the needle shaped particles appear to be Cu deficient, so they are likely the Nb impurity phases in Figure 105 (p) and (q). Also, it can be seen that for the 50 μm window the Cu:Nb ratio is greater than 3. However, a Cu rich particle can be seen in both the 50 μm and

10 μm windows (lowering the Cu:Nb ratio of the 10 μm window); an extra Cu phase was not identified via PXRD but could have just been below the detection limit or had low crystallinity.

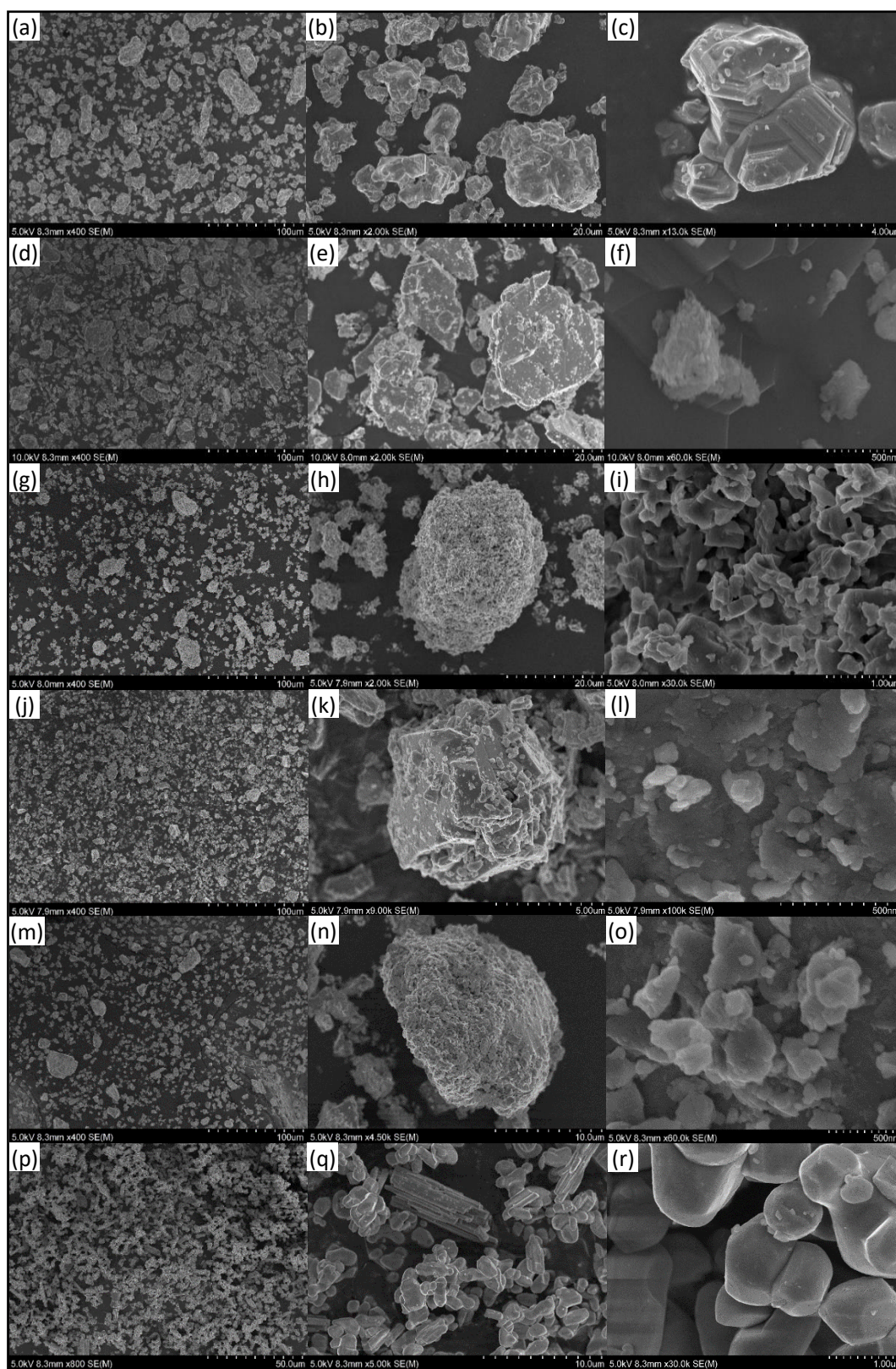


Figure 104 - SEM images for CuFeO_2 (a-c), CuCrO_2 (d-f), CuAlO_2 (g-h), CuRhO_2 (j-l), CuNbO_3 (m-o), CuNb_3O_8 (p-r).

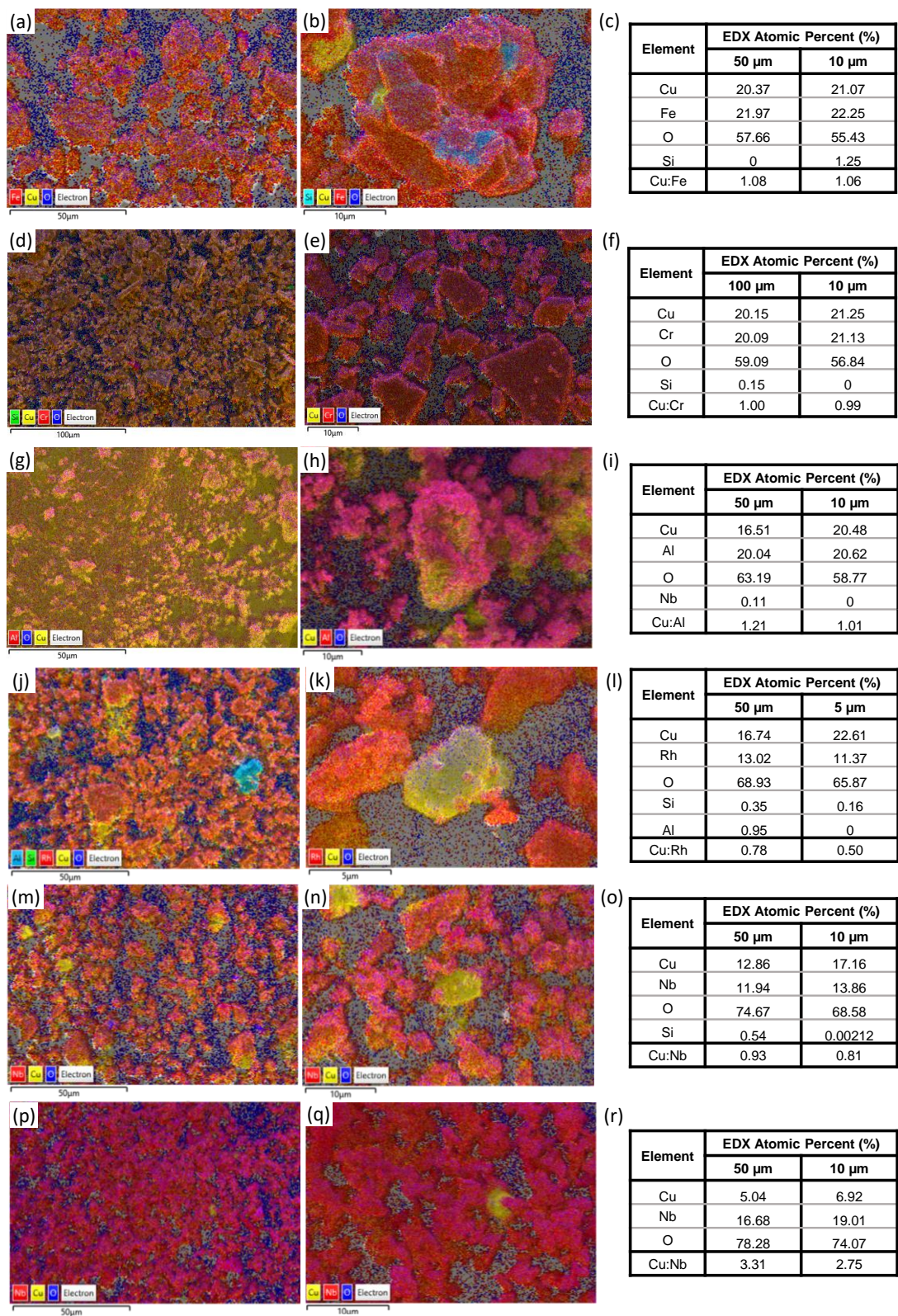


Figure 105 - SEM images with EDX mapping overlay for 2 different magnifications and tables of the EDX atomic percentages of each element for CuFeO_2 (a-c), CuCrO_2 (d-f), CuAlO_2 (g-h), CuRhO_2 (j-l), CuNbO_3 (m-o), CuNb_3O_8 (p-r).

5.3.2 Photocatalytic Testing

Following characterisation of the metal oxides, their photocatalytic properties were evaluated. Materials were first tested for H₂ evolution before moving onto studying possible activity towards CO₂ reduction. Within earlier literature of the delafossite materials, the compounds studied in this project, except CuRhO₂, were reported to evolve H₂ and O₂ from water under vigorous stirring in the dark, showing mechano-catalytic activity. However, the activity reported for these materials was found to be dependent on the stirrer bar used. Activity was only recorded in the dark when using a triangular prism stirrer bar, which causes friction between the stirrer bar, photocatalyst and base of the reactor. When a floating stirrer bar was used, no activity was observed.^{151–153}

Within this project, either no stirrer bar was used, or just a small magnetic flea was used, where potential mechano-catalytic activity would be minimised. Also, it was found that materials activity was wavelength dependent; when a UV filter was applied, little to no activity was observed.

5.3.2.1 H₂ Evolution Studies

The materials were initially tested for H₂ evolution under N₂ atmosphere in the presence of 20% methanol (MeOH) as a hole scavenger and H₂PtCl₆ for the *in-situ* photo-deposition of Pt onto the surface of the metal oxide particles. A Pt co-catalyst was used as no activity was observed without it. Pt on the surface of a semiconductor can enhance charge separation as well as lowering the overpotential for hydrogen formation from water at the surface and potentially stabilizing the material against self-reducing.¹⁵⁴ These tests were performed in a 4mL quartz cuvette with headspace (19 mL) and was illuminated over a 24-hour period with visible light using a 300 W Xe lamp with a water filter and light intensity of ~100 mWcm⁻², after purging with N₂ for 30 minutes (see 2.4.1 for lamp and filter spectra). The headspace of each experiment was then sampled and tested via GC injection to determine the quantity of gases evolved.

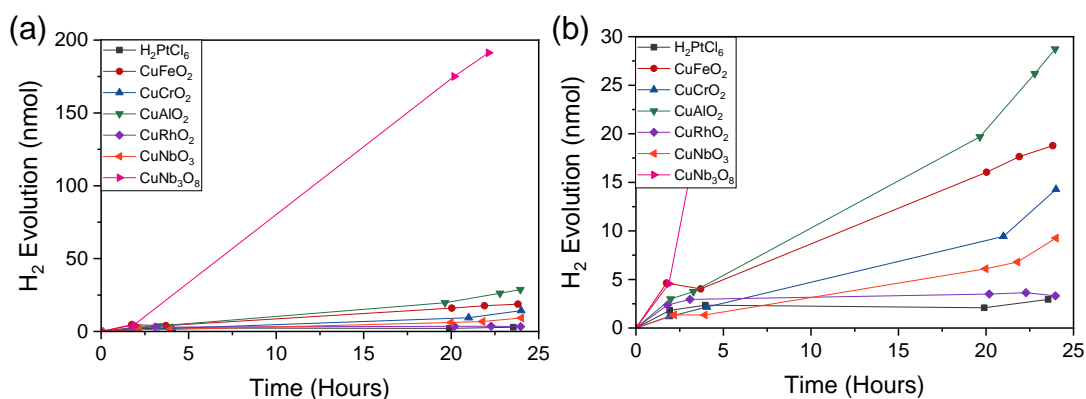


Figure 106 - Nanomoles of H₂ produced over the course of 24 hours for 4 mg photocatalyst in 4 ml 20% MeOH with 1 μ l H₂PtCl₆ (8 wt%) under UV-Vis irradiation at \sim 100 mW cm⁻² in a quartz cuvette under N₂ atmosphere tested on the 300 W Xe lamp. (a) full data set and (b) magnified region of the same data set.

Figure 106 shows the amount of H₂ produced, in nmol, over the course of 24 hours of UV-Vis irradiation. Initial activity, within the first 4 hours, for all materials was quite similar and closely followed the activity of just H₂PtCl₆ in solution. This level of activity is likely due to deposition of Pt nanoparticles via the reduction of H₂PtCl₆, releasing H₂. After those first few hours, in almost all cases the H₂ activity greatly increased, except for CuRhO₂ whose activity appeared to plateau, much like H₂PtCl₂, and finally its activity dropped. The material with the greatest activity was CuNb₃O₈, with a H₂ evolution rate of 2.230 μ mol g⁻¹h⁻¹, almost an order of magnitude larger than the second most active material CuAlO₂, (0.282 μ mol g⁻¹h⁻¹) (Figure 107).

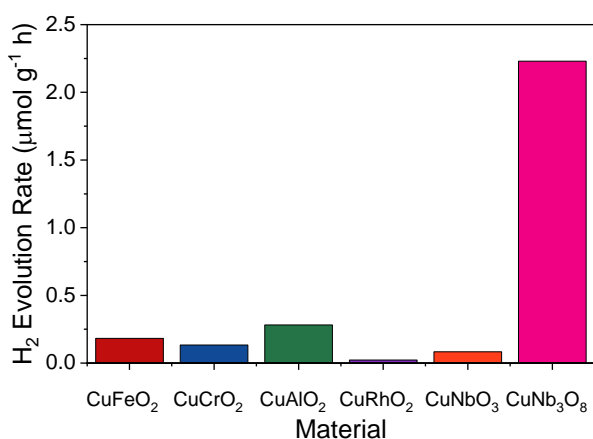


Figure 107 – Rate of H₂ produced in μ mol per gram of photocatalyst per hour for 4 mg photocatalyst in 4 ml 20% MeOH with 1 μ l H₂PtCl₆ (8 wt%) over 24 hours of UV-Vis irradiation at \sim 100 mWcm⁻² in a quartz-cuvette under a N₂ atmosphere, tested on the 300 W Xe lamp set-up.

The significant difference in activity for CuNb_3O_8 could be due to several factors. CuNb_3O_8 has the smallest band gap so is able to utilise a larger portion of the visible spectrum. Although CuFeO_2 has a similar band gap to CuNb_3O_8 , the CB of CuNb_3O_8 lies at a more negative potential and as such has a greater drive for photocatalytic H_2 evolution. Furthermore, CuNb_3O_8 has a larger surface area and smaller particle size, which likely means a greater amount of the Pt co-catalyst will have deposited. CuCrO_2 and CuAlO_2 have wide band gaps so can utilise fewer wavelengths of illumination, therefore have lower photoactivity. Despite CuCrO_2 and CuAlO_2 having similar band gaps, CuAlO_2 has almost double the activity, this may be due to its larger surface area and smaller particle size. The reasons that CuRhO_2 and CuNbO_3 have the lowest activities are unknown. Both materials have band gaps well into the visible region and band structures which should allow for H_2 evolution with significant enough driving force. There does not seem to be any indications as to why activity is lower in these materials when taking band gap, band structure, surface area or particle area into consideration. To understand this, charge lifetimes and conductivities would need to be studied.

5.3.2.2 CO_2 Reduction

In contrast to H_2 evolution studies, where a single experiment can be carried out to assess activity a significantly greater number of experiments are required to assess a materials ability to photocatalytically reduce CO_2 . Therefore, to determine if materials were active for CO_2 reduction, they were tested with and without the presence of a molecular co-catalyst on the high throughput screening set-up described in Chapter 2. This set-up consists of an array of white LEDs ($\sim 100 \text{ mWcm}^{-2}$) allowing testing of up to 10 samples at once. In most cases only up to 5 different experiments were carried out at any one time to allow for testing in duplicate, due to the error in evolved gases found across positions during set-up development (see Chapter 2), hence the error bars in Figure 108.

The metal oxides were tested on a scale of 2 mg of photocatalyst in 2 mL 10 mM ethylenediaminetetraacetic acid disodium salt (EDTA) hole scavenger in a glass vial. Though MeOH is a stronger hole scavenger, it is not a suitable hole scavenger for use in these CO_2 reduction experiments as the presence of MeOH vapour interferes with CO detection. Prior

to illumination the samples were purged with either N₂ or CO₂ for 30 minutes and then placed under illumination for 4 hours. For experiments where NiCycP was used as a co-catalyst, it was used in solution at a concentration of 1 mM and allowed to soak onto the photocatalyst in the dark for 24 hours before purging and illumination, so NiCycP remained in solution during the photocatalytic experiments.

Previously, NiCycP has been immobilised on ZnSe quantum dots and ZrO₂ particles; in the soaking experiments, NiCycP was found immobilised on surfaces after 2 and 48 hours, respectively.^{136,137} The metal oxides presented in this work have much lower surface areas, so having the NiCycP remain in solutions should ensure that throughout the experiment that some NiCycP is in contact with the semi-conductor surface. As NiCycP in solution has very weak light absorption, it does not act as an internal filter. Although there is no characterisation data explicitly showing that the NiCycP is attached to the metal oxide, it can be seen in Figure 108 that when NiCycP is in solution, under both N₂ and CO₂ atmosphere, there is an enhancement in H₂ evolution which is a good indication that the semiconductor and catalyst are in contact and allow for electron transfer. Other soaking times, concentrations or methods were not explored as this was performed as a screening test, to determine hit materials.

The H₂ and CO evolution rates for each material with and without a co-catalyst under N₂ and CO₂ can be found in Figure 108. Overall, the rate of activity for all materials under all conditions is low, but this was expected as these materials all have very low surface areas. If a potentially interesting CO₂ reduction photocatalyst had been identified, alternative synthetic pathways to a high surface area material would have been explored. Because of the low surface area, it is expected that only a small amount of the catalyst will be able to bind to the particles surface, therefore, despite activity with and without the catalyst being quite similar, it is difficult to determine whether the presence of the catalyst bound to the semiconductor makes a critical difference in activity. However, most materials, except for CuNb₃O₈, looked promising as CO evolution was higher under CO₂ purged samples than the N₂ purged samples. To identify the significance of the difference in CO levels a total of 2 experiments were carried out and error bars on the CO evolution rates identified. Consequently, a few of the materials that were determined to be 'hits' (CuFeO₂, CuAlO₂ and CuNbO₃) and 'fails' (CuNb₃O₈) were carried

forward for testing on the Xe lamp set-up, which allows for more accurate testing under a variety of conditions.

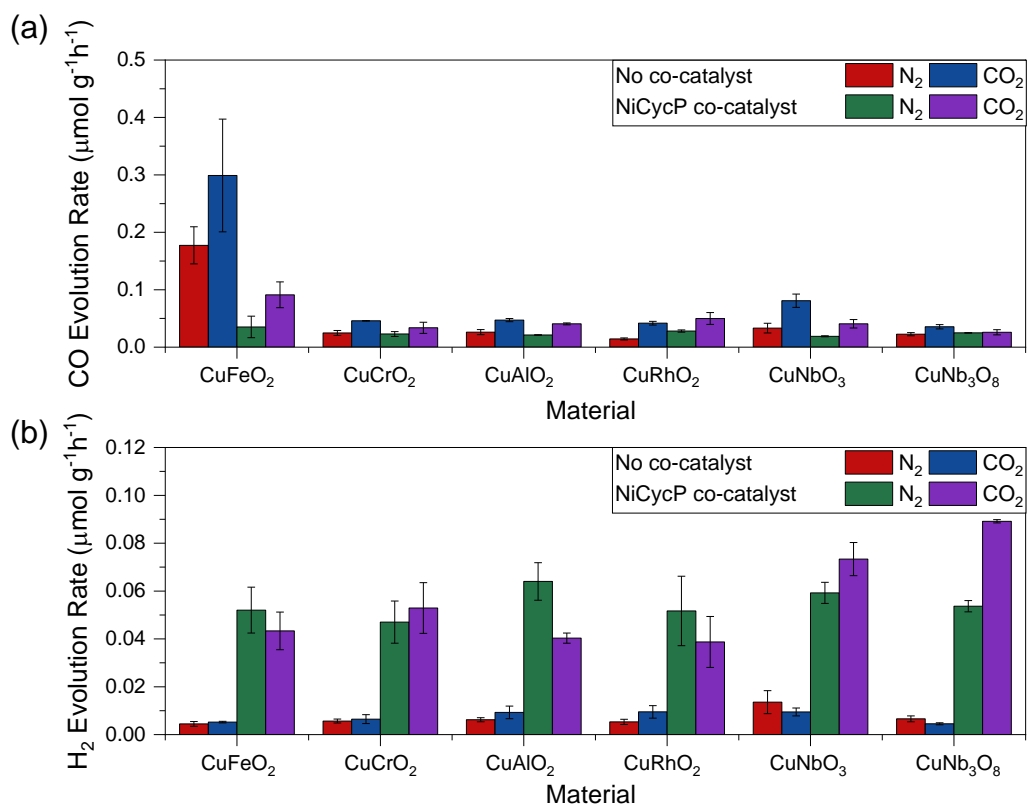


Figure 108 - Rate of (a) CO and (b) H₂ evolved in μmol per gram of photocatalyst per hour for 2 mg of photocatalyst in 2 ml 10 mM EDTA over 4 hours visible light irradiation at $\sim 100 \text{ mWcm}^{-2}$ in a glass vial, tested on the screening set-up. NiCycP was used as a co-catalyst in solution at 1 mM concentration and samples were left to soak in the dark for 24 hours prior to purging and illumination.

Of all the materials tested on the Xe lamp (Figure 109), CuNbO₃ appeared to be most active, with a higher CO evolution under CO₂ than in the N₂ purged experiments. Another good indicator is the decrease in the H₂ evolution between the N₂ and CO₂ purged samples. This means that the charges that were going towards H₂ production in the N₂ purged experiments have gone on to produce something else in the CO₂ purged experiment. Though this also happens with the other metal oxides tested, it is unclear as to how this charge could be employed as no other gaseous or liquid products were detected. The concentration of liquid products could be below the detection limit but are unlikely to form when NiCycP is used as a co-catalyst as it selective for reduction to CO as the carbon product.

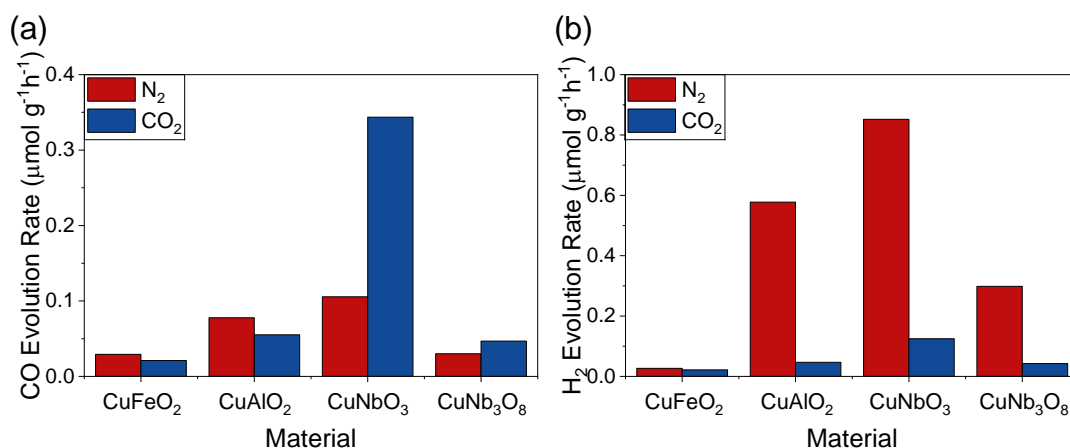


Figure 109 - Rate of (a) CO and (b) H_2 produced in μmol per gram of photocatalyst per hour for 4 mg photocatalyst in 4 ml 10 mM EDTA 1 mM NiCycP. Samples were left to soak for 24 hours in the dark prior to purging with N_2 or CO_2 and 4 hours of UV-Vis illumination at $\sim 100 \text{ mWcm}^{-2}$ in a quartz-cuvette, tested on the 300 W Xe lamp set-up. The Xe lamp was equipped with a water filter only.

Despite CuFeO_2 showing the greatest activity when tested on the high throughput system, it had the lowest activity in the Xe lamp. On the high throughput set-up, experiments were carried out under only visible illumination, whereas on the Xe lamp only a water filter was used. This was done to provide as many wavelengths of light as possible to the semiconductor to enhance the formation of charges at the surface in hopes of improving photoactivity. However, CuFeO_2 is known to photocorrode under harsher light conditions, and a higher concentration of electrons could lead to reduction of Cu at the surface. Normally this could be confirmed by PXRD or SEM EDX, but these tests were not carried out on a large enough scale and there was not enough time to look into this further. We note however that this behaviour has been reported before, albeit under different illumination conditions after longer periods of illumination.^{34,35}

As CuNbO_3 still looked promising it was carried forward for further control studies, to determine whether the observed photoactivity was real. To do so, CuNbO_3 was tested without the presence of NiCycP under N_2 and CO_2 on the Xe lamp set-up. Figure 110 shows a comparison of the CO and H_2 evolution rates for the hybrid $\text{CuNbO}_3/\text{NiCycP}$ with the blank CuNbO_3 and shows that CuNbO_3 appeared to be more active, indicating that the NiCycP in solution was hindering activity. The catalyst molecules bound to the surface could block active sites for CO_2 reduction. However, the presence of NiCycP on the surface of the metal oxide particles has not been confirmed, due to the likely small amounts that have attached. The $\text{CuNbO}_3/\text{NiCycP}$ still

shows better activity towards H₂ evolution when tested on the Xe lamp, still indicating that NiCycP was on the surface of the metal oxide aiding charge separation and giving an enhancement in activity.

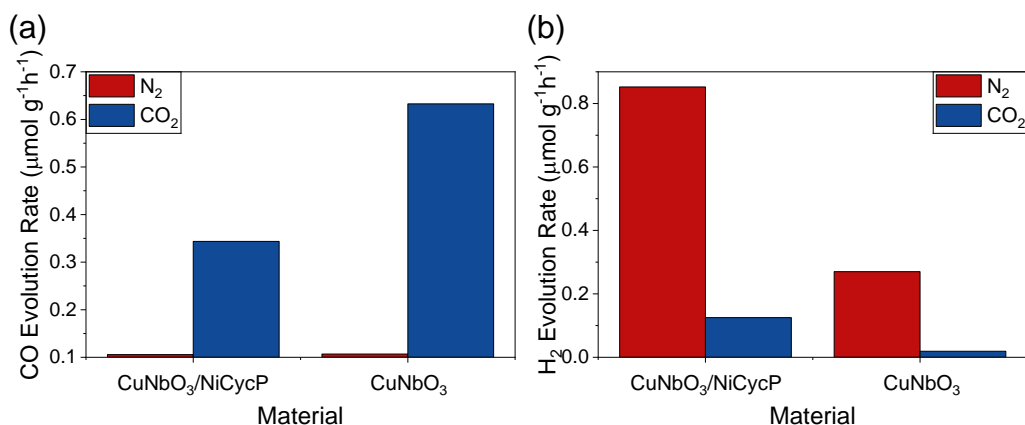


Figure 110 - Rate of (a) CO and (b) H₂ produced in μmol per gram of photocatalyst per hour for 4 mg photocatalyst in 4 ml 10 mM EDTA, with and without soaking in 1 mM NiCycP for 24 hours. Samples were then purged with N₂ or CO₂ and then put under UV-vis illumination at $\sim 100 \text{ mWcm}^{-2}$ in a quartz-cuvette, tested on the 300 W Xe lamp set-up for 4 hours. The Xe lamp was equipped with a water filter only.

It was noticed that after prolonged light exposure CuNbO₃ began to turn from red to black. After leaving in the dark overnight the material did not revert to its original red colour, meaning that it is likely not an excited state causing the colour change. Only after exposure to air for several hours did the colour change back to red (Figure 111). Therefore, the most likely explanation to the initial colour change is the reduction of the surface during illumination and following re-oxidation upon air exposure the colour reverted. It is also worth noting that when experiments were performed in MeOH the colour change was not observed, likely because MeOH is a stronger hole scavenger, stabilizing the material.

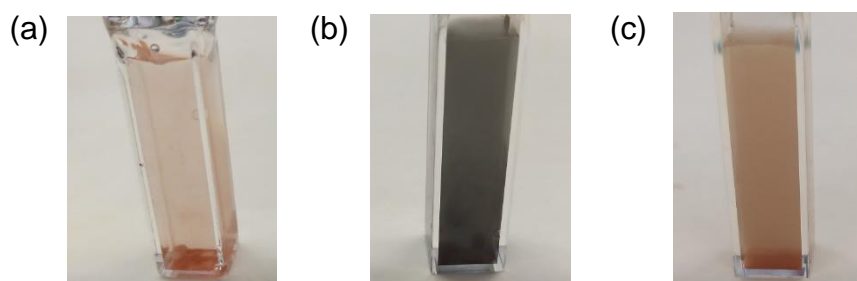


Figure 111 - Photographs of CuNbO₃ in 10mM EDTA (a) pre-photocatalysis, (b) after 21 hours of illumination on the 300 W Xe lamp and (c) after 3 hours exposed to air.

To determine if the sample was undergoing a phase change during photocatalysis, PXRD was measured before and after photocatalysis and showed that it was the same phase (Figure 112). However, it is noted that PXRD is a bulk measurement, so if any changes occur only at the surface, the bulk phase will swamp the pattern. It has previously been reported that TiO₂ annealed under a H₂ atmosphere leads to a quite distinct colour changes without observation of phase change via PXRD.¹⁵⁵ This colour change was attributed to the formation of oxygen vacancies creating impurity/defect states that lie within the band gap below the conduction band. Previously it has been reported that for CuRhO₂ photoelectrodes, the presence of oxygen in experiments helped to stabilise electrodes against self-reduction by scavenging electrons.¹⁹ So injecting air into the photocatalytic system was tested, to see if this could help stabilise the colour of the material, or improve activity. However, it was found to reduce activity towards both CO and H₂ evolution and had no effect on the CuNbO₃ colour change. This line of study was not followed any further as there was a fundamental issue of Cu leaching into solution.

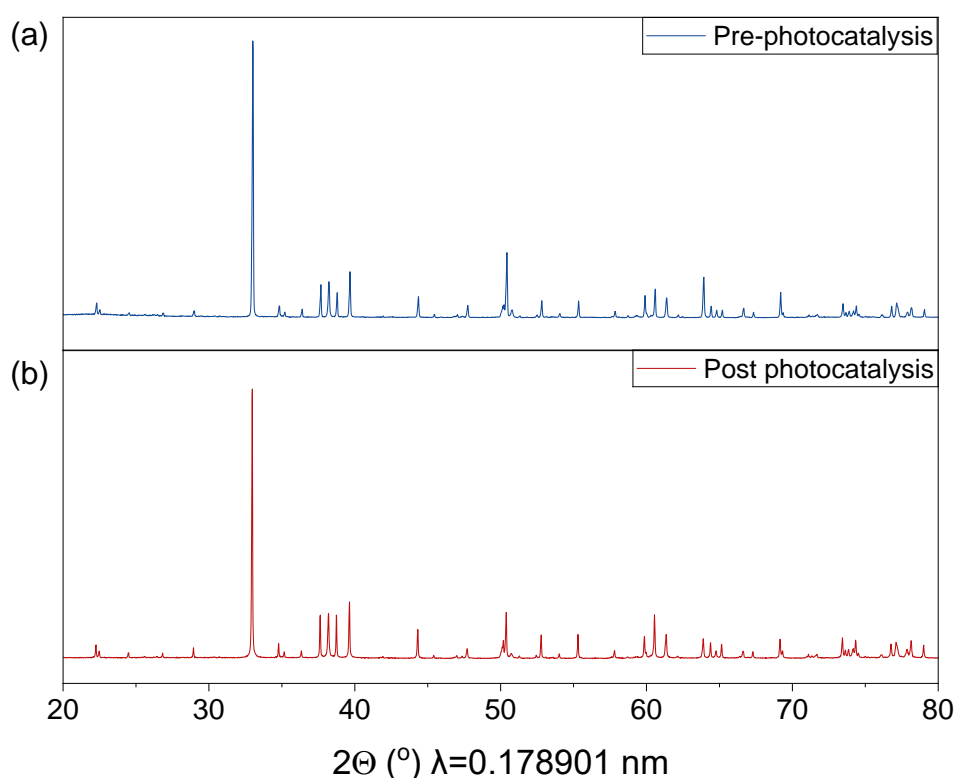


Figure 112 - PXRD Pattern of CuNbO₃ (a) before illumination and (b) after 24 hours UV-vis illumination on the 300 W Xe lamp.

Following the photocatalysis experiment, it was found that in the case of CuNbO_3 in EDTA; the solution had turned blue. PXRD (Figure 101, Section 5.3.1.1) found that there was a Cu impurity phase found in the synthesised CuNbO_3 and it was possible that the Cu impurity was leaching out into the EDTA solution during photocatalysis. When experiments were performed in MeOH the Cu leaching was not observed.

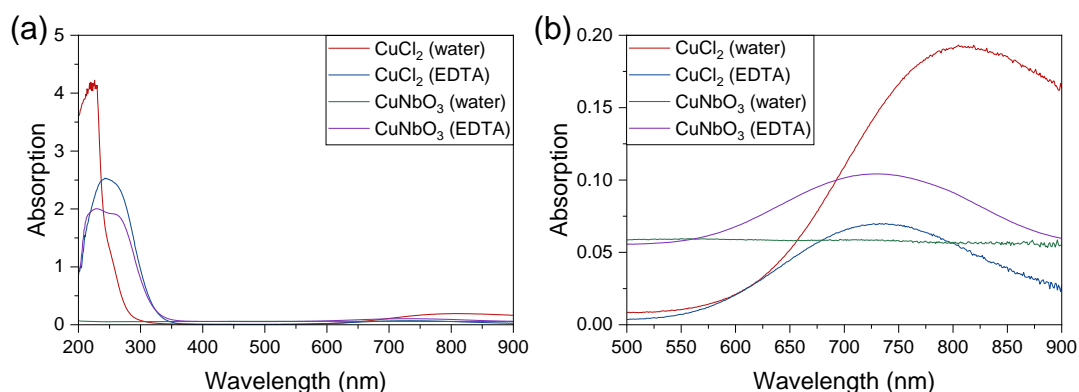


Figure 113 – UV-Vis spectra of 0.875 mM CuCl_2 in water and 10mM EDTA solution and supernatants from CuNbO_3 soaked in water and 10 mM EDTA for ~ 20 hours. (a) full spectrum and (b) magnified region.

As EDTA is a very good chelating agent, it is likely that the Cu in solution was present as a Cu-EDTA complex, which could have been active by itself or acting as a co-catalyst on the CuNbO_3 . Figure 113 shows the UV-Vis spectra of the supernatants taken from CuNbO_3 having been soaked in water or 10 mM EDTA overnight compared with 0.875 mM CuCl_2 in water and 10 mM EDTA. CuCl_2 in solution gives peaks at 225 nm and 805 nm, but these shift to 245 nm and 730 nm, respectively, when in solution with EDTA, likely due to the formation of a Cu-EDTA complex.^{156–158} This same peak is present in the supernatant of CuNbO_3 soaked in EDTA overnight, confirming the presence of the Cu-EDTA in the photocatalysis solutions. Also, when soaked in water, this peak is not observed. To determine if Cu-EDTA was acting as a co-catalyst; the photoactivity for CuNbO_3 in EDTA under N_2 and CO_2 was compared with that of CuCl_2 and CuNbO_3 with CuCl_2 in solution (Figure 114). Other CuCl_x were not pursued as CuCl_2 gave activity and Cu^{II} is characteristically blue in solution. As the CuCl_2 experiment had higher activity than the CuNbO_3 it was believed that combining the two would result in improved activity, however, this was not the case, in fact the activity was lower.

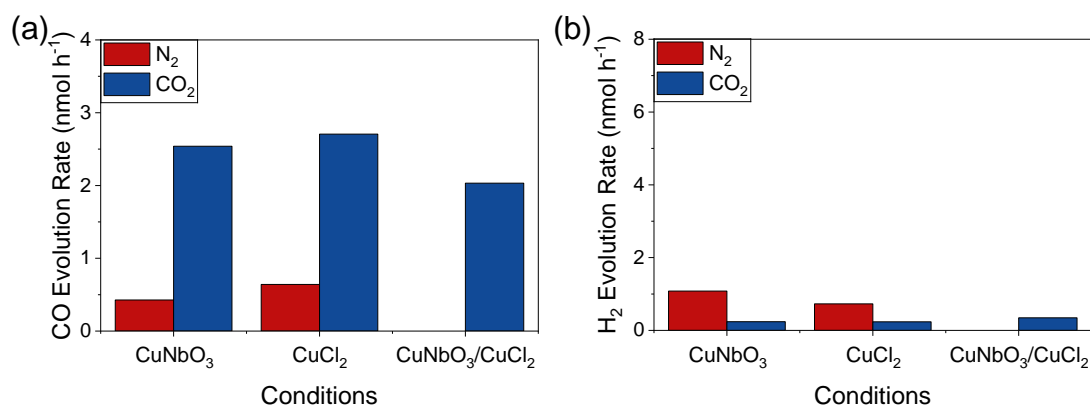


Figure 114 - Rate of (a) CO and (b) H₂ produced in nmol per hour for 4 ml 10 mM EDTA 2 mM CuCl₂ with and without 4 mg CuNbO₃ under N₂ or CO₂. Samples were put under UV-vis illumination at ~100 mWcm⁻² in a quartz-cuvette, tested on the 300 W Xe lamp set-up for 4 hours. The Xe lamp was equipped with a water filter only.

To understand why no improvement in the activity was observed when the materials were combined, further control experiments were performed. EDTA solutions under N₂ and CO₂ without any extra species in solution were placed under illumination with and without filters on the Xe lamp, as these types of blank tests had previously only been performed in glass cells. Unfortunately, it was found that EDTA under UV-Vis illumination had higher activity for CO production than the other experiments shown in Figure 115, indicating that something within the EDTA is active towards CO₂ reduction. It seemed that when other coloured species were in solution or particles were in suspension in the EDTA, photoactivity dropped, likely because they block light getting to the active species in EDTA. Also, the EDTA was mainly active under UV and visible light, when a KG1 (340-720 nm) filter was used activity dropped significantly. It is important to keep in mind when looking at other results, in earlier chapters, that experiments in EDTA were performed in glass sample vials/cuvettes, which act as a UV filter, and these experiments were completed before this was discovered. Also, in the literature when EDTA is used as a hole scavenger, experiments are often performed with a UV filter and no activity is reported.^{159,160}

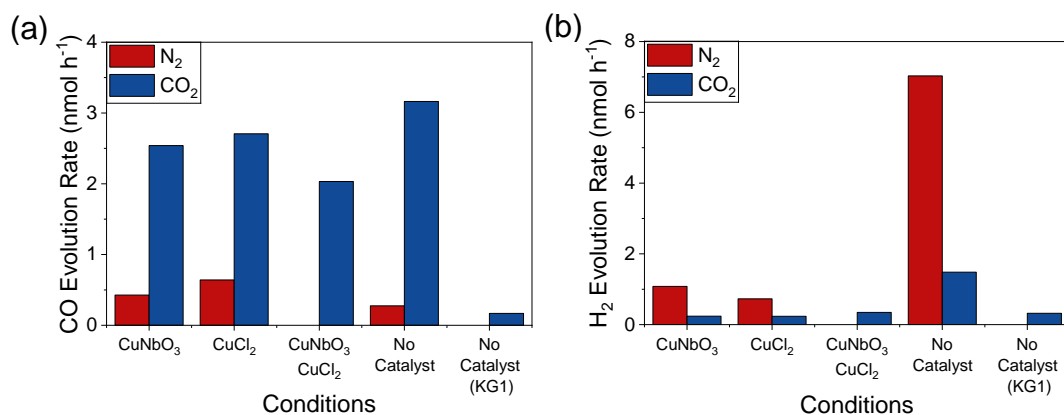


Figure 115 - Rate of (a) CO and (b) H₂ produced in nmol per hour for 4 ml 10 mM EDTA, with and without 2 mM CuCl₂ with and without 4 mg CuNbO₃ under N₂ or CO₂. Samples were put under UV-vis illumination at ~100 mWcm⁻² in a quartz-cuvette, with and without a KG1 filter, tested on the 300 W Xe lamp set-up for 4 hours. The Xe lamp was equipped with a water filter only.

Previously, it has been reported the Cu-EDTA is not photoactive but Fe^{III}-EDTA is active under UV illumination.¹⁶¹ A possible Fe source is the EDTA salt which had been purchased from Sigma Aldrich, contains <0.01% Fe. In order to assess which dissolved Fe ion was the active species in previous experiments, both FeCl₂ and FeCl₃ were dissolved in 10 mM EDTA (Figure 116). It was found the FeCl₃ had higher activity for both CO and H₂ evolution.

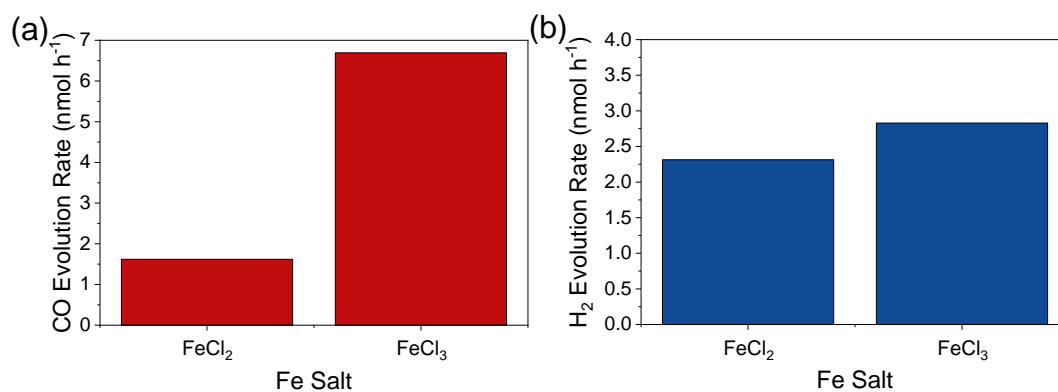


Figure 116 - Rate of (a) CO and (b) H₂ produced nmol per hour for 4 ml 10mM EDTA, with 1 mM FeCl₂ or 1 mM FeCl₃ under CO₂. Samples were put under UV-vis illumination at ~100 mWcm⁻² in a quartz-cuvette, tested on the 300 W Xe lamp set-up for 4 hours. The Xe lamp was equipped with a water filter only.

From the comparison of the UV-vis spectra of 10 mM EDTA with and without 1 mM FeCl₃ in Figure 117, it can be seen that there is a peak in the FeCl₃ solution, which indicates the presence of Fe-EDTA and agrees well with UV-vis spectra in the literature.¹⁶¹ Also there appears to be a small shoulder in the 10 mM EDTA sample at the same point, which could

indicate the presence of a very small amount of Fe-EDTA. As Fe^{III} was found to be more active towards CO₂ reduction, a range of FeCl₃ concentrations (0.5 to 2 mM) in 10 mM EDTA were tested, as it was hypothesised that operating at greater Fe^{III} concentrations would lead to greater levels of photocatalytic activity under CO₂ atmosphere and UV-vis illumination (Figure 118). It was found that with increasing concentrations of FeCl₃ the amount of CO evolved does increase, indicating that it is photoactive (N₂ studies are required to confirm). However, the 0.5 mM experiment appeared to produce less CO than the blank EDTA, but these were performed as single experiments and the difference in activity is within error.

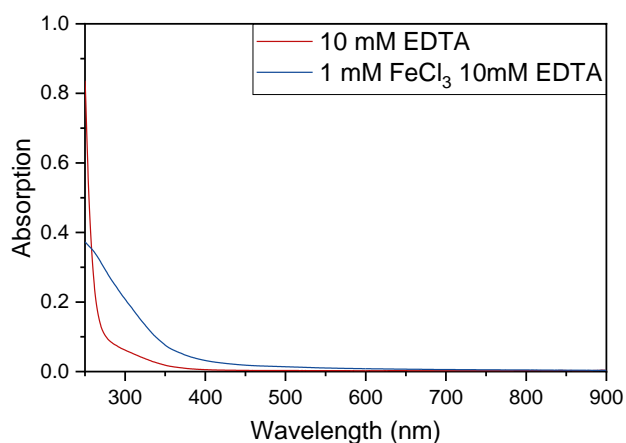


Figure 117 – UV-Vis spectra of 10 mM EDTA and of 1 mM FeCl₃ in 10mM EDTA.

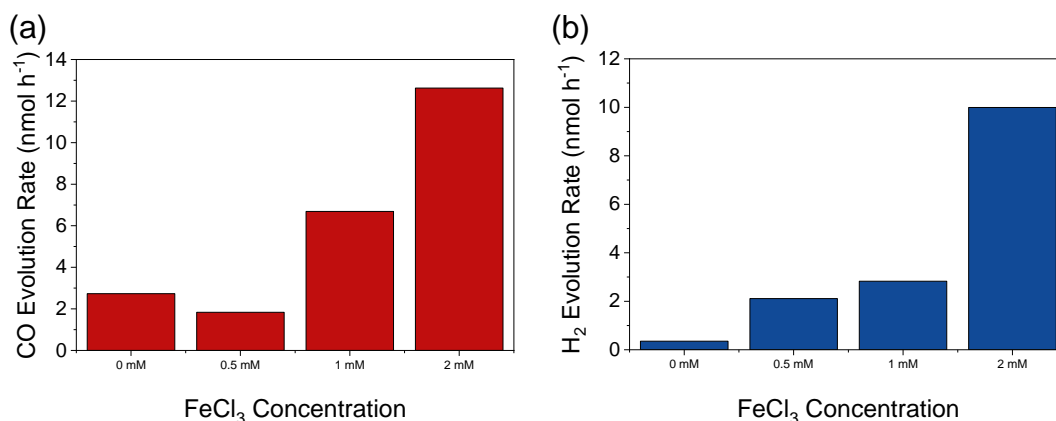


Figure 118 - Rate of (a) CO and (b) H₂ produced in nmol per hour for 4 ml 10 mM EDTA, with different concentrations of FeCl₃ (0. 0.5, 1 and 2 mM) under CO₂. Samples were put under UV-vis illumination at ~100 mWcm⁻² in a quartz-cuvette, tested on the 300 W Xe lamp set-up for 4 hours. The Xe lamp was equipped with a water only.

Table 38 shows the theoretical and inductively coupled plasma optical emission spectrometry (ICP OES) determined Fe content of the EDTA compared with the theoretical Fe content of the FeCl₃ solutions. Concentrations of Fe in the EDTA were much lower than the theoretical values for Fe content in the FeCl₃, yet still produced similar activities. Also, the EDTA Fe

content did not increase linearly with EDTA concentration, likely because signals lay within in the background noise. It is clear that the Fe could be detected but was below the quantification limit. Therefore, it was concluded that Fe^{III} was not the active species in the EDTA. ICP also detected the presence of Na, K, Ca, Al, and Zn, none of which are likely candidates for CO₂ reduction active species. Overall, it is unclear as to why the EDTA solutions appeared to be able to perform CO₂ reduction and a more in-depth study is required to understand this. Even doing labelling experiments would have shown that the material was active, this highlights the need for understanding systems and discovering the active species via thorough control experiments.

Table 38 - Theoretical and ICP determined Fe Concentration for various EDTA and FeCl₃ solutions.

Solution	Theoretical Fe Concentration ^[a] (ppm)	ICP Fe Concentration (ppm)
10 mM EDTA	0.37	0.01
20 mM EDTA	0.74	0.01
50 mM EDTA	1.86	0.01
100 mM EDTA	3.72	0.01
0.5 mM FeCl ₃	27.9	-
1 mM FeCl ₃	76.9	-
2 mM FeCl ₃	153.8	-
5 mM FeCl ₃	384.5	-

[a] Theoretical EDTA concentrations were calculated assuming a maximum Fe content of 0.01%

5.4 Conclusions and Future Work

Within this chapter, six metal oxides, CuFeO_2 , CuCrO_2 , CuAlO_2 , CuRhO_2 , CuNbO_3 and CuNb_3O_8 , have been synthesised via solid state methods, characterised and initial photocatalytic studies have been carried out. It was found that CuNb_3O_8 yielded the highest H_2 evolution. Further measurements to examine charge recombination will likely help to gain some understanding as to the differences in activity towards H_2 evolution of the other materials.

Overall, it has been determined that this selection of metal oxides do not exhibit photocatalytic activity towards CO evolution above that of the background control experiments, especially that of EDTA alone. The results obtained from the EDTA control experiments demonstrates the inherent problems with using EDTA as a hole scavenger. The results reported in this chapter reveal EDTA has the ability to pull copper from CuNbO_3 and also scavenge other metals, such as Fe, creating its own photoactive species, complicating photocatalytic experiment results.

Within this study, control experiments were performed that would usually not be considered. Typically, the materials would have been tested under N_2 then CO_2 and finally a labelling experiment would have been performed to confirm that the CO_2 was the carbon source. However as was found with the EDTA experiments, this would have resulted in a false positive, as all results would indicate that CO_2 reduction was occurring, but not the active species which was executing it. Moreover, these results highlight the importance of thorough control and blank studies; careful filtering and additional control experiments must be performed to enable understanding of the photoactive species within these studies.

Whilst results from the NiCycP screening experiments did not show the activity that was expected for CO evolution, an improvement in H_2 evolution was observed, meaning that there is contact between the semiconductors and molecular co-catalyst which allows for electron transfer. Despite the issues with the EDTA hole scavenger, the generally low activity is likely due to very low surface areas. Low surface area leads to low catalyst loadings, easy desorption, and little to no activity. There have been a number of methods reported in the

literature that have yielded higher surface area delafossite materials including hydrothermal^{75,83,162,163} templating^{28,164} and combustion^{71,73,77,165} techniques. Once a material with adequate surface area has been produced, a more in-depth study could be undertaken to evaluate the activity of the hybrid photocatalyst towards CO₂ reduction in the presence of a different hole scavenger.

Unfortunately, some of these materials have band gaps which are just too large to harvest significant amount of the solar spectrum. In the literature there have been several reports of doping which has been found to decrease the band gaps of CuCrO₂ and CuAlO₂, however these decreases have been small.^{166–169} Another method to enhance light absorption is via sensitization with dyes. Both CuCrO₂ and CuAlO₂ have found use in dye-sensitised solar cells.^{47,72,84,89,90,100,101} Furthermore, CuCrO₂ has previously been sensitised and combined with a molecular co-catalyst for enhanced photoelectrochemical H₂ evolution.⁷² Other materials have a conduction band which is incompatible with the chosen molecular catalyst, as it lies below the reduction potential of NiCycP or does not have a great enough driving force for electron transfer to the molecular catalyst, so would have to be re-considered for use with NiCycP, but may be compatible with other molecular co-catalysts.

5.5 References

- 1 I. Sullivan, B. Zoellner and P. A. Maggard, *Chem. Mater.*, 2016, **28**, 5999–6016.
- 2 J. Y. Li, L. Yuan, S. H. Li, Z. R. Tang and Y. J. Xu, *J. Mater. Chem. A*, 2019, **7**, 8676–8689.
- 3 A. T. Garcia-Esparza, K. Limkraisiri, F. Leroy, S. Rasul, W. Yu, L. Lin and K. Takanahe, *J. Mater. Chem. A*, 2014, **2**, 7389–7401.
- 4 B. P. Rai, *Sol. Cells*, 1988, **25**, 265–272.
- 5 B. K. Meyer, A. Polity, D. Reppin, M. Becker, P. Hering, P. J. Klar, T. Sander, C. Reindl, J. Benz, M. Eickhoff, C. Heiliger, M. Heinemann, J. Bläsing, A. Krost, S. Shokovets, C. Müller and C. Ronning, *Phys. Status Solidi Basic Res.*, 2012, **249**, 1487–1509.
- 6 A. D. Handoko and J. Tang, *Int. J. Hydrogen Energy*, 2013, **38**, 13017–13022.
- 7 C. Li, Y. Li and J.-J. Delaunay, *ACS Appl. Mater. Interfaces*, 2014, **6**, 480–486.
- 8 A. Paracchino, V. Laporte, K. Sivula, M. Grätzel and E. Thimsen, *Nat. Mater.*, 2011, **10**, 456–461.
- 9 C. J. Engel, T. A. Polson, J. R. Spado, J. M. Bell and A. Fillinger, *J. Electrochem. Soc.*, 2008, **155**, F37.
- 10 S. Bailey, G. F. Froment, J. W. Snoeck and K. C. Waugh, *Catal. Letters*, 1995, **30**, 99–111.
- 11 K. W. Frese, *J. Electrochem. Soc.*, 1991, **138**, 3338.
- 12 M. Hara, T. Kondo, M. Komoda, S. Ikeda, J. N. Kondo, K. Domen, M. Hara, K. Shinohara and A. Tanaka, *Chem. Commun.*, 1998, **8**, 357–358.
- 13 S. Kakuta and T. Abe, *Electrochem. Solid-State Lett.*, 2009, **12**, P1.
- 14 K. L. Sowers and A. Fillinger, *J. Electrochem. Soc.*, 2009, **156**, F80.
- 15 M. Le, M. Ren, Z. Zhang, P. T. Sprunger, R. L. Kurtz and J. C. Flake, *J. Electrochem. Soc.*, 2011, **158**, E45.
- 16 H. Gerischer, *J. Electroanal. Chem. Interfacial Electrochem.*, 1977, **82**, 133–143.
- 17 M. Harb, D. Masih and K. Takanahe, *Phys. Chem. Chem. Phys.*, 2014, **16**, 18198–18204.
- 18 B. Beverskog and I. Puigdomenech, *Corros. Sci.*, 1997, **39**, 43–57.
- 19 J. Gu, Y. Yan, J. W. Krizan, Q. D. Gibson, Z. M. Detweiler, R. J. Cava and A. B. Bocarsly, *J. Am. Chem. Soc.*, 2014, **136**, 830–833.
- 20 M. S. Prévot, N. Guijarro and K. Sivula, *ChemSusChem*, 2015, **8**, 1359–1367.
- 21 A. K. Díaz-García, T. Lana-Villarreal and R. Gómez, *J. Mater. Chem. A*, 2015, **3**, 19683–19687.
- 22 M. S. Prévot, Y. Li, N. Guijarro and K. Sivula, *J. Mater. Chem. A*, 2016, **4**, 3018–3026.
- 23 B. Zoellner, S. Stuart, C.-C. Chung, D. B. Dougherty, J. L. Jones and P. A. Maggard, *J. Mater. Chem. A*, 2016, **4**, 3115–3126.
- 24 S. Omeiri, Y. Gabes, A. Bouguelia and M. Trari, *J. Electroanal. Chem.*, 2008, **614**, 31–40.
- 25 U. Kang, S. K. Choi, D. J. Ham, S. M. Ji, W. Choi, D. S. Han, A. Abdel-Wahab and H. Park, *Energy Environ. Sci.*, 2015, **8**, 2638–2643.
- 26 C. G. Read, Y. Park and K.-S. Choi, *J. Phys. Chem. Lett.*, 2012, **3**, 1872–1876.
- 27 J. Wang, Y.-J. Lee and J. W. P. Hsu, *J. Mater. Chem. C*, 2016, **4**, 3607–3613.
- 28 B. Das, A. Renaud, A. M. Volosin, L. Yu, N. Newman and D.-K. Seo, *Inorg. Chem.*, 2015, **54**, 1100–1108.
- 29 S. Y. Choi, C.-D. Kim, D. S. Han and H. Park, *J. Mater. Chem. A*, 2017, **5**, 10165–10172.
- 30 A. Kay, I. Cesar and M. Grätzel, *J. Am. Chem. Soc.*, 2006, 15714–15721.
- 31 V. V. Pavlishchuk and A. W. Addison, *Inorganica Chim. Acta*, 2000, **298**, 97–102.
- 32 U. A. Joshi and P. A. Maggard, *J. Phys. Chem. Lett.*, 2012, **3**, 1577–1581.
- 33 M. S. Prévot, Y. Li, N. Guijarro and K. Sivula, *J. Mater. Chem. A*, 2016, **4**, 3018–3026.
- 34 J. Gu, A. Wuttig, J. W. Krizan, Y. Hu, Z. M. Detweiler, R. J. Cava and A. B. Bocarsly, *J. Phys. Chem. C*, 2013, **117**, 12415–12422.
- 35 U. Kang and H. Park, *J. Mater. Chem. A*, 2017, **5**, 2123–2131.
- 36 O. Yehezkeli, N. M. Bedford, E. Park, K. Ma and J. N. Cha, *ChemSusChem*, 2016, **9**, 3188–3195.
- 37 X. Yang, E. A. Fugate, Y. Mueanngern and L. R. Baker, *ACS Catal.*, 2017, **7**, 177–180.

- 38 U. Kang, S. H. Yoon, D. S. Han and H. Park, *ACS Energy Lett.*, 2019, **4**, 2075–2080.
- 39 J. Yuan, L. Yang and C. Hao, *Int. J. Electrochem. Sci.*, 2019, **14**, 8569–8578.
- 40 J. Yuan, L. Yang and C. Hao, *J. Electrochem. Soc.*, 2019, **166**, H718–H720.
- 41 S. Bassaid, M. Chaib, S. Omeiri, A. Bouguelia and M. Trari, *J. Photochem. Photobiol. A Chem.*, 2009, **201**, 62–68.
- 42 W. C. Sheets, E. Mugnier, A. Barnabe, T. J. Marks and K. R. Poeppelmeier, *Chem. Mater.*, 2006, **18**, 7–20.
- 43 A. B. Garg and R. Rao, *Crystals*, 2018, **8**, 255.
- 44 R. Daou, R. Frésard, V. Eyert, S. Hébert and A. Maignan, *Sci. Technol. Adv. Mater.*, 2017, **18**, 919–938.
- 45 A. P. Mackenzie, *Reports Prog. Phys.*, 2017, **80**, 032501.
- 46 M. Kumar, H. Zhao and C. Persson, *Semicond. Sci. Technol.*, 2013, **28**, 065003.
- 47 M. Yu, T. I. Draskovic and Y. Wu, *Phys. Chem. Chem. Phys.*, 2014, **16**, 5026.
- 48 A. P. Amrute, Z. Łodziana, C. Mondelli, F. Krumeich and J. Pérez-Ramírez, *Chem. Mater.*, 2013, **25**, 4423–4435.
- 49 A. Derbal, S. Omeiri, A. Bouguelia and M. Trari, *Int. J. Hydrogen Energy*, 2008, **33**, 4274–4282.
- 50 A. Y. Cherif, O. Arous, M. Amara, S. Omeiri, H. Kerdjoudj and M. Trari, *J. Hazard. Mater.*, 2012, **227**, 386–393.
- 51 S. H. Yoon, U. Kang, H. Park, A. Abdel-Wahab and D. S. Han, *Catal. Today*, 2019, **335**, 345–353.
- 52 Q.-L. Liu, Z.-Y. Zhao, R.-D. Zhao and J.-H. Yi, *J. Alloys Compd.*, 2020, **819**, 153032.
- 53 M. Ferri, J. Elliott, M. Farnesi Camellone, S. Fabris and S. Piccinin, *J. Phys. Chem. C*, 2019, **123**, 29589–29598.
- 54 M. Younsi, A. Aider, A. Bouguelia and M. Trari, *Sol. Energy*, 2005, **78**, 574–580.
- 55 Q. Xu, R. Li, C. Wang and D. Yuan, *J. Alloys Compd.*, 2017, **723**, 441–447.
- 56 S. Lee, U. Kang, G. Piao, S. Kim, D. S. Han and H. Park, *Appl. Catal. B Environ.*, 2017, **207**, 35–41.
- 57 Y. J. Jang, Y. Bin Park, H. E. Kim, Y. H. Choi, S. H. Choi and J. S. Lee, *Chem. Mater.*, 2016, **28**, 6054–6061.
- 58 X. Cheng, J. Ding, Y. Wu, H. Liu and G. Dawson, *Chem. Phys.*, 2018, **513**, 241–245.
- 59 T. Jiang, Y. Zhao and H. Xue, *J. Mater. Sci.*, 2019, **54**, 11951–11958.
- 60 K. Karmakar, A. Sarkar, K. Mandal and G. G. Khan, *Nanotechnology*, 2017, **28**, 325401.
- 61 F. A. Benko and F. P. Koffyberg, *Mater. Res. Bull.*, 1986, **21**, 753–757.
- 62 S. Saadi, A. Bouguelia and M. Trari, *Sol. Energy*, 2006, **80**, 272–280.
- 63 W. Ketir, A. Bouguelia and M. Trari, *J. Hazard. Mater.*, 2008, **158**, 257–263.
- 64 W. Ketir, A. Bouguelia and M. Trari, *Water. Air. Soil Pollut.*, 2009, **199**, 115–122.
- 65 W. Ketir, A. Bouguelia and M. Trari, *Desalination*, 2009, **244**, 144–152.
- 66 W. Ketir, S. Saadi and M. Trari, *J. Solid State Electrochem.*, 2012, **16**, 213–218.
- 67 S. Zhou, X. Fang, Z. Deng, D. Li, W. Dong, R. Tao, G. Meng, T. Wang and X. Zhu, *J. Cryst. Growth*, 2008, **310**, 5375–5379.
- 68 D. Li, X. Fang, A. Zhao, Z. Deng, W. Dong and R. Tao, *Vacuum*, 2010, **84**, 851–856.
- 69 T. S. Tripathi, J.-P. Niemelä and M. Karppinen, *J. Mater. Chem. C*, 2015, **3**, 8364–8371.
- 70 J. Crépellière, P. L. Popa, N. Bahlawane, R. Leturcq, F. Werner, S. Siebentritt and D. Lenoble, *J. Mater. Chem. C*, 2016, **4**, 4278–4287.
- 71 T. Ahmad, R. Phul, P. Alam, I. H. Lone, M. Shahazad, J. Ahmed, T. Ahamad and S. M. Alshehri, *RSC Adv.*, 2017, **7**, 27549–27557.
- 72 C. E. Creissen, J. Warnan and E. Reisner, *Chem. Sci.*, 2018, **9**, 1439–1447.
- 73 A. Varga, G. F. Samu and C. Janáky, *Electrochim. Acta*, 2018, **272**, 22–32.
- 74 S. Dursun, I. C. Kaya, V. Kalem and H. Akyildiz, *Dalt. Trans.*, 2018, **47**, 14662–14678.
- 75 I. C. Kaya, S. Akin, H. Akyildiz and S. Sonmezoglu, *Sol. Energy*, 2018, **169**, 196–205.
- 76 Y. Ma, X. Zhou, Q. Ma, A. Litke, P. Liu, Y. Zhang, C. Li and E. J. M. Hensen, *Catal. Letters*, 2014, **144**, 1487–1493.
- 77 P. Zhang, Y. Shi, M. Chi, J.-N. Park, G. D. Stucky, E. W. McFarland and L. Gao, *Nanotechnology*, 2013, **24**, 345704.
- 78 Z. Y. Liu, G. Y. Wang, X. P. Liu and Y. J. Wang, *Ranliao Huaxue Xuebao/Journal Fuel Chem. Technol.*, 2013, **41**, 1473–1480.
- 79 D. Xiong, H. Chang, Q. Zhang, S. Tian, B. Liu and X. Zhao, *Appl. Surf. Sci.*, 2015, **347**,

- 747–754.
- 80 W. Ketir, M. Trari and Y. Bessekhoud, *Renew. Energy*, 2014, **69**, 1–6.
- 81 W. Ketir, G. Rekhila, M. Trari and A. Amrane, *J. Environ. Sci.*, 2012, **24**, 2173–2179.
- 82 M. F. Kuehnel, C. E. Creissen, C. D. Sahm, D. Wielend, A. Schlosser, K. L. Orchard and E. Reisner, *Angew. Chemie Int. Ed.*, 2019, **58**, 5059–5063.
- 83 C. E. Creissen, J. Warnan, D. Antón-García, Y. Farré, F. Odobel and E. Reisner, *ACS Catal.*, 2019, **9**, 9530–9538.
- 84 X. D. Zhu, J. Tian, S. R. Le, J. R. Chen and K. N. Sun, *Mater. Lett.*, 2013, **107**, 147–149.
- 85 L. Shao, K. Wu, X. Lin, M. Shui, R. Ma, D. Wang, N. Long, Y. Ren and J. Shu, *J. Electroanal. Chem.*, 2014, **717–718**, 153–156.
- 86 P. Wang, P. Li, T.-F. Yi, X. Lin, Y.-R. Zhu, L. Shao, M. Shui, N. Long and J. Shu, *Ceram. Int.*, 2015, **41**, 6668–6675.
- 87 S. Akin, Y. Liu, M. I. Dar, S. M. Zakeeruddin, M. Grätzel, S. Turan and S. Sonmezoglu, *J. Mater. Chem. A*, 2018, **6**, 20327–20337.
- 88 J. Duan, Y. Zhao, Y. Wang, X. Yang and Q. Tang, *Angew. Chemie - Int. Ed.*, 2019, **58**, 16147–16151.
- 89 S. Powar, D. Xiong, T. Daeneke, M. T. Ma, A. Gupta, G. Lee, S. Makuta, Y. Tachibana, W. Chen, L. Spiccia, Y. B. Cheng, G. Götz, P. Bäuerle and U. Bach, *J. Phys. Chem. C*, 2014, **118**, 16375–16379.
- 90 D. Xiong, Z. Xu, X. Zeng, W. Zhang, W. Chen, X. Xu, M. Wang and Y.-B. Cheng, *J. Mater. Chem.*, 2012, **22**, 24760–24768.
- 91 P. W. Sadik, M. Ivill, V. Craciun and D. P. Norton, *Thin Solid Films*, 2009, **517**, 3211–3215.
- 92 J. Wang, T. B. Daunis, L. Cheng, B. Zhang, J. Kim and J. W. P. Hsu, *ACS Appl. Mater. Interfaces*, 2018, **10**, 3732–3738.
- 93 M. T. N. Koriche, A. Bouguelia, A. Aider, *Int. J. Hydrogen Energy*, 2005, **30**, 693–699.
- 94 R. Brahim, Y. Bessekhoud, A. Bouguelia and M. Trari, *J. Photochem. Photobiol. A Chem.*, 2007, **186**, 242–247.
- 95 J. R. Smith, T. H. Van Steenkiste and X.-G. Wang, *Phys. Rev. B*, 2009, **79**, 041403.
- 96 N. Benreguia, S. Omeiri, B. Bellal and M. Trari, *J. Hazard. Mater.*, 2011, **192**, 1395–1400.
- 97 R. Brahim, Y. Bessekhoud, N. Nasrallah and M. Trari, *J. Hazard. Mater.*, 2012, **219–220**, 19–25.
- 98 Y. Oh, W. Yang, J. Tan, H. Lee, J. Park and J. Moon, *Nanoscale*, 2018, **10**, 3720.
- 99 R. Hinogami, K. Toyoda, M. Aizawa, S. Yoshii, T. Kawasaki and H. Gyoten, *Electrochem. commun.*, 2013, **35**, 142–145.
- 100 A. Nattestad, *J. Photonics Energy*, 2011, **1**, 011103.
- 101 H. Kawazoe, M. Yasukawa, H. Hyodo, M. Kurita, H. Yanagi and H. Hosono, *Nature*, 1997, **389**, 939–942.
- 102 J. Ding, Y. Sui, W. Fu, H. Yang, B. Zhao and M. Li, *Nanotechnology*, 2011, **22**, 295706.
- 103 J. Ding, H. Yang and W. Deng, *Superlattices Microstruct.*, 2014, **70**, 33–38.
- 104 H. F. Jiang, X. B. Zhu, H. C. Lei, G. Li, Z. R. Yang, W. H. Song, J. M. Dai, Y. P. Sun and Y. K. Fu, *J. Alloys Compd.*, 2011, **509**, 1768–1773.
- 105 J. Ding, Y. Sui, W. Fu, H. Yang, S. Liu, Y. Zeng, W. Zhao, P. Sun, J. Guo, H. Chen and M. Li, *Appl. Surf. Sci.*, 2010, **256**, 6441–6446.
- 106 A. N. Banerjee and K. K. Chattopadhyay, *J. Appl. Phys.*, 2005, **97**, 084308.
- 107 F. A. Benko and F. P. Koffyberg, *J. Phys. Chem. Solids*, 1984, **45**, 57–59.
- 108 R. Brahim, M. Trari, A. Bouguelia and Y. Bessekhoud, *J. Solid State Electrochem.*, 2010, **14**, 1333–1338.
- 109 J. Tate, H. L. Ju, J. C. Moon, A. Zakutayev, A. P. Richard, J. Russell and D. H. McIntyre, *Phys. Rev. B*, 2009, **80**, 165206.
- 110 J. Pellicer-Porres, A. Segura, A. S. Gilliland, A. Muñoz, P. Rodríguez-Hernández, D. Kim, M. S. Lee and T. Y. Kim, *Appl. Phys. Lett.*, 2006, **88**, 2–5.
- 111 A. N. Banerjee, R. Maity and K. K. Chattopadhyay, *Mater. Lett.*, 2004, **58**, 10–13.
- 112 R.-S. Yu, S.-C. Liang, C.-J. Lu, D.-C. Tasi and F.-S. Shieu, *Appl. Phys. Lett.*, 2007, **90**, 191117.
- 113 N. N. Som, V. Sharma, V. Mankad, M. L. C. Attygalle and P. K. Jha, *Sol. Energy*, 2019, **193**, 799–805.
- 114 J. Pellicer-Porres, A. Segura, A. S. Gilliland, A. Muñoz, P. Rodríguez-Hernández, D.

- Kim, M. S. Lee and T. Y. Kim, *Appl. Phys. Lett.*, 2006, **88**, 181904.
- 115 J. Shook, P. D. Borges, L. M. Scolfaro and W. J. Geerts, *J. Appl. Phys.*, 2019, **126**, 075702.
- 116 R. Laskowski, N. E. Christensen, P. Blaha and B. Palanivel, *Phys. Rev. B*, 2009, **79**, 165209.
- 117 L.-J. Shi, Z.-J. Fang and J. Li, *J. Appl. Phys.*, 2008, **104**, 73527.
- 118 F. Khmaissia, H. Frigui, M. Sunkara, J. Jasinski, A. M. Garcia, T. Pace and M. Menon, *Comput. Mater. Sci.*, 2018, **147**, 304–315.
- 119 K. Toyoda, R. Hinogami, N. Miyata and M. Aizawa, *J. Phys. Chem. C*, 2015, **119**, 6495–6501.
- 120 K. T. Jacob, T. H. Okabe, T. Uda and Y. Waseda, *Bull. Mater. Sci.*, 1999, **22**, 741–749.
- 121 S. Shibasaki, W. Kobayashi and I. Terasaki, *Phys. Rev. B*, 2006, **74**, 235110.
- 122 T. K. Le, D. Flahaut, H. Martinez, N. Andreu, D. Gonbeau, E. Pachoud, D. Pelloquin and A. Maignan, *J. Solid State Chem.*, 2011, **184**, 2387–2392.
- 123 T. Elkhouni, M. Amami, E. K. Hlil and A. Ben Salah, *J. Supercond. Nov. Magn.*, 2013, **26**, 2353–2360.
- 124 T. Elkhouni, M. Amami, E. K. Hlil and A. Ben Salah, *J. Supercond. Nov. Magn.*, 2016, **29**, 547–555.
- 125 B.-O. Marinder, P.-E. Werner, E. Wahlström, G. Malmros, J. Sjöblom, T. G. Strand and V. F. Sukhoverkhov, *Acta Chem. Scand.*, 1980, **34a**, 51–56.
- 126 E. Wahlström and B.-O. Marinder, *Inorg. Nucl. Chem. Lett.*, 1977, **13**, 559–564.
- 127 S. Yamazoe, S. Yanagimoto and T. Wada, *Phys. status solidi - Rapid Res. Lett.*, 2011, **5**, 153–155.
- 128 V. Pralong, M. A. Reddy, V. Caignaert, S. Malo, O. I. Lebedev, U. V Varadaraju and B. Raveau, *Chem. Mater.*, 2011, **23**, 1915–1922.
- 129 U. A. Joshi, A. M. Palasyuk and P. A. Maggard, *J. Phys. Chem. C*, 2011, **115**, 13534–13539.
- 130 N. Priyadarshani, T. C. Sabari Girisun and S. Venugopal Rao, *Chem. Phys. Lett.*, 2017, **681**, 95–100.
- 131 F. A. da Silva, I. Dancini-Pontes, M. DeSouza and N. R. C. Fernandes, *React. Kinet. Mech. Catal.*, 2017, **122**, 557–574.
- 132 P. P. Sahoo and P. A. Maggard, *Inorg. Chem.*, 2013, **52**, 4443–4450.
- 133 N. King, P. P. Sahoo, L. Fuoco, S. Stuart, D. Dougherty, Y. Liu and P. A. Maggard, *Chem. Mater.*, 2014, **26**, 2095–2104.
- 134 X. Liu, W. Que, Y. Xing, X. Yin, Y. He and H. M. A. Javed, *J. Cryst. Growth*, 2015, **419**, 149–152.
- 135 N. Priyadarshani, T. C. Sabari Girisun and S. Venugopal Rao, *Mater. Chem. Phys.*, 2018, **220**, 342–350.
- 136 G. Neri, M. Forster, J. J. Walsh, C. M. Robertson, T. J. Whittles, P. Farràs and A. J. Cowan, *Chem. Commun.*, 2016, **52**, 14200–14203.
- 137 M. F. Kuehnel, C. D. Sahm, G. Neri, J. R. Lee, K. L. Orchard, A. J. Cowan and E. Reisner, *Chem. Sci.*, 2018, **9**, 2501–2509.
- 138 L. Zhang and J. M. Cole, *ACS Appl. Mater. Interfaces*, 2015, **7**, 3427–3455.
- 139 S. P. Pujari, L. Scheres, A. T. M. Marcelis and H. Zuilhof, *Angew. Chemie - Int. Ed.*, 2014, **53**, 6322–6356.
- 140 S. A. Paniagua, A. J. Giordano, O. L. Smith, S. Barlow, H. Li, N. R. Armstrong, J. E. Pemberton, J. L. Brédas, D. Ginger and S. R. Marder, *Chem. Rev.*, 2016, **116**, 7117–7158.
- 141 G. Guerrero, J. G. Alauzun, M. Granier, D. Laurencin and P. H. Mutin, *Dalt. Trans.*, 2013, **42**, 12569–12585.
- 142 K. Maeda, *Adv. Mater.*, 2019, **31**, 1808205.
- 143 R. Boissezon, J. Muller, V. Beaugeard, S. Monge and J.-J. Robin, *RSC Adv.*, 2014, **4**, 35690.
- 144 H. Kumagai, G. Sahara, K. Maeda, M. Higashi, R. Abe and O. Ishitani, *Chem. Sci.*, 2017, **8**, 4242–4249.
- 145 K. C. Christoforidis and P. Fornasiero, *ChemCatChem*, 2019, **11**, 368–382.
- 146 Z. Xu, J. Jiang, Q. Zhang, G. Chen, L. Zhou and L. Li, *J. Colloid Interface Sci.*, 2020, **563**, 131–138.
- 147 N. P. de Moraes, F. A. Torezin, G. V. Jucá Dantas, J. G. M. de Sousa, R. B. Valim, R. da Silva Rocha, R. Landers, M. L. C. P. da Silva and L. A. Rodrigues, *Ceram. Int.*,

- 2020, **46**, 14505–14515.
- 148 W.-J. Chen, X. Sun, Y. Liu, M. Huang, W. Xu, X. Pan, Q. Wu and Z. Yi, *ACS Appl. Nano Mater.*, 2020, **3**, 2573–2581.
- 149 Q. Dai, B. Yuan, M. Guo, K. Zhang, X. Chen, Z. Song, T. T. Nguyen, X. Wang, S. Lin, J. Fan, Y. Li, H. Liu and Z. Guo, *Ceram. Int.*, 2020, **46**, 13210–13218.
- 150 M. Thommes, K. Kaneko, A. V. Neimark, J. P. Olivier, F. Rodriguez-Reinoso, J. Rouquerol and K. S. W. Sing, *Pure Appl. Chem.*, 2015, **87**, 1051–1069.
- 151 S. Ikeda, T. Takata, M. Komoda, M. Hara, J. N. Kondo, K. Domen, A. Tanaka, H. Hosono and H. Kawazoe, *Phys. Chem. Chem. Phys.*, 1999, **1**, 4485–4491.
- 152 S. Ikeda, A. Tanaka, H. Hosono, H. Kawazoe, M. Hara, J. N. Kondo and K. Domen, *Stud. Surf. Sci. Catal.*, 1999, **121**, 301–304.
- 153 K. Domen, S. Ikeda, T. Takata, A. Tanaka, M. Hara and J. N. Kondo, *Appl. Energy*, 2000, **67**, 159–179.
- 154 A. L. Linsebigler, G. Lu and J. T. Yates, *Chem. Rev.*, 1995, **95**, 735–758.
- 155 G. Wang, H. Wang, Y. Ling, Y. Tang, X. Yang, R. C. Fitzmorris, C. Wang, J. Z. Zhang and Y. Li, *Nano Lett.*, 2011, **11**, 3026–3033.
- 156 K. L. Ciesinski, K. L. Haas and K. J. Franz, *Dalt. Trans.*, 2010, **39**, 9538–9546.
- 157 Y. Zhang, Y. Yan, J. Wang and J. Huang, *RSC Adv.*, 2016, **6**, 33295–33301.
- 158 Y. Zhang, X. Gao, Y. Yan, J. Wang and J. Huang, *RSC Adv.*, 2016, **6**, 101725–101730.
- 159 A. Nakada, T. Nakashima, K. Sekizawa, K. Maeda and O. Ishitani, *Chem. Sci.*, 2016, **7**, 4364–4371.
- 160 J. C. Wang, H. C. Yao, Z. Y. Fan, L. Zhang, J. S. Wang, S. Q. Zang and Z. J. Li, *ACS Appl. Mater. Interfaces*, 2016, **8**, 3765–3775.
- 161 P. Natarajan and J. F. Endicott, *J. Phys. Chem.*, 1973, **77**, 2049–2054.
- 162 R. Wang, H. An, H. Zhang, X. Zhang, J. Feng, T. Wei and Y. Ren, *Appl. Surf. Sci.*, 2019, **484**, 1118–1127.
- 163 D. Xiong, Z. Xu, X. Zeng, W. Zhang, W. Chen, X. Xu, M. Wang and Y.-B. Cheng, *J. Mater. Chem.*, 2012, **22**, 24760.
- 164 Y. Oh, W. Yang, J. Tan, H. Lee, J. Park and J. Moon, *Nanoscale*, 2018, **10**, 3720–3729.
- 165 B.-Y. Hwang, S. Sakthinathan and T.-W. Chiu, *Int. J. Hydrogen Energy*, 2019, **44**, 2848–2856.
- 166 Y. S. Zou, H. P. Wang, S. L. Zhang, D. Lou, Y. H. Dong, X. F. Song and H. B. Zeng, *RSC Adv.*, 2014, **40**, 41294–41300.
- 167 T. W. Chiu, J. H. Shih and C. H. Chang, *Thin Solid Films*, 2016, **618**, 151–158.
- 168 I. C. Kaya and H. Akyildiz, *Phys. Status Solidi Appl. Mater. Sci.*, 2018, **215**, 1700795.
- 169 Y. H. Lin, B. S. Yu, C. M. Lei, Y. Fu, J. H. Park and T. W. Chiu, *Thin Solid Films*, 2018, **660**, 705–710.

6

Conclusions and Future Work

In this thesis, the synthesis, characterisation and photocatalytic activity of a range of organic and inorganic semiconductors towards H₂ evolution and CO₂ reduction, as both simple and hybrid systems, has been studied.

In Chapter 3, the synthesis of a range of carbon nitride materials using different calcination conditions and precursors was investigated. This resulted in the synthesis of 16 carbon nitrides with slightly differing properties and quite varied photocatalytic activities. The 16 materials could be split into 5 different groups based upon their synthesis; copolymerisation of dicyandiamide with barbituric acid (CN-BA), use of different precursor materials (CN-Precursor), variation of ratios of 2 precursors (CN-UT) and variations in calcination times and temperatures (CN-Time and CN-Temp). Characterisation via CHN, BET surface area, PXRD, SEM, DRIFTS, Raman, XPS, SS NMR and UV-Vis, was performed in an attempt to fully understand the materials and the clear differences observed in their photocatalytic activity. Photocatalytic activity for H₂ evolution was evaluated in the presence of a 1 wt% Pt co-catalyst and EDTA hole scavenger. The two most interesting groups of materials with the greatest variation in activities towards H₂ evolution were the CN-UT and CN-BA series. However, it was determined that the CN-UT series difference in activity was likely following a trend with variations in surface area. The CN-BA series, on the other hand, showed no such trend with any properties measured using the initial characterisation techniques, despite variations in band gap and surface area and potentially band gap. To delve further into understanding the variations in activity across the CN-BA series, PL emission spectroscopy, TAS, TR³, MS method and XPS were employed, of which TR³ has not been previously reported for carbon nitride materials. From these methods it was found that there was a strong correlation in activity with charge lifetimes and band structure, specifically the PL emission lifetimes and XPS/UV-Vis measurements were key to understanding the variations in photocatalytic activity.

Within the CN-BA series, CN-DCDA was found to have the lowest photocatalytic activity due to short charge lifetimes and a relatively large band gap. It was found that by incorporating a small amount of barbituric acid into the structure, for CN-BA(5), the charge lifetimes were increased and the band gap was decreased, which caused an upshift in both CB and VB. This means that the material could absorb photons over a greater wavelength range, utilising a

larger portion of visible light. The photogenerated charges would then have a greater probability of reaching the surface, where they would then be able to transfer to adsorbed species and have a greater driving force for reduction reactions. By adding more barbituric acid it was found that the charge lifetimes decreased, and band positions were further shifted causing decreases in activity, for materials CN-BA(10) and CN-BA(20). Though this series of materials had previously been reported, full characterisation of the whole series was not investigated, only the band structure of the 0% and 20% barbituric acid samples had been determined and the lifetimes of photogenerated charges were not explored and the paper only gave a very brief explanation as to the variations in photocatalytic activity. Despite the substantial number of publications on carbon nitride materials, very little is still understood about its structure and photocatalytic behaviour. Though unable to extract any further understanding on the chemical structure of the synthesised carbon nitrides, this chapter highlights the importance of full sets of characterisation data, using a wide range of techniques, especially band structure and charge lifetime determination for all samples in a series to be able to understand any enhancements or reduction in photocatalytic activity.

Chapter 4 builds upon the work presented in Chapter 3 and explores different methods for the modification of carbon nitride materials towards the improvement of photocatalytic activity for both H₂ production and CO₂ reduction. From initial screening experiments, it was observed that none of the bulk carbon nitride hybrid catalysts were capable of CO₂ reduction, which was thought to be due to low surface areas limiting co-catalyst attachment. As the CN-BA series was determined to be the most interesting set of materials in Chapter 3 it was decided that the materials would be carried forward for further modification. The CN-BA series were modified by thermal exfoliation and were found to have between 13- and 22-times larger surface areas which gave up to 16 times enhancement in photocatalytic H₂ evolution in the presence of a Pt co-catalyst and EDTA scavenger. These higher surface area materials were then successfully combined with FeTCPP molecular co-catalysts and tested for CO₂ reduction in the presence of TEOA as a hole scavenger. Within this series of hybrid materials, it was determined that 3 of the 4 hybrid materials were capable of CO₂ reduction to CO and H₂ with >60% selectivity towards CO production. The highest activity was achieved by HSA-CN-BA(5)/FeTCPP with variations in activity agreeing well with the band structures and charge lifetimes determined in

the previous chapter. Control and isotopically labelled experiments confirmed that the CO produced was via photocatalytic CO₂ reduction. However, these experiments also indicated that between 4 and 24 hours of illumination that the TEOA was being consumed, leading to the formation of ¹²CO₂ which was going on to be reduced, forming more CO. Further work is required to fully understand the materials and photocatalytic mechanism, including time resolved studies in the presence of scavengers and additional isotopically labelled experiments. The degradation of organic charge scavengers is something that is known within the literature but is not well discussed or reported on. Nor is it common practice to perform time course experiments along with isotopically labelled experiments of different lengths to gain greater understanding of changes in product formation. Although this system has been explored by another group, this work explores how the variations in band structure effect the activity of the hybrid system with known catalyst loadings, which has not been studied previously. Furthermore, the hybrid system presented in this chapter produce CO in mainly aqueous solutions with >60% selectivities.

Chapter 5 explores the synthesis and characterisation of 6 different Cu(I) metal oxides (CuFeO₂, CuCrO₂, CuAlO₂, CuRhO₂, CuNbO₃ and CuNb₃O₈). The materials were initially tested for H₂ evolution in the presence of a Pt co-catalyst and EDTA hole scavenger and CuNb₃O₈ was found to be the most active. When testing these materials as photocatalyst towards CO₂ reduction it was found that none of the catalysts in combination with NiCycP were capable of doing so. This is believed to be due to low surface areas leading to little/no catalyst attachment, which was also observed in Chapter 4 for the carbon nitrides. Moreover, these tests and the control experiments that were performed indicated that the EDTA hole scavenger was itself acting as a photoactive system, which is something that is not widely reported in the literature. Additional characterisation of charge lifetimes may allow us to elucidate why low/no activity was observed for some materials. Future work would be to produce higher surface area materials, which could then be re-evaluated for photocatalytic H₂ production and CO₂ reduction in the absence and presence of molecular co-catalysts. Though no significant photocatalytic activity was observed for any of the metal oxides explored within this work, it does emphasise the importance of good understanding of each part of the photocatalytic system which can only be gleaned from thorough and rigorous control experiments.

The ultimate goal of this project would be to create heterojunction systems capable of performing CO₂ reduction and overall water splitting without the use of scavengers. This could be achieved by taking and improving upon any active materials determined from this study and combining with an active water oxidation system in a z-scheme type system. Within this work, the material that has been determined to be the most promising photocatalytic system towards CO₂ reduction is HSA-CN-BA(5)/FeTCCP. As the band structure of this system has been determined, an appropriate water oxidation catalyst could be identified. For example, this material could be combined with a water oxidation photocatalysts such as Fe₂O₃ or WO₃, for a z-scheme system capable of CO₂ reduction and overall water splitting. This is possible as they have the appropriate band structures which would allow for charge transfer to occur via a Z-scheme mechanism. By combining these materials, the system should be capable of performing the photocatalytic reactions in the absence of any scavengers.

Appendix

i.i Carbon Nitride XPS Surface States Spectra

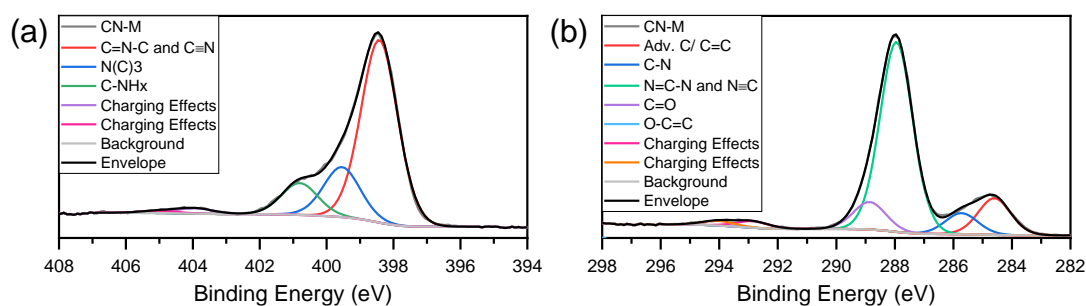


Figure 119 - High resolution deconvolution of N1s (a) and C1s (b) spectra for CN-M.

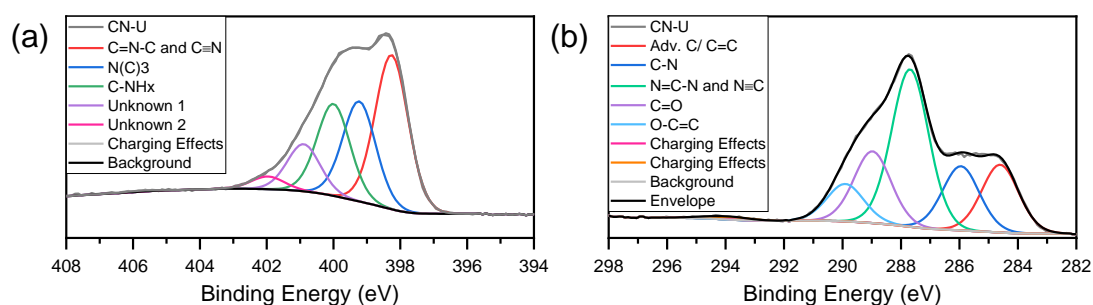


Figure 120 - High resolution deconvolution of N1s (a) and C1s (b) spectra for CN-U.

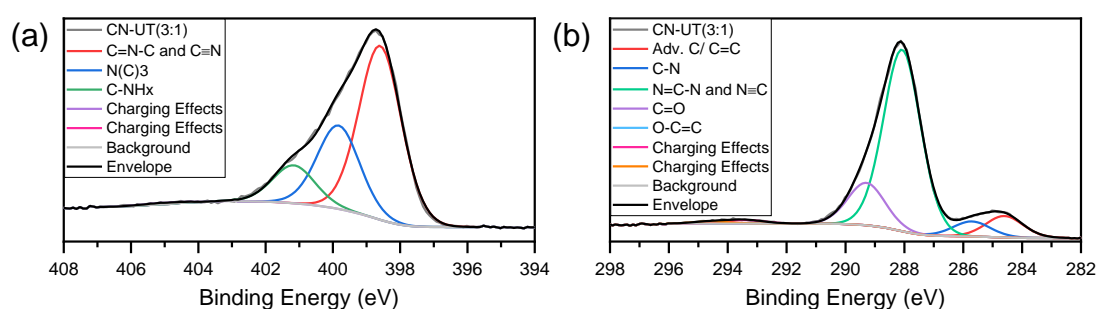


Figure 121 - High resolution deconvolution of N1s (a) and C1s (b) spectra for CN-UT(3:1).

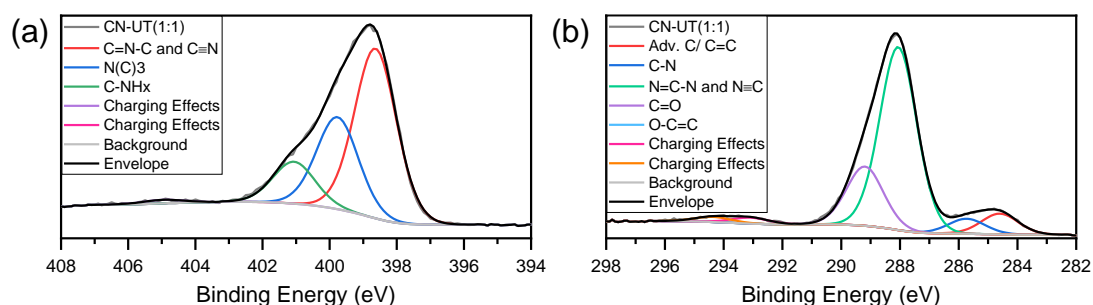


Figure 122 - High resolution deconvolution of N1s (a) and C1s (b) spectra for CN-UT(1:1).

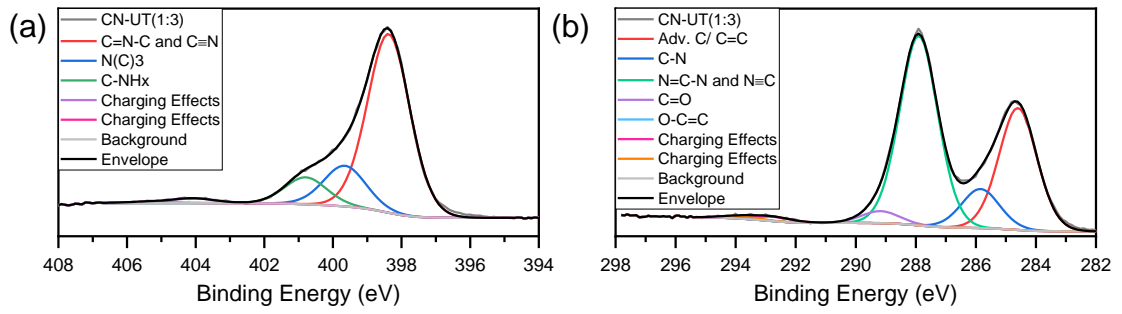


Figure 123 - High resolution deconvolution of N1s (a) and C1s (b) spectra for CN-UT(1:3).

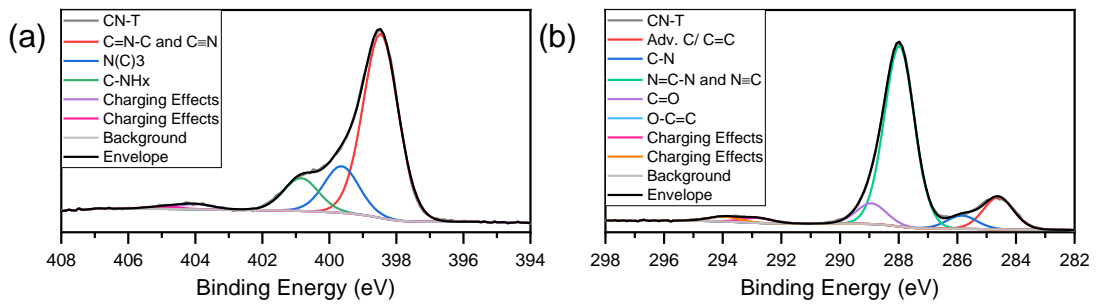


Figure 124 - High resolution deconvolution of N1s (a) and C1s (b) spectra for CN-T.

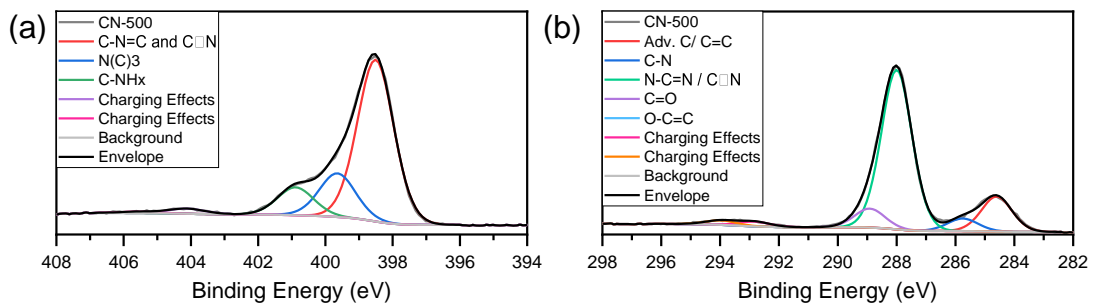


Figure 125 - High resolution deconvolution of N1s (a) and C1s (b) spectra for CN-500.

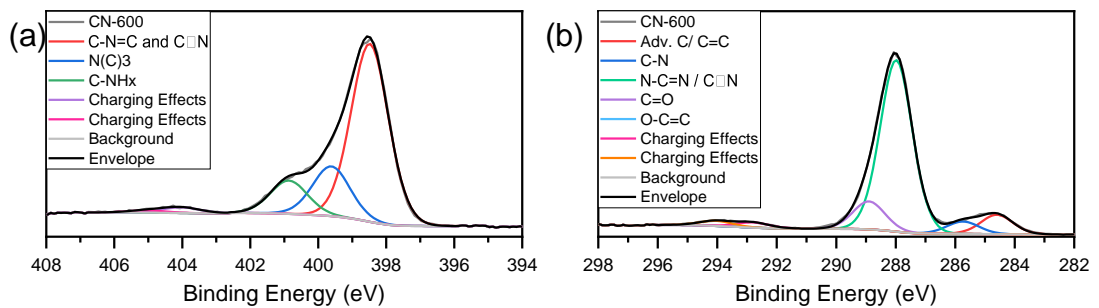


Figure 126 - High resolution deconvolution of N1s (a) and C1s (b) spectra for CN-600.

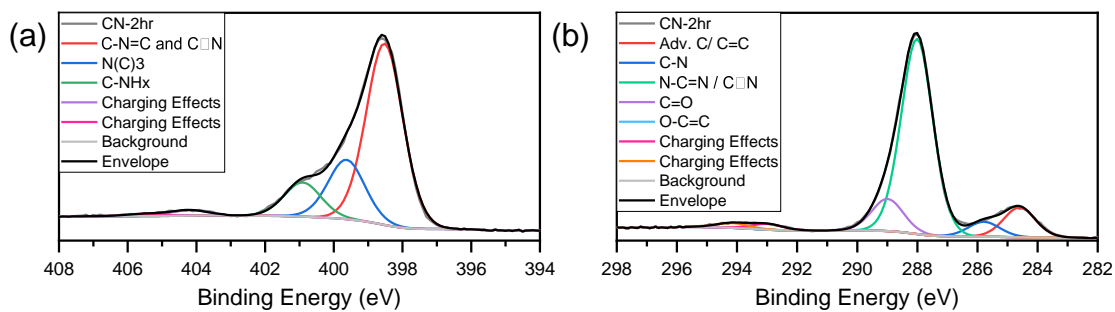


Figure 127 - High resolution deconvolution of N1s (a) and C1s (b) spectra for CN-2hr.

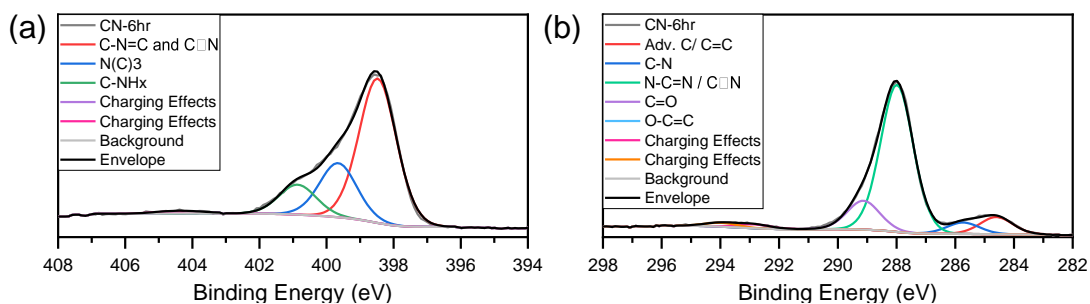


Figure 128 - High resolution deconvolution of N1s (a) and C1s (b) spectra for CN-6hr.

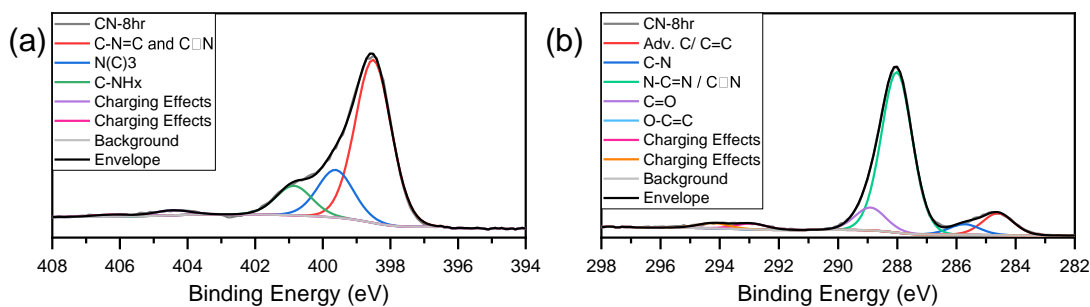


Figure 129 - High resolution deconvolution of N1s (a) and C1s (b) spectra for CN-8hr.

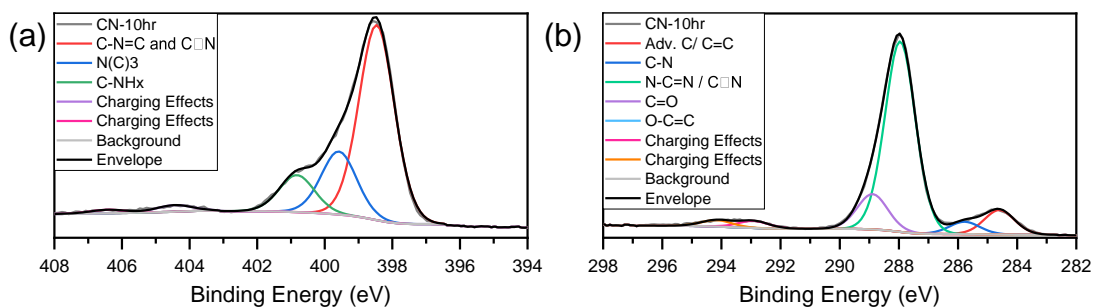


Figure 130 - High resolution deconvolution of N1s (a) and C1s (b) spectra for CN-10hr.